MAGNETORHEOLOGY OF HEAVY OIL-FERROFLUID MIXTURES.

Study of the magnetorheological behavior and magnetic-induced microstructure of heavy crude oils and ferrofluids mixtures

Maria Daniela Contreras Mateus

A thesis submitted to the School of Chemical Engineering in Partial Fulfillment of the Requirements for the Degree of Doctor in Chemical Engineering

Supervisors

Professor Arlex Chaves Guerrero

PhD in Chemical Engineering

Professor Francisco Homero Sánchez

PhD in Physics

Universidad Industrial de Santander

Faculty of Physicochemical Engineering

School of Chemical Engineering

PhD in Chemical Engineering

2023

Dedication

This dissertation is dedicated to my beloved mother and sister: my whole world.

Acknowledgements

This thesis has been supported by the Office of Research and Extension of Universidad Industrial de Santander through research Project No. 3728, and by the Ministerio de Ciencias – MINCIENCIAS through research Project No. 8282.

The author of this doctoral thesis acknowledges the financial support provided by the School of Chemical Engineering of Universidad Industrial de Santander through the Ph.D. scholarship assigned by contract No. 69 of 2018.

A great acknowledgment to the Emerging Leaders in the Americas Program (ELAP) supported by the Government of Canada for granting the fellowship to carry out part of this research at the University of Calgary. Likewise, sincere acknowledgments to the Natural Sciences and Engineering Research Council of Canada (NSERC) (Grant No. RGPIN-2015-05222), as well as the Department of Chemical and Petroleum Engineering at the Schulich School of Engineering at the University of Calgary.

All the genuine acknowledgments to the support of Universidad Nacional de la Plata for the collaboration provided with the Mössbauer and magnetometric characterizations; the X-ray Laboratory at Universidad Industrial de Santander for providing assistance with the X-ray Diffraction pattern of the nanoparticles; the Laboratory of Microscopy of Universidad Industrial de Santander for assistance with the Scanning Electron Microscopy images presented; and the University of Calgary for providing assistance with the Transmission Electron Microscopy images.

My eternal gratitude and admiration to my supervisors, Professors Arlex Chaves Guerrero, and Francisco H. Sánchez. Likewise, I would like to express my honest gratitude, to whom I also

consider my mentors, Professors Nashaat Nassar, and Ronald Mercado for their valuable contributions to the thesis.

I am deeply grateful to God, my beloved family, and my cherished friends and students. A special mention is reserved for my life mentor and best friend, Diana Marcela Cañas; words cannot express how much you mean to me.

MAGNETORHEOLOGY OF HEAVY OIL-FERROFLUID MIXTURES.

Table of Contents

Thesis roadmap 21

1 Theory, challenges, and status of the application of ferrofluids and magnetism in the petroleum industry 29

1.1 Introduction 29

1.2 Ferrofluids: fundamentals and applications 33

1.3 Magnetic properties and constitutive equations 36

1.3.1 Magnetoviscous effect in highly diluted ferrofluids: Rotational viscosity 41

1.4 Magnetic induced ferrofluid flows in porous media 43

1.5 Ferrofluid-assisted enhanced oil recovery 50

1.6 Ferrofluid flow: Prospects for pipeline transportation 58

2 Rheological implications of the inclusion of ferrofluids and the presence of uniform magnetic field on heavy and extra-heavy crude oils 62

2.1 Abstract 62

2.2 Introduction 63

2.3 Materials and Methods 67

2.3.1 Materials 67

2.3.2 Preparation of the heavy crude oil-ferrofluid models. 68

2.3.3 Rheological evaluation. 69

2.3.4 Magneto-rheological evaluation. 70

2.3.5 Morphological assessment of magnetic field-induced assembly on NPs-asphaltene complexes. 71

2.4 Results and Discussion 71

2.4.1 Linear viscoelasticity of the crude oils 71

2.4.2 Rheological modifications of the heavy crude oil-ferrofluid models 78

2.4.2.1 Steady-state flow curves. 79

2.4.2.2 Dynamic moduli and complex viscosity curves as a function of frequency..... 81

2.4.2.3 Dynamic moduli and complex viscosity curves as a function of temperature 83

2.4.3 Magneto-rheological behavior of the heavy crude oil-ferrofluid models..... 85

2.4.4 Morphological assessment of magnetic field-induced assembly on NPs-asphaltene complexes 96

2.5 Conclusions..... 99

3 Effect of asphaltene adsorption on the magnetic and magnetorheological properties of heavy crude oils and Fe_3O_4 nanoparticles systems 101

3.1 Abstract..... 101

3.2 Introduction..... 102

3.3 Materials and methods 107

3.3.1 Materials 107

3.3.2 Evaluation of the synthetic heavy crude oil and adsorption experiments..... 109

3.3.2.1 Preparation of the stock stable dispersions 109

3.3.2.2 Batch adsorption experiments..... 109

3.3.2.3 Modeling adsorption kinetics and isotherms 111

3.3.3 Characterization of the interacting complexes..... 114

3.3.4 Magnetic evaluation..... 114

3.3.4.1 Preparation of the dispersions and magnetometric characterization 114

3.3.4.2 Theoretical approach of the isothermal magnetization curve 115

3.3.5 Characterization of the functionalized nanoparticles 116

3.3.6 Magnetorheological evaluation 117

3.3.6.1 Preparation of natural heavy crude oil models 117

3.3.6.2 Magnetorheological characterization 117

3.4 Results and discussion 118

3.4.1 Adsorption kinetics and isotherms 118

3.4.1.1 Adsorption kinetics 118

3.4.2 Adsorption isotherms 121

3.4.2.1 Characterization of the interacting complexes 126

3.4.3 Magnetic evaluation 127

3.4.4 Magnetorheological characterization 136

3.5 Conclusions 139

3.6 Supplementary information 142

4 Toward understanding induced microstructural changes of magnetic modified crude oils by applying non-linear rheology and magnetometry 147

4.1 Abstract 147

4.2 Introduction 148

4.3 Materials and Methods 157

4.3.1 Materials 157

4.3.2 Formulation of the magnetic modified heavy crude oil model 158

4.3.3 Characterization of the non-linear rheological properties in LAOS experiments .. 158

4.3.4 Physicochemical characterization 160

4.3.4.1 Nanoparticles 160

4.3.5 Magnetometric characterization..... 160

4.3.5.1 Theoretical approaches of the isothermal magnetization curves M vs H 161

4.3.5.2 Theoretical derivation of the susceptibility (χ) and coercivity (H_c) of a distribution of monodomain nanoparticles 162

4.4 Results and Discussions..... 165

4.4.1 LAOS characterization..... 165

4.4.2 Physicochemical characterization 173

4.4.3 Magnetometric characterization..... 178

4.4.3.1 Isothermal magnetization curves 178

4.4.3.2 Susceptibility (κ) and coercivity (H_c) 182

4.4.3.3 Zero-field cooled (ZFC) and field-cooled (FC) magnetization curves 184

4.5 Conclusions..... 199

4.6 Supplementary information 201

4.6.1.1 Magnetic modified heavy crude oil (C_{1-5}) 203

General remarks and ongoing research..... 205

References..... 209

List of Tables

Table 1 Summary of the state-of-the-art applications of ferrofluids and magnetism in the petroleum industry. 32

Table 2 Set of counter-current imbibition phenomenon equations, dealing with an external effect of magnetic field. 54

Table 3 Governing equations of oscillating fluid-fluid interfaces, dealing with an external effect of magnetic field. 57

Table 4 Asphaltene concentration, API gravity, and viscosity of the heavy crude oils. 68

Table 5 SARA Fractionation and API gravity of $\boldsymbol{C1}$. 108

Table 6 Estimated parameter values of the mixed-order (MO) and the phenomenological external mass transfer (EMT) kinetic models. 120

Table 7 Adsorption isotherms parameters and statistical parameters. 124

Table 8 Calculated parameters such as mean apparent nanoparticle magnetic moment $\boldsymbol{\mu}$, total magnetic moment per formula unit $\mu\boldsymbol{Fe}$, the volume fractions of the magnetic cores and the surfactant ($\boldsymbol{\phi N}$ and $\boldsymbol{\phi Surf}$), the diameter of the magnetic cores ($\boldsymbol{DN}$), the critical magnetic field and magnetic flux density ($\boldsymbol{Hcrit}$. and $\boldsymbol{Bcrit}$.), the nanoparticle magnetic moment standard deviation ($\boldsymbol{SD}$). 134

Table 9 Calculated parameters obtained from the model adjustment of the obtained TEM number weighted diameter histogram. 135

Table 10 Linear viscoelastic mechanical models used for bituminous binders and mixtures. .. 150

Table 11 Quantitative approaches for analyzing stress waverform responses to LAOS 153

Table 12 Parameters of the $\boldsymbol{P(Di)}$ log-normal distribution function (3). 162

Table 13 Parameters for crystallite size calculations using the Scherrer equation. 174

List of Figures

Figure 1 Thesis roadmap. 28

Figure 2 Attractive and repulsive energy potentials between a pair of functionalized Fe_3O_4 nanoparticles (M_0= $4.5 \cdot 10^5$ Am^{-1})..... 35

Figure 3 Magnetization curves of monodisperse spherical Fe_3O_4 nanoparticles (M_0= $4.5 \cdot 10^5$ Am^{-1}). 37

Figure 4 Master curve obtained by applying the Time-Temperature Superposition (TTS) principle to a set of frequency sweeps (between 0.1-10 Hz) at different temperatures under a controlled strain (LVE region). The reference temperature is 30 °C. The model employed to fit the experimental values was the generalized Maxwell model. A. C_1, temperature range 0°C to 60°C. B. C_2, temperature range 5°C to 30°C. 73

Figure 5 The shift factor values (a_T) as a function of temperature obtained from the master curve and fitted to the Arrhenius and WLF models. A. C_1. B. C_2. 75

Figure 6 Relaxation time spectrum of C_1 and C_2 at the reference temperature, Tr, 30°C. 78

Figure 7 Measured flow-curves of the heavy crude oil-ferrofluid models at a shear rate from 0.1 s^{-1} to 100 s^{-1} and constant temperature, T_{C1}=30°C, and T_{C2}=25°C. 81

Figure 8 Dynamic moduli as a function of the frequency of $C1-k-x$ models under a controlled strain (linear viscoelastic region). 82

Figure 9 Dynamic moduli as a function of the temperature of $C2-k-x$ models at an angular frequency of 10 rad/s. 84

Figure 10 Transient shear stress arising during a stepwise increase in the shear rate of the $\boldsymbol{C1-k-5.0}$ sample, changing the concentration of the ferrofluid to 20, 30, and 40 wt% at 30°C. .. 87

Figure 11 A. Magnetoviscous effect (relative change of viscosity) as a function of time of $C1-k-5.0$ sample, applying a logarithmic ramp of magnetic flux density from $1.85\ to\ 875.61\ mT$ (δB-filled symbols) at different shear rates 10 s^{-1}, 50 s^{-1}, 70 s^{-1}, and considering the time-dependent transient viscosity in the absence of magnetic flux density (B^0-unfilled symbols). B. Effect of uniform magnetic flux density (B) at a constant shear rate 70 s-1; and in the absence of magnetic flux density (B^0). 91

Figure 12 Comparative assessment of the effect of ferrofluid concentration in C_1 after applying a logarithmic ramp of magnetic flux density from $\mathbf{1.85\ to\ 875.61\ mT}$ (δB- filled symbols) at different shear rates 10s^{-1}, 50 s^{-1}, 70 s^{-1}; and in the absence of magnetic flux density (B^0). A. Concentration of ferrofluid of 30 wt.% (1.5 wt.% NPs-heavy crude oil); B. Net effect of the external magnetic field at a concentration of ferrofluid of 30wt.%; C. Concentration of ferrofluid of 40 wt.% (2.0 wt.% NPs-heavy crude oil); D. Net effect of the external magnetic field at a concentration of ferrofluid of 40 wt.%. 93

Figure 13 Magnetoviscous effect (relative change of viscosity) of $\mathbf{C2-k-5.0}$ sample, applying a logarithmic ramp of magnetic flux density from $\mathbf{0\ to\ 875.61\ mT}$ (δB filled symbols) at different shear rates 1 s^{-1}, 10 s^{-1}, 50 s^{-1}. 94

Figure 14 Time dependency of the viscosity of the heavy crude oil-ferrofluids models of C_2. The shear rate was 25 s^{-1}. At region I magnetic flux density B= 0, region II magnetic flux density B= 647.3 mT and region III magnetic flux density B= 0. 96

Figure 15 SEM images of magnetic field-induced assemblies of NPs-asphaltene complexes prepared by the drop-casting method at different magnifications. A. At zero-magnetic field, and

MAGNETORHEOLOGY OF HEAVY OIL-FERROFLUID MIXTURES.

B. In the presence of a uniform longitudinal magnetic field of 1T provided by a Halbach cylinder. The insert represents the Halbach array with the sample illustrated with the black circle. 98

Figure 16 A. Adsorption kinetics at 25 °C of A1 (1 mg/mL) onto Fe_3O_4 nanoparticles (7.5 mg/mL) fitted to the mixed-order (MO) model, and the phenomenological external mass transfer (EMT) model. B. Overall adsorption rate in terms of the pseudo-first-order (PFO), pseudo-second-order (PSO), and external mass transfer (EMT) rate contributions. 121

Figure 17 Adsorption isotherms at 25 °C of A. Sample A_1, B. Sample A_1-hR_1 (0.15 hR_1 per 1 g of A_1), and C. Sample A_1-hR_1 (0.3 hR_1 per 1 g of A_1) onto Fe_3O_4 nanoparticles (7.5 mg/mL) fitted to the Langmuir (LM) and exponential Langmuir (ELM) models. D. Comparison of all samples fitted to the LM..... 125

Figure 18 SEM images of the A. Fe_3O_4 nanoparticles and B. Complexes of Asphaltenes (A_1) and Fe_3O_4 nanoparticles after magnetic separation. 127

Figure 19 A. Isothermal magnetization cycles of $\boldsymbol{fNA1S-\omega}$ samples, displaying mostly superparamagnetic behavior. B. Rescaled magnetization curves of the $\boldsymbol{fNA1S-\omega}$ magnetic cores. The insert figure represents the low-magnetic field interval $\pm\sim\mathbf{2\times104}\boldsymbol{Am}$ employed to the estimation of the apparent susceptibly $\boldsymbol{\kappa}$..... 132

Figure 20 Calculated apparent susceptibilities $\boldsymbol{\kappa}$ as a function of the volume fractions of the magnetic cores $\boldsymbol{\phi N}$ in the low-magnetic field zone. The continuous line corresponds to the DMF analysis Eq. 28 (64, 267, 269)..... 133

Figure 21 Isothermal magnetization cycles of $\boldsymbol{fNA1S-0}$ adjusted to the Eq. 32 in the high-magnetic field zone..... 134

Figure 22 TEM images of Fe_3O_4 nanoparticles (scale bar of 20 nm). Annotations indicate the mean size distribution and standard deviation determined from a fit to the lognormal size distribution. 135

Figure 23 Time dependency of the dynamic moduli ($\boldsymbol{G'}$ and $\boldsymbol{G}$") of the magnetic modified maltenes $\boldsymbol{M1S-\omega m}$ and crude oil $\boldsymbol{C1m}$ measured at 15°C, 10 rad/s, 1 and 10% of strain for $\boldsymbol{C1m}$and $\boldsymbol{M1S-\omega m}$; respectively. At region I: the magnetic flux density was $\boldsymbol{B=0}$, region II: $\boldsymbol{B=0.094\,T}$, and region III: $\boldsymbol{B=0}$. 139

Figure 24 Shear-strain-amplitude sweep protocol. 159

Figure 25 Dynamic moduli, $\boldsymbol{G'}$ and $\boldsymbol{G''}$depicted by $C_{1\text{-}5}$, at frequency $\boldsymbol{\omega=10\,rads}$ and temperature $\boldsymbol{T=278.15\,K}$, applying three cycles, in the absence of the magnetic field B=0 (blue), steric hardening cycle B=0 (red), and B ≠0 (black). The inset shows time dependency of $\boldsymbol{G'}$ and $\boldsymbol{G''}$ measured at $\boldsymbol{T=288.15\,K}$, $\boldsymbol{\omega=10\,rads}$, $\boldsymbol{\gamma=1}$%, a pulse of magnetic field (B=0.094 T) was applied between 5-10 min, the axis on the right represents the relative changes $\boldsymbol{\delta G'/G'}$ and $\boldsymbol{\delta G''G''}$; adapted from (3). 167

Figure 26 A. Elastic Lissajous-Bowditch (e L-B) curve, and B. Viscous Lissajous-Bowditch (v L-B) in MAOS regime ($\boldsymbol{\gamma=6.31}$%). C. e L-B curve, and D. v L-B curve in LAOS regime ($\boldsymbol{\gamma=63.1}$%). Three cycles were applied on $C_{1\text{-}5}$, in the absence of magnetic field B=0 (blue), steric hardening cycle B=0 (red dashed), and under a magnetic field B =0.172 T (black). 171

Figure 27 Parametric plot of $\boldsymbol{\partial 2\tau\partial\gamma 2}$ vs $\boldsymbol{\gamma}$ in A. MAOS, and B. LAOS regimes. Three cycles were applied on $C_{1\text{-}5}$, in the absence of magnetic field B=0 (blue), steric hardening cycle B=0 (red dashed), and B =0.172 T (black)..... 172

Figure 28 Two-dimensional visualization of viscoelastic SPP metrics, represented by the parametric plot of ($\boldsymbol{\omega\eta t}$) vs ($\boldsymbol{Gt}$) in A. MAOS, and B. LAOS regimes. Three cycles were applied on $C_{1\text{-}5}$, in the absence of magnetic field B=0 (blue), steric hardening cycle B=0 (red dashed), and B =0.172 T (black). 172

Figure 29 Enhanced strain amplitude sweep in the parametric space ($\boldsymbol{\omega\eta t}$) vs ($\boldsymbol{Gt}$) at 10 rad/s, A. In the absence of the magnetic field B=0 (cycle 1), and B. in the presence of the magnetic field B =0.172 T. (red dots represent the first harmonic dynamic moduli) 173

Figure 30 Nanoparticles XRD patterns. 173

Figure 31 Mössbauer effect spectrum. The inset represents an approximate correlation between sub-spectra and nanoparticle sizes. To obtain this correlation, Néel relaxation times were calculated at 300 K using values of τ_0, K_{eff}, and V presented in this work. Relaxation times have been tentatively assigned to the sub-spectra within the frame of H.H Wickman results.(345) .. 175

Figure 32 Experimental values and low-field (LF) fitting of the FSR model. 179

Figure 33 Experimental values and high-field (HF) fitting of the FSR model (up to H^{-2}). The blue and red curves of the right are the zoom of the fitted HF interval. 179

Figure 34 Set of estimated parameters of the FSR model (Eq. 39 and 40) for $C_{1\text{-}1}$ and $C_{1\text{-}5}$ (empty plot markers) samples.(325) A. The ratio of the effective anisotropic constant and the saturation magnetization ($\boldsymbol{KeffMS}$), B. the saturation magnetization of the magnetic-core phase ($\boldsymbol{MS}$), C. Ferromagnetic susceptibility of the magnetic-core phase ($\boldsymbol{\kappa}$), D. The coercivity field ($\boldsymbol{HC}$), E. The number of particles per volume unit in the sample. ($\boldsymbol{n}$), and F. The corrected magnetic moment was calculated by approximating the particle density by its value at 320 K, at which the effect of interactions is the lowest, i.e., $\boldsymbol{\mu corr(T) = \mu sample(T) n(320)}$. 181

Figure 35 A. Evolution of $\boldsymbol{MS - \infty T}$. B. Fitted function of $\boldsymbol{DCT}$. The plot markers are the estimated values based on Eq. 52. C. Normalized saturation magnetization $\boldsymbol{f(T)}$ for $C_{1\text{-}5}$ sample. The plot markers are the estimated values from Eq. 40 (Up to H^{-2}). 183

Figure 36 A. Magnetic susceptibility ($\boldsymbol{\kappa}$) for $C_{1\text{-}5}$ sample, obtained from Eq. 39. The line corresponds to the deduced theoretical expression (Eq. 49). B. Magnetic coercivity ($\boldsymbol{Hc}$) for $C_{1\text{-}5}$ sample, obtained from Eq.39. The line corresponds to the deduced theoretical expression (Eq. 50). 184

Figure 37 Log-normal fit of $\boldsymbol{\partial MZFC - MFC\partial T}$ at 40.12 K (continuous black line), and Lorentz fit of the second peak of $\boldsymbol{\partial MZFC - MFC\partial T}$ at 273.96 K (continuous magenta line). Inset corresponds to the ZFC and FC experimental curves. 188

Figure 38 The ZFC-FC magnetic moment curves; the red dashed line is an assumption of the behavior of the magnetic moment of non-interacting magnetic nanoparticles, which is expected to be higher than the aggregated state. B. The ZFC-FC susceptibilities were estimated at H= 100 Oe. 191

Figure 39 A. The $\boldsymbol{\partial \mu ZFC - \mu FC\partial T}$ curve fitted to a Lorentz distribution function. B. The number of unblocked aggregates per temperature unit $\boldsymbol{P'T}$ estimated with Eq. 66, the blue dashed line corresponds to the approximation using the experimental data. 192

Figure 40 A. The total number of particles per unit volume of an aggregate as a function of $\boldsymbol{T}$. B. The number of particles in the aggregates unblocked at temperature $\boldsymbol{T}$. C. the accumulated number of nanoparticles in the total unblocking aggregates as a function of $\boldsymbol{T}$. 194

Figure 41 Magnetic susceptibility of nanoparticles in the aggregates while getting oriented ($\boldsymbol{\kappa A}$), in reoriented (unblocked, $\boldsymbol{\kappa OA}$), and randomly oriented (blocked, $\boldsymbol{\kappa RA}$) aggregates. 196

Figure 42 Evolution of the effective demagnetizing factor of the aggregates $\boldsymbol{NE, A}$ (Eq. 40), The dashed blue line did not consider the polymeric and asphaltene layers. 197

Figure 43 A. Evolution of the volume of the aggregates. B. Major and minor axes (a,b)..... 198

Figure 44 Schematic representation of the coupled magnetic device. 208

Figure 45 Selective results of the flow of a ferrofluid and a ferrofluid emulsion in a laboratory-scale flowline system, under the effect of alternating linearly increasing magnetic fields. 208

MAGNETORHEOLOGY OF HEAVY OIL-FERROFLUID MIXTURES.

List of Supplementary Figures

Figure S1 A. Adsorption spectra of asphaltene (A_1) suspensions at different concentrations, before and after the precipitation of asphaltene/nanoparticles complexes. B. Calibration curve of asphaltenes (A_1) at a wavelength of 405 nm..... 142

Figure S2 FTIR spectra of the asphaltenes, nanoparticles, asphaltene/nanoparticle and asphaltene/resin/nanoparticle complexes..... 143

Figure S3 A. Efficiency $E = [(C0 - Ceq)C0] \cdot 100$ and, B. Adsorption capacity $q = [(C0 - Ceq)m] \cdot V$ as a function of Fe_3O_4 nanoparticles concentration..... 144

Figure S4 EDS analyses of A. Asphaltenes, B. nanoparticles, and C. asphaltene/nanoparticles complexes. 145

Figure S5 Calculated apparent susceptibilities κ as a function of the volume fractions of the magnetic cores ϕN in the low-magnetic field zone, using different Ms values. The continuous line corresponds to the DMF analysis..... 146

Figure S6 Fitted log-normal distribution as a function of the size $\partial MZFC - MFC\partial D$) from ZFC-FC magnetization curves (Red), and log-normal distribution function obtained from TEM (Blue). 201

Figure S7 Brownian and Néel relaxation times as a function of the temperature. Assuming a nominal diameter of the magnetic core equal to 10 nm, a hydrodynamic diameter of 20 nm, effective anisotropy constant $K=2\cdot10^4$ J·m^{-3}, $\tau_0=10^{-9}$. 202

Figure S8 DSC curves for $C_{1\text{-}5}$, under dynamic nitrogen atmosphere (50 ml min^{-1}), at a heating rate of 3 °C min^{-1}..... 203

Figure S9 Fitted viscosity function of $C_{1\text{-}5}$. The blue points are the experimental values measured as a function of the temperature. 204

MAGNETORHEOLOGY OF HEAVY OIL-FERROFLUID MIXTURES.

Abstract

Title: Study of the magnetorheological behavior and magnetic-induced microstructure of heavy crude oils and ferrofluids mixtures[†]

Author(s): Maria Daniela Contreras Mateus[‡]

Keywords: Rheology, Magnetorheology, Ferrohydrodynamics, Flow assurance, Heavy crude oils, Ferrofluids.

Description:

Global energy policies are undergoing a profound reorientation to provide a more secure, sustainable, and affordable system, moving towards net-zero emissions by 2050. Although investment in clean fuels is set to increase significantly in the coming years, parts of the fossil fuel system remain critical to energy security, such as refineries to supply residual users of transportation fuels. In this context, unconventional hydrocarbons have been a major candidate for current and future oil production, since they exist in abundant quantity on Earth's crust, representing nearly 70% of proven reserves. Accordingly, great attention has been fundamentally directed towards exploring the promising and growing nanotechnology modern era. Against this background, this thesis is framed in the theoretical and experimental study of the inclusion of ferrofluids in the matrix of heavy crude oils with the aim of proving the induction of magnetorheological effects, primarily focused on improving the flow properties of these complex fluids in pipeline transportation applications. Therefore, it has been demonstrated that the integration of nanoparticles plays a fundamental role as adsorbent and smart magnetically controllable agent, effectively modifying the rheological properties of heavy crude oils. Likewise, surface modification of nanoparticles by adsorption of asphaltenes supported the role of this fraction as facilitator in promoting the spontaneous formation of aggregates. The orientation of these aggregates could be manipulated using external magnetic fields to stimulate more favorable flow properties in heavy crude oils. These findings serve as a fundamental theoretical basis for the development of an innovative technological approach aimed at flow assurance of heavy crude oils.

[†] PhD thesis

[‡] Faculty of Physicochemical Engineering. School of Chemical Engineering. Supervisors: Arlex Chaves Guerrero, Francisco H. Sánchez.

Thesis roadmap

The opening chapter of this thesis is devoted to an in-depth literature review, delving into the fundamental theory of ferrofluids, their unique properties, and the evolution of their applications in various scientific and industrial spheres. A specific focus was directed towards exploring the experimental and theoretical progress of fluid dynamics of ferrofluids, influenced by magnetic fields, in scenarios resembling the intrinsic macro-processes of the oil industry. Fundamentally, the aim was to provide contextualization of the potential integration of ferrofluid technologies in two pivotal oil macro-processes*: recovery and transportation*, which have been widely acknowledged as the pillars of the oil supply chain. We also dedicated some sections to discuss a selection of experimental approaches implemented in systems that closely emulate real-world scenarios, involving the integration of ferrofluids and crude oils, under the influence of external magnetic fields, and at thermodynamic flow conditions similar to reservoir environments. These studies collectively reveal that, while initial efforts have showcased substantial technological promise within the oil industry, there remains a significant knowledge gap on the multiple intricate physicochemical mechanisms governing the interaction of rheologically complex crude oils and magnetic stimuli-responsive nanoparticles.

The literature extensively acknowledges that the integration of nanoparticles as *adsorptive, heat carries, and catalytic agents,* produces attractive phenomena in the crude oil rheological properties since structural changes inside their matrices are promoted (*e.g.,* inhibiting the formation of complex long-range viscoelasticity). Research has widely discerned the kinetics, isotherms, and thermodynamic modeling of the adsorption of asphaltenes onto multiple nanoparticles; and it has found a place in diverse oil recovery and production applications,

encompassing alteration of wettability, inhibition of asphaltene formation damage, reduction of interfacial tension, enhancement of the bulk viscosity and viscoelasticity of crude oils, stabilization of emulsions, among others. These explorations have marked a pivotal juncture in industry and academia, which, to date, continue to join efforts to demonstrate the critical role of nanoparticles in mitigating the adverse impacts of asphaltenes; recognized as one of the most challenging crude oil fractions and a major financial burden for the industry. The author of this thesis has contributed to the field through the publication of a book chapter, in which these topics are discussed in detail. Refer to (1).

In this context, we recognize the relevance of studying the rheology exhibited by mixtures of heavy crude oils and ferrofluids, by adding a second dimension: *the application of external magnetic fields*. This fundamental principle holds potential for the development of technological approaches focused on improving the efficiency of oil transportation and production, and its motivation is based on the well-proven magnetic induced flow approaches of magnetorheological fluids in these scenarios. Nevertheless, a fundamental knowledge of nanoparticle-asphaltene physicochemical interactions is imperative, alongside the study of their impact on the induced magnetorheological properties. Furthermore, it should be highlighted that the inherent rheological behavior of these mixtures presents a more formidable challenge compared to conventional ferrofluids. The intrinsic viscoelastic properties of heavy crude oils deviate from the coarse knowledge of the magnetorheolgy and ferrohydrodynamics of ferrofluids, which has been mainly focused on formulating and modeling them with Newtonian carrier liquids.

Considering the discussed progresses, this research thesis has been developed with the fundamental objective of studying the ***magnetorheological behavior and magnetic-induced***

microstructure of heavy crude oils and ferrofluids mixtures. The specific objectives embrace a visionary framework that spans from macroscopic to microscopic scales, starting from the understanding of the rheology of heavy crude oils, followed by the evaluation of the effect of inclusion of ferrofluids on the rheological and magneto-rheological properties of heavy crude oils, and culminating in an in-depth understanding of the effect of physicochemical interactions between asphaltenes and nanoparticles on the magnetically induced microstructures of these mixtures. From the last, a systematic methodology was developed for the modeling and description of the effects of asphaltene adsorption on the nanoparticle magnetic dipolar interactions, as well as the formation and alignment of induced magnetic structures under the influence of uniform perpendicular static magnetic fields. Against this background, the doctoral dissertation was structured in three fundamental chapters complementing the above-discussed literature review and providing the context for our own contributions to the field. Each of the three chapters is composed of a research article; to date, two of them have been published, while the third is about to be submitted. A schematic representation of the roadmap is presented in Figure 1.

The first chapter, entitled ***Rheological implications of the inclusion of ferrofluids and the presence of uniform magnetic field on heavy and extra-heavy crude oils[§],*** provides a general overview of the rheological and magnetorheological behavior of two selected samples of Colombian heavy crude oils, based on two fundamental criteria. First, the *thermo-rheological*

[§] 2. Contreras–Mateus MD, López–López MT, Ariza-León E, Chaves–Guerrero A. Rheological implications of the inclusion of ferrofluids and the presence of uniform magnetic field on heavy and extra-heavy crude oils. Fuel. 2021;285:119184.

simplicity of these fluids with the aim of modeling their viscoelastic properties and relaxation mechanisms through the application of the time-temperature superposition (TTS) principle and the empirical generalized Maxwell model, within the dynamic flow field. Second, the rheological behavior exhibited by the samples when mixed with Fe_3O_4 kerosene-based ferrofluids, with the aim of encompassing the entire spectrum from *Newtonian to non-Newtonian* behavior. Against this background, we focused on the rheological characterizations of the heavy oils and their mixtures with the aim of elucidating the well-established effect of asphaltene adsorption onto the surface of the nanoparticles by exploring the modifications of the stationary flow and viscoelastic curves. Essentially, it was conclusively proven that the inclusion of the kerosene-based ferrofluids significantly reduced the viscosity. Likewise, a specific critical concentration of nanoparticles was found, further influencing both the viscosity and structural elasticity. On the other hand, this study was the first to demonstrate the induction of moderate magnetoviscous effects of mixtures of heavy crude oils and ferrofluids. This groundbreaking finding opened a new pathway, aiming to emulate analogous magnetorheological effects, such as the known “negative viscosity” observed in ferrofluids under the influence of oscillating and rotating magnetic fields. However, several concerns emerged from these results, mainly because the induced effects were less pronounced than those typically observed in commercial ferrofluids under the influence of uniform static magnetic fields. These intriguing outcomes prompted further inquiries into the underlying physicochemical mechanisms that inhibited the magnetorheological response, and the potential implications of such effects in complex mixtures.

MAGNETORHEOLOGY OF HEAVY OIL-FERROFLUID MIXTURES.

The second chapter, entitled ***Effect of asphaltene adsorption on the magnetic and magnetorheological properties of heavy crude oils and Fe_3O_4 nanoparticles systems,***[**] builds upon the proven magnetorheological effects of the preceding chapter and aims to provide a comprehensive understanding of the underlying physicochemical interactions within these systems when exposed to external magnetic fields, with a particular focus on the role of the adsorbed asphaltenes on the dipolar interparticle interactions. On this basis, this research simplified the system by separating the asphaltenes from their original matrices to formulate toluene-based models; and involved the development of two stages. First, an evaluation of the adsorption kinetics and isotherms of asphaltenes on Fe_3O_4 nanoparticles was carried out in the toluene-based model systems, considering the potential ambiguous effect of the presence of resins on the nanoparticles/asphaltene interactions; and applying the well-established phenomenological models and methods from the existing literature. Second, magnetometry and magnetorheological characterizations were conducted, involving nanoparticles/asphaltene complexes in different matrices, as a function of the asphaltene concentration, to elucidate their implications on the magnetorheological properties. An important outcome of this research was the groundbreaking demonstration of the existence of a functionally proportional dependence of the apparent magnetic susceptibility with the asphaltene concentration, proving that this fraction was completely adsorbed in the form of layers onto the nanoparticles surface, resulting in the appearance of steric

[**] 3. Contreras–Mateus MD, Sánchez FH, Cañas-Martínez DM, Nassar NN, Chaves–Guerrero A. Effect of asphaltene adsorption on the magnetic and magnetorheological properties of heavy crude oils and Fe3O4 nanoparticles systems. Ibid. 2022;318:123684.

repulsive effects. Furthermore, the analysis of the magnetic-modified dynamic moduli suggested that, in the colloidal state configuration, additional attractive interactions, potentially involving interdigitation, might be feasible at specific asphaltene concentrations (<1 wt.%). This finding implied the spontaneous formation of isotropic aggregates of nanoparticles/asphaltenes, even in the absence of an applied magnetic field.

The third chapter, entitled ***Toward understanding induced microstructural changes of magnetic modified crude oils by applying non-linear rheology and magnetometry,*** expands upon the groundwork laid in the preceding chapters, which deepened into the overarching magnetorheological behavior of heavy crude oil and ferrofluid mixtures, and the simultaneous steric repulsions of the adsorbed asphaltenes onto the nanoparticle surfaces. The primary objective was to study and model the formation and reorientation of asphaltene/nanoparticle complexes to provide fundamental insights that could be applied to enhance the flow properties of heavy crude oils. A new methodology combining Large Amplitude Oscillatory Shear (LAOS) tests and magnetometry was proposed. From the former, the sequence of physical processes (SPP) framework was implemented to provide intra-cycle structure-rheological interpretations during the nonlinear viscoelastic characterization of heavy crude oil- ferrofluid mixtures, upon the application of an external field perpendicular to the flow direction. This approach was supported and validated through the development of a phenomenological model that captured the intricate processes involved in the formation and reorientation of aggregates, based on the experimental data acquired from zero-field cooled (ZFC) and field-cooled (FC) magnetization curves. In general, it was demonstrated that disordered asphaltene aggregates are highly extended and naturally formed in the absence of a magnetic field. In contrast, in the presence of a uniform field, the formation of

interacting structural aggregates of several hundred nanometers was observed, analogous to ferrofluids-magnetically controlled suspensions.

Accordingly, the initial perception of asphaltenes as antagonists created a sense of uncertainty, it seems that asphaltenes unveiled a captivating paradox – could their presence serve as a control agent in promoting the formation of aggregates, whose orientation could be manipulated by external magnetic fields to induce favorable flow properties of heavy crude oils?

Finally, a section on general remarks and ongoing research was included where the main findings of this thesis are highlighted. We also dedicated some discussions about the design, assembly, and operation of a flowline system aimed at studying the effect of alternative magnetic field configurations (longitudinal linear increasing and oscillating) with the potential of enhancing the flow properties of mixtures of heavy crude oils and ferrofluids, as observed in magnetorheological fluids by the induction of Kelvin-body forces and “negative viscosity” effects.

MAGNETORHEOLOGY OF HEAVY OIL-FERROFLUID MIXTURES.

Figure 1

Thesis roadmap.

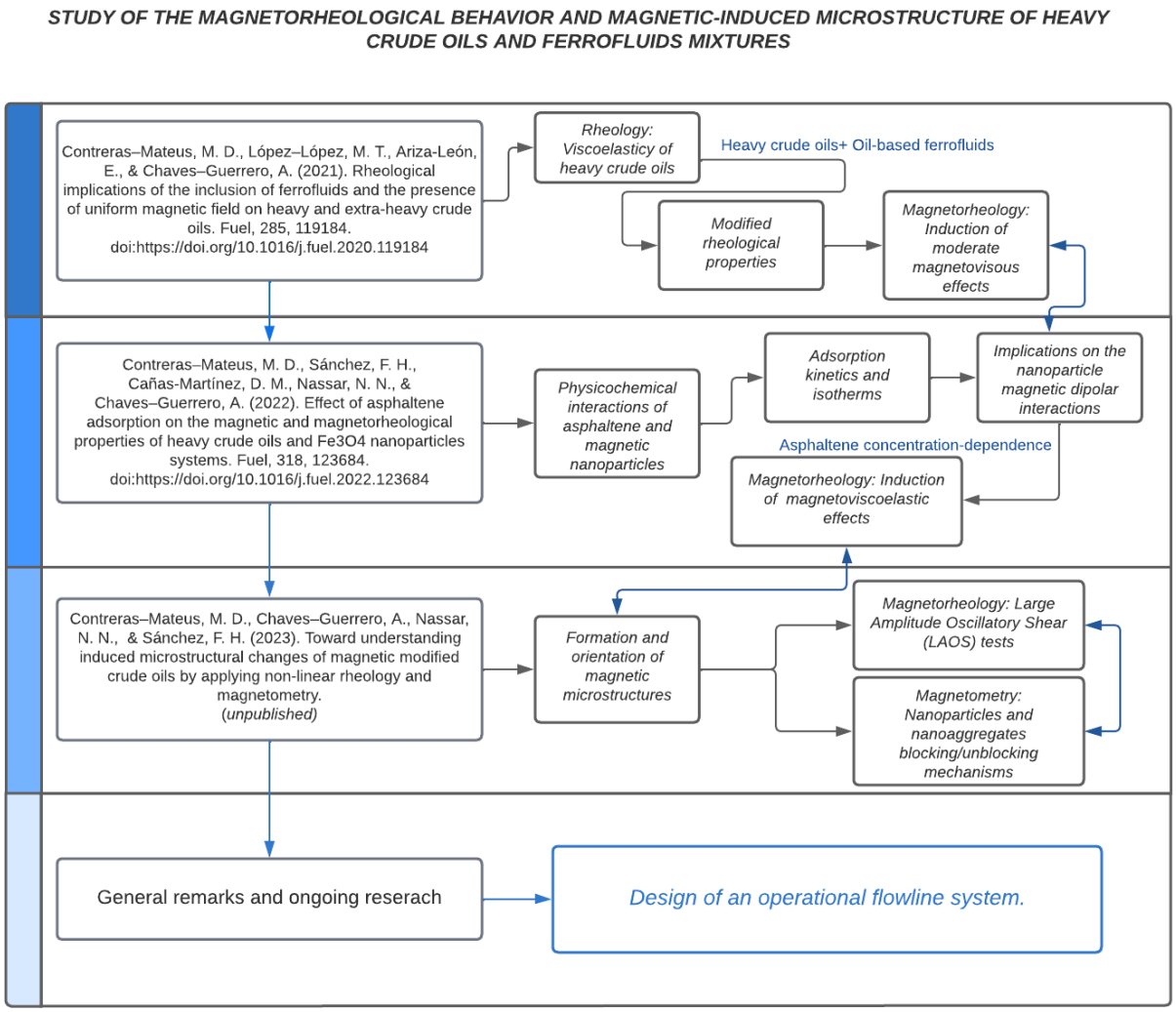

1 Theory, challenges, and status of the application of ferrofluids and magnetism in the petroleum industry

1.1 Introduction

Fast-evolving international plans toward more sustainable scenarios represent a major challenge for the oil industry, which implies an urgent priority in the investment and exploration of non-conventional technological alternatives with the potential to reduce the ecological footprint and reach the international climate targets, while preventing severe supply disruptions and destabilizing price volatility; especially in aviation, shipping, and petrochemicals that rely on oil for the medium term (4). Nanotechnology, which is focused on manipulating matter on the nanoscale, is emerging as one of the alternative solutions that offer the imminent advantage of both, adding profitable economic scenarios and preventing long-term negative impacts on the environment. Accordingly, significant efforts have been devoted to studying the application of nanomaterials to intensify upstream, midstream, and downstream oil operations. Specialized literature has demonstrated that nanoparticle technologies stimulate oil exploration and production processes by altering wettability, inhibiting asphaltene formation damage, reducing interfacial tension, changing the viscosity of the flooding fluid, and enhancing the stability of foams and emulsions. Nanomaterials have also found room in heavy oil transportation and storage, since they act as asphaltene sorbents and dispersants, promoting viscoelastic structural changes due to the disruption of asphaltene aggregates and the decrease of precipitation rates (2, 3, 5-7).

Among the well-known functional nanomaterials, growing interest has been assigned to metal oxides that, besides providing large functional surface areas and asphaltene selectivity, also exhibit enhanced structural properties, thermal and electric conductivity, as well as

superparamagnetism. Regarding this last property, plenty of advances in fluid dynamics using colloidal suspensions of ferri- or ferromagnetic single-domain nanoparticles (*i.e.*, ferrofluids) have been reported in areas as diverse as engineering, biomedicine, electronics, environment, and computing (8-11). Although these magneto-controllable features have not yet gained a foothold in oil flow assurance and recovery, several works have hinted at their true potential. Most of the available literature has focused primarily on the recovery of heavy oil by enhanced metal-nanoparticle incorporating electromagnetic heating (EMNIEH) (12). In theory, high-frequency magnetic fields can cause magnetic nanoparticles to release heat in various ways: hysteresis loss and, Brownian and Néel relaxation (13), whose significance is conditioned to the particle size. For instance, for typical parameters (at a frequency of 200 kHz and anisotropy energy density of 25 kJ/m^3) (13), the critical size is in the order of 15 nm, below which, magnetic relaxation mechanisms dominate and the thermal energy dissipation is accomplished by the rotating magnetic moment of each particle against an energy barrier, either due to the rotation of the magnetic moment while the particle remains fixed (Néel relaxation), (13-15) and/or the unison rotation of the magnetic moment with the particle itself (Brownian relaxation) (13-15). Although the relevance of hysteresis loss has been controversial, in particles larger than 100 nm, thermal dissipation can also be ascribed to shifting domain walls (13). Concerning this specific topic, Bera and Babadagli (12) reviewed some of the early laboratory-scale attempts at the application of nanotechnology in electromagnetic (EM) heating for enhanced heavy oil/bitumen recovery. Some of the mentioned reports proved the reliable ability of the nanoparticles for heat dissipation, which resulted in heavy oil viscosity reduction and, thus, enhanced recovery efficiency (16). Further down the line, Ali *et al.* (17) expanded the scope of the state-of-the-art application of electromagnetic-assisted magnetic

and dielectric nanofluids; favorable results, such as those reported by Soleimani *et al.* (18) showed encouraging signs. Pioneering water-based ferrofluids composed of ferromagnetic $Co^{2+}_{x}Fe^{2+}_{1-x}Fe^{3+}_{2}O_4$ nanoparticles (x=0.75, saturation magnetization of 65.23 emu/g) reached 71.44% of residual oil-in-place recovery (ROIP) efficiency, and 85% ROIP with the simultaneous EM irradiation (78 MHz). Recently, Hassan *et al.* (19) also reviewed promising results in oil recovery with the concurrent EM treatment, using water-based Nickel-Zinc ferrite ferrofluids[††] (20), water-based Yttrium Iron Garnet-YIG ferrofluids[‡‡] (21), water-based Fe_2O_3-Al_2O_3 nanofluids[§§] (22), brine-based ZnO and Al_2O_3 dielectric nanofluids[***] (23, 24). Although this subject seems to be well-documented, limited discussion has been devoted to the potential and applicability of induced magnetoviscous effects of ferrofluids in oil flow assurance and recovery. The possibility of stimulating new classes of fluid dynamic phenomena because of the action of moderate magnetic fields that effectively compete with the gravitational forces, could provide several development opportunities. Recently, Zhou *et al.* (25) presented an interesting breakthrough in the application of magnetic nanoparticles in the petroleum industry. While their overview was broad regarding

---

[††] 0.1 wt.% $Ni_{1-x}Zn_xFe_2O_3$, x=0.5, saturation magnetization of 52,6 emu/g, 13.5 MHz irradiation, recovery of 26.07% ROIP.

[‡‡] 1 wt.% $Y_3Fe_5O_{12}$, saturation magnetization of 18.17 emu/g, 13.6 MHz irradiation, recovery up to 43.64% ROIP.

[§§] 0.01 wt.% Fe_2O_3-Al_2O_3, saturation magnetization of 0.11 emu/g, 13.6 MHz irradiation, incremental recovery up to 30% OOIP.

[***] 0.01-0.1 wt.% of nanoparticles, 0.017-0.025 wt.% of SDBS, 3 wt.% brine, 18.8 MHz irradiation, up to ~40% of reduction in the interfacial tension and contact angle, up to 72.3% OOIP of total oil recovery.

the potential of magnetic nanoparticles, just a couple of the reviewed research implemented simultaneously magnetic nanoparticles (or ferrofluids) and magnetic fields in areas such as drilling and completion improvement (26, 27), magnetic separation (oil-in-water (28-31) and water-in-oil (32) emulsions, desalination (33, 34)), reservoir sensing and imaging (35-42), enhanced oil recovery (43-46), heavy oil upgrading (EMNIEH (16, 47)), as well as flow assurance and conformance control (dewaxing/inhibition of wax deposition by magnetic hyperthermia (48-50), conformance control by magnetic hyperthermia (51), and magnetorheological effects (52)). Though Zhou *et al*. (25) and other authors (17, 19, 53-55) have introduced some general principles and practical approaches to the magnetoviscous properties of ferrofluids, an outline of the magnetic-induced physical and fluid dynamics fundamentals governing ferrofluids is still essential to provide in-depth insight into the diverse applications and their potential in the petroleum industry.

Against this background, we have identified two approaches that have gathered ground in recent years and, to the best of our knowledge, have not been thoroughly reviewed: ferrofluid-assisted enhanced oil recovery, and pipeline transportation. Therefore, we have proposed a programmatic line focused on exploring the theoretical and technical aspects, challenges, and perspectives grounded on these pillars, as shown schematically in Table 1.

Table 1

Summary of the state-of-the-art applications of ferrofluids and magnetism in the petroleum industry.

	Theory	Magnetoviscous effect	Highly diluted ferrofluids Rotational viscosity

Ferrofluids and magnetism in the petroleum industry	***Applications, challenges, status, and perspectives***	"Negative" viscosity
		Magnetic induced ferrofluid flows in porous media
		Ferrofluid-assisted enhanced oil recovery
		Ferrofluid flow: Prospects for pipeline transportation

1.2 Ferrofluids: fundamentals and applications

Magnetic ferrofluids consist of stable colloidal dispersions of single-domain ferrite/metal particles in a non-conducting liquid carrier, typically in the size range between 3-15 nm (8, 14, 56, 57). Based on this dimension domain, the particles are permanently magnetized and, thus, experience strong-long range magnetostatic attraction, besides the gravitational field. To avoid agglomeration and the subsequent sedimentation, repulsive mechanisms can be induced either by coating the surface of the particles with a surfactant/polymer to produce an steric barrier or by charging them to enable electrostatic repulsion (14, 56, 58).

Theoretically, to prevent settling or big gradients of concentration, the thermal energy of the particles $e_T = \kappa_B T$ (where, κ_B is the Boltzmann constant, and T the absolute temperature) must be higher than the magnetic $e_H = \mu_0 MHV$ and gravitational $e_g = \Delta\rho V g L$ energies (where μ_0 is the permeability of free space; H and M are the magnetic field, and the spontaneous magnetization of the magnetic material; V tis he volume of the particles; $\Delta\rho$ is the density difference; g denotes the gravitational acceleration; and L is the elevation in the gravitational field). Thus, for example, the condition for the maximum allowable size for spherical particles to remain stable against segregation in a field gradient can be expressed as (14, 56),

$$d \leq (6\kappa_B T/\pi\mu_0 MH)^{1/3} \quad (1)$$

Since typical ferrofluids contain N~10^{14}-10^{18} particles per cubic centimeter (8, 59, 60), the collision rate is high because of Brownian motion, fluid shear, differential settling or magnetic field, causing attachment and the subsequent aggregation; hence, active diameters could exceed

the maximum established in Eq. 1, and induce sedimentation. Analogously, thermal energy (e_T) must counteract the attachment energies, *i.e.*, magnetic dipole-dipole pair energy (e_{dd}) and electric dipole fluctuation energy (van der Waals attractive forces, $e_{v.d.W}$) (10, 14, 56). In the former, the maximum energy required to separate a pair of permanently magnetized spherical particles is when they are aligned; thus $e_{dd} = (\pi\mu_0 M^2 d^3)/(9(l+2)^3)$, where d is the diameter of the particles and $l = 2s/d$, s denotes the surface-to-surface separation distance. Besides, e_{dd} reaches its maximum when the particles come into contact ($l = 0$). Accordingly, to inhibit agglomeration, particle size should obey the inequality $e_T \geq e_{dd}$, which gives (56),

$$d \leq (72\kappa_B T/\pi\mu_0 M^2)^{1/3} \tag{2}$$

Regarding the van der Waals interaction, it causes irreversible coagulation of bare magnetic particles. In contrast to the magnetic dipole-dipole interaction energy (which is finite for contacting pairs ($l \to 0$)), infinite $e_{v.d.W}$ is required to separate a particle pair, as depicted in Eq. 3 and Figure 2.

$$e_{v.d.W} = -(A/6)[(2/(l^2+4l)) + (2/(l+2)^2) + \ln((l^2+4l)/((l+2)^2))] \tag{3}$$

where A is the Hamaker constant.

As mentioned before, contact inhibition is crucial to guarantee colloidal stability. Adsorption onto the nanoparticles surface of long-chain molecules with compatible tails with the surrounding matrix, promote steric repulsion since they act as elastic bumpers. Eq. 4 is a semiquantitative description of these repulsive energies induced by the active-group shell layers (14, 56).

$$e_{steric} = (\pi d^2 \xi/2)\left[2 - \left(((l+2)/t)\ln((1+t)/(1+l/2))\right) - l/t\right] \quad (4)$$

where ξ is the surface concentration of adsorbed molecules, $t = 2\delta/d$, δ denotes the thickness of the surfactant layer.

Considering the foregoing, Figure 2 is a schematic representation of the attractive and repulsive energy potentials between a pair of functionalized core-shell magnetite (Fe_3O_4) nanoparticles of typical bare diameter of 10 nm, 2 nm, and 1 nm^{-2} of surfactant shell (δ) and density (ξ), respectively. As shown, the net potential energy curve exhibits an energy barrier over 20 $\kappa_B T$, which is an order of magnitude higher than the average thermal energy per particle, implying that, statistically, the agglomeration rate should be negligible under this common condition.

Figure 2

Attractive and repulsive energy potentials between a pair of functionalized Fe_3O_4 nanoparticles ($M_0 = 4.5 \cdot 10^5$ Am^{-1}).

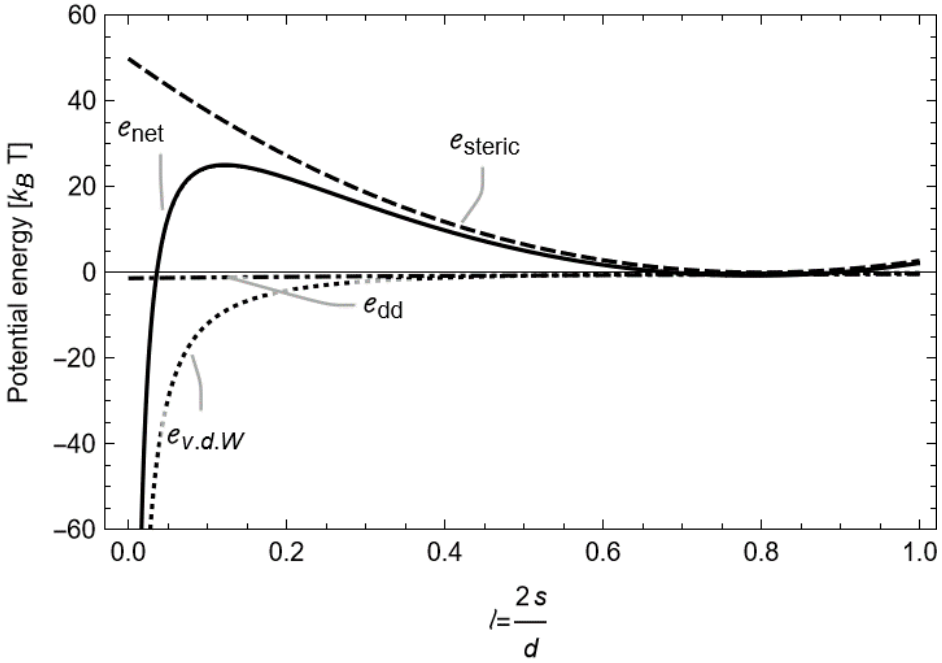

Note: Adapted from Ref. (14, 56).

1.3 Magnetic properties and constitutive equations

The straightforward manner of studying the magnetic properties of ferrofluids is to assume them as a system of non-interacting spherical particles, each with its embedded magnetic moment m~$2 \cdot 10^4$ μ_B (Bohr magnetons) and randomly oriented, analogous to the molecules of a paramagnetic gas. However, under the action of a moderate magnetic field (few tens of mT), the dipole moments tend to align along the direction of the field, enabling a net magnetization in the system that obeys a state of thermodynamic equilibrium. This ordered state is proportional to the field strength, until the magnetic field is high enough such that the magnetic forces overcome the thermal forces and the magnetization reaches its saturation value (M_s) (8, 14, 56). Based on the above, the classical theory of Langevin $L(\alpha)$ can be adapted to describe the superparamagnetic features of ferrofluids, as shown in Eq. 5 and Figure 3.

$$M_{eq}/M_s = \coth \alpha - 1/\alpha \equiv L(\alpha) \tag{5}$$

where $\alpha = (\pi/6)\,\mu_0 M_0 H d^3/\kappa_B T = \mu_0 m H/\kappa_B T$ is the Langevin parameter, $M_s = \phi M_0$, ϕ is the volume fraction of the magnetic cores, and M_0 is the spontaneous magnetization

Figure 3

Magnetization curves of monodisperse spherical Fe_3O_4 nanoparticles (M_0= 4.5·10^5 Am^{-1}).

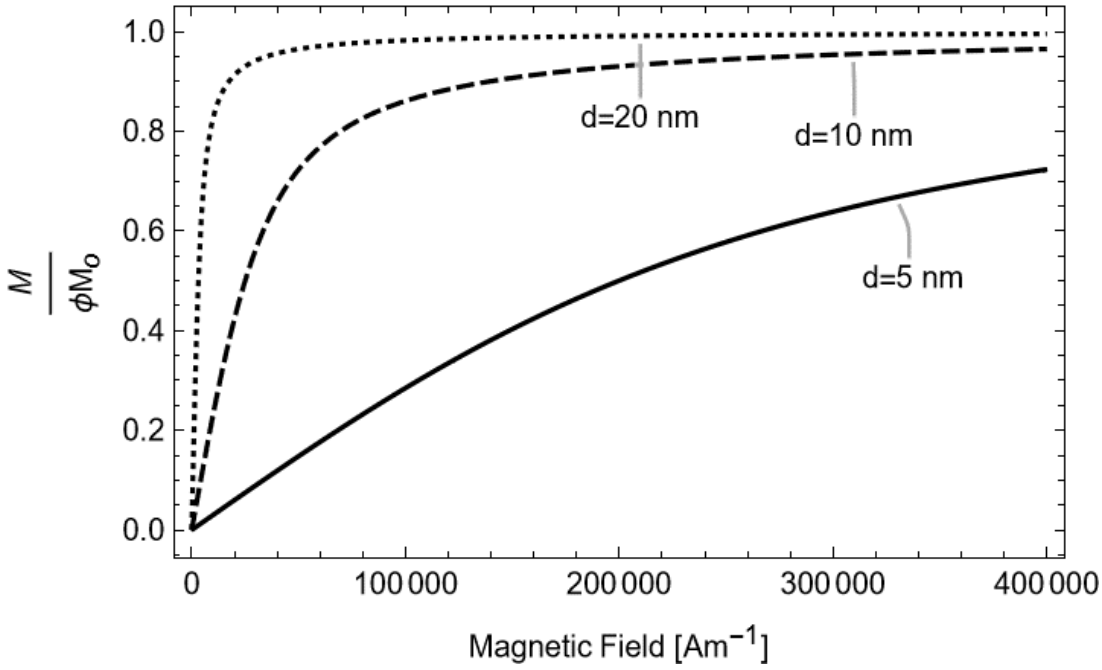

Note: Adapted from Ref.(14).

At this point, one feature to highlight is that the magnitude of the initial susceptibility (χ_i) of a ferrofluid is about four orders of magnitude stronger than that of a paramagnetic salt solution. The above can be easily analyzed in the limit condition of low magnetic fields ($\alpha \ll 1$), at which, the Langevin function reduces to $L(\alpha) \cong \alpha/3$ and, thus, the equilibrium magnetization is directly proportional to the magnetic field,

$$\chi_i = M_{eq}/H = (M_s/3)\,(\mu_0 m/k_B T) = (1/V)\mu_0 m^2/(3k_B T) \quad (6)$$

It should be noted that, in a paramagnetic gas, the net magnetic moment only reaches a few Bohr magnetons per constituent (m~2 μ_B) (61).

As outlined, the superparamagnetism of ferrofluids leads off the window of possibilities to control their fluid dynamic properties by the action of moderate magnetic fields. Among these, the

induced modifications on the apparent viscosity seem to be one of the most influential effects and one of the most challenging subjects of ferrohydrodynamics (56). The complexity arises from the deviation of the early theory of magnetization (M) collinearity with the magnetic field (H), which is valid in sufficiently small particles (or solidified systems in static equilibrium), at which, the magnetic moment rotates freely within the particle, as the thermal energy largely overcomes the energy barrier provided by the effective anisotropy of the magnetic cores ($KV \ll k_B T$, where K is the effective anisotropy constant). The induced fluctuations of the magnetization inside the grain have a characteristic time, known as Néel relaxation time τ_N (Eq. 7) (14, 56, 62).

$$\tau_N = (1/f_0)e^{KV/k_B T} \tag{7}$$

where $f_0 \approx 10^9$ Hz (8, 56).

Besides, if $KV \lessapprox k_B T$, the magnetization of the grain is in equilibrium, but the potential anisotropy energy still plays a role, and the theory of Langevin (Eq. 5) is no longer a good description of the magnetization process (63). In such case, other approaches must be employed (64).

On the other hand, for particles in a larger size domain ($KV \gg k_B T$), the magnetic moment is fixed concerning its crystal structure, the relaxation takes place by the unison rotation of the moment and the particle itself, in a process known as Brownian relaxation with characteristic time τ_B (Eq. 8) (14, 56, 62).

$$\tau_B = 3\mathcal{V}\eta/k_B T \tag{8}$$

where, $\mathcal{V} = \pi(d + 2\delta)^3/6$ is the hydrodynamic volume of the particle (*i.e.*, including the active-group shell layer and assuming spherical forms), η is the viscosity of the liquid carrier.

However, within the limit of the critical diameter, the relaxation takes place by a combination of both processes, as described by the effective relaxation time (Eq. 9).

$$1/\tau = 1/\tau_B + 1/\tau_N \tag{9}$$

The situation is even more challenging in ferrofluids since the size distribution is mostly polydisperse, which implies the simultaneity of both relaxation mechanisms. Thus, for each particle size, the relaxation time is determined by the shorter between both (Néel or Brown), and so the average relaxation time of the suspension must be estimated by observing this condition. Now then, changes in the orientation of H produce non-collinear responses of M, because of the slower process of particle rotation, which is resisted by the fluid viscous-drag torque (i.e., a lack of synchronization between the rate of rotation of a fluid element/particle and the rate of internal spin of the matter making up the fluid element). Hence, the hydrodynamics becomes less straightforward, and its continuum description requires body couples, internal angular momentum density, antisymmetric and couple stresses (8, 14, 56, 62). The following basic laws of continuum mechanics and constitutive relations comprise the whole set of ferrohydrodynamic equations (14). It is worth pointing out that we will limit the scope to isothermal incompressible ferrofluids, assuming a spatially uniform distribution of spherical, rigid, non-interacting, and monodisperse particles. Therefore, the continuity equation is established, as shown in Eq. 10.

$$\boldsymbol{\nabla} \cdot \mathbf{v} = 0 \tag{10}$$

Now, the linear momentum equation for incompressible ferrofluids (Eq. 11).

$$\begin{aligned} \rho(D\mathbf{v}/Dt) = &-\boldsymbol{\nabla} p + \rho\mathbf{g} + \mu_0 \mathbf{M} \cdot \boldsymbol{\nabla}\mathbf{H} + 2\zeta(\boldsymbol{\nabla} \times \boldsymbol{\omega}) \\ &+ (\lambda + \eta - \zeta)\boldsymbol{\nabla}(\boldsymbol{\nabla} \cdot \mathbf{v}) + (\eta + \zeta)\boldsymbol{\nabla}^2\mathbf{v} \end{aligned} \tag{11}$$

where ρ is the density, $\mathbf{v}$ is the translational velocity, $\boldsymbol{\omega}$ is the average rotation rate of the subcontinuum units (*i.e.*, particles' spin velocity), p is the pressure, $\mathbf{g}$ is the gravitational field, $\mathbf{M}$, λ, η, ζ are the magnetization, the bulk viscosity, the shear viscosity, and the vortex viscosity of the suspension; respectively.

The hydrodynamic description implies the consideration of the internal angular momentum as an independent variable, the rate of change of volume density of which (denoted by $\boldsymbol{s}(\mathbf{x},t) = \rho(\mathbf{x},t)I(\mathbf{x},t)\boldsymbol{\omega}(\mathbf{x},t)$), can be obtained by subtracting the moment of the linear momentum density from the total angular momentum density, as shown in Eq. 12 (8, 14).

$$\rho I(D\boldsymbol{\omega}/Dt) = \mu_0\mathbf{M}\times\mathbf{H} + 2\zeta(\boldsymbol{\nabla}\times\mathbf{v} - 2\boldsymbol{\omega}) + (\lambda' + \eta')\boldsymbol{\nabla}(\boldsymbol{\nabla}\cdot\boldsymbol{\omega}) + \eta'\boldsymbol{\nabla}^2\boldsymbol{\omega} \tag{12}$$

where $I(\mathbf{x},t)$ is the moment of inertia density of the subcontinuum units (particles) in the ferrofluid and will depend on the shape and concentration of the particles, λ' is the bulk spin viscosity, and η' is the shear spin viscosity.

Finally, the magnetization relaxation process depicts simultaneous magnetization and reorientation. The average spin rate of the particles in a unit volume of fluid shifts the magnetic vector of the fluid sample through $\boldsymbol{\omega}\times\mathbf{M}$ in unit time. Thus, the time rate of change of magnetization in a moving but nonrotating frame can be expressed as shown in Eq. 13 (8, 14).

$$\partial\mathbf{M}/\partial t + \mathbf{v}\cdot\boldsymbol{\nabla}\mathbf{M} = \boldsymbol{\omega}\times\mathbf{M} - (1/\tau)\left(\mathbf{M} - \mathbf{M}_{\mathrm{eq}}\right) \tag{13}$$

Nevertheless, it is important to point out that, Eq. 13 describes accurately the magnetization for low magnetic field strengths and frequencies, which are very common conditions in several ferrofluid applications and imply feasibility of the Maxwell equations in the magnetoquasistatic limit (Eq. 14) (8).

$$\boldsymbol{\nabla} \times \mathbf{H} = \mathbf{0}, \boldsymbol{\nabla} \cdot (\mathbf{M} + \mathbf{H}) = \mathbf{0} \quad (14)$$

Thus, the above corresponds to the set of ferrohydrodynamic equations (Eq. 5-14) describing the flow of a ferrofluid under the influence of a moderate magnetic field. Detailed descriptions can be found in Rosensweig's book (14).

1.3.1 Magnetoviscous effect in highly diluted ferrofluids: Rotational viscosity

Consider a ferrofluid with non-interacting and magnetically hard elemental nanoparticles (*i.e.,* Brownian relaxation time being shorter than Néelian one), experiencing a shear flow under the effect of an external magnetic field. For instance, the flow of a ferrofluid between two parallel plates $\mathbf{v} = v_z(x)\mathrm{i}_z$, generated by the movement of the upper plate at a constant velocity U. For this situation, the fluid has a local angular velocity, $\Omega_y = -\frac{dv_z}{dx}$, that coincides in direction and magnitude with the angular velocity of the particles ω_y. In the case of applying a magnetic field in the direction perpendicular to the vorticity, *i.e.,* in the *x*-direction, a magnetic torque is generated trying to align the magnetic moment of the particles in this direction and making the angular velocity of the particle to be different from the local vorticity of the fluid, which translates into an increase in viscosity. This phenomenon was experimentally observed by McTague in 1969 and explained by Shliomis in 1972 (56).

In general, an intriguing scenario unfolds, which involves a non-collinearity between the orientation of the magnetization vector (**M**) of the embedded particles and the encompassing magnetic field (**H**), emerging due to a temporal misalignment between the rotational behavior of the nanoparticle spins ($\boldsymbol{\omega}$) and the vorticity of the ferrofluid $\left(1/2\,(\boldsymbol{\nabla} \times \mathbf{v})\right)$ (65-67). Hence, an intertwined dual counteracting phenomenon emerges. On the one hand, a mechanical torque stemming from the spin–vorticity asynchrony, actively seeking to draw the dynamic magnetization

vector away from its equilibrium orientation; and, on the other hand, a magnetostatic torque stemming from the non-collinearity of **M** and **H**, exerting its influence to realign the magnetization vector back to its original equilibrium position. Consequently, this induced contrarotation between the vorticity and the magnetized nanoparticle spin results in an increased local dissipation in the flow and, eventually, a rising in the viscosity of the fluid, known as *rotational viscosity* (56, 59, 68). Eq. 15 shows the mathematical derivation proposed by Shliomis (56).

$$\Delta\eta = (3/2)(\phi'\eta_0)((\alpha - \tanh\alpha)/(\alpha + \tanh\alpha))\langle\sin^2\beta\rangle \quad (15)$$

where, ϕ' denotes the volume fraction of the particles including the surfactant, η_0 the viscosity of the solvent, α is the argument of the Langevin function (L, Eq. 5), β the angle between the vorticity of the flow and the magnetic field direction, and $\langle ... \rangle$ denotes the spatial average of the respective quantity.

Now, based on Eq. 15, under low magnetic fields, $\Delta\eta$ grows proportionally to α^2, thus (68),

$$\Delta\eta = (1/4)(\phi'\eta_0)\alpha^2, \qquad \alpha \ll 1 \quad (16)$$

And tends to saturation, under high magnetic field strengths, thus (68),

$$\Delta\eta = (3/2)(\phi'\eta_0), \qquad \alpha \gg 1 \quad (17)$$

Later, the system of equations was refined based on the Fokker-Planck equation for colloidal ferromagnet particles (69).

$$\Delta\eta = (3/2)(\phi'\eta_0)(\alpha L^2/(\alpha - L))\langle\sin^2\beta\rangle \quad (18)$$

While this approach has served as the foundational framework of ferrohydrodynamics (56), it is worth noting that changing the configuration of the magnetic field reveals a plethora of captivating phenomena. In fact, the research led Shliomis and Morozov (68) to explore an

intriguing possibility: what if the vorticity of the fluid and the spin of the magnetized nanoparticles coincide synchronously, where the nanoparticle spin velocity surpasses that of the fluid vorticity? This hypothetical alignment implies that a fraction of the internal angular momentum within the nanoparticles transfers to the fluid, thus mitigating fluid dissipation. This phenomenon was proved with frequency oscillating linearly polarized magnetic fields $\boldsymbol{H} = (H_0 \cos \omega t\,, 0{,}0)$, and the expression derived by the authors is shown in Eq. 19.

$$\Delta\eta = (1/4)(\phi'\eta_0\alpha^2)[(1-\omega^2\tau_B^2)/(1+\omega^2\tau_B^2)^2], \qquad \alpha \ll 1 \tag{19}$$

Note that, for $\omega = 0$, Eq. 19 reduces to Eq. 16. While at, $\omega_0\tau_B = 1$, the function $\Delta\eta$ changes its sign, passing from the domain of positive ($\omega < \omega_0$) to the domain of negative ($\omega > \omega_0$) values, defined by the authors as ***negative viscosity*** (59, 68, 70, 71).

Other authors have delved into alternate configurations of magnetic fields, encompassing rotating (72-74), traveling wave (75-77), static linear increasing fields (78, 79), among others. Some of these approaches will be discussed in detail in subsequent sections.

1.4 Magnetic induced ferrofluid flows in porous media

Ferrofluid applications in porous media have gained increasing awareness due to the small size, dispersibility, and ultra-stability of the suspended particles, which enables them to flow appropriately through these complex media (*e.g.*, natural sediments or fractured rock) by the action of gravitational, pressure gradient, capillary, and magnetic forces (80, 81). Furthermore, it has been theoretically demonstrated by Zahn and Rosensweig (82) the potential use of ferrofluids to prevent the well-known viscous fingering destabilization (usually denoted as Saffman–Taylor instability), occurring when an immiscible fluid pushes another more viscous one through the voids of a porous medium. The key factor here is the effective stabilizing role of a magnetic field applied tangentially

to a flat fluid interface separating the magnetizable and non-magnetizable fluids. The authors also performed experimental tests in a vertical Hele-Shaw cell coupled to a Helmholtz-like configuration that generated a uniform magnetic field directed tangentially to the interface; using an upper fluid more viscous ($\eta_{upper} > \eta_{ff}$) but less dense ($\rho_{upper} < \rho_{ff}$) than the pusher ferrofluid (to avoid Rayleigh–Taylor instability). The fingering patterns revealed that the magnetic field had a stabilizing effect and tended to decrease the finger growth rate while increasing the spacing between fingers. Afterward, Zahn and Rosensweig (83) evaluated the effect of magnetic field gradient on fingering stabilization in the recovery of reservoir-type fluids, using sand-pack flood tests coupled to two individual magnetic arrays: i) a Helmholtz pair generating uniform magnetic fields directed tangentially to the undisturbed fluid interface in the sand-pack; and, ii) an iron yoke electromagnet providing the gradient magnetic field, which was oriented tangentially to the driving interface and possessed a gradient of the field in the normal direction (*i.e.,* field increasing from the top towards the bottom of the sand-pack). One of the main observations confirmed that uniform magnetic field stabilization is not effective in realistic three-dimensional formations (*i.e.*, it only stabilizes suitably short waves traveling along the field lines) (82), the tests not only revealed that fingering was not prevented, but also recovery was very low. Meanwhile, the gradient magnetic field showed, in all scenarios, a favorable influence on fingering stabilization and significant increases in ultimate recovery (up to 62%). This gradient-field stabilization mechanism was further proved by Miranda (84), based on linear stability analysis for flow in a rotating Hele-Shaw cell, assuming that one of the fluids was a ferrofluid and that a nonuniform, azimuthal, in-plane magnetic field was applied. The physical explanation of the stabilizing role of the magnetic field obeyed the induction of a force directed radially inward which opposes the

centrifugal force and favors interface stabilization. This analytic study was then validated with numerical evaluations, that complementary proved the appearance of nonlinear instabilities, forming diamond-ring–shaped patterns, when the droplet is nearly stabilized (85). Verma and Rajput (86) also established, based on a mathematical formulation of Darcy's law, a stabilization of fingers in a homogeneous porous medium saturated with a native non-magnetic liquid of higher viscosity, and subjected to a uniform injection of a magnetic liquid and the influence of a unidirectional magnetic field. Shah and Verma (87) further discussed an analytical one-dimensional formulation of the phenomenon of fingero-imbibition (*i.e.,* the simultaneous occurrence of fingering and imbibition) in displacement processes through a saturated homogeneous porous matrix, with the injection of wetting ferrofluids and the presence of magnetic field, it was proved a decreasing tendency of saturation of the injected fluid since the average cross-sectional area occupied by the fingers was reduced (stabilization of fingers). These analyses have also been discussed considering the effects of gravitational force and capillary pressure (88). More recently, Borglin *et al.* (80) conducted some laboratory-scale experiments on the flow of ferrofluids in porous media. The authors demonstrated that ferrofluids could be mobilized by permanent magnets over distances in the order of 0.25 m on timescales of hours to days, depending on the permeability of the porous arrays, which also implied preferences of the direction of the flow pathway followed by the ferrofluid. Although, in all cases, the final ferrofluid distribution (regardless of the medium nature and gravity) held a static and predictable arc-shaped configuration around the magnet. Based on this reproducible final structure, the authors highlighted the potential use of ferrofluids in applications such as geo-physically image tracing, or the formation of overlapping barrier layers to seal tanks or pipes. Pacitto *et al.* (89, 90) further

described the magnetoviscous fingering instability in radial and linear Hele-Shaw flows subjected to different configurations of external uniform magnetic fields (normal, perpendicular, and tangential to the driven interface) and flow regimes (linear and nonlinear); the theoretical and experimental approaches led to the introduction of an effective surface tension depending on the amplitude of the magnetic field, which provided a qualitative understanding of the stabilizing/destabilizing phenomena. Miranda and Widom (91) also contemplated Kelvin-Helmholtz type of instabilities occurring in parallel flow (*i.e.*, fluids flow parallel to the interface separating them) in Hele-Shaw cells with ferrofluids, by performing a linear stability analysis under different magnetic field configurations (normal, perpendicular, and tangential to the unperturbed interface) to demonstrate that stability of the interface depends on the field's direction; on the one hand, tangential field showed stabilizing nature, while sufficiently strong normal and perpendicular magnetic field configurations led to a possible destabilization of the interface, as the ferrofluid evolves into a mazelike structure; as established by Rosensweig *et al.* (83, 92) Additionally, the authors noted that the magnetic fields may create an effective interaction between solitons (*i.e.*, localized perturbations on the flat interface) since a net dipole moment is acquired. Moatimid (60, 93) further obtained a dispersion relation of the Kelvin-Helmholtz instability of two miscible ferrofluids in porous media, by using the method of multiple scales, in linear and non-linear (Ginzburg–Landau equation) stability approximations. From the former, the author proved that both the tangential magnetic field and the surface tension are stabilizing, while Darcy's coefficients play a dual role in stability (*i.e.*, being stabilizing through porous media). Besides, from the nonlinear approximation, the streaming velocities showed stabilizing influence. Another kind of induced instabilities of a ferrofluid drop surrounded by an immiscible nonmagnetic fluid

confined in glass Hele-Shaw cells have been also reported, due to the simultaneous application of in-plane-rotating and dc-axial uniform magnetic fields (94-96). Besides monitoring the flow patterns, the authors modeled them by applying the minimum magnetization and surface energy analysis developed for labyrinth spacing (92). In general, the combination of both magnetic configurations led to the formation of a discrete droplet structure (when the clockwise rotating magnetic field is applied, followed by the DC axial field at a critical value near the saturation magnetization) or the development of clockwise spiral patterns (when the DC axial field is applied first). In that respect, Jackson and Miranda (97) explored two competing magnetic forces: (destabilizing) uniform perpendicular magnetic field, and a (stabilizing) nonuniform azimuthal magnetic field, through linear stability and numerical analyses, to design a convenient mode-selection feature that offers precise control of pattern formation.

On the other hand, some authors have relied on more realistic scenarios; Larachi and Desvigne (65-67) studied the ferrohydrodynamic ferrofluid flow in Müller porous medium of spherically shaped grains, a special class of porous media presenting pronounced effects of wall bypass flows, and subjected to external constant gradient magnetic fields (bulk-flow oriented positive and negative). They focused on formulating a simplified zero-order three-dimensional axisymmetrical (volume-averaged) model to analyze general Forchheimer non-turbulent flows, assuming incompressible Newtonian ferrofluids of non-interacting magnetic nanoparticles. Based on a series of simplifying assumptions to decouple the problem into a hydrodynamic sub-model and a magnetostatic sub-model, they demonstrated that the ferrofluid flow exhibit only magnetoviscothickening with co-rotative vorticity and spin density, acting mostly as a skinning mechanism in the wall region to produce the desired effect of slowing down channeling alongside

the wall (67). Likewise, the induced Kelvin body force, due to the magnetic field gradients, produced hypo- and hyper-gravity conditions, because of magnetic levitation, which modified the pressure drop. In general, such decoupling provided reasonable estimations of the velocity field, the spin density, and magnetization fields, but only for large and positive gradient magnetic fields (66). More recently, Kaloni and Mahajan (98) obtained a set of no definite form of the general ferrohydrodynamic equations extended to porous media, by deriving the Reynolds-Orr energy equivalence for a ferrofluid in these complex media, they established the stability bounds and conditions when these flows are asymptotically stable, based on restrictions on Reynolds, magnetic Reynolds, spin and Darcy numbers. In a complementary direction, Bashtovoi *et al.* (99) and Rahmani *et al.* (100) studied the deformations (detachment and the subsequent evolution) of a non-wetting incompressible and inviscid ferrofluid blob surrounded by a wetting non-magnetic fluid confined in a capillary tube, under the action of a uniform longitudinal magnetic field. The former (99), theoretically, and experimentally proved the elongation of the ferrofluid meniscus under the effect of the axial field, which also produced a decrease of up to twice the pressure drop. By implementing analytical and numerical methods, Rahmani *et al.* (100) solved Maxwell's, Stokes, and Young-Laplace equations, as well as the extended effect of nonlinear magnetization on the ferrofluid blob evolution. On the one side, the pre-critical state of detachment was analyzed numerically, considering that the magnetic field inside the blob was non-uniform, by employing an integral representation of the ferrohydrodynamic equations. On the other hand, the post-critical state was solved analytically, assuming an ellipsoidal configuration. Among the extended results, they proved that nonlinear magnetization has drastic effects on the critical magnetic field intensities and prevents the blob from evolving infinitely after detachment; this nonlinearity also

showed the existence of a maximum blob length beyond which detachment does not occur. Rahmani *et al.*, further explored blob configurations in complex solid geometries, using a magnetic-modified level set method, although this first approximation was limited to the assumptions of linear magnetization and constant magnetic field inside the elongated/deformed blob. Soares *et al.* (45) went further than Rahmani *et al.* by considering to deal, on the one hand, the mobilization of residual oil by a wetting ferrofluid under the application of a magnetic field (better suited to reservoir applications), but also coupling between the magnetic field and the wetting/nonwetting interface displacement. The analyses were conducted on a pore-scale model based on a two-dimensional sinusoidal snap-off geometry trapping a discrete oil ganglion; the model considered a modified Young-Laplace equation, assuming constant susceptibility (linear magnetization) and accounting for magnetic stresses: fluid-magnetic pressure and magnetic normal traction. The numerical level set representation was implemented to track the quasi-static motion of the fluid interface under the effect of magnetic stresses, and the immersed interface method (IIM) was coupled to accurately represent the field distribution in the vicinity of the interface with non-magnetic media. The results confirmed that the application of magnetic fields parallel to the flow path, led to blob detachment from the wall, because of magnetic permeability contrasts producing higher magnetic field strengths near the contacts between the oil blob and the pore wall. Furthermore, the study revealed that fluid-magnetic pressure played a more significant role in the displacement of fluids than magnetic normal traction. Therefore, increasing the strength of the applied magnetic field and/or ferrofluid susceptibility was found to enhance fluid displacement. Afterward, Zakinyan *et al.* (81) studied the capillary ascension of ferrofluids through a sandy porous medium, and under the simultaneous action of upward/downward directed gradient

magnetic fields. The experimental and theoretical observations showed that an upward-directed field gradient increased the maximum reachable height and accelerated the ferrofluid capillary rise. The authors also highlighted the advantages of measuring the inductance, by using a solenoid and a small sensing coil, to evaluate the porous material parameters as an alternative technique (relative differences below 10%); especially when using materials with visually indistinguishable wet and dry regions.

1.5 Ferrofluid-assisted enhanced oil recovery

The earliest approaches reported on enhanced oil recovery processes with the simultaneous application of ferrofluids and magnetic field could be ascribed to the analytical formulation reported by Shah and Verma (87) on saturation profiles of fingero-imbibition phenomenon in homogeneous porous media, discussed previously. Based on the same mathematical formulation; *i.e.,* one-dimensional cylindrical block, two immiscible fluids, less viscous and wetting ferrofluid, magnetization directly proportional to the magnetic field intensity, and the macroscopic behavior of fingers is governed by a statistical treatment (see Table 2); Gohil and Meher (101) extended this study, by implementing the Analytical Homotopy solution Method (HAM) to counter-current imbibition phenomenon in heterogeneous porous media, while also considering the effects of inclination and viscosity of native fluids (1-100 cP) on the saturation and recovery rates of the reservoir. According to the results, the saturation profile and recovery rates are slightly favored due to the presence of the magnetic field, but mainly in reservoirs with low viscous native fluids. Huang *et al.* (102) previously reported a numerical simulation on ferrofluid flow, acting as a displacing fluid for flooding in fractured porous media, based on a discrete-fracture model. Similarly, the authors applied the magnetic modified Darcy's law for the seepage velocity ($v_w =$

$-\frac{k_w}{\mu_w}\boldsymbol{K}\cdot[\nabla P_w - g\rho_w\nabla D - \mu_0 M\nabla H]$, where D denotes highness and $\boldsymbol{K}$ the permeability tensor, which changes to scalar K in isotropic porous media), assuming isothermal flow of an incompressible fluid, and neglecting capillary and magneto-strictive pressure $\left(P_s = \int_0^H \left[\frac{\partial(MV)}{\partial V}\right]_{H,T} dH \approx 0\right)$. Two scenarios were considered, single- and complex-fracture porous media subjected to non-uniform distribution of magnetic field provided by NdFeB magnets (residual flux density $Br = 1.19\ T$) located in the upper left and lower right corner (for the single-fracture scenario) and the upper left (for the complex one), over a square area of 25 cm^2 and 72 cm^2, respectively. In the former, the modeled flow patterns of the ferrofluid were compared with experimental results, in which an acceptable equivalence was observed. These validated flow patterns were compared with water-flooding in the complex scenario, showing that the ferrofluid in the presence of the magnetic field increased the swept area, resulting in enhanced displacement efficiency (recovery ratio improved from 40% to 62%). More recently, Huang *et al.* (103) extended the study to heterogenous and fractured porous media, using the Galerkin finite element method for discrete equations, whose validity and accuracy were verified through the 1-D horizontal tube configuration, analytically studied by Moridis (104). The authors demonstrated the induction of flow in very low permeability areas or secondary fractions under the effect of the magnetic field, as well as the modification of the direction of flow and velocity. Meanwhile, El-Amin and Brahimi (105) applied the same fundamental equations, but considering the capillary, Brownian diffusion, magneto-strictive (P_s), and fluid-magnetic (P_m) pressures in the momentum (extended Darcy's law) and mass conservation (saturation equation) equations (see **Table *2***), which can have a significant impact on two-phase flow, as proved by Prodanovic *et al.* (106) The results showed

that saturation profiles, nanoparticle concentration distribution, and deposition are attractively affected by the magnetic field. The authors also demonstrated that inducing a positive gradient of magnetic field in the direction of ferrofluid flow can lead to a higher saturation profile of nanoparticles, suggesting that the field can potentially aid in promoting flow (107). Therefore, it is worth emphasizing that, although these theoretical studies have proved the potential of inducing non-uniform magnetic pressures to both enhance the transport of ferrofluids to target locations in reservoirs and facilitate immiscible ferrofluid-fluid two-phase flow, only a limited number of them have validated these findings with experimental data.(102) Divandari *et al.* (108) were the pioneers in implementing functional experimental arrays such as 2D heterogeneous and homogeneous glass micromodels, to assess the effectiveness of ferrofluids in enhancing the oil recovery factor. However, the high magnetic field intensities applied during the experiment had a detrimental impact on the stability of the formulated ferrofluids. Despite exhibiting this atypical behavior, with a visible precipitated magnetic phase, the experimental results showed that the recovery factor was maximized (up to 83%) with the simultaneous application of the magnetic field, which was 22% more effective. The images captured during the experiment showed the formation of column-like structures that produced a piston-sweeping flow. Ningyu Wang *et al.* (109, 110) studied the mobilization of oil blobs (decane-mineral oil mixtures) in 2.5D converging-diverging single channel and foot-long micromodels, influenced by water-based ferrofluid (EMG 700, Ferrotec) flooding and the simultaneous application of uniform static or rotating magnetic fields (< 5 mT). On the one hand, microfluidic experiments showed an enhanced mobilization of oil blobs under the effect of static magnetic fields (oil saturation decreased from 24% to 12%), which was essentially attributed to non-uniform magnetic induced pressure. On the other hand, the authors

proved the formation of nanoparticle clusters/chains attached to the oil blob interfaces under a rotating magnetic field, which led to the formulation of a second mechanistic explanation involving the induction of torques that promoted the rotational motion of the oil blobs. Several authors also agree with the induction of columnar structures that may prompt a piston-like flow, ultimately leading to enhanced oil recovery.(43, 46, 108) Esmaeilnezhad *et al.* (46) have emerged as trailblazers in applying core flooding tests with the simultaneous use of ferrofluids and static magnetic fields. Notably, increases in the oil recovery factor of up to 10% were reached in the presence of the magnetic field using light oil and Berea sandstone cores. Intriguingly, this effect was not replicated when dealing with heavy oil. While the authors did not provide a comprehensive explanation for this discrepancy, it is plausible that the observed differences could be effectively attributed to the formation of aggregates in the light oil. This conjecture gains strength from the fact that Brownian relaxation mechanisms have a direct correlation with fluid viscosity, potentially shedding light on these outcomes. In this direction, Divandari *et al.* (108) conducted similar experiments using 2D heterogeneous and homogeneous glass micromodels. Their work yielded remarkable outcomes, showcasing recovery factor enhancements of up to 50% through the concurrent application of ferrofluids and static magnetic fields. Particularly noteworthy is their successful identification of the formation of distinct columnar-like structures, providing deeper insights into the underlying mechanisms at play. Notwithstanding, we must highlight a crucial aspect that remains inadequately explored, associated with the stability of the formulated ferrofluids in water-based carrier liquids containing dissolved salts that induce detrimental effects. On the other hand, alternative research attempts have leveraged the presence of these salts alongside the incorporation of nanoparticles (Fe_2O_3 (111), Al_2O_3 (111), MgO (112)) to promote

the emergence of a reciprocal interplay between fluid dynamics and magnetic fields, a phenomenon known as magnetohydrodynamics.

Table 2

Set of counter-current imbibition phenomenon equations, dealing with an external effect of magnetic field.

Ref.		Constitutive Equations	Assumptions
(**101**)	Conservation of mass(113)	$\frac{\partial}{\partial t}(\varphi(x)S_i\rho_i) + \nabla\cdot(\rho_i v_i) = 0$ $\varphi = \varphi(x) = \frac{1}{a-bx}, a - bx \geq 1, K = K_C\phi(x)$ where, $i = w, nw$ refers to the wetting (aqueous) and non-wetting (oil) phases respectively, ϕ is the porosity of soil, K_C is a constant of proportionality, and S, ρ, v_i are the saturation, density, and Darcy's velocity of the phase; respectively.	Incompressible fluids (ρ_i is constant)
	Seepage velocities Darcy's Law(87, 101)	$v_{nw} = -K(x)\frac{k_o}{\mu_o}(\nabla\cdot P_o - g\rho_o\sin\alpha)$ $v_w = -K(x)\frac{k_w}{\mu_w}(\nabla\cdot P_w - g\rho_w\sin\alpha + \gamma H(\nabla\cdot H))$ $\gamma = \mu_0\chi + \frac{16\pi\mu_0\chi^2 r^3}{9(l+2)^2}$, where, μ_0 is the magnetic permeability of free space, χ is the susceptibility, r is the radius of magnetic fluid particles, l is the center-to-center distance of magnetic particles, α is the inclination angle, P_i, k_i and μ_i are the pressure, relative permeability, and viscosity of fluids. K is the permeability of the porous medium.	$v_{nw} = -v_w$(114)
	Capillary pressure, relative permeability and phase saturation(115).	$P_c = P_{nw} - P_w = \beta({S_w}^{-\frac{1}{2}} - C)$ $k_w = {S_w}^3$ $k_{nw} = 1 - 1.11S_w$ where, β and C are constants	Relative permeability curves are S-shaped
(**105**, **107**)	Magnetization(116)	$M = a_1\tan^{-1}(b_1 H)$ a_1 and b_1 are parameters that depend on the ferromagnetic material. $M(S_w, c) = M(S_w = 1, c = 1)S_w c$ Magnetization increases linearly with the ferrofluid saturation, c is ferrofluid mass fraction.	$a_1 \sim 10^4 - 10^5$ $b_1 \sim 10^{-6} - 10^{-5}$
	Seepage velocities Darcy's Law	$v_{nw} = -\boldsymbol{K}\frac{k_o}{\mu_o}(\nabla\cdot P_o - g\rho_o)$ $v_w = \lambda_w f_0 \boldsymbol{K}\cdot(\nabla {P_c}^* - \nabla g\rho_w - \mu_0 M(S_w, c)\nabla H)$ ${P_c}^* = P_c - (P_m + P_s)$ $P_s = \mu_0\int_0^H v(\partial M/\partial v)_{H,T}dH$	$v_{nw} = -v_w$ Countercurrent imbibition

	$$P_m = \mu_0 \int_0^H M\, dH$$ where, P_c, P_m, P_s denote the capillary, fluid magnetic, and magnetostrictive pressures, respectively. K is the permeability, $\lambda_w = k_w/\mu_w$, $f_0 = \lambda_0/\lambda_t$ is the flow fraction, $\lambda_t = \lambda_{nw} + \lambda_w$ is the total mobility.	
Capillary pressure,(117) relative permeability and phase saturation	$$S = (S_w - S_{iw})/(1 - S_{rnw} - S_{iw}),\ 0 < S < 1$$ $$k_w = {k_w}^0 S^{a_2}$$ $$k_{nw} = {k_{nw}}^0 (1 - S)^{b_2}$$ where, P_d is the entry pressure for the imbibition and S is the normalized water phase saturation. S_{iw} and S_{rnw} denote the irreducible water saturation and residual oil saturation, respectively. ${k_w}^0 = k_w(S = 1)$ and ${k_{nw}}^0 = k_{nw}(S = 1)$ are the endpoint relative permeability of the water and oil phase, respectively. a_2 and b_2 are positive numbers.	$P_c = P_d \ln S$
Nanoparticles Transport Model	$$\phi\, \partial(S_w c)/\partial t - \partial c_{s1}/\partial t - \partial c_{s2}/\partial t + \partial/\partial z\left(v_w c - \phi S_w \left(D_{diff} + D_{disp}\right) \partial c/\partial z\right) = 0$$ $$\partial c_{s1}/\partial t = \begin{cases} \gamma_d |v_w| c, & v_w \le v_c \\ \gamma_d |v_w| c - \gamma_e |v_w - v_c| c_{s1} & v_w > v_c \end{cases}$$ $$\partial c_{s2}/\partial t = \gamma_{pt} |v_w| c$$ where, c, c_{s1}, c_{s2} denote the volume concentration of nanoparticles in the water phase, in contact with the water phase available on the pore surfaces per unit bulk volume of the porous medium, entrapped in pore throats from the water phase per unit bulk volume of porous medium due to plugging and bridging; respectively. D_{diff} is the molecular diffusion coefficient, D_{disp} is the mechanical dispersion coefficient. γ_d, γ_e are the rate coefficient for surface retention of the nanoparticles in the water phase, for entrainment of the nanoparticles, respectively. γ_{pt} is the pore throat blocking constant, v_c is the critical velocity for the water phase. Nanoparticles deposition – Porosity variation(118) $$\phi = \phi_0 - \delta\phi,\ \ \delta\phi = c_{s1} + c_{s2}$$ $$K = K_0\left[(1 - f)k_f + f(\phi/\phi_0)\right]^l$$ $$f = 1 - \gamma_f c_{s2}$$ where, ϕ_0 is the initial porosity, K_0 the initial permeability, $k_f$is constant for fluid seepage allowed by the plugged pores, f is the flow efficiency factor expressing the fraction of unplugged pores available for flow, γ_f is the coefficient of flow efficiency for the nanoparticles. Nanoparticles reposition - Relative permeabilities(105) $$k_{i,p} = [1 + r_a(\theta_a - 1)]k_i, i = w, nw$$	Nanoparticles exist only in the water phase and have only one size interval. l~2.5 – 3.5

	$\theta_a = k_{i,c}/k_i$ $r_a = a_{tot}/a_{sp}$ $a_{sp} = A\phi(\phi/K)^{1/2}$ $a_{tot} = (6\beta/d)\delta\phi$ where, θ_a is the ratio of the phase i relative permeability due to nanoparticles adhering, $k_{i,c}$ is the relative permeabilities of water/oil phase when the surfaces per unit bulk volume of the porous media is completely occupied by the nanoparticles. $a_{sp}$is a specific area of the sand core, A is the cross-sectional area, a_{tot} is the total surface area in contact with fluids per unit bulk volume, d is the diameter of the nanoparticles.

Magnetic nanoparticles have also garnered recognition as nanosensors to determine the hydrocarbon saturation distribution in subsurface formations. Along this line, Prodanovic *et al.* (106) proposed a parallel application geared towards modeling and detecting the acoustic response of hydrocarbon/water-based ferrofluid interfaces movements, induced by an imposed oscillating magnetic field. The authors coupled the Maxwell, modified Young-Laplace and Navier-Stokes equations (see Table 3) to theoretically evaluate the effect of density difference, and susceptibility (χ) of particles on the composite pressure in a straight capillary (p^*, see Table 3), proving that the relative densities of the fluid phases strongly affect the displacement, *i.e.*, the sum of magnetostrictive (p_s) and fluid-magnetic (p_m) pressures is inversely proportional to the difference in the densities of the fluids and directly proportional to the density of the non-magnetic fluid, $\left(\frac{1}{2\mu_0}\frac{\chi}{(\chi+1)^2}\right)\left(\chi {B_{1n}}^2 - {B_1}^2\right)\left(\frac{\rho_1}{\rho_1-\rho_2}\right)$. Likewise, these pressure-like terms depend on imposed magnetic field (B) quadratically, which in the case of a sinusoidal magnetic field leads to a doubled frequency in resulting interface displacement. Those theoretical predictions were confirmed in an experimental setup, using phase-shift optical coherence tomography (PS-OCT) to detect oscillations of water-based ferrofluid (with iron-oxide nanorods) and dodecane interfaces. The

study was further extended to pore scale arbitrary geometries, using a quasi-static numerical interface-tracking model, based on the level-set method ($F(\vec{x},\tau,t) = p_c - (p_s(t) + p_m(t) + p_n(t)) - \sigma\kappa(\vec{x},\tau) = 0$). In a subsequent study, Ryoo *et al.* (119) expanded upon their earlier experimental and modeling work. On the one side, by studying interface displacements of air/water-based ferrofluids of in-house synthesized and surface-modified iron-oxide nanoparticles, as a function of the magnetic field strength, nanoparticle concentration, nano-cluster size, and the applied frequency. In all cases, the amplitude of the displacement of the interface was proportional to the magnetic field strength and independent of the applied frequency; there was also a functional proportionality with the nano-cluster sizes. On the other hand, the numerical method was improved to ensure volume conservation, leading to more precise quantitative matching.

Table 3

Governing equations of oscillating fluid-fluid interfaces, dealing with an external effect of magnetic field.

	Constitutive Equations	**Assumptions**
Navier-Stokes(14)	$\rho(D\mathbf{v}/Dt) = -\boldsymbol{\nabla}P^* + \rho\mathbf{g} + \mu_0\mathbf{M}\cdot\boldsymbol{\nabla}\mathbf{H} + \eta\boldsymbol{\nabla}^2\mathbf{v}$ $P^* = P(\rho,T) + P_s + P_m$ $P_s \equiv \mu_0\int_0^H \mathbf{v}\left(\frac{\partial\mathbf{M}}{\partial\mathbf{v}}\right)_{H,T} d\mathrm{H}$ $P_m \equiv \mu_0\int_0^H \boldsymbol{M}\, d\mathrm{H}$ where, P^* is the composite pressure, P_s is the magneto-strictive pressure, and P_m the fluid-magnetic pressure.	Incompressible fluids (ρ is constant) $\boldsymbol{\nabla}\cdot\mathbf{v} = 0$
Capillary pressure	Boundary conditions (magnetic modified Young-Laplace equation) $P_c - (P_s + P_m + P_n) - \sigma\kappa = 0$ $P_n \equiv \mu_0\,(H_{2n} - H_{1n})^2/2$ where, p_n is the magnetic normal pressure. H_{1n} is the component of the magnetic field strength in fluid 1 normal to the interface.	The wetting fluid is magnetizable (W, water). $\mathbf{M} = \chi\mathbf{H}$

1.6 Ferrofluid flow: Prospects for pipeline transportation

Acknowledging the substantial breadth of literature dedicated to the exploration of fluid dynamics and magnetorheology of ferrofluids (8, 9, 120, 121), we embark on this section with a clear purpose focused on delving into the intricacies of ferrofluid flow, fundamentally through pipelines, under the influence of magnetic field configurations with the potential of enhancing flow properties. The goal is to lay the groundwork for guiding the significant prospect of this technology within the reality of the oil industry.

Now, revisiting the groundbreaking notion of *negative viscosity* ($-\Delta\eta$) introduced by Shliomis and Morozov (68), which served as a stepping stone in the investigation of alternative magnetic field configurations; it is pertinent to highlight the experimental endeavors of Bacri *et al.*(70) and Zeuner *et al.*(122) dedicated to substantiating this theoretical concept through experimental approaches at laminar flow regimes, satisfying the condition, $\Omega\tau_B \ll 1$, where Ω is the azimuthal component of the flow vorticity $\mathbf{\Omega} = (\boldsymbol{\nabla} \times \mathbf{v})/2$. On the one hand, Bacri *et al.* (70) evaluated the Poiseuille flow in a horizontal capillary tube (d=1 mm) of a 20 vol.% Co-ferrite water-based ferrofluid (particle size d=10 nm, effective anisotropy constant K=2 $\cdot 10^6$ erg cm^3, grain magnetization M_s= 400 G), under the application of a longitudinal alternating magnetic field of up to H= 1 kOe at a frequency (f) varying from 0 to 1 kHz. The same qualitative behavior of the rotational viscosity ($\Delta\eta$) was observed as theoretically established; a decrease of $\Delta\eta$ was reached from 143 cP at $f = 0$ Hz to -19 cP at $f \geq 700$ Hz. The authors additionally introduced a refined magnetization equation, obtained through the adaptation of the Fokker-Planck equation for rotary diffusion of colloidal particles with the assistance of the effective field method, which led to obtaining improved alignment with the experimental results. Particularly, in instances where

$\omega\tau_B \geq 1$, both the theoretical and the experimental data showed that the ferrofluid viscosity under an alternating magnetic field can be smaller than the viscosity in a zero field. On the other hand, Zeuner *et al.* (122) evaluated the Poiseuille flow of a commercial 3.5 vol.% F_3O_4 water-based ferrofluid (d~12 nm, saturation magnetization Ms=0.02 T) in two horizontal capillary pipes in series (d=1 mm), wherein one pipe was connected to a solenoid while the other acted as a reference. The advantage of this arrangement lies in its independence to temperature fluctuations, as only the ratio of the viscosities is determined. The applied magnetic field strength of interest was ranged up to 15 kA·m^{-1}, and the frequency (f) was varied between ~1- 22 kHz. Similarly, the results were qualitatively in agreement with the theory, although some critical remarks in terms of the quantitative comparison were highlighted by the authors, fundamentally associated with nanoparticle polydispersity, concentration, and aggregation, all influencing the dynamics of Brownian relaxation. On this basis, the authors proposed an analytical approximation modified by a phenomenological frequency-dependent Brownian expression, which effectively fitted the experimental results for small alternating magnetic fields. Felderhof (123) supported these remarks by integrating the effect of the demagnetizing field (H^D) into the magnetization relaxation equations of Shliomis,(59) modified Shliomis,(69) and Felderhof and Kroh (124) in the flow of a ferrofluid in a tube under an alternating magnetic field, considering that H^D has a significant effect in systems with moderate initial magnetic susceptibility. The analysis developed by the authors led to the conclusion that, the modified Shliomis magnetization equation is adequate for dilute ferrofluids. Later, Schumacher *et al.* (125) extended the Poiseuille flow experiments under alternating fields to turbulent regimes, using a similar setup to the one designed by Zeuner *et al.* (122). The applied magnetic field was increased up to 1264 Oe, the frequency was varied between

~0- 1 kHz, and the studied fluid was a commercial water-based ferrofluid. The experimental results were numerically evaluated by a model based on the ferrohydrodynamics equations, which adequately predicted the fractional pressure drop as a function of flow rate, magnetic field, and oscillation frequency, in both laminar and turbulent flow. Although, a functional dependence of the magnetic susceptibility on the magnetic field and relaxation time, in laminar flow, had to be imposed. Furthermore, these works have provided the foundation for numerous publications engaging in a captivating assortment of analytical and numerical approaches (126-128), as well as simulations (129). These efforts have provided support and improvement of the foundational models (123, 126), but also have led to instances where they have been challenged and contradicted.(130) Other authors have further explored alternative time-varying magnetic field configurations, Krauß *et al.* (131) studied the surface driving macroscopic flow of two kinds of ferrofluids (magnetite- and cobalt-based) under the application of an external *rotating* magnetic field, employing a circular duct with a mean diameter of 100mm and a square cross-section of 5mm×5mm. The experimental results proved that the rotating magnetic field led to a motion of the fluids in azimuthal direction of the channel, moving at a velocity proportional to the square of the amplitude of the driving external magnetic field. Finally, one of the most recent advances in the field has been documented by Mao *et al.*, (75) who experimentally demonstrated a fascinating phenomenon of direct body pumping of ferrofluids at controllable speeds in closed-loop geometries, when subjected to *traveling wave* magnetic fields. The experimental setup involved the use of a commercial 7.7 vol.% Fe_3O_4 oil-based ferrofluid, electromagnetic coils generating magnetic field strengths up to 9000 A/m peak-to-peak and frequencies spanning from 0 to 2 kHz, as well as polyvinyl chloride (PVC) pipes with an inner diameter of 15.4 mm and a thickness of

2.8 mm. Perhaps the most significant insight drawn from the work involved the dynamical formation of particle dimers; a finding that wielded profound influence over the ferrohydrodynamic flow, even in scenarios of moderate magnetic fields. This dimer phenomenon, unanticipated from the foundational equations, undoubtedly took center stage in the observations, setting an unprecedented dimension for the understanding of ferrofluid behavior.

2 Rheological implications of the inclusion of ferrofluids and the presence of uniform magnetic field on heavy and extra-heavy crude oils[†††]

2.1 Abstract

This study embraces the evaluation of the rheological and magneto-rheological properties of heavy and extra-heavy crude oils by applying nanotechnology and magnetism as technological solutions in reducing viscosity. Mixtures of heavy oils with ferrofluids were used to study the viscous effects induced by the action of external magnetic fields. The rheological evaluation covered rotational and oscillatory tests as a function of time and temperature. In the magneto-rheological characterization, there were analyzed the magnetoviscous effects. The results revealed that the crude oils are viscoelastic materials that follow the Generalized Maxwell Model over a wide range of temperatures (-5 to 60°C). It was also proved that the synergy between the carrier liquid and the nanoparticles promoted a significant reduction of viscosity (~98-99%) and viscoelasticity, which was directly related to the simultaneous action of the solvent and the asphaltene adsorption onto the nanoparticles surface. Critical concentrations of nanoparticles (0.2 wt.% and 0.6 wt.%) were proved to promote the maximum decrease in viscosity (additional ~0.3-0.5% or 1000-3000cP) and the elastic storage modulus, which was crucial evidence of their effect on hindering the aggregation mechanisms of asphaltenes. In the heavy oil-ferrofluid mixtures, a magneto-rheological effect was demonstrated. The magnetic field attenuated the initial relaxation

[†††] 2. Contreras–Mateus MD, López–López MT, Ariza-León E, Chaves–Guerrero A. Rheological implications of the inclusion of ferrofluids and the presence of uniform magnetic field on heavy and extra-heavy crude oils. Fuel. 2021;285:119184.

processes, leading to an increase in the viscosity and shear stress. The phenomenon was attributed to the formation of magnetic chains, such as that observed in magneto-rheological fluids. These results were supported by Scanning Electron Microscopy, which showed the formation of magnetic-field induced thick columnar assemblies of nanoparticles-asphaltene complexes.

2.2 Introduction

Heavy crude oils are defined as oils with specific gravity scale developed by the American Petroleum Institute (API) and viscosity below 22.3 and 10.000 cP (10 Pa·s), respectively; while extra-heavy oils are those with API gravity under 10 and viscosity above 10.000 cP (10 Pa·s) at reservoir conditions (132). Generally, they consist in complex mixtures of hydrocarbon families (hydrogen 8-12 wt.% and carbon 80-88 wt.%) (133); heteroatoms like sulfur (0-9 wt.%) (134), nitrogen (0-2 wt.%)(134) and oxygen (0-2 wt.%) (134); and traces of heavy metals (V, Ni, Fe) contained in metalloporphyrins (133, 135-137). Because of the chemical complexity of the heavy and extra-heavy crude oils, industries and academy generally employ a practical fractionation technique based on solubility and polarity parameters known as SARA analysis, which divides their components into Saturates, Aromatics, Resins, and Asphaltenes.

From the microscopic structural viewpoint, heavy crude oils are also defined as viscoelastic colloidal suspensions, whose dispersed elastic phase is attributed to asphaltene aggregates over a semi-continuous matrix of maltenes (saturates, aromatics and resins) (138-141). Under certain thermodynamic conditions (*i.e.*, modifications of the composition, temperature or pressure (142)), these components are prone to self-associate and to precipitate due to their compositional complexity that varies from single aromatic cores (island) to bridged aromatic moieties (archipelago), with short and long alkyl units, and multi-heteroatom functionalities (143). One of

the well-known consequences of the agglomeration and precipitation of asphaltenes consists of dramatic increases in viscosity and non-Newtonian rheological behavior (*i.e.*, viscoelasticity (138, 144), thixotropy (145)), as well as, the formation of deposits on steel surfaces (146). This complex behavior hinders their mobility and flowability through pipelines, causing several operational and economic problems in oil industries. As a result, the oil transportation industry has implemented conventional technological solutions, mainly based on viscosity and friction reduction, to reach the required viscosity specifications, which must be in the range of 250-400 cSt at 37.8°C (147). Martínez-Palou *et al.* (136) and Hart (148) describe in detail some of these techniques and discuss their advantages and disadvantages. As an important conclusion from the reports, it is observed that industry has not yet developed an effective technique to be implemented at operational level; these conventional solutions imply high energy consumption, high operational cost, and technical difficulties (*i.e.*, flow turbulence), evidencing the need to propose and study alternative approaches.

Over the last decades, the non-conventional magnetic and electric technologies have shown to be effective in reducing viscosity and flow turbulence (mainly when using waxy crude oils) (149), showing lower energetic and economic costs. Several studies have concluded that the magnetic field may reduce viscosity and modify wax crystallization mechanisms of waxy crude oils without affecting their thermodynamic equilibrium (150-154). It has also been reported that magnetic fields influence the resinous-asphaltic fraction (152, 155) and can even modify the rheology due to the presence of paramagnetic ions in the water phase (156). Some researchers have explained that the magnetic/electric fields improve the flow properties by induction of an anisotropic viscosity, which is the result of aggregation phenomena of the colloidal phase (149,

151, 157, 158). In contrast, other authors have described the influence of magnetic fields as promoters of disaggregation (153, 154). Equally important, various studies have also shown the high selectivity of the magnetic treatment over the nature of crude oils (156, 159), and in several cases, the non-functionality of this method; which have been justified by the well-known diamagnetism of these fluids (150, 156, 159, 160). Certainly, so far, it has not been possible to establish the interaction mechanism between the crude oil and the magnetic field, as well as its role in preventing or promoting the association of heavy organic materials, such as asphaltenes, in the case of heavy crude oils. Thus, it is fundamental to propose experimental strategies to facilitate the elucidation and functionality of this approach, seizing their technical and operational benefits.

Additionally, another useful innovative approach for improving the rheological properties of heavy crude oils is nanotechnology, which harnesses the considerably high ratios of surface area/volume as well as the functionalizable surface area of nanoparticles (NPs) for adsorption of asphaltenes (5, 6, 142, 146, 161-164). Among the NPs successfully employed are included, iron oxides (Fe_2O_3 (165), Fe_3O_4 (161, 164, 165), γ-Fe_2O_3 (142), α-Fe_2O_3 (142)), aluminum oxides (γ-Al_2O_3 (146), Al_2O_3 (5)), nickel oxide (NiO (161)), cobalt oxide (Co_3O_4 (161)), titanium oxide (TiO_2 (161)), silica (SiO_2 (5, 6)), among others; and several theoretical assumptions about asphaltene adsorption mechanisms have been proposed, including both chemisorption (166) and mostly, physisorption (146, 161, 167-169). Furthermore, it has been concluded that asphaltenes are mainly adsorbed on the surface of NPs forming single layers, *i.e.*, the adsorption isotherms are typically Langmuir Type I (142, 146, 165, 170).

Particularly, metallic oxide NPs have attracted great interest because of their highly selective physicochemical properties, enabling broad applicability in hydrocarbon Exploration and

Production-E&P (171). Within their unique properties are included, significant surface area and amount of active sites (165), thermal conductivity and heat transfer (171), enhanced catalytic effect (161, 167), and in some cases, such as magnetite (Fe_3O_4), superparamagnetic behavior (3-15 nm (14)). Fundamentally, because of the latter property, magnetic NPs have been widely used in other fields, such as the development of stable magnetic colloidal suspensions, known as ferrofluids, to solve a wide variety of technical problems related to fluid dynamics. Ferrofluids exhibit an extraordinary high initial susceptibility, and thus, they present high magnetization for moderate magnetic field strength (~50 mT) (56); accordingly, their flow properties can be controlled by such magnetic fields. For example, some studies have demonstrated increases in viscosity and a magnetoviscous effect (*i.e.*, concentrated magnetic suspensions (56)) under the influence of uniform static magnetic fields (172, 173), but it has also been possible to induce "negative" viscosity responses under the action of alternating magnetic fields (174, 175); and even, flow appearance using rotational and traveling magnetic fields (73, 75, 176-179).

It is worth noting that, to the best of our knowledge, there is no research in which magnetic nanoparticles and externals magnetic fields have been simultaneously applied to improve the flow behavior of heavy and extra heavy crude oils. However, this approach has already been evaluated as an alternative for improving crude oil demulsification (180-184), spill control (185), pavement engineering (186), and Enhanced Oil Recovery (EOR) (187).

Motivated by the possibility of using magnetic fields to control the rheological behavior of heavy oils effectively, this research reports the rheological and magneto-rheological characterization of mixtures of ferrofluids and heavy crude oils (hereinafter, crude oil-ferrofluid models), considering the fundamentals of the induction of magnetoviscous effects. Accordingly,

this work is divided into two parts: (1) a rheological characterization of the crude oils and the crude oil-ferrofluid models, including steady-state flow curves and dynamic experiments to generate a baseline for comparison purposes, and (2) a magneto-rheological characterization of the crude oil-ferrofluid models to evaluate modifications in the rheological behavior by the application of a magnetic field. The experiments were carried out under the effect of static uniform magnetic fields, using a magneto-rheometer. The results revealed that the action of a uniform external magnetic field had a direct effect on the rheological properties of the heavy crude oil-ferrofluid models, and this effect was hindered by the complexity of the flow behavior of the samples, particularly, the structural properties and the viscoelastic effects. These results could be the basis for the applicability of this hybrid approach in decreasing the energy consumption, due to the possibility of controlling the flow properties of heavy crude oils by the action of external magnetic fields that overcome the gravitational and viscous forces.

2.3 Materials and Methods

2.3.1 Materials

The samples used corresponded to two Colombian heavy crude oils (hereinafter, C_1 and C_2), which were characterized by the determination of i) the concentration of asphaltenes (ASTM 6560-12 (188)), ii) the density by the pycnometer method (ASTM D70-18a (189)), and iii) the zero-shear viscosity by rheometry; their properties are shown in Table 4. Commercial magnetite NPs (EMG 1300) were obtained from Ferrotec (USA) Corporation and were used without any further treatment. According to the providers, NPs have a nominal diameter in the order of 10 nm, iron oxide content between 60-80 wt.%, saturation magnetization in the order of 50-70 emu/g, and a polymeric surfactant. Commercial kerosene was used as the carrier fluid of the ferrofluids,

considering that López-López *et al*. (190) reported that oleate-covered magnetite in carrier liquids with dielectric constants, $\varepsilon_r < 5$, such as kerosene, are thermodynamically stable due to the very low lyophobic attraction between NPs.

Table 4

Asphaltene concentration, API gravity, and viscosity of the heavy crude oils.

Properties	**C_1**	**C_2**
Asphaltene concentration (wt.%)	21.93 ± 4.689	21.55 ± 4.688
API gravity	7.87	10.6
Viscosity (Pa·s)	2070 (25°C)	44.1 (25°C)
	976 (30°C)	24.1 (30°C)

2.3.2 Preparation of the heavy crude oil-ferrofluid models.

The procedure was based on the methodologies employed in refs. (190-192) and it consists of the following stages: i) the NPs were added to the kerosene in concentrations of 0.2; 0.6; 1 and 5.0 wt.%. ii) The suspensions were agitated by hand and then immersed in an ultrasonic bath for 15 min. Subsequently, they were stirred in an orbital shaker at 150 rpm and 40°C for 2 h. This temperature was previously tested and suggested by the providers as the optimum to stabilize the tails of the polymeric surfactant. iii) Finally, the ferrofluids were mixed with the heavy crude oils in a concentration of 20 wt.%, employing a sequence of an ultrasonic bath for 6 h, followed by orbital shaking during 12 h at 350 rpm and 50°C, and finally, they were reincorporated to the ultrasonic bath for another 6 h to guarantee the colloidal stability of the samples (192). C_{n-k-x} notation was used to differentiate each heavy crude-oil ferrofluid model; n refers to the sample of the crude oil ($n = 1$ or 2), *k-x* the NPs concentration in kerosene. For example, $C_{1-k-0.2}$, corresponds to a mixture of the heavy oil 1 (C_1) and Kerosene-Based Ferrofluid (KBF) with

0.2 wt.% of NPs. A standard sample of kerosene and crude oil without NPs ($C_{n-k-0.0}$, according to the notation) was included for comparative purposes.

2.3.3 Rheological evaluation.

The rheological characterization had the purpose of establishing a baseline to gain information about the rheological implications of the KBFs inclusion at zero-magnetic field. The following rheological measurements were carried out in a rheometer (MCR 302 Physica-Anton-Paar) using a parallel plate measuring system (20 mm) at a gap of 0.5 mm:

Preliminary rheological characterization of the unmodified heavy crude oils by Small-Amplitude Oscillatory Shear (SAOS) experiments, to characterize the linear viscoelastic properties. The protocol followed the methodology proposed by Abivin *et al.*, (144) consisting of: first, a thermodynamic stabilization of the sample for 30 min at a constant temperature and zero shear rate. After the equilibrium was reached, isothermal amplitude sweep tests were performed at a constant angular frequency of 10 rad/s to identify the Linear Viscoelastic (LVE) region, followed by frequency sweep experiments from 0.1 to 10 Hz and employing a constant strain amplitude within the LVE region, at fixed temperatures. The temperature range of the experimental tests was varied from 60°C to 0°C in C_1 and 30°C to -5°C in C_2, using the same sample.

Steady-state flow curves of the heavy crude oil-ferrofluid models, applying a logarithmic ramp of shear rate ($\dot{\gamma}$) from 0.1 to 100 s^{-1} at 30°C and 25°C for C_1 and C_2, respectively. The protocol used can be described as: i) thermodynamic stabilization of the samples for 5 min at the evaluation temperature (25 or 30 °C) with no shearing, ii) pre-shearing of the samples at $\dot{\gamma} = 0.5\ s^{-1}$ for 5 min; and iii) application of the logarithmic ramp of shear rate. Each point was determined at a steady state by using the "steady-state sensing" option on the rheometer software.

MAGNETORHEOLOGY OF HEAVY OIL-FERROFLUID MIXTURES.

Dynamic moduli curves of the heavy crude oil-ferrofluid models as a function of frequency at 25°C from 0.1 Hz to 10 Hz. Preliminary amplitude sweeps were applied to identify the LVE region.

Dynamic moduli curves of the heavy crude oil-ferrofluid models as a function of temperature, applying a linear temperature ramp from 30°C to -5°C at an angular frequency of 10 rad/s, employing a strain amplitude into the LVE region.

2.3.4 Magneto-rheological evaluation.

The magneto-rheological measurements were conducted on the MCR 302 Physica-Anton-Paar coupled with a Magneto-Rheological Device (MRD) that induces a magnetic flux density up to 1 Tesla (MRD170/1T). To ensure temperature homogeneity and stability of the fluid sample between the parallel plates (which is affected by the thermal energy dissipation due to the current flow in the MRD), an external temperature control system (T-CS) was paired to the device. The TC-S consists of a PT-100 thermocouple that measures the temperature in the lower plate containing the fluid sample. It simultaneously sends the signal to a refrigerated circulator (Julabo F32), which acts as the control system, changing the temperature of the MRD device until reaching the temperature setpoint. The following rotational and oscillatory tests were performed:

Measurements of viscosity *vs.* magnetic flux density (magnetoviscous effect (56)) applying a logarithmic current ramp from 0.01 to 5 A (1.85 to 875.61 mT) at constant shear rates of 10, 50, and 70 s^{-1} at 30 °C for $C_{1-k-5.0}$, and 1, 10, and 50 s^{-1} at 25°C for $C_{2-k-5.0}$.

Viscosity as a function of time, applying constant magnetic flux densities of 34.45, 174.51 and 349.58 mT (at 70 s^{-1}, 30°C, during 180 s) for $C_{1-k-5.0}$, and 647.3 mT (at 25 s^{-1}, 25°C, during 5 min) for C_{2-k-x} samples.

2.3.5 Morphological assessment of magnetic field-induced assembly on NPs-asphaltene complexes.

A glass slide covered with carbon tape (0.5x0.5 cm^2) was placed in the center of an N48H Halbach cylinder array, parallel to the magnetic field direction. The cylinder provides a uniform diametral magnetic flux density of 1 Tesla (T). A stable dispersion of C_1 asphaltenes (ASTM 6560-12 (188)) was prepared at a concentration of 1 mg/ml in toluene, by submitting the mixture of asphaltene-toluene to reflux at 80 °C for 5 h (this procedure will be described in detail in a separated work). Subsequently, 1.0 wt.% of NPs were added to the asphaltene-toluene dispersion and then immersed in an ultrasonic bath for 20 min. To investigate the assembly behavior, the *"synthetic"* crude oil-ferrofluid model (*i.e.*, asphaltenes-NPs-toluene) was dropped on the carbon tape and left until the toluene was completely evaporated, following the drop-casting method (193). The samples (either in the presence or absence of the magnetic field) were analyzed by Scanning Electron Microscopy coupled with Energy Dispersive Spectroscopy (SEM-EDS), using a high-resolution Quanta FEG 650 microscope, operating at 30 kV and high vacuum conditions.

2.4 Results and Discussion

2.4.1 Linear viscoelasticity of the crude oils

As previously discussed, heavy crude oils can be described as colloidal viscoelastic suspensions, where the components having the highest molecular weights (*i.e.*, the asphaltenes) are dispersed, forming fractal aggregates with sizes between 2−9 nm (133, 139, 194). According to Lesueur, Behzadfar, and Hatzikiriakos (133, 138, 140), the complexity of the system lies in the role of resins acting as stabilizing agents (resin shell), as well as the wide range of melting temperatures of maltenes, that span from $\sim -50°C$ to $\sim 30°C$, depending, particularly, on the

origin of the crude oil. In consequence, modifications in the thermodynamic equilibrium of the system result in phase transitions of maltenes, which have a direct repercussion on the effective volume of the disperse phase. Thus, many ambiguities have been found when studying the rheology of heavy crude oil and bitumen. One of the most relevant of these controversies is related to the thermo-rheological simplicity of these fluids (133, 138, 139, 144), which implicates that all the relaxation times and moduli have the same functional dependence on temperature. This fact considerably simplifies the analysis of the thermo-rheological behavior and has led to the establishment of the Time-Temperature Superposition (TTS) principle (195). For instance, it has been proved that, for bitumen with a high content of asphaltenes (around 24 wt.%) and waxes, the TTS principle does not hold (133, 139, 144). According to Chailleux (196), the validity conditions for the construction of the master curve draw on two general requirements: i) the absence of macromolecular rearrangements caused by temperature, such as phase transformations, and ii) the test must be performed in the LVE region.

Consequently, a previous analysis of the phase behavior of the crude oils based on calorimetry measurements was carried out, proving the absence of high amounts of crystalline fractions. Based on this thermal analysis, the TTS principle was used to perform a more detailed mechanical characterization at a temperature range varying from 60 to 0 °C for C_1, and 30 to -5 °C for C_2. The master curves of dynamic moduli were constructed at the reference temperature T_r of 30 °C and they are shown in Figure 4. It is important to highlight that it was assumed that the product of temperature times density $\left[\frac{T_r \rho_r}{T \rho} \approx 1\right]$ remained constant, therefore, the final curves were the result of horizontal displacements only. The procedure employed in the construction of the master curves followed the applicability criteria proposed by Ferry (197), which suggest i) exact

matching of the shapes of adjacent curves; ii) the same values of the shift factor (a_T) must superpose all the viscoelastic functions, and iii) the temperature dependence of a_T must have a reasonable form consistent with empirical models (Figure 5).

Figure 4

Master curve obtained by applying the Time-Temperature Superposition (TTS) principle to a set of frequency sweeps (between 0.1-10 Hz) at different temperatures under a controlled strain (LVE region). The reference temperature is 30 °C. The model employed to fit the experimental values was the generalized Maxwell model. A. C_1, temperature range 0°C to 60°C. B. C_2, temperature range 5°C to 30°C.

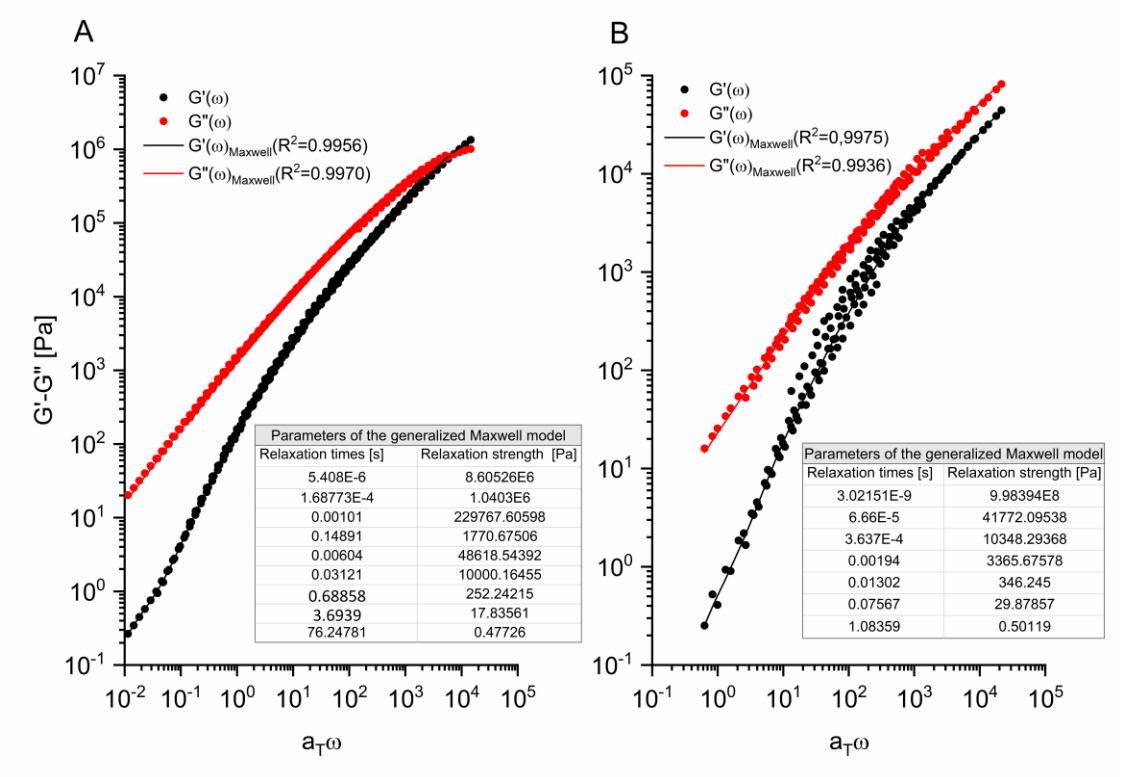

As recommended by Ferry (197) and for comparative purposes, a_T values as a function of temperature, obtained from the master curves, were fitted to both the Arrhenius model

$\left[a_T = exp^{\frac{-E_a}{R}\left(\frac{1}{T}-\frac{1}{T_r}\right)}\right]$ and the Williams-Landel-Ferry (WLF) model $\left[\log a_T = -\frac{k_1(T-T_r)}{[k_2+(T-T_r)]}\right]$; where E_a is the activation energy, and k_1 and k_2 are constants that depend on the reference temperature T_r. The modelling approaches are shown in Figure 5.

As it can be noted, the experimental values of the dynamic moduli of C_1 hold the applicability criteria (197). The elastic storage modulus ($G'(\omega)$) and the viscous loss modulus ($G''(\omega)$) showed total overlap in the dynamic frequency range (Figure 4A); a_T also satisfied the WLF equation, $k_1 = 13.128, k_2 = 196.594$ with $R^2 = 0.9996$ (Figure 5A). These constants were reasonably consistent with those reported by Behzadfar and Hatzikiriakos (138) in a bitumen (T_r=10 °C, $k_1 = 17.57$ and $k_2 = 84.821$) and by Soto-Castruita *et al.* (198) in samples of heavy crude oil (k_1~$9.972 - 12.139$; k_2~$137.868 - 160.999$ at T_r in the range of 49-88 °C). The activation energy E_a values were also in agreement with those found in the literature (117–168 kJ/mol (138, 139, 199)).

In the case of C_2, it was observed that the applicability criteria were partially fulfilled; some deviations appeared between -5 to 10°C (Figure 4B). Nevertheless, a_T fitted the WLF equation (Figure 5B), $k_1 = 11.874$, and $k_2 = 199.026$ ($R^2 = 0.9964$) were found to be consistent with the reported in the literature, as well as E_a. Similar anomalies were reported by Ferry (197) and Morrison (195), which were interpreted as multiple viscoelastic mechanisms with different temperature dependencies. For example, for some polymethacrylates, Ferry (197) proposed that the observed storage compliance, J', was the sum of a contribution J'_α from backbone motions, whose relaxation times followed the WLF equation, and another J'_β from side-chain motions, whose maximum value was far smaller than J'_α. These anomalies could be analogous to the

observed in C_2, whose elastic storage modulus G' showed a secondary relaxation in the same temperature range (Figure 9), as it will be further discussed.

Figure 5

The shift factor values (a_T) as a function of temperature obtained from the master curve and fitted to the Arrhenius and WLF models. A. C_1. B. C_2.

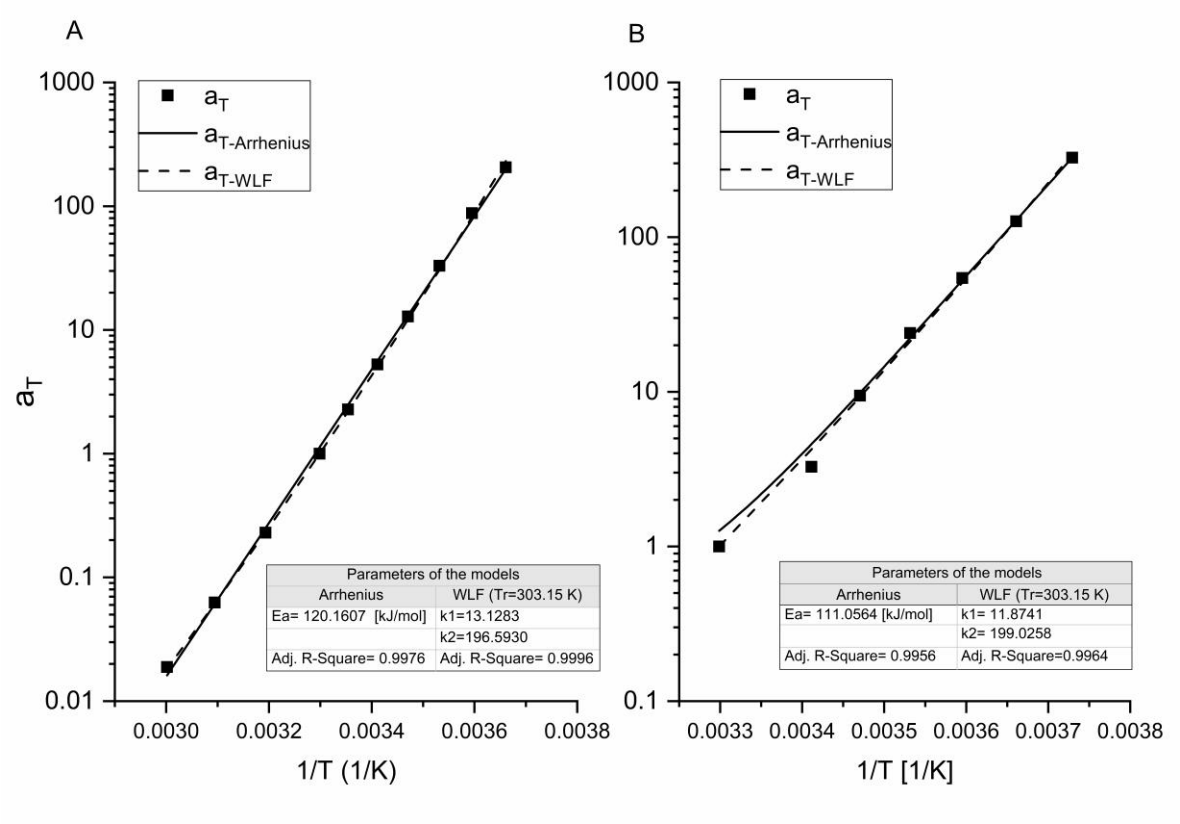

As shown (Figure 4A), in the sample C_1, G'' is higher than G' at temperatures above 0°C; however, in the order of 0°C, a transition of the material to elastic behavior took place. It was also observed that a tendency towards the development of a plateau on G' at low frequency, which is characteristic of a solid-like behavior. This plateau has been previously reported in the literature (with ωa_T between 10^{-6} – 10^{-2} rad/s (138, 139, 200, 201)), and it is related to a secondary relaxation

time. This phenomenon has been associated with the interactions of asphaltene aggregates forming a weak network, whose equilibrium conformation poses characteristically high relaxation times due to the minimization of their steric interactions. On the other hand, the parallelism of the dynamic moduli in the transition zone (marked by a change in the slopes of G' and G'') is also attributed to a weak gel-like behavior (144). These results confirmed that C_1 behaves as a viscoelastic fluid with a slight elastic character, predominantly visible at low frequency.

In the case of C_2, the transition point and the development of the plateau were not observed. Similarly, the sample was dominated mostly by the viscous contribution with a minor influence of the elastic character. Further investigation is necessary to establish differences in the molecular structures and the arrangements of these materials that might be linked to the relaxation mechanisms.

In order to confirm the formation of the aforementioned weak three-dimensional elastic networks, the linear viscoelasticity (*i.e.*, experimental dynamic moduli) of the crude oils was fitted to the generalized Maxwell model in SAOS, whose material functions are defined as follows (195):

$$G''(\omega) = \sum_{i=1}^{N} \frac{g_i \lambda_i \omega}{1 + {\lambda_i}^2 \omega^2} \tag{20}$$

$$G'(\omega) = \sum_{i=1}^{N} \frac{g_i {\lambda_i}^2 \omega^2}{1 + {\lambda_i}^2 \omega^2};\ g_i = \frac{\eta_i}{\lambda_i} \tag{21}$$

Where, η_i, g_i, and λ_i are the i^{th} viscosity parameter, the i^{th} relaxation strength, and the i^{th} relaxation time, respectively, while N represents the number of relaxation modes.

The experimentally determined dynamic moduli were estimated using discrete-time spectra, pursuing the best fit with the smallest number of parameters (parsimonious modeling

(202)), as shown in Figure 4 and Figure 6. It was employed the Broyden-Fletcher-Goldfarb-Shanno (BFGS) quasi-Newtonian unconstrained search procedure, which showed the minimum computation time compared to the Levenberg-Marquardt, and the Davidson-Fletcher-Powell (DFP) algorithms, commonly applied in the literature (203). The search procedure took into account the methodology suggested by (195, 202-204), including a change of variables to scale g_i and λ_i in the same order of magnitude: $a_i = \ln g_i$; $t_i = \ln \lambda_i$; and an adjustment of the parameters N, a_i and t_i, considering that N might be between 1 and 2 per decade. As depicted in Figure 4A and Figure 4B (continuous lines), the calculated number of Maxwell modes fitted the experimental data ($R^2 \geq 0.9936$ in the adjusted dynamic moduli of both samples). The modes were 9 and 7 for C_1 and C_2, respectively (they are listed in the tables of Figure 4); which agreed with the proposed methodology.

As illustrated in Figure 6, the relaxation strengths of both samples decreased to minimum values on the logarithmic scale (terminal zone) as increasing the relaxation times, which means that the systems tended to reach a steady-state flow. This kind of behavior is characteristic of uncross-linked viscoelastic liquids (197). In addition, it was observed a gradual drop (transition zone), which was related to a broad molecular weight distribution (197). As shown, the slopes were 1.033 for C_1 and 1.049 for C_2 (slightly superior to the values commonly reported in polymers), reasonably similar to the reported by Behzadfar and Hatzikiriakos (138) in a bitumen (1.13).

Figure 6

Relaxation time spectrum of C_1 and C_2 at the reference temperature, Tr, 30°C.

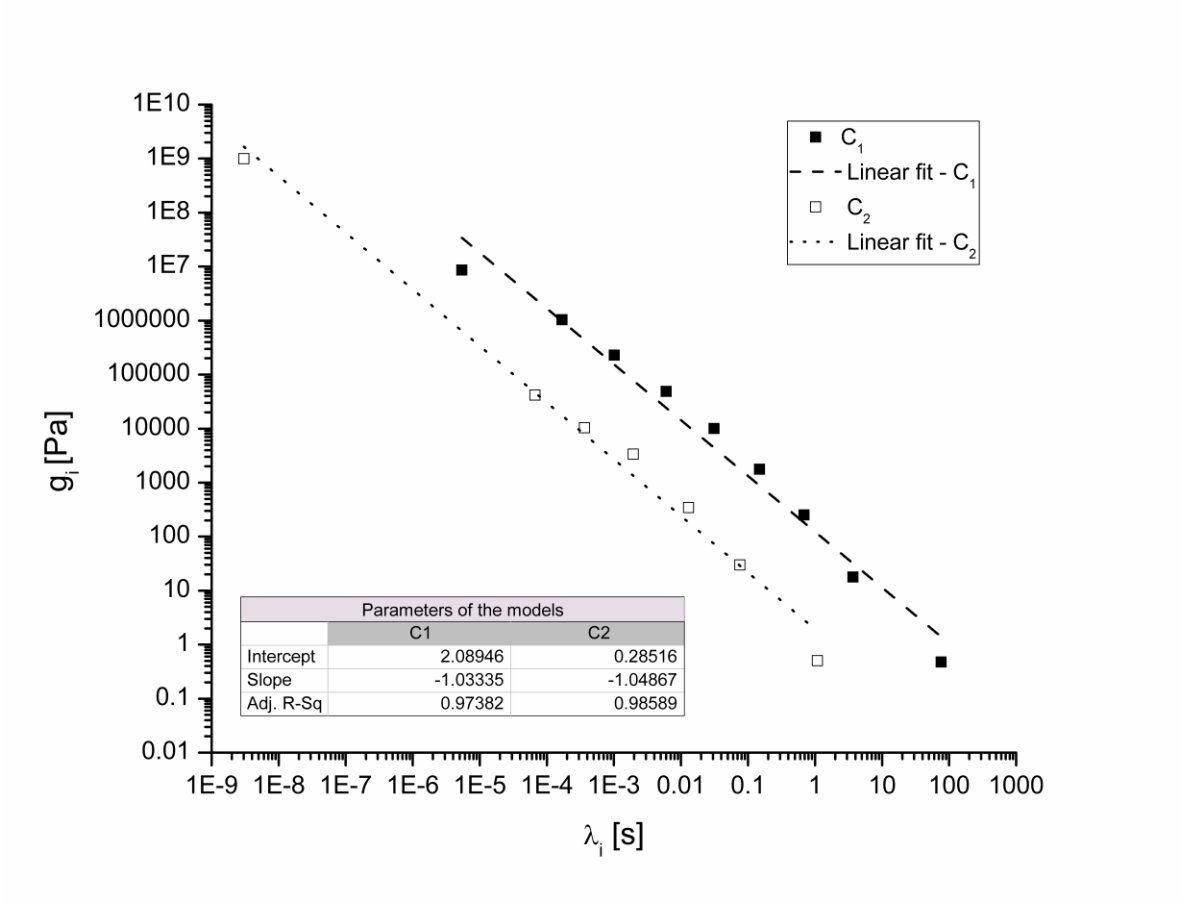

2.4.2 Rheological modifications of the heavy crude oil-ferrofluid models

We performed three different rheometric tests to evaluate the effect of the inclusion of the KBFs in the viscoelasticity and flow properties of the heavy oils at zero-magnetic field state, considering the concentration of magnetic NPs and temperature. The results were compared to the experimental findings reported in the literature (5, 6, 163, 164).

2.4.2.1 Steady-state flow curves.

Figure 7 exhibits the steady shear viscosity $\eta(\dot{\gamma})$ of the heavy crude oil-ferrofluid models. In the case of C_{1-k-x} models (Figure 7A), this material function revealed that all the samples presented shear-thinning flow behavior, which is common in this kind of fluids (133, 144, 198, 205). The phenomenon has been interpreted as a disruption from the equilibrium of some structural and relaxation dynamic properties that cannot bear high shear rates (133, 144, 145, 198). On the other hand, C_{2-k-x} models showed a Newtonian behavior (Figure 7B), which means that the inclusion of the KBF had a greater effect on its rheological properties, in comparison to C_1.

The inclusion of the kerosene led to a significant reduction of the viscosity of the crude oils in the order of 99% and 98% for C_1 and C_2, respectively. However, it is important to mention that despite these significant reductions, at this concentration of ferrofluid, the viscosity specifications for transportation were still not reached (250-400 cSt at 37.8°C (147)). As illustrated in Figure 7A, in the case of C_1, there were noticeable differences in viscosity when changing the concentration of magnetic NPs in the KBFs, beyond the diminishing reached exclusively by the inclusion of the kerosene ($C_{1-k-0.0}$). The main modification was observed at a concentration of 0.6 wt.% of NPs ($C_{1-k-0.6}$), in which it was evidenced a decrease in viscosity of approximately 29% compared to $C_{1-k-0.0}$; demonstrating a synergy between the carrier fluid and the NPs. Nonetheless, further increasing the concentration of NPs had the opposite effect and the value of viscosity was observed to rise, for example, when using 5.0 wt.% of NPs ($C_{1-k-5.0}$), the mean value of this property was nearly 25% higher than the reported for $C_{1-k-0.0}$. Sample C_2 (Figure 7B) showed a 35% additional viscosity reduction at the critical concentration of 0.2 wt.% of NPs ($C_{2-k-0.2}$). According to Taborda *et al*., (6, 163) this non-monotonically dependence with NPs

concentration might be related to the appearance of different kinds of interparticle interactions, such as the formation of particle-particle and particle-oil matrix complexes. The results were consistent with those reported in refs. (5, 6, 163, 164), in which it was proved that SiO_2 NPs at the specific concentration of 1000 mg/L led to reductions between 12-45% in the viscosity of a heavy crude oil at different temperatures. A similar tendency in equivalent orders of magnitude was observed with Al_2O_3 and Fe_3O_4 NPs (5, 164). The differences in the rheological effect as a function of the concentration of NPs were attributed mainly to the surface area (S_{BET}) and, to a lesser extent, the NPs chemical nature. In particular, Fe_3O_4 NPs are characterized by their non-porous surface, which contributes to high initial rates of asphaltene adsorption through single-step processes (206). Magnetite NPs are also prone to aggregation and flocculation in nonpolar carriers due to Van der Waals attraction, leading to lower colloidal stability and available surface area for asphaltene adsorption (5); as a consequence, the NPs used in this work were acquired with surface treated with a polymer surfactant to avoid the occurrence of aggregates. Even with the presence of surfactants at the surface of the NPs, the samples evidenced viscosity modifications associated with asphaltenes adsorption, as previously stated. It is assumed that the NPs in synergy with the carrier liquid contributed to higher Brownian forces, preventing the formation of clusters and, thus, increasing the available surface area for adsorption. This synergistic effect was also observed by (163, 164).

Figure 7

Measured flow-curves of the heavy crude oil-ferrofluid models at a shear rate from 0.1 s^{-1} to 100 s^{-1} and constant temperature, T_{C1}=30°C, and T_{C2}=25°C.

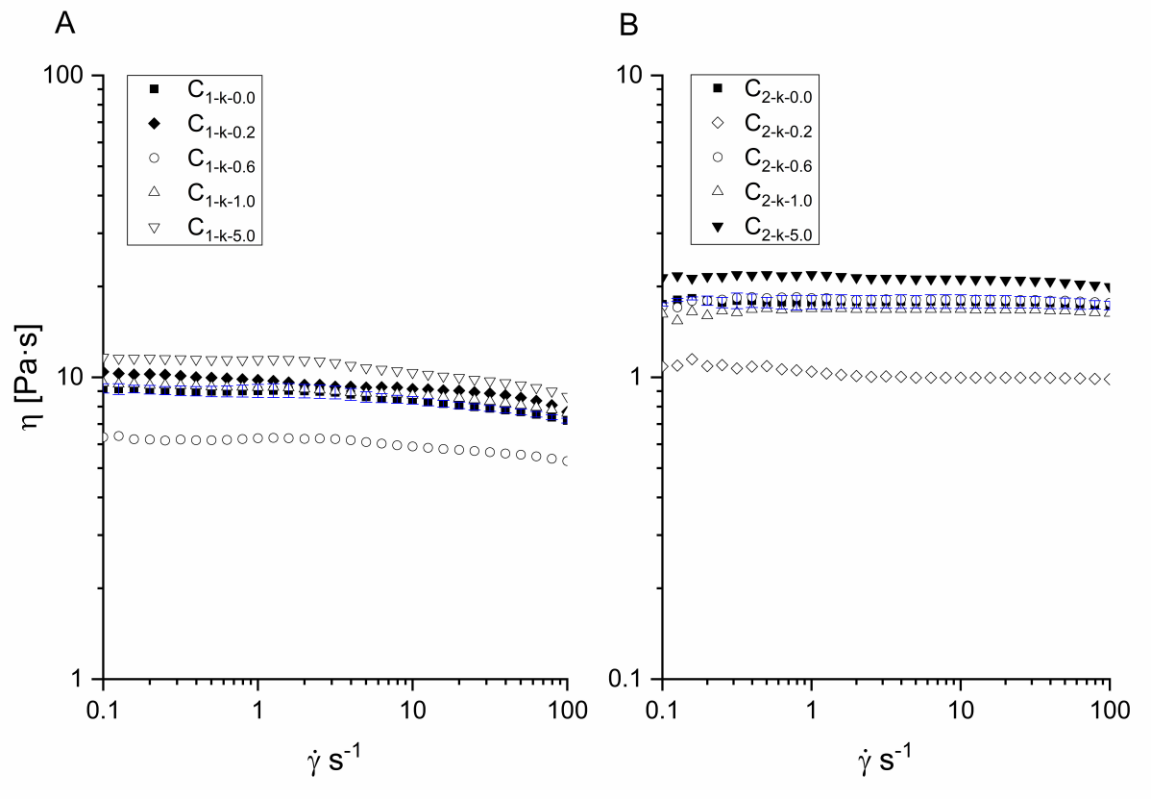

2.4.2.2 Dynamic moduli and complex viscosity curves as a function of frequency.

As shown in Figure 8, the inclusion of the KBFs did not change the viscoelastic nature of C_1; nevertheless, the carrier liquid, as well as the NPs reduced the magnitude of both the viscous loss modulus (G'') and the elastic storage modulus (G') in nearly four and two orders of magnitude, respectively. Likewise, the dynamic moduli exhibited the same tendency observed in the measured flow-curve (Figure 7A), which is, for $C_{1-k-0.6}$, the dynamic moduli experienced the highest decrease, particularly G' became distorted and disrupted as increasing frequency, which means

that the inclusion of the NPs had a significant effect on this material property. According to (138, 139, 196, 201), and as it was proved in this research, asphaltenes are primarily responsible for the elastic behavior of the heavy oils, in consequence, these results also suggest that the magnetic NPs are highly selective in the adsorption of asphaltenes. As described in the last section, NPs act on the aggregation mechanisms of these components, as reported by (5, 6, 163).

Furthermore, the inclusion of the KBFs in C_2 led to a significant decrease in G', which could not be detected by the tolerance of the equipment. These results (not shown here for brevity) were consistent with the discussed in the steady-state flow curves, in which it was demonstrated the appearance of a Newtonian behavior of C_{2-k-x} models.

Figure 8

Dynamic moduli as a function of the frequency of C_{1-k-x} models under a controlled strain (linear viscoelastic region).

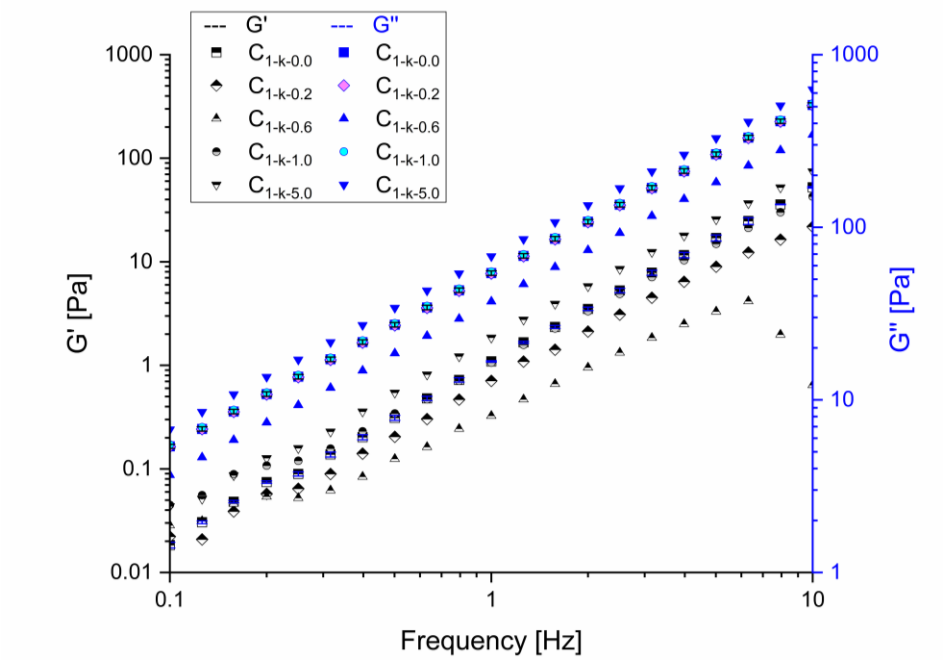

2.4.2.3 Dynamic moduli and complex viscosity curves as a function of temperature

Heavy crude oils experience a transition of their flow behavior from Newtonian to non-Newtonian viscoelastic flow as decreasing temperature, due to the disappearance of the Brownian motion of the asphaltene micelles, as suggested and experimentally proved by (133, 139, 198). This "transition temperature" is usually reported at around 50°C in heavy crude oils and bitumen. Thus, Dynamic Mechanical Thermal Analysis (DMTA) tests were carried out using the model samples to acquire additional information about the implications of the KBFs on the structural properties. At the same time, it was possible to evaluate any alteration on the increasing rate of the elastic storage modulus (G') with the change of temperature that could be directly related to the adsorption mechanisms of asphaltenes over the NPs surface. On the one hand, C_{1-k-x} samples showed the same tendency observed in the last sections (results not shown here for brevity); this is, $C_{1-k-0.6}$ had a differential effect, both G' and G'' presented the lowest values in all the range of temperature. Moreover, the samples did not experience phase transformations; the increases in the dynamic moduli were purely related to structural changes. It was also proved that the magnetic NPs inhibited the asphaltene agglomeration as suggested by the decreasing of G' when changing the concentration of NPs. This tendency showed that the adsorption capability of the NPs was maintained, even at lower temperatures, at which interparticle attractions are promoted, and the contribution of the viscous forces in the maltene continuous phase is higher, that is, the Brownian motion is inhibited.

In the case of C_{2-k-x} models, an interesting phenomenon appeared; a sol/gel transition temperature or a "gelation temperature" was observed (crossing point between $G'$and G''), which was a function of the NPs concentration (207). As shown in Figure 9, this transition was only

observed in the heavy crude oil-ferrofluid models. Particularly, the sample $C_{2-k-0.2}$ presented the lowest value in this transition point, which was consistent with the results discussed in the last sections. About this transition point and the change in the slope of G' in C_2, it is important to highlight that it was presented in the same temperature range of the deviation discussed in the TTS principle. A possible explanation of this phenomenon could be associated with the fact that C_2 asphaltenes might be more aliphatic and branched, showing secondary relaxation mechanisms or hardening. When asphaltenes are adsorbed onto the surface of the NPs, the temperature dependence of the relaxation modes of the side chains becomes dominant, and it might promote accelerated growth of G'.

Figure 9

Dynamic moduli as a function of the temperature of C_{2-k-x} models at an angular frequency of 10 rad/s.

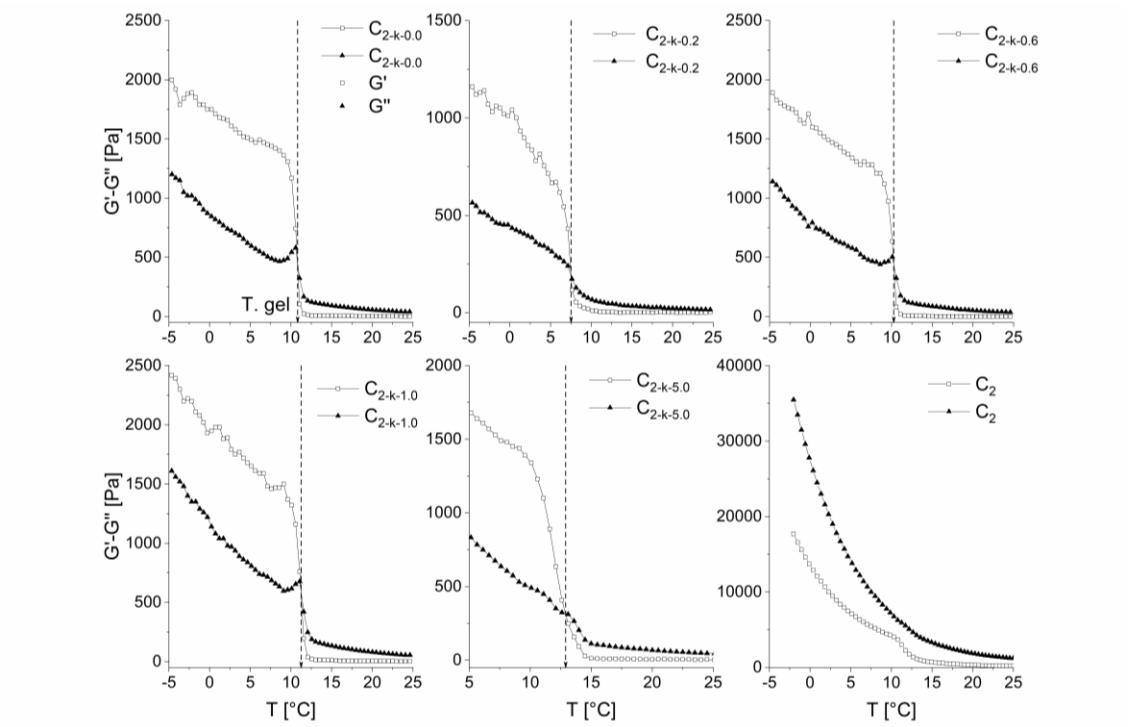

2.4.3 Magneto-rheological behavior of the heavy crude oil-ferrofluid models

One of the most relevant experimental remarks regarding the magnetoviscous characterization was the time-dependent flow behavior of the samples, before and after the inclusion of the KBFs in the oil matrices, which made it necessary to apply a correction procedure that allowed the evaluation of the real effect of the magnetic field on the rheology of the samples. As shown in Figure 10, the shear stress increased with time, evidencing the time-dependent microstructure of the samples (208). Particularly, the resulting shear stress transient of $C_{1-k-5.0}$ (20 wt.% of ferrofluid) exhibited an initial decrease until reaching a minimum (at around $t = 116\ s$). After this, a short viscoelastic relaxation was observed, followed by a monotonically increase in the shear stress under the high-shear interval (70 s^{-1}). This curious increasing phenomenon was also maintained under low-shear rate.

To further investigate the effect of the inclusion of the ferrofluid on the time-dependent flow behavior, the concentration of KBFs was increased to 30 and 40 wt.%. As observed in Figure 10 (aiming for more clarity, a secondary axis, with reduced scale, was added at the right of the graph), when increasing the concentration of the ferrofluid, the shear stress was diminished by a factor of almost four and ten, respectively; and the viscoelastic relaxation was suppressed. Nonetheless, the gradually growing structure was maintained. These results not only suggested that asphaltenes still have a significant influence on the diluted heavy crude oil but also supported the well-proved stability problem associated with the dilution method with light oils (136).

According to Mezger (207), this behavior is neither dilatant nor rheopectic; instead, it is related to a permanently remaining shear-induced structure (SIS) or shear-induced structural change behavior, which might show anisotropic properties. It is important to mention that, to the

best of our knowledge, this behavior has not been reported in heavy crude oils. Mukherjee *et al.* (209) have evidenced similar tendencies in transient flow with ceramic suspensions. The discussions about the explanation of the phenomenon observed in ceramic suspensions are extensive though they are not very well defined. So far, the phenomenon has been ascribed to volumetric dilatancy of condensed phases in highly concentrated suspensions (210); shear banding, or shear localization (207); formation of clusters by hydrodynamic lubrication (hydro-clusters); as well as shear-induced hydrodynamic diffusion (209, 211, 212). The pieces of evidence of the present work and the colloidal nature of the heavy oil samples suggest that the increasing shear stress phenomenon could be analogous to the rationales proposed in ceramic suspensions. Mainly, the discussion of Mukherjee *et al.*, (209) whose experimental results showed similar tendencies, indicate that the diffusion mechanisms might be a possible physical explanation of the phenomenon. Likewise important, Masson *et al.* (213) also demonstrated the link between the segregation of asphaltenes and the presence of steric hardening of bitumen over time at room temperature.

Figure 10

Transient shear stress arising during a stepwise increase in the shear rate of the $\boldsymbol{C_{1-k-5.0}}$ *sample, changing the concentration of the ferrofluid to 20, 30, and 40 wt% at 30°C.*

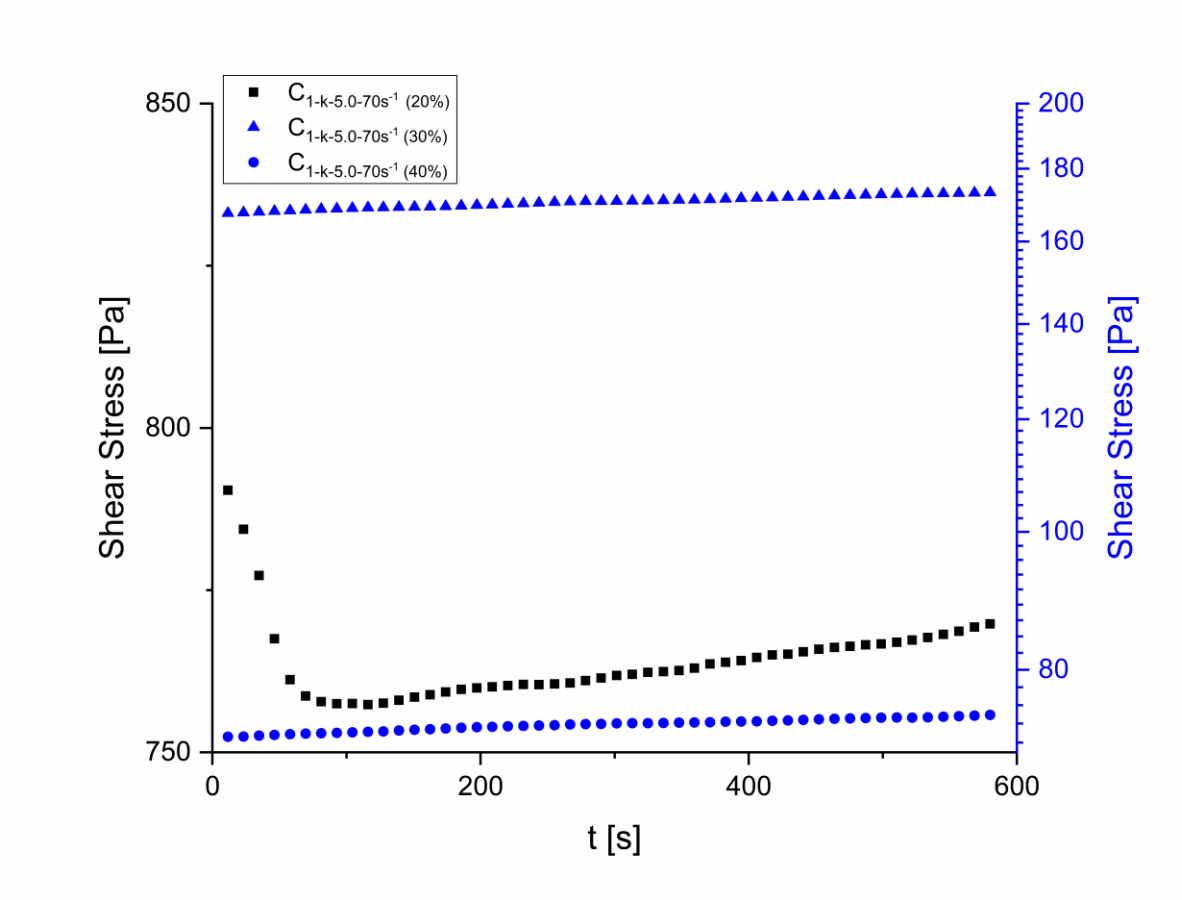

Therefore, the magnetoviscous effect was studied considering the time-dependent behavior of the samples. For this purpose, it was used the crude oil-ferrofluid model with the most concentrated KBF ($C_{n-k-5.0}$) in both C_1 and C_2, to facilitate the elucidation and analysis of the rheological modifications in the presence of an external magnetic field.

Figure 11 illustrates the relative change of viscosity ($\delta\eta \equiv \eta(t) - \eta_0$) of $C_{1-k-5.0}$, in the absence (B^0) and the presence (δB) of a uniform static magnetic field. As shown, in the absence of

a magnetic field (B^0), the sample exhibited an initial breakdown structure followed by a viscoelastic relaxation, confirming the shear-dependent structural nature of the model samples. In the presence of a logarithmic ramp of magnetic flux density (δB), as seen in Figure 11A, the relative viscosity presented the same initial decrease, followed by a shorter viscoelastic relaxation. Nevertheless, it is observed that the magnetic field generated a gradual increase of the viscosity at 50 and 70 s^{-1}, in the range of time between 60-90 s.

To further reduce the number of variables involved in the experimental assessment and considering the rheological complexity of the model samples, the relative viscosity of $C_{1-k-5.0}$ was evaluated under the influence of a uniform (B) magnetic flux density of 34.45, 174.51, and 349.58 mT; where the lowest magnetic field strength value (34.45 mT) corresponds to the transition point (global minimum) observed in the presence of δB at 70 s^{-1}. As shown in Figure 11B, the uniform magnetic field applied in these ranges of strength contributed to diminishing the initial breakdown and relaxation process of the model samples; it was also demonstrated that the magnetic field increased the relative viscosity and shear stress.

Accordingly, the induced magnetic effect seems to be affected by the viscous forces of the continuous phase, the viscoelasticity, as well as the shear-dependent behavior of the C_1 models. Thus, an enhanced effect on the increased viscosity due to the presence of the magnetic field was observed more clearly at higher shear rates, which promoted the breakdown structures in the oil matrix.

Similar effects to those presented in Figure 11 have been reported in diluted and concentrated ferrofluids, as well as magneto-rheological fluids. The theoretical explanation of the magnetic phenomenon in diluted ferrofluids, given by Shliomis (59), established that the oriented

magnetic field impedes the free rotation of particles in shearing flow, because of the superparamagnetism exhibited by the NPs. Then, the increase in the ferrofluid viscosity is a consequence of an additional energy dissipation generated by a difference between the local angular velocity of the particles (ω) and the vorticity of the fluid (Ω), known as rotational viscosity ($\delta\eta$). Soto-Aquino and Rinaldi (214) also proved, by using Brownian dynamics simulations, that the rotational viscosity (diluted ferrofluids) is a function of the magnetic field strength and its orientation with respect to the vorticity of the fluid. It was observed a shear-thinning behavior when increasing the magnetic field strength, which, according to (214), appears when the hydrodynamic torque exceeds the maximum magnetic torque of the particles, and hence the particles begin to rotate with the surrounding fluid. However, it is important to highlight that this model neglects the interparticle interactions and, therefore, it is only applicable for highly diluted ferrofluids, *i.e*., those following Einstein's formula for the effective viscosity.

For more realistic scenarios, that is, commercial ferrofluids (concentrated), the magnetoviscous effect is higher in several orders of magnitude (215, 216); thus, they are not described by the preceding theory. According to Odenbach (56), this is attributed to chain-like clustering effects due to greater interparticle interactions; as a result, the magnetoviscous effect presents a strong shear-rate dependence. Odenbach also highlights that this aggregation mechanism is only valid for large particles (d> 16 nm), where the ratio between dipole-dipole energy to thermal energy is higher than unity. Therefore, the shear-thinning behavior is explained in terms of the increased hydrodynamic force that tends to pull the particles apart. In consequence, larger shear rates do not produce a significant magnetoviscous effect; thus, it can be assumed that the field-induced changes of the viscosity are mainly due to the hindrance of the free rotation of

the large particles and permanent agglomerates in the flow. Due to the existence of these dual phenomena (*i.e.*, the hindrance of free rotation (59) and the formation of chain-like clusters (56)), the theoretical approach is known as the bi-disperse model.

However, it seems necessary to highlight that the aforementioned theoretical explanations for diluted and concentrated ferrofluids, contemplate only Newtonian carrier liquids and no other type of particles or aggregates apart from magnetic NPs; this prevents a direct comparison with the case presented in this investigation.

MAGNETORHEOLOGY OF HEAVY OIL-FERROFLUID MIXTURES.

Figure 11

A. Magnetoviscous effect (relative change of viscosity) as a function of time of $C_{1-k-5.0}$ *sample, applying a logarithmic ramp of magnetic flux density from* 1.85 *to* 875.61 *mT (δB-filled symbols) at different shear rates 10 s-1, 50 s-1, 70 s-1, and considering the time-dependent transient viscosity in the absence of magnetic flux density (B0-unfilled symbols). B. Effect of uniform magnetic flux density (B) at a constant shear rate 70 s-1; and in the absence of magnetic flux density (B0).*

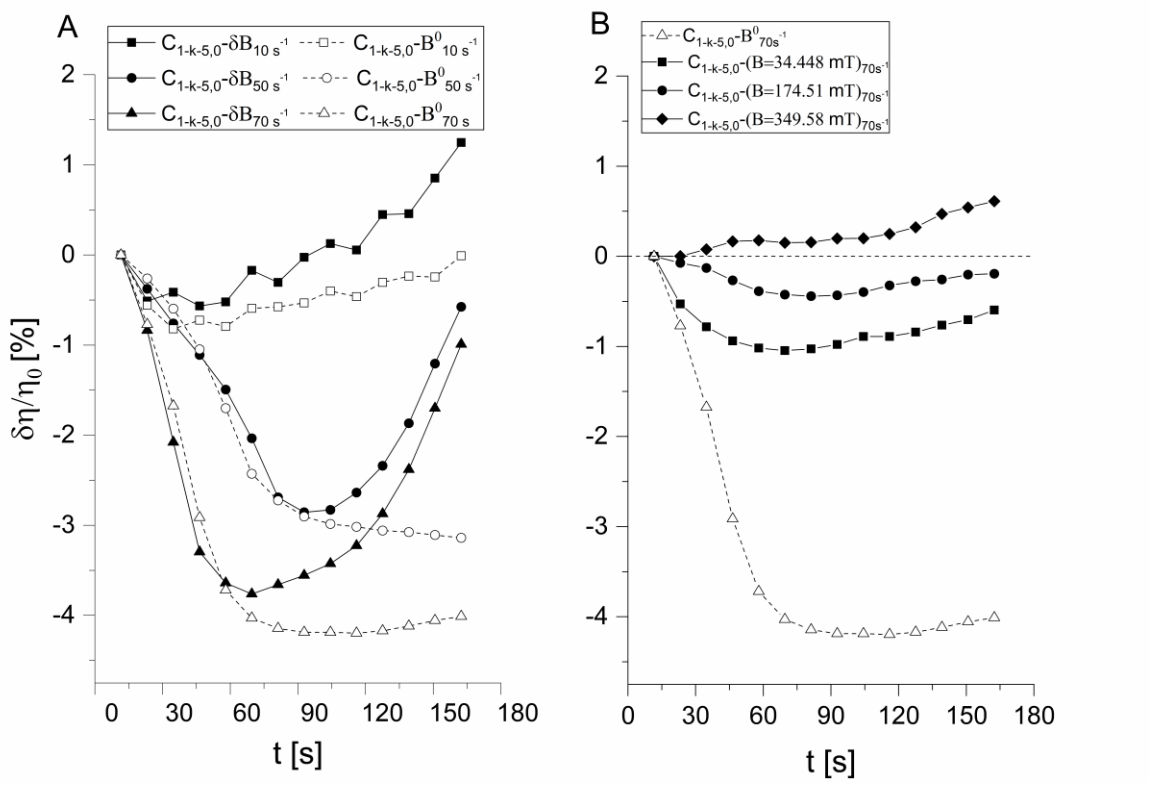

Furthermore, the ferrofluid concentration was increased to 30 wt.% and 40 wt.% to diminish the viscosity of the crude oil-ferrofluid models and, at the same time, increase the NPs-heavy oil ratio (from 1.0 wt.% of NPs to 1.5 wt.% and 2.0 wt.%, respectively). This allowed us to individually assess the synergistic implication of the increase of the volume fraction of NPs

and the reduction of viscosity, over the magnetoviscous effect. It is observed in Figure 12 that, at these concentrations of KBF, there were not breakdown structures that could influence the presence of negative $\delta\eta$. Likewise, the magnetic field promoted the reappearance of viscoelastic effects, as well as the increases of the relative viscosity as a function of the magnetic field strength; this behavior is indicative of the rapid initial formation of magnetic structures (217). This tendency was observed with both concentrations of KBF (30 and 40%), although there were not substantial quantitative differences in the magnitude of the magnetoviscous effect. Likewise, this increasing viscosity was several orders of magnitude smaller than those observed in commercial ferrofluids ($\delta\eta \sim 30\%$ (56, 217)). As it has been discussed, in this work, the NPs were suspended in a complex rheological fluid, which is shear-dependent and time-dependent. Therefore, a direct comparison with ferrofluids is not entirely valid. On the other hand, it was proved that the asphaltenes tend to be adsorbed on the surface of the NPs, which could lead to a decrease in the dipole-dipole interactions, hindering the formation of aggregates and thus reducing the magnetoviscous effect.

Additionally, it seems that the sample at a concentration of 40 wt.% of KBF (Figure 12D) followed the tendency observed in the bi-disperse model, that is, a shear-dependence on the relative viscosity in the presence of the magnetic field. Nevertheless, it was not possible to note significant differences when applying higher shear rates (50 and 70 s^{-1}), which also implies that, from this point, the units interacting with the field are reduced to single-particle sizes (59).

In consequence, the deviations of the present results from the magnetoviscous effect proposed for ferrofluids are mainly related to the role of the asphaltenes in both, the hydrodynamic particle volume (because of adsorption) and the appearance of magnetic interparticle interactions (reducing the magnitude of the maximum relative viscosity). However, further experiments are

necessary to get more in-depth knowledge about the microscopic phenomena involved in the magnetoviscous effect.

Figure 12

Comparative assessment of the effect of ferrofluid concentration in C_1 after applying a logarithmic ramp of magnetic flux density from $\mathbf{1.85\ to\ 875.61\ mT}$ *(δB- filled symbols) at different shear rates 10s^{-1}, 50 s^{-1}, 70 s^{-1}; and in the absence of magnetic flux density (B^0). A. Concentration of ferrofluid of 30 wt.% (1.5 wt.% NPs-heavy crude oil); B. Net effect of the external magnetic field at a concentration of ferrofluid of 30wt.%; C. Concentration of ferrofluid of 40 wt.% (2.0 wt.% NPs-heavy crude oil); D. Net effect of the external magnetic field at a concentration of ferrofluid of 40 wt.%.*

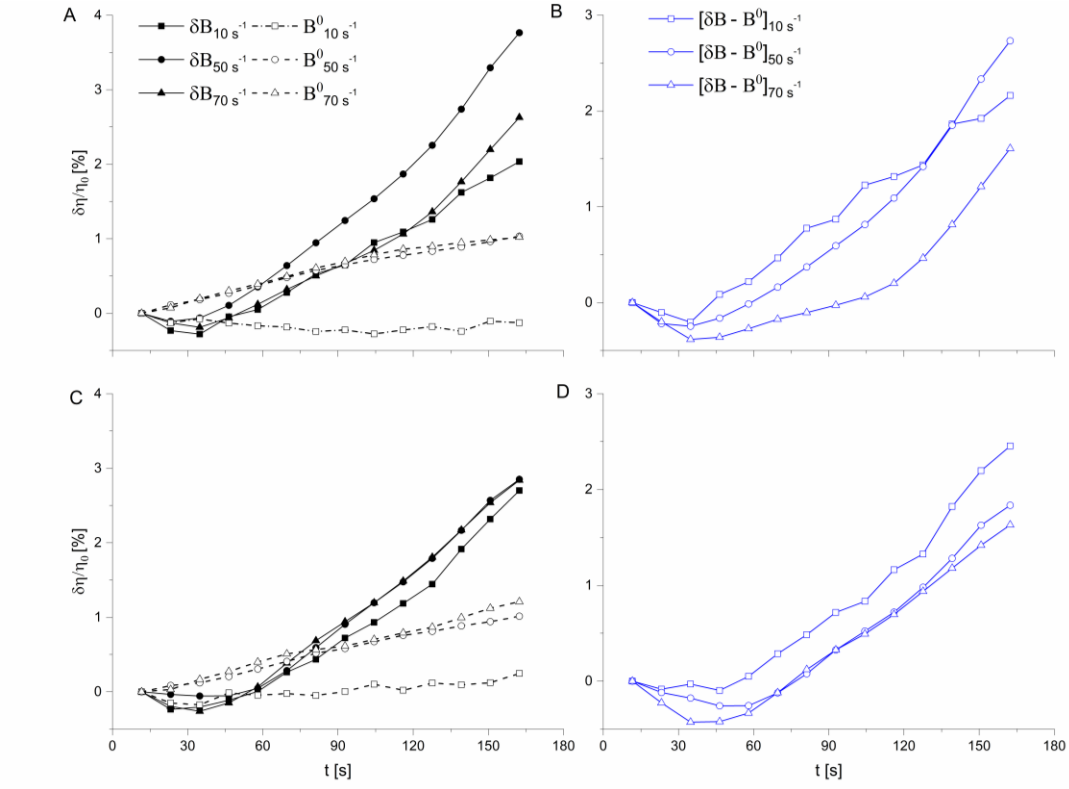

MAGNETORHEOLOGY OF HEAVY OIL-FERROFLUID MIXTURES.

The magnetoviscous effect was markedly differential in $C_{2-k-5.0}$, as can be observed in Figure 13. It is shown a clear shear-dependent magnetoviscosity, that is, when increasing shear rate, the relative change of viscosity was reduced. In this case, there was a direct relation to the bi-dispersed model of concentrated ferrofluids (56). Thus, the increased shear rate promotes the breakage of the aggregates, resulting in a reduction of the relative change of viscosity.

As previously discussed, the magnitude of the magnetoviscous effect was smaller than those observed in commercial ferrofluids, showing a maximum increase of relative viscosity in the order of 12%, which was almost 40% of the values reported for ferrofluids (56, 217). It is important to highlight that, to the best of our knowledge, this effect has not been reported in the literature.

Figure 13

Magnetoviscous effect (relative change of viscosity) of $\boldsymbol{C_{2-k-5.0}}$ *sample, applying a logarithmic ramp of magnetic flux density from* $\boldsymbol{0\ to\ 875.61\ mT}$ *(δB filled symbols) at different shear rates 1 s^{-1}, 10 s^{-1}, 50 s^{-1}.*

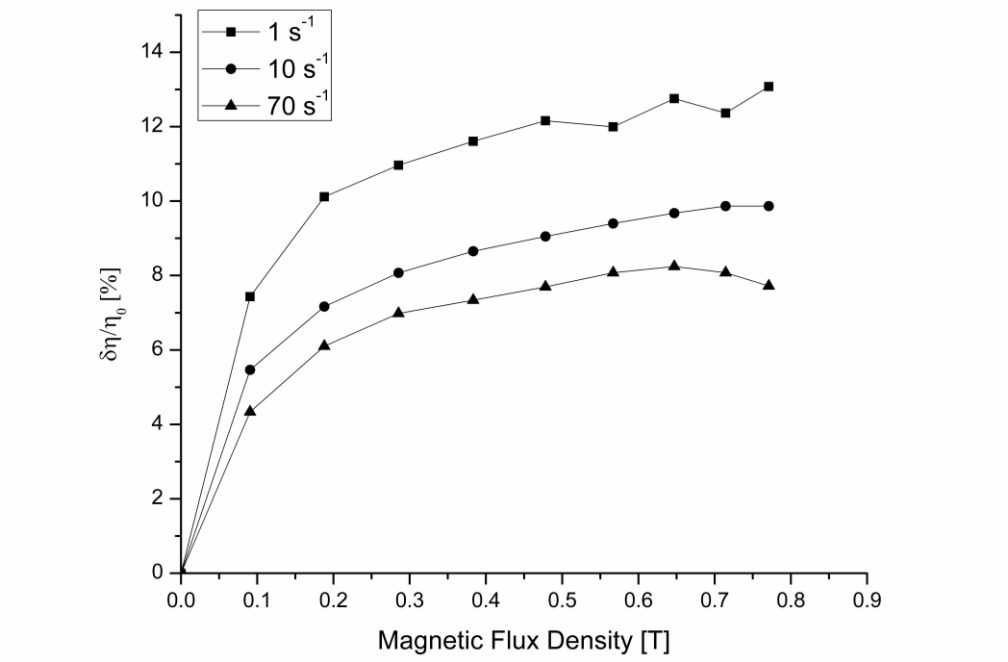

MAGNETORHEOLOGY OF HEAVY OIL-FERROFLUID MIXTURES.

A different assessment was used in the heavy crude oil-ferrofluid models of C_2, considering the observed magnetoviscous effect (Figure 13). The viscosity was measured at a constant shear rate of 25 s^{-1}, and three regions were considered (Figure 14): i) in the first region, at $B = 0$, the viscosity showed the shear-induced structure (SIS) behavior; ii) in the second region, when the magnetic field was applied, the viscosity suddenly increased in all the samples, which enabled to reinforce the hypothesis about the fast formation of chains due to the rearrangement of the bigger NPs (similar results in ferrofluids were proved by (218, 219)). Also, it was observed in $C_{2-k-0.6}$, $C_{2-k-1.0}$ and $C_{2-k-5.0}$ a viscoelastic relaxation which might have been related to the appearance of viscoelastic effects due to the magnetic field (217). This phenomenon, to the best of our knowledge, has not been reported in ferrofluids; however, Hosseini *et al.* (219) exhibited a similar tendency using a Υ-Fe_2O_3 paraffin-based ferrofluid; iii) finally, in the third region, in which no magnetic field was applied, it was observed a sudden decrease of viscosity, evidencing that the formation of structures was disrupted and the samples returned to their original state. The results also proved that the magnetoviscous effect is proportional to the concentration of NPs, and that it is possible to reach significant changes in viscosity in the presence of moderate magnetic fields such as those observed in ferrofluids.

Figure 14

Time dependency of the viscosity of the heavy crude oil-ferrofluids models of C_2. The shear rate was 25 s^{-1}. At region I magnetic flux density B= 0, region II magnetic flux density B= 647.3 mT and region III magnetic flux density B= 0.

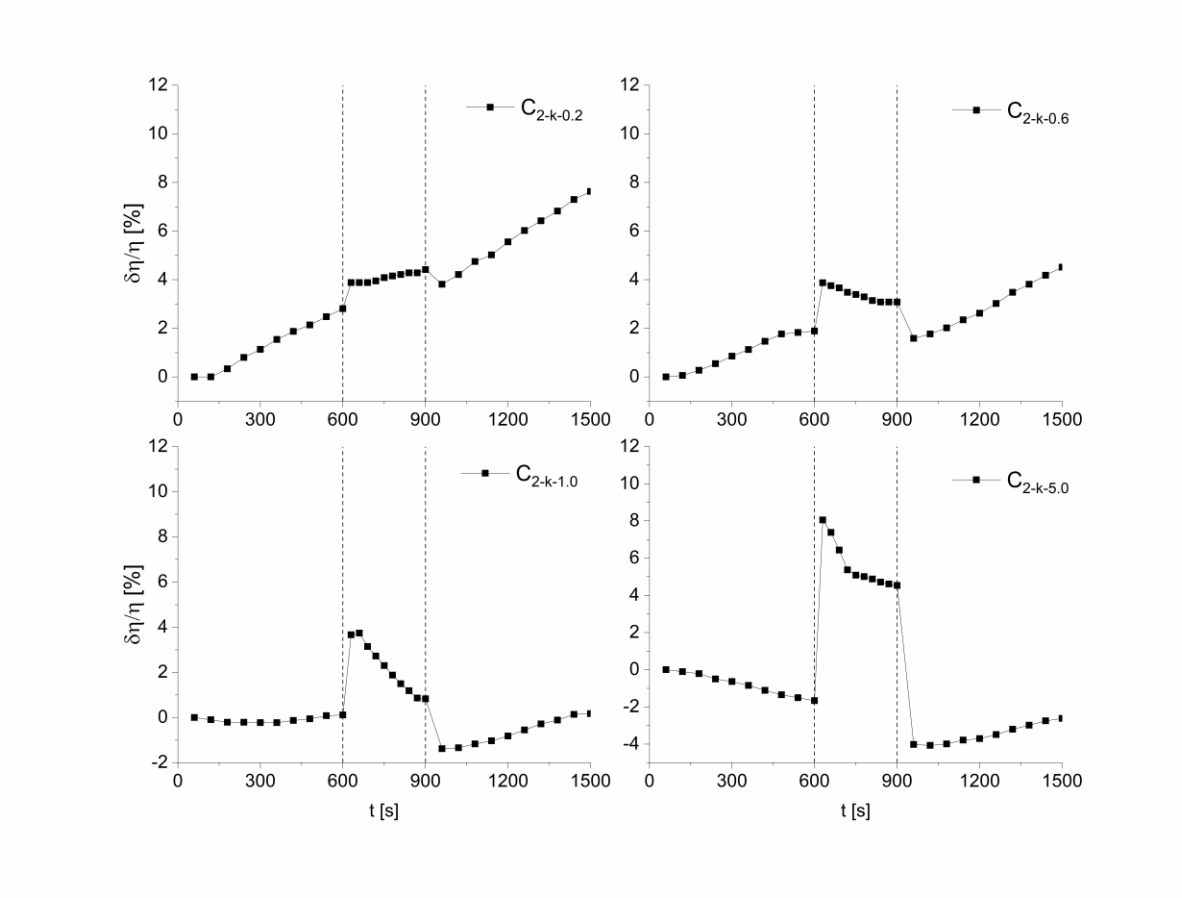

2.4.4 Morphological assessment of magnetic field-induced assembly on NPs-asphaltene complexes

To further study the induction of magnetic assemblies in the presence of a uniform magnetic field, *"synthetic"* crude oil-ferrofluid models were prepared by the drop-casting method and analyzed by SEM-EDS. Considering the compositional complexity of the heavy crude oil

matrices, a first approach was made with a dispersion of asphaltene in toluene as the carrier fluid. One of the advantages of toluene as carrier liquid relies on its affinity with asphaltenes and its high boiling point, necessary to obtain well-ordered structures (193). The comparison between the micrographs of the dispersion at zero-magnetic field and those in the presence of magnetic field (Figure 15) revealed marked differences in the morphological features of the magnetic assemblies. At zero-magnetic field (Figure 15A), the samples exhibited uniform spherical structural agglomerates. One possible explanation of the presence of these agglomerates could be related to an apparent inefficient control of the evaporation rate of toluene, which might have impeded the formation of a monodisperse film of NPs (220); however, the spherical morphology pattern of the NPs was evidenced. The EDS analyses confirmed the presence of asphaltenes, adsorbed onto the surface of the NPs; the elemental microanalysis (not shown) revealed increments in the concentration of carbon when asphaltenes were present in the model (*i.e.,* "NPs-Toluene" presented 6.23 wt.% of C, while the model "Asphaltene-NPs-Toluene" showed a concentration of 22.9 wt.%.). EDS results also revealed the presence of sulfur (1.27 wt.%), which is a typical heteroatom of the asphaltene structure (134).

On the other hand, in the presence of the in-plane magnetic field (Figure 15B), the samples exhibited the formation of thick and straight superstructures that were aligned along the direction of the magnetic field. The development of these ordered stacking superstructures was not affected by the presence of asphaltenes, as observed in the images at different magnifications; they follow highly ordered packing patterns at microscales. As shown in the magnetorheological characterization, these results provided crucial evidence of the formation of chains oriented in the direction of the magnetic field, as suggested by the bi-dispersed model (56). However, further

investigation using more complex systems that can describe oil matrices more accurately is required (221). An improved control of the solvent evaporation rate and/or the use of Cryo-TEM (Cryogenic Transmission Electron Microscopy) are also suggested (221).

Figure 15

SEM images of magnetic field-induced assemblies of NPs-asphaltene complexes prepared by the drop-casting method at different magnifications. A. At zero-magnetic field, and B. In the presence of a uniform longitudinal magnetic field of 1T provided by a Halbach cylinder. The insert represents the Halbach array with the sample illustrated with the black circle.

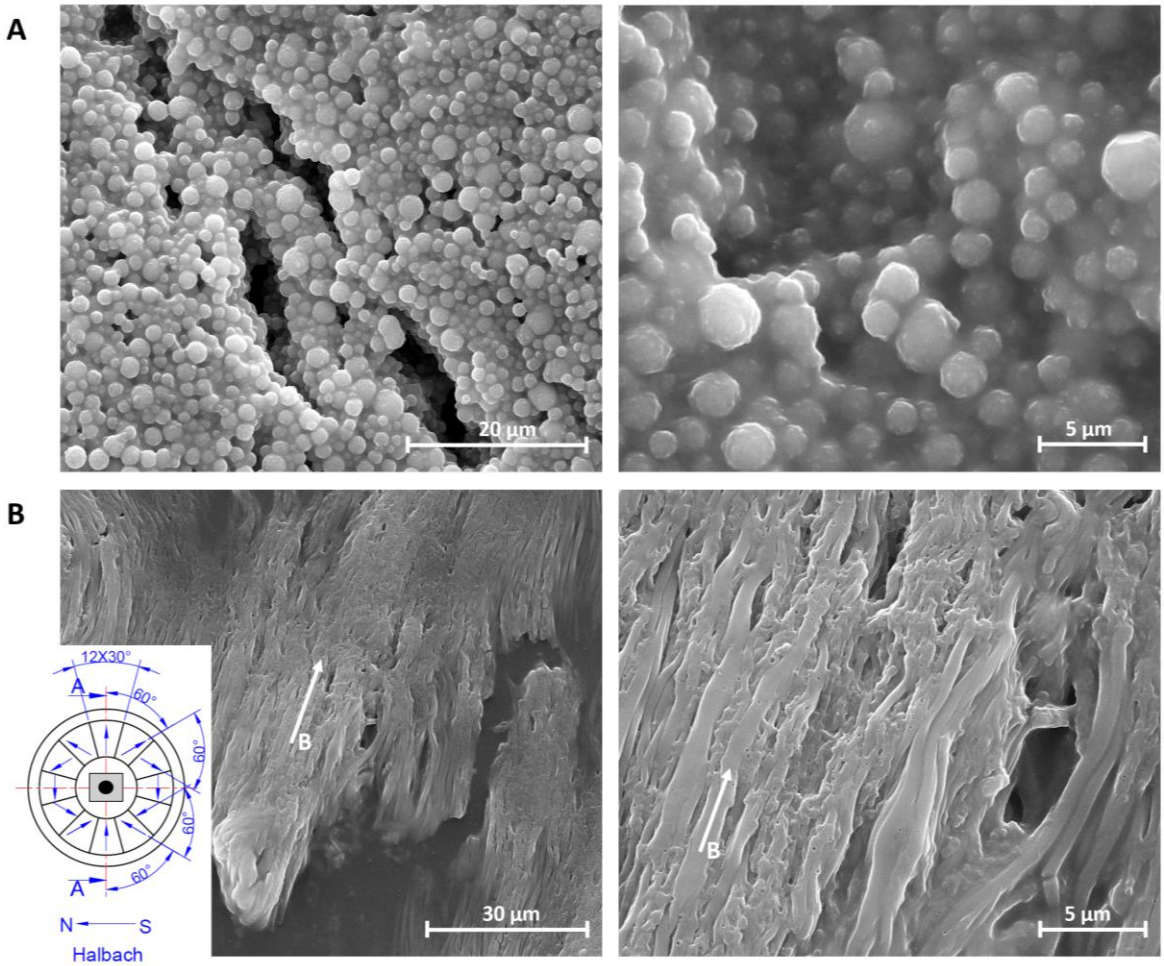

2.5 Conclusions

According to the viscoelastic characterization and the applicability of the TTS principle, the extra-heavy crude oil C_1 showed to be thermorheologically simple, *i.e.,* it did not experience first-order phase transitions with temperature. Although the heavy crude oil C_2 exhibited partial applicability of the principle, both samples showed an excellent fit to the generalized Maxwell model in the dynamic flow field. It could be inferred that the elastic structural properties in both samples are mainly coordinated by asphaltenic aggregates; the applicability of the TTS principle could be linked to the complexity of the structures present in the crude oil matrix.

The synergy between the carrier liquid and the NPs of the KBFs promoted a significant reduction of the viscosity of the crude oils, directly related to the simultaneous action of the solvent and the asphaltene adsorption onto the NPs surface. It was demonstrated the presence of a critical NP concentration (0.6 wt% for C_1 and 0.2 wt.% for C_2) that promoted the maximum decrease in viscosity and G', which was crucial evidence of the effect of the NPs in hindering the aggregation mechanisms of asphaltenes.

It should be highlighted that the crude oil samples without NPs did not show any type of rheological alteration under the presence of a magnetic field, contrary to those reported by other researchers (150, 151, 156). However, in the presence of magnetic NPs and magnetic fields, both heavy crude oil-ferrofluid models showed a magnetoviscous effect. In the case of the models of C_1, the magnetic field contributed to attenuating the initial breakdown and relaxation processes, which was followed by an increase of the relative viscosity and shear stress; this was attributed to the possible formation of magnetic chain-like clusters or aggregates. These assumptions were supported by SEM-EDS analyses that showed the formation of well-aligned columnar

microstructures in the direction of the applied magnetic field. On the other hand, the diluted samples of C_2 followed the bi-dispersed model, in which a small fraction of large particles (>16 nm) form chains determining the field-dependent changes of viscosity. In both cases, a magneto-rheological effect was demonstrated, despite the magnitude of the viscous forces and the adsorption mechanisms that could contribute to hinder the magnetic interactions. Nevertheless, further research is needed to evaluate the applicability of this synergistic approach that could enable to control and to improve the rheological properties of crude oils in different stages of transportation and production, thus, reducing the energy consumption associated with pumping. For our next phase of research, special magnetic arrays are being proved to reduce the viscosity and to control the rheological behavior of these fluids, as it has been studied in ferrofluids.

3 Effect of asphaltene adsorption on the magnetic and magnetorheological properties of heavy crude oils and Fe_3O_4 nanoparticles systems

3.1 Abstract

An essential understanding of the adsorptive phenomena involving nanomaterials and asphaltenes has received considerable attention in oil recovery and production applications. Particularly, iron oxide-based nanoparticles have emerged as advanced materials due to their unique physicochemical properties, including thermal conductivity and superparamagnetism. On this basis, the kinetics and adsorption isotherms of magnetite (Fe_3O_4) nanoparticles/asphaltene systems were investigated, as well as the synergistic effect of resins acting as stabilizing colloidal agents. The results indicated rapid asphaltene adsorption that, essentially, follows the phenomenological external mass transfer (EMT) model. At the equilibrium, the asphaltene adsorption was adequately described by the monolayer Langmuir model. By these findings, it was studied for the first time the effect of the adsorbed asphaltenes on the magnetic dipolar interactions in nanoparticles/asphaltene powder state configurations, by applying a simple analytical model based on magnetic susceptibility and demagnetizing field concepts. It was proven accurately that asphaltenes coated the surfaces of the nanoparticles forming layers that stimulate a steric repulsive barrier between particles and, thus, reducing the intensity of interactions. Accordingly, a theoretical method was validated to estimate the magnetic-size distribution parameters by comparison with the physical distribution data obtained by Transmission Electron Microscopy (TEM). Finally, from the magnetically modified dynamic rheological properties, it was inferred that isotropic aggregates are naturally formed in the absence of the magnetic field, and these morphological features were not dramatically changed after the imposition of the field, leading to

direct extrapolation of the modeling-based procedure for powders to real colloidal configurations applied in oil field operations.

3.2 Introduction

Oil is still considered one of the main global primary energy sources; according to the 2020 World Energy Outlook edition, until 2019, it supplied more than 31% of the global energy demand and it is projected to remain the fuel with the largest share of the worldwide energy mix until 2045 (222). Despite the vast changes that the world is facing, in which renewable fuels retain the position of the fastest-growing energy source, emerging markets still represent strong oil demand for mobility, and essentially, oil will continue leading as a feedstock in the petrochemical sector with the imminent advantage of zero combustion (222). Heavy and extra-heavy crude oils are framed as the mainstay of the energy market due to their large availability in world reservoirs (136). However, their well-discussed compositional complexity, that mainly promotes undesirable asphaltene phase transitions, makes them difficult and expensive to produce, transport, and refine (136, 223-225).

Asphaltenes have been historically considered the most problematic oil fraction in the petroleum industry, their surface-active properties, as well as their self-association tendency, arise from the conglomeration of several types of intermolecular interactions, including π−π stacking, acid−base interactions (typically between oxygen and nitrogen functional groups, and to a lesser extent, sulfur (226, 227)), hydrogen bonding, metal coordination complexes (metal porphyrins containing mainly vanadium, nickel, and iron), hydrophobic pockets (van der Waals), and interaction with resins (225, 228). Because of thermodynamic perturbations, asphaltenes that exist as a distribution of nanoaggregates, tend to self-assemble to form clusters (with size between 2

and 10 nm (133, 227)) and/or organic deposits that promote critical flow-assurance issues, such as clogging within pipelines and high viscosity (224, 229, 230). It seems that the most polar and metal-containing asphaltenes are directly associated with the deposition processes (225); however, the key factor that determines whether the asphaltenes are stable in the oil matrices is still uncertain. One of the most accepted hypotheses is related to the *"stabilizing"* role of resins, attributed to their capability to serve as a continuous bridge-binding between the polarity of the asphaltenes and the non-polarity of the saturates in the maltene continuous phase (225, 230-234). Koots and Speight (235) quantified that around 75% of the total resins are necessary to maintain asphaltene stabilization. Accordingly, it has been postulated that resins can contribute to the disruption and/or deflocculation of asphaltene aggregates through adsorption mechanisms, mainly by weak van der Waals forces (interaction enthalpies between 3-5 kJ mol^{-1} (223, 224, 236)), and hydrogen bonding (237). On the one hand, some researchers have proposed dispersions of lipophilic colloids of asphaltenes surrounded by a steric stabilization layer of the adsorbed resins (essentially, weak-self interacting resins (224)) that promotes deflocculating effects (224, 230, 234). It has also been discussed the formation of mixed asphaltene-resin aggregates, in which the adsorbed resins hold the capacity to break the stacking of the aromatic sheets in the asphaltenes (233, 236-238). For example, León *et al.* (233) observed multilayer adsorption and proposed penetration mechanisms of resins into the microporous structure of asphaltene aggregates, which could act synergistically to disrupt and dissolve asphaltenes. Liu *et al.* (230), supported the postulates of the penetration theory and demonstrated that the efficiency in inhibiting the formation of asphaltene aggregates depends on the chemical nature of resins; *i.e.*, heavy resins (those extracted by solubility in *n*-pentane), which are more polar and aromatic, showed enhanced

efficiency in heptol (heptane/toluene) dilutions. However, the presence of a critical resin concentration was observed, at which, a complete occupancy of the asphaltene periphery (A2-type molecules with higher solubility parameter (239)) is reached and, consequently, the disaggregated asphaltenes tend to expose the less soluble aromatic colloidal cores (A1-type (239)), promoting the reappearance of self-association mechanisms. Derakhshani-Molayouse and McCullagh (231) validated by molecular dynamics (MD) simulations that the most polar and heteroatom-containing resins have the largest hindering effect on asphaltene precipitation in *n*-heptane. Soorghali *et al.* (232) have also reported that non-native resins showed a better performance in preventing asphaltene deposition, although no chemical analyses were contemplated. Nonetheless, Pereira *et al.* (224) also stipulated that resins that strongly self-interact, exhibit high adsorption and produce a thick and sticky adsorbed layer that promotes flocculation effects. As a conclusion of these discussions, the big gap of ambiguity about the resin stabilization/deflocculation role is clear. Although some of these works have demonstrated a modest inhibition effect (equivalent to low concentrations of model amphiphiles (230, 232, 240)), the implementation of complementary cost-effective solutions to prevent asphaltene destabilization/deposition is still needed.

Adams (225) proposed two paradigms to mitigate flow-assurance issues: asphaltene conservation (by adding diluents, stabilizing agents; among others) and asphaltene rejection (considering them as “waste” byproducts). From the last one, we highlight the selective adsorption methods due to their direct link with nanoparticle technology, as well as, their non-specificity in regards to the oil nature (225). Within this framework, several authors have harnessed the physicochemical properties of the nanoparticles in multiple petroleum processes, mainly focused on the reduction of heavy oil viscosity by emulsifying oil, adsorbing/dispersing asphaltenes, and/or

catalytic oil upgrading (225, 241-243). Particularly, nanoparticles have been categorized as selective asphaltene sorbents and dispersants with the capability of promoting structural changes inside the oil matrices, such as reducing the asphaltene self-association and thus, decreasing precipitation rates (206, 227, 244, 245); promoting the oxidation of asphaltenes through surface exposure (161, 165, 167, 227, 229, 246, 247); and inhibiting the formation of complex long-range viscoelastic structures (2, 6, 7). Nonetheless, asphaltene adsorption constitutes a very complex process since it depends on several factors (*i.e.*, nanoparticle surface acidity, type, size; asphaltene origin, acid-base pairs, and aromatic backbone; water content (225, 241)). Among the well-known functional nano-adsorbents, which are classified as mineral-based, silica, alumina, glass, carbon, metals, metal oxides, and polymers (225, 243), growing interest has been devoted to metal oxides, which, in addition to the large functional surface areas and selectivity, also exhibit exclusive thermal conductivity and superparamagnetism. Regarding the last one, just a couple of works have demonstrated the potential of magneto-controllable features of nanoparticles as an additional advantage in oil flow assurance and recovery (2, 12, 17, 46, 47). The center of attention has been mainly the recovery of heavy oil by enhanced metal-nanoparticle incorporating electromagnetic heating (EMNIEH); however, several constraints have been argued, for example, the limited electromagnetic heating propagation in porous media (12). Alternative approaches have also been reported, such as the inclusion of aqueous-based ferrofluids and external uniform magnetic fields to induce piston flow in a porous medium and, thus, to improve sweeping efficiency and oil recovery (46). Contreras-Mateus *et al.* (2) also demonstrated the induction of magnetoviscous effects in mixtures of heavy crude oils and kerosene-based ferrofluids (KBFs), similar to the experimental observations in ferrofluids under the influence of uniform static magnetic fields (56,

172, 173). Although these works have laid the foundations of the synergistic effect of nanoparticle technology and magnetic fields as prominent flow assurance and recovery approaches, to the best of our knowledge, none of them has provided a fundamental explanation and interpretation of the possible physicochemical interacting phenomena occurring in these systems in the presence of magnetic fields, since all of them have focused on macroscopic approaches, which has limited the awareness of the scale performance of these technologies. Therefore, it is particularly important to acquire a microstructural understanding of the role of asphaltenes on the induced magnetic interparticle interactions (*i.e.,* nanoparticles/asphaltene complexes) that enable a precise description of these interactions and the scope of their field applicability. Against this background, this research is focused on evaluating the effect of asphaltenes on the magnetorheological behavior of magnetic modified heavy crude oil systems by studying the adsorption phenomena of asphaltenes onto Fe_3O_4 nanoparticles, and by evaluating their role on the ordering and strength of magnetic dipolar interactions in oil/nanoparticles specimens. Although adsorption kinetics and isotherms of asphaltenes onto metals and metal oxide nanoparticles have constituted the topic of plentiful experimental studies (142, 161, 165, 167, 227, 229, 248, 249), these works are mostly limited to the analyses of thermophysical phenomena, encountering, in most of the cases, Langmuir Type I isotherm for asphaltene adsorption (161, 165, 167, 227, 229, 250-253). There are also a handful of works that have observed multilayer adsorption (142, 248, 249). Another couple of studies have considered the effect of resins on the adsorption of asphaltenes (161, 170, 252), concluding mainly that resins impact asphaltene adsorption by competition for sorbent adsorption sites and/or disruption of the colloidal state of asphaltene aggregates. Nonetheless, to the best of our knowledge, no research has evaluated the implications of asphaltene adsorption on the

magnetic dipolar interactions in oil/nanoparticles systems, as an influencing factor on the magnetorheological properties. Bearing in mind the stated main objective, this research was divided into two stages: i) an assessment of the adsorption kinetics and isotherms of asphaltenes onto Fe_3O_4 nanoparticles in synthetic systems (toluene dispersions), contemplating the potential ambiguous effect of the presence of resins on the nanoparticles/asphaltene interactions; and, ii) a magnetic characterization of nanoparticles/asphaltene complexes as a function of asphaltene concentration, to elucidate their implications on the magnetorheological properties of oil/nanoparticles systems. The results demonstrated that the adsorbed asphaltenes impact the magnetic dipolar interactions due to the induction of steric effects. Furthermore, this hindering effect was highly dependent on the concentration of asphaltenes; there were observed exponential increases that had a direct repercussion on the magnetorheological effects. This fundamental analysis could serve as the basis for the design and implementation of magnetism and nanoparticle technology as prominent solutions in flow assurance processes.

3.3 Materials and methods

3.3.1 Materials

A Colombian heavy crude oil (hereinafter, C_1) was used as the feedstock from which the asphaltene and resin fractions were extracted. The compositional characterization of C_1 was carried out by SARA fractionation analysis, following the ASTM D6560 (254), ASTM D1319 (255), and ASTM D2549 (256) methods. The mass percent compositions and the API gravity (ASTM D70 (257)) are shown in Table 5. Asphaltenes (hereinafter, A_1) and heavy resins (hereinafter, hR_1) were obtained by solvent extraction, following the procedure proposed by Liu *et al.*, (230) considering the remarkable inhibition effect of heavy resins over asphaltene

aggregation. *n*-Pentane (EMSURE® grade, Merck) and toluene (EMSURE® grade, Merck) were added in a volumetric ratio of $40{:}\,1$ (mL of *n*-pentane: mL of toluene) to $1\ g$ of C_1. The mixture was subjected to reflux at $80°C$ for $4\ h$ and then, left in darkness for $24\ h$ at ambient conditions. Finally, the sample was sonicated for $2\ h$ at $15°C$ under controlled conditions (avoiding solvent evaporation) to ensure the complete precipitation of the insoluble compounds, which were then collected by gravity filtration using a Whatman Grade 42 paper. The filter cake was washed with *n*-pentane in a Soxhlet extractor until the solvent was colorless ($\sim$24-72 h), subsequently, using *n*-heptane (EMSURE® grade, Merck) and finally, toluene, to isolate hR_1 and A_1; respectively. At each step, the solvent was removed by evaporation in the airflow of a fume hood until the fractions reached constant weight. For comparison purposes, another batch of asphaltenes (hereinafter, A_{1S}) were also isolated by following the standardized ASTM D6560 method (254).

On the other hand, Fe_3O_4 nanoparticles were obtained from Sigma Aldrich for the first stage of this study (50-100 nm, SEM), and from Ferrotec (USA) Corporation of the series EMG 1300M for the second stage ($9.43 \pm 0.14\ nm$, TEM), considering that the latter have a polymeric surfactant that enables excellent stability and dispersibility in organic carrier liquids, iron oxide content between 60 and 80 $wt.\%$, and saturation magnetization in the order of $50–70\ Am^2/kg$. The nanoparticles were used without any further treatment.

Table 5

SARA Fractionation and API gravity of $\boldsymbol{C_1}$.

Fraction	$\boldsymbol{wt.}\%$
Saturates	24.5
Aromatics	24.6
Resins	25.21

Asphaltenes	25.0
Volatile matter (VM)	0.7
API gravity	11.46

3.3.2 Evaluation of the synthetic heavy crude oil and adsorption experiments

3.3.2.1 Preparation of the stock stable dispersions

According to the literature, most of the works have not standardized an optimum procedure for the preparation of stable asphaltene dispersions. Additionally, in most cases, the effect of the centripetal force in the adsorption experiments has not been analyzed; it is important to note that, the action of this force could induce to inaccurate mass balances since a substantial fraction of the non-adsorbed asphaltenes might precipitate when using this non-selective technique, especially at concentrations of asphaltenes above $1\,mg/mL$. Therefore, a standardized approach was implemented in this work: stable stock dispersions of A_1, A_{1S}, and $A_1 - hR_1$ (0.15 and 0.3 g of hR_1 per 1 g of A_1) were prepared at a concentration of $1\,mg/mL$ in toluene, by subjecting the mixture to reflux at $80°C$ for $5\,h$. The stability of each dispersion was corroborated when no precipitated material was observed after subjecting the dispersions to centrifugation at $4000\,rpm$ for $30\,min$. The volume of solvent was calibrated using a volumetric flask before and after reflux.

3.3.2.2 Batch adsorption experiments

For the batch-mode adsorption experiments, an effective mass of nanoparticles (as proposed by (142)) was added to glass scintillation vials, followed by the slow addition of equal and calibrated volumes of the oil fraction dispersions (A_1, A_{1S}, and $A_1 - hR_1$ in toluene) at the initial concentrations ranging between $0.05 - 1\ mg/mL$. Next, the vials were properly sealed to avoid solvent evaporation and sonicated until equilibrium was attained. The nanoparticles/oil

fraction complexes were separated from the dispersions by the application of an external magnetic field at the bottom of the vials. We highlight that this method, in an equivalent way, ensures the selective precipitation of non-interacting nanoparticles and interacting nanoparticles/oil fraction complexes. We also emphasize that, to the best of our knowledge, just a couple of works have implemented this selective separation technique (167, 229, 244). The supernatants were analyzed by UV-Vis spectrophotometry over the wavelength range of 250-900 nm, using a UV-Vis GENESYS 10S, Thermo Scientific spectrophotometer. Depending on the oil fraction concentration range, the dispersions were diluted until the spectra were in accordance with the Beer-Lambert law (258).

The absorbance spectra of asphaltenes suspensions exhibit the presence of two main signals (Figure S1A): a broad signal centered at around 288 nm, which is attributed to graphene sheets that conform the asphaltenes (259, 260), and a peak located at 405 nm, attributed to the Soret band of petro-porphyrins (233, 242). As seen, the intensity of both signals decreases when decreasing the asphaltene concentration. Furthermore, a comparison of the spectra before and after the adsorption of asphaltenes showed that the samples experienced changes in intensity (not in shape nor position) after the precipitation of the nanoparticles/asphaltene complexes, evidencing the presence of the same absorbing chromophores at different concentrations. The diminishing in the intensity at 405 nm after precipitation indicates that the band of porphyrins is appropriate to estimate the concentration of asphaltenes, as they both decrease at the same extent. In addition, toluene absorptivity (~285 nm (261)) might interfere with the more intense signal at 288 nm, and thus, the calibration curves were constructed at a wavelength of 405 nm. It was possible to corroborate that the absorbance of the samples at such wavelength increases linearly as a function

of the asphaltene concentration (Figure S1B). We also complemented these results by demonstrating the adsorption of asphaltenes, using FTIR spectra of the magnetically precipitated complexes (Figure S2).

Accordingly, Eq. 22 was used to determine the difference in the concentration of A_1, A_{1S}, and $A_1 - hR_1$, and thus, to calculate the equilibrium adsorbed quantities (q_{eq} in mg/g).

$$q_{eq} = \frac{(C_0 - C_{eq})V}{m} = \frac{(Abs_0 - Abs_{eq})V}{1000\varepsilon m} \tag{22}$$

where Abs_0 and Abs_{eq} are the initial and equilibrium absorbance of the dispersions; respectively. They are related to the bulk concentration of the adsorbate (C, mg/mL) by the expression of the Beer-Lambert law, $Abs = \varepsilon Cl$; being ε, the extinction coefficient (*i.e.*, the slope of the linear/calibration plots), and l, the path-length (*i.e.*, cuvette width ~1 cm). Likewise, V (mL) is the volume of the dispersion, and m (g) is the mass of nanoparticles.

3.3.2.3 Modeling adsorption kinetics and isotherms

The Mixed-Order (MO) (Eq. 23) and the phenomenological external mass transfer (EMT) (Eq. 24) models were used to describe the kinetic experimental data.

On the one hand, the MO model holds the great advantage of combining the pseudo-first-order (PFO) and the pseudo-second-order (PSO) kinetic models, enabling the analysis without exclusion of i) any stage of adsorption (initial-PFO and final-PSO); ii) any mass transfer controlling step (external/internal diffusion and/or few active sites–PFO, and abundant active

sites-PSO); and, iii) arbitrary initial adsorbate concentration, C_0 (high C_0-PFO, and low C_0-PSO) (262, 263).

$$\frac{dq}{dt} = k_1'(q_{eq} - q) + k_2'(q_{eq} - q)^2 \quad (23)$$

where q is the adsorbed amount of the asphaltenes at time t (min), k_1' $(1/min)$ and k_2' $(g/mg \cdot min)$ are the pseudo-first-order and pseudo-second-order rate constants of the MO model, respectively.

On the other hand, considering that Fe_3O_4 nanoparticles are essentially nonporous (206), and that the theoretical derivation of the MO model arises from the assumption that the initial stage of adsorption is controlled by the availability of active sites (262), it was appropriate to consider a phenomenological analysis of the external diffusional phenomenon, based on the morphological features of the adsorbent (264). Accordingly, the EMT model was contemplated (Eq. 24), recognizing that the diffusion in the surrounding film is the slowest step, and the equilibrium is reached on the surface of the adsorbent (263, 265, 266).

$$\frac{dq}{dt} = k_{ext}(C_t - C_{et}) \quad (24)$$

Where k_{ext} is the universal external mass transfer coefficient $(mL/g \cdot min)$, C_t is the adsorbate concentration at time t (mg/mL), C_{et} (mg/mL) is the equilibrium adsorbate concentration at the surface of the adsorbent. The equilibrium phenomenon is described by the

adsorption isotherm model, $q_{et} = f(C_{et})$. In this case, the estimated parameters of the Langmuir model were coupled to the calculation of q_{et} (see (263)).

In keeping with the asphaltene adsorption studies reported in the literature, most of these studies reported adsorption behaviors that are well-described by Langmuir isotherms (161, 165, 167, 227, 229, 250-253), whose theoretical bases ascribe monolayer adsorption on homogeneous surfaces; showing shapes similar to Type I IUPAC isotherms (225, 226). Although Adams (225) described several factors that could impact the formation of mono-/multi-layer coverages, such as the type and size of the adsorbent, the source and concentration of asphaltenes, sample preparation, nature of the solvent, and sorption conditions (static or dynamic); these factors have not been conclusive in all studies. For example, some works have shown monolayer adsorption at asphaltene concentrations above $40000\ mg/L$, while others have observed transitions to multilayer adsorption at concentrations in the order of $\sim$2500-5000 mg/L (225). Thus, the Langmuir (Eq. 25) and exponential Langmuir model (that includes a concentration-dependent factor, x, Eq. 26) were used for fitting the experimental asphaltene adsorption isotherms.

$$q_{eq} = q_m \frac{K_L C_{eq}}{1 + K_L C_{eq}} \tag{25}$$

$$q_{eq} = q_m \frac{K {C_{eq}}^x}{1 + K {C_{eq}}^x} \tag{26}$$

where q_m (mg/g) is the maximum adsorbed amount of adsorbate forming a monolayer on the adsorbent surface, and K_L (mL/mg) is the Langmuir equilibrium adsorption constant related to the affinity of binding sites. Equivalently, K is the exponential Langmuir constant.

3.3.3 Characterization of the interacting complexes

The nanoparticles and some samples from the dried bulk precipitates after magnetic separation, were selected and analyzed by Scanning Electron Microscopy coupled with Energy Dispersive Spectroscopy (SEM-EDS), using a high-resolution Quanta FEG 650 microscope, operating at $15\ kV$ and high vacuum conditions.

3.3.4 Magnetic evaluation

3.3.4.1 Preparation of the dispersions and magnetometric characterization

The procedure was based on the methodology employed in a previous work (2). In brief, dispersions of the functionalized nanoparticles (series EMG 1300M) at a constant concentration of $43.8\ mg/mL$ ($\sim 5\ wt.\%$) and A_{1S} fraction at concentrations of 0.1, 1.0, and $10\ wt.\%$ were added to a calibrated volume of toluene. The vials were properly sealed to avoid solvent evaporation and sonicated for $6\ h$, followed by orbital shaking for $15\ h$ at $350\ rpm$ and $25\ °C$. Finally, aliquots of $1\ mL$ of sample were collected and dried under vacuum at room temperature, considering the sensitivity of asphaltenes to high-temperature conditions. The powder specimens ($9\text{-}15\ mg$) were used to carry out the isothermal magnetometry measurements, using a vibrating sample magnetometer (VSM, VersaLab^{TM}, Quantum Design, USA). The magnetic field strength applied ($\bar{H}^A$) was varied between -3.00×10^4 and 3.00×10^4 Oe at $25\ °C$.

The $fN_{A1S-\omega}$ notation was used to differentiate the dried functionalized Fe_3O_4/A_{1S} powder specimens obtained from the toluene dispersions, ω refers to the (A_{1S}) asphaltene weight fraction. For example, $fN_{A1S-0.1}$, corresponds to the dried powder of the model dispersion of nanoparticles at the defined concentration ($\sim 5\ wt.\%$), and $0.1\ wt.\%$ of asphaltenes. A standard

sample of dried nanoparticles without asphaltenes (*i.e.*, fN_{A1S-0}) was included for comparative purposes.

3.3.4.2 Theoretical approach of the isothermal magnetization curve

The obtained Fe_3O_4/A_{1S} ($fN_{A1S-\omega}$) powders can be modeled as a homogeneously distributed specimen with randomly directed easy axes for the particle moments. Considering this spatial proximity or packed arrangement, which is simultaneously controlled by the asphaltene-coating thickness; it is necessary to analyze the effect of the magnetic dipolar interactions, as they could modify the response of the specimen to an applied magnetic field; in particular, its susceptibility, relaxation time, and coercivity (267, 268). Thus, a suitable way to analyze the magnetic properties, implies assessing and removing any possible demagnetizing-field (DMF) effects by establishing DMF corrections (269).

Herein, it is essential to provide a fundamental contextualization of the dipolar field, originated in the elemental magnetic moments of any uniformly magnetized specimen by an applied magnetic field $(\vec{H}^A)$, as established in Eq. 27 (267, 269, 270).

$$\vec{H}^E = \vec{H}^A + \vec{H}^D \tag{27}$$

where, $\vec{H}^E$ is the internal effective field in the specimen (experienced by the nanoparticles), which has a reduced value because the contribution of the demagnetizing field $(\vec{H}^D)$, produced by the magnetization distribution of the sample, acts in the opposite direction. In the simplest case, the demagnetizing field can be analyzed by the approximation $\vec{H}^D = -N_u^E \vec{M}$, where N_u^E is the magnetic-phase effective demagnetizing factor in the measurement direction u (due the sample

shape, because of the dipole-dipole interactions between packed magnetic cores) and defines $\vec{H}^D$ in terms of the cores magnetization $\vec{M}$ (61, 64, 267, 271).

Against this background, we analyzed the low-field susceptibility since it is one of the affected functions. Consequently, the extrinsic or apparent susceptibility $\kappa = \lim_{H^A \to 0} \frac{\partial M}{\partial H^A}$ was related to the intrinsic or actual susceptibility $\chi = \lim_{H^E \to 0} \frac{\partial M}{\partial H^E}$ (*i.e.*, in the absence of interactions) by applying a DMF correction, as shown in Eq. 28 (64, 267, 269).

$$\kappa = \frac{\chi}{1 + N_{su}^E \chi} \tag{28}$$

where $N_{su}^E = \phi_N N_u^E$ can be expressed in terms of the demagnetizing factor of the bare nanoparticles (*i.e.*, considering only the magnetic cores), being ϕ_N the volume fraction of the magnetic cores in the specimen, as they coexist with the surfactant (ϕ_{Surf}) and the adsorbed asphaltenes (ϕ_A).

3.3.5 Characterization of the functionalized nanoparticles

The functionalized nanoparticles (series EMG 1300M) were dispersed in toluene and dropped on ultra-thin carbon grids for Transmission Electron Microscopy (TEM). The samples were left until the toluene was completely evaporated. The images were acquired using a Hitachi H7650 operating at 80 kV acceleration voltage.

3.3.6 Magnetorheological evaluation

3.3.6.1 Preparation of natural heavy crude oil models

The preparation of the natural oil models was based on the methodology employed in a previous study (2). The functionalized nanoparticles (series EMG 1300M) at a constant concentration of $43.8\,mg/mL$ ($\sim 5.0\,wt.\%$) and A_{1S} fraction at concentrations of 0.1, 1.0, and $10\,wt.\%$ were added to a calibrated volume ($3\,mL$) of maltenes extracted from C_1 (collected mixture of resins, aromatics and saturates after A_{1S} separation), hereafter M_{1S}. An additional sample using the original oil C_1 (with $25\,wt.\%$ of A_{1S}, see Table 5) and the nanoparticles at the same calibrated volume and nanoparticle concentration was prepared. Subsequently, the mixtures were immersed in an ultrasonic bath for $6\,h$, followed by orbital shaking for $15\,h$ at $350\,rpm$ and $50\,°C$, and finally, they were reincorporated to the ultrasonic bath for another $6\,h$ to completely ensure colloidal stability of the samples (192). C_1^m and $M_{1S-\omega}^m$ notation was used to differentiate the "magnetically modified" C_1 oil and M_{1S} maltenes; respectively. Likewise, ω refers to the asphaltene weight fraction. For example, $M_{1S-0.1}^m$, corresponds to a mixture of M_{1S}, nanoparticles at the defined concentration ($\sim 5.0\,wt.\%$), and $0.1\,wt.\%$ of asphaltenes. A standard sample of M_{1S} and nanoparticles without asphaltenes (*i.e.*, M_{1S-0}^m) was included for comparative purposes.

3.3.6.2 Magnetorheological characterization

The magneto-rheological measurements were conducted on a MCR 302 Physica-Anton-Paar coupled with a Magneto-Rheological Device (MRD) that induces a magnetic flux density up to 1 Tesla (MRD170/1T). To ensure temperature homogeneity and stability of the fluid sample between the parallel plates (which is affected by the thermal energy dissipation due

to the current flow in the MRD), an external temperature control system (T-CS) was paired to the device (further details are described in (2)). The following oscillatory tests were performed:

Before every test, a thermodynamic stabilization of the sample was performed for $30\ min$ at constant temperature and zero shear rate. Then, the time-dependent dynamic moduli (G' and G'' against t) were analyzed at $15\ °C$, $10\ rad/s$, 1 and 10% of strain for C_1^m and $M_{1S-\omega}^m$, respectively; considering three regions: i) G' and G'' were measured during $600\ s$ in the absence of magnetic flux density ($B = 0$); ii) G' and G'' were measured during $300\ s$, applying a constant magnetic flux density of $B = 0.094\ T$; and finally, iii) G' and G'' were measured during $600\ s$ at $B = 0$.

3.4 Results and discussion

3.4.1 Adsorption kinetics and isotherms

3.4.1.1 Adsorption kinetics

The adsorption of A_1 (at $1\ mg/mL$) onto Fe_3O_4 nanoparticles at a fixed-optimum concentration (7.5 mg/mL see (142), and Figure S3) was analyzed for 80 min, as shown in Figure 16. The rate of adsorption revealed a rapid increase during the first 20 min of contact, from which, adsorption equilibrium was reached. These observations were in good agreement with the reported in the literature (167, 206, 229, 249). According to Nassar *et al.*, (206) this rapid increase is ascribed mainly to the nonporous characteristics of Fe_3O_4 nanoparticles that favor a rapid first step or predominantly single-step of asphaltene adsorption. The above has been phenomenologically justified by the Double Exponential Model (DEM), which describes the kinetics of adsorption in two steps, namely, a fast and a slow step (142). Accordingly, in Fe_3O_4 nanoparticles/asphaltene model systems, it has been demonstrated that the rate constant (k_s) and the adsorption coefficient (D_s) of the slow step have shown negligible values; for instance, Shayan and Mirzayi (142)

observed that, in the rapid step of the DEM, almost 90% of adsorption onto maghemite (γ-Fe_2O_3) and hematite (α-Fe_2O_3) nanoparticles was reached in less than 1 h; they explained this rapid rate in terms of the smaller size and, thus the larger available surface area of the nanoparticles.

The PFO and PSO models have been mainly used to describe the adsorption kinetics in solid/solution systems, although it seems that a theoretical interpretation in terms of the mass transfer steps (*i.e.,* diffusion from the bulk of the solution, across the liquid film surrounding the sorbent particles, along the sorbate pores, or "surface reactions" (272)) is typically not provided. Therefore, to accurately represent the experimental kinetic data and the fundamentals of the whole adsorption process, the MO and EMT models were used. By the graphical assessment of the kinetic isotherm (Figure 6A) and the statistical parameters (Table 6), both models showed qualitative and quantitative comparable fitting with the experimental data; which was the expected trend considering the limited number of experimental points. However, directing the attention to the corrected Akaike information criterion (AICc) parameter, the lowest value was observed with the EMT model. In accordance with the state-of-the-art discussion, and the morphological features of the nanoparticles (see Figure 18A), it seems logical to establish the external diffusional kinetics as the dominant process, especially at the initial stage. Furthermore, a theoretical comparison of the overall adsorption rate was estimated in terms of the PFO (Eq. 29), PSO (Eq. 30), and EMT (Eq. 31) driving forces, as follows:

$$\text{PFO-rate} = k_1'(q_{eq} - q) \tag{29}$$

$$\text{PSO-rate} = k_2'(q_{eq} - q)^2 \tag{30}$$

$$\text{EMT-rate} = k_{ext}(C_t - C_{et}) \quad (31)$$

As shown in Figure 16B, the external diffusion rate was higher in several orders of magnitude, thus, it was the leading kinetic process at the initial adsorption stage, which strengthened the previous discussion. Likewise, near the equilibrium, the PSO-rate dominated the adsorption, which was also an expected behavior, considering that the final stage of the adsorption process is one of the conditions that the PSO model can accurately describe (262, 263).

Table 6

Estimated parameter values of the mixed-order (MO) and the phenomenological external mass transfer (EMT) kinetic models.

Model	Parameters		Model	Parameters	
MO	$k_1{}'\ [1/min]$	5.51×10^{-5}	EMT	$k_{ext}\ [1/min]$	4.70
	$k_2{}'\ [g/mg \cdot min]$	0.052			
	$adjR^2$	0.986		$adjR^2$	0.972
	χ^2	0.24		χ^2	0.44
	SSE	4.34		SSE	8.05
	$AICc^*$	10.66		$AICc$	7.98

*$AICc$ is the corrected Akaike information criterion.

Figure 16

A. Adsorption kinetics at 25 °C of A1 (1 mg/mL) onto Fe_3O_4 nanoparticles (7.5 mg/mL) fitted to the mixed-order (MO) model, and the phenomenological external mass transfer (EMT) model. B. Overall adsorption rate in terms of the pseudo-first-order (PFO), pseudo-second-order (PSO), and external mass transfer (EMT) rate contributions.

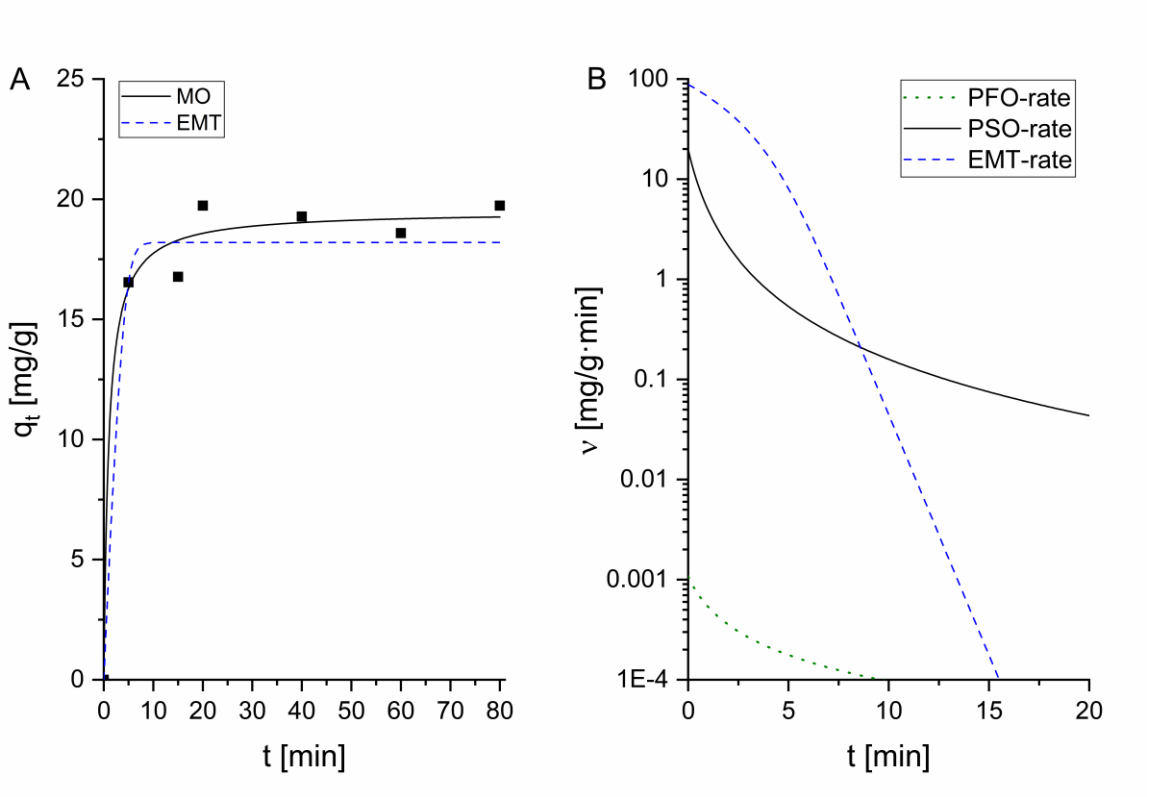

3.4.2 Adsorption isotherms

Figure 17 exhibits the adsorption isotherms (at 25 °C) for A_1 and $A_1 - hR_1$ (0.15 and 0.3 g of hR_1 per 1 g of A_1) onto Fe_3O_4 nanoparticles. The samples followed Type I isotherm behavior, which is typically well-described by the Langmuir model (LM) (273), and corresponds to the most reported behavior in the literature for these systems (161, 165, 167, 227, 229, 250-253). It is worth noting, that the samples exhibited similar behavior regardless the addition of hR_1. Likewise, the

adsorption isotherms parameters and statistical parameters are detailed in Table 7. As shown, for the Langmuir model, the coefficient of determination (R^2) and mean squared weighted deviation (MSWD, $\chi^2_{Red.}$) for the individual fraction isotherms were in all cases > 0.96 and $\ll 1$, respectively, which indicates that the extent of the match between the experimental results and theoretical estimations was adequately described by the LM. Although the Exponential Langmuir model (ELM) showed, in general, fair acceptable regression coefficients (R^2, poorer with A_1 and A_{1S} fractions), it is important to highlight that the adjusted model parameters were systematically in good agreement with the LM, which makes it reasonably adequate to consider monolayer coverage of the surface by at least asphaltene monomers, dimers, and/or trimers under this regime of concentration (165, 227).

Furthermore, according to the LM adjusted parameters q_m and K_L, hR_1 might have had an influence on the adsorption. As shown, increasing the concentration of hR_1 to $15\ wt.\%$ promoted a decrease of $6.55 \pm 1.75\ mg/g$ in the maximum adsorbed amount of adsorbate (q_m), but interestingly an increase of $2.79 \pm 0.72\ ml/mg$ in the affinity of binding sites (K_L). Nevertheless, samples with $30\ wt.\%$ of hR_1 followed an inverse effect, *i.e.*, an increase of 2.41 ± 0.65 in q_m and a decrease of 1.87 ± 0.50 in K_L. If we analyze these results based on the fundamentals of the penetration model proposed by León *et al.* (233) and Liu *et al.*, (230) the interactions between A_1 and hR_1 are dependent on the regime of concentration of heavy resins. Thus, at the lower concentration ($15\ wt.\%$) and, as discussed in (230), based on the approaches of Pereira *et al.*, (224) heavy resins interact preferentially with the peripheral structure of asphaltenes (A2-type) by adsorption and penetration mechanisms, which could promote disruption of asphaltene aggregates and the formation of smaller resin-asphaltene complexes with more exposed

aromatic core structures (A1-type) to the surroundings. In that regard, it is expected that these new-formed complexes exhibit stronger affinity with the sorbent binding sites (*i.e.*, higher K_L values), considering the well-documented capability of the most polar and aromatic asphaltenes to effectively interact and adsorb on the surface of metal-oxide nanoparticles (161, 167, 225, 274), as well as the demonstrated fact that surface-asphaltene interactions are stronger than those of asphaltene-asphaltene (275). In parallel, due to the possible formation of smaller nanoparticles$-A_1 - hR_1$ complexes, the adsorption capacity may slightly decrease, impacting the maximum amount of absorbed asphaltenes (q_m). This last phenomenon was also demonstrated by Alboudwarej *et al.* (252) and, indirectly, by Nassar *et al.* (161) According to (252), the resins are able to reduce the extent of self-associated asphaltenes or to compete for binding sites. Nassar *et al.* (161) also observed that asphaltene extracted by adding *n*-pentane (C5, which are more resinous) showed slightly lower adsorption capacity in comparison with asphaltenes extracted by using *n*-heptane (C7), the authors argued that such alteration could be associated with the aromaticity and colloidal state differences of these fractions. On the other hand, the sample with $30\ wt.\%$ of hR_1 showed an opposite trend. This behavior is also justified by the fact that this concentration was reasonably near the critical concentration ($\sim 40\ wt.\%$) reported by Liu *et al.*, (230) above which, hydrodynamic diameters of these complexes abruptly increase. Hence, this excess could reduce the effectiveness of resins to disaggregate asphaltenes since the A2-type periphery saturates, and it implies that may coexist slightly larger reaggregated complexes with resins incorporated within the asphaltene structure, as suggested by Adams (225). This reaggregation impacts the affinity with the sorbent and, equally, it could slightly contribute to the saturation adsorption. Ekholm *et al.* (275) also demonstrated by using a quartz crystal

microbalance with dissipation measurements (QCM-D) that the inclusion of high concentrations of resins in heptol (50:50)/asphaltene systems impacts the adsorption of asphaltenes onto gold surfaces since the adsorbed amount was higher than the one reached adding only virgin asphaltenes. Likewise, they observed that the adsorbed layer in the presence of resins was less compact than the one obtained for the system with virgin asphaltenes; in effect, both aspects were in accordance with the LM parameters observed under the higher concentration. For further illustration, Nassar *et al.* (167) reported reversed equivalencies between K_L and q_m parameters for different molecular weight asphaltenes.

Table 7

Adsorption isotherms parameters and statistical parameters.

Fraction	Model	Adjusted parameters				
A_1	Langmuir (LM)	$q_m\ [mg/g]$	$K_L\ [ml/mg]$		R^2	$\chi^2_{Red.}$
		22.99 ± 1.52	4.40 ± 0.30		0.966	4.14×10^{-6}
	Exponential Langmuir (ELM)	q_m	$K[ml/mg]^x$	x	R^2	$\chi^2_{Red.}$
		20.36 ± 3.43	8.26 ± 8.90	1.22 ± 0.42	0.939	1.19
A_1-(0.15)hR$_1$	LM	q_m	K_L		R^2	$\chi^2_{Red.}$
		16.44 ± 0.64	7.19 ± 0.66		0.982	5.34×10^{-6}
	ELM	q_m	K	x	R^2	$\chi^2_{Red.}$
		16.35 ± 1.98	7.50 ± 5.66	1.02 ± 0.25	0.941	0.72
A_1-(0.3)hR$_1$	LM	q_m	K_L		R^2	$\chi^2_{Red.}$
		25.40 ± 1.84	2.53 ± 0.05		0.965	5.65×10^{-6}
	ELM	q_m	K	x	R^2	$\chi^2_{Red.}$
		25.43 ± 6.33	2.48 ± 1.84	0.99 ± 0.22	0.979	0.77
A_{1S}	LM	q_m	K_L		R^2	$\chi^2_{Red.}$
		22.10 ± 1.30	5.08 ± 0.48		0.972	4.37×10^{-6}

	q_m	K	x	R^2	$\chi^2_{Red.}$
ELM	19.31 ± 3.03	9.11 ± 10.38	1.14 ± 0.42	0.929	0.77

In addition, we also highlight that the A_{1S}, *i.e.*, the asphaltenes that were extracted by the standardized method (ASTM D6560) showed the same behavior observed for A_1, the LM parameters were in the same order of magnitude and the experimental data were nearly superimposed, as it can be detailed in Table 7. In that regard, these results not only validated the above observations, but also the proposed methodology for the extraction of A_1 and hR_1, as well as the discussed implications of heavy resins on asphaltene adsorption.

Figure 17

Adsorption isotherms at 25 °C of A. Sample A_1, B. Sample A_1-hR_1 (0.15 hR_1 per 1 g of A_1), and C. Sample A_1-hR_1 (0.3 hR_1 per 1 g of A_1) onto Fe_3O_4 nanoparticles (7.5 mg/mL) fitted to the Langmuir (LM) and exponential Langmuir (ELM) models. D. Comparison of all samples fitted to the LM.

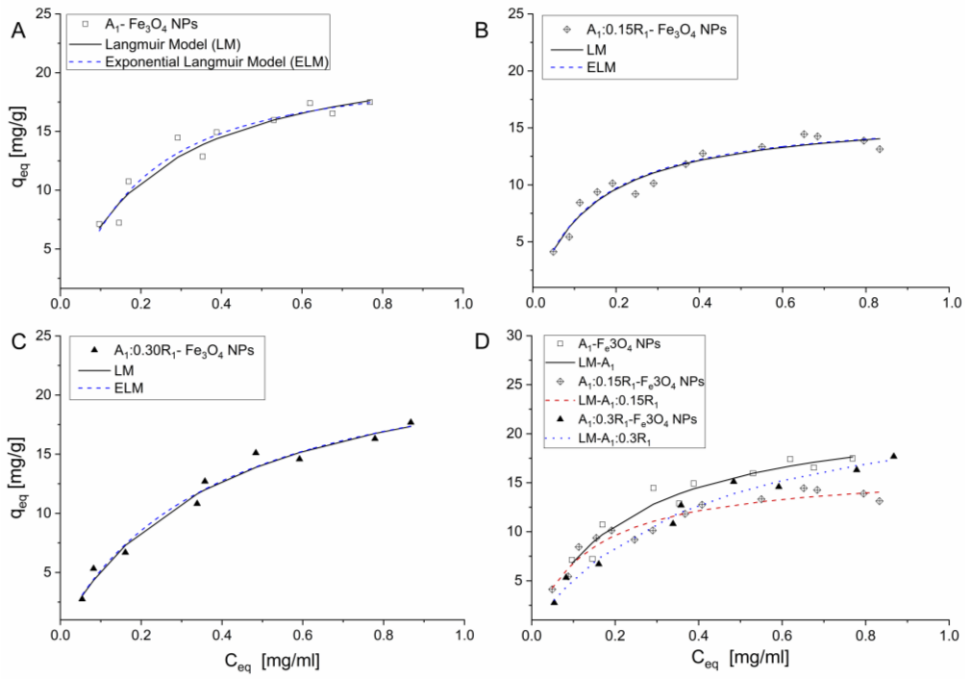

Although these experimental results were consistent with the conclusions extracted from other works, the experimental demonstration of the impact on the hydrodynamic diameter by including heavy resins that could support the discussed hypothesis was beyond the scope of this work, thus, further investigation is required. Nevertheless, we could prove that under this regime of concentration, the approximation of asphaltene monolayer coverage was adequate. This fact was also reinforced by the analysis of the dried bulk precipitates after magnetic separation, employing SEM-EDS, as discussed in the following section.

3.4.2.1 Characterization of the interacting complexes

The SEM micrographs of the Fe_3O_4 nanoparticles before and after asphaltene (A_1) adsorption are shown in Figure 18. As explained before, the interacting Fe_3O_4/A_1 complexes and bare nanoparticles correspond to the dried bulk precipitates of the stock stable dispersions (at the maximum concentration). As shown, the nanoparticles in both cases present rather uniform and spherelike patterns. Nevertheless, the comparison between the micrographs revealed marked differences in the textural features of the nanoparticles surface in the absence and presence of asphaltenes (A_1). As observed in Figure 18A, the bare nanoparticles revealed smooth surfaces, which was in accordance with the kinetics analysis and the rapid adsorption mechanisms discussed previously. However, the nanoparticles containing the asphaltenes, exhibited a rugose thin coating over the surface of the nanoparticles, clearly related to the formation of an asphaltene layer. Likewise, the EDS analyses (Figure S4) confirmed the presence of the adsorbed A_1; the elemental microanalysis revealed the presence of heteroatoms such as sulfur ($0.34\ wt.\%$) and nitrogen ($1.50\ wt.\%$) when asphaltenes were present.

Figure 18

SEM images of the A. Fe_3O_4 nanoparticles and B. Complexes of Asphaltenes (A_1) and Fe_3O_4 nanoparticles after magnetic separation.

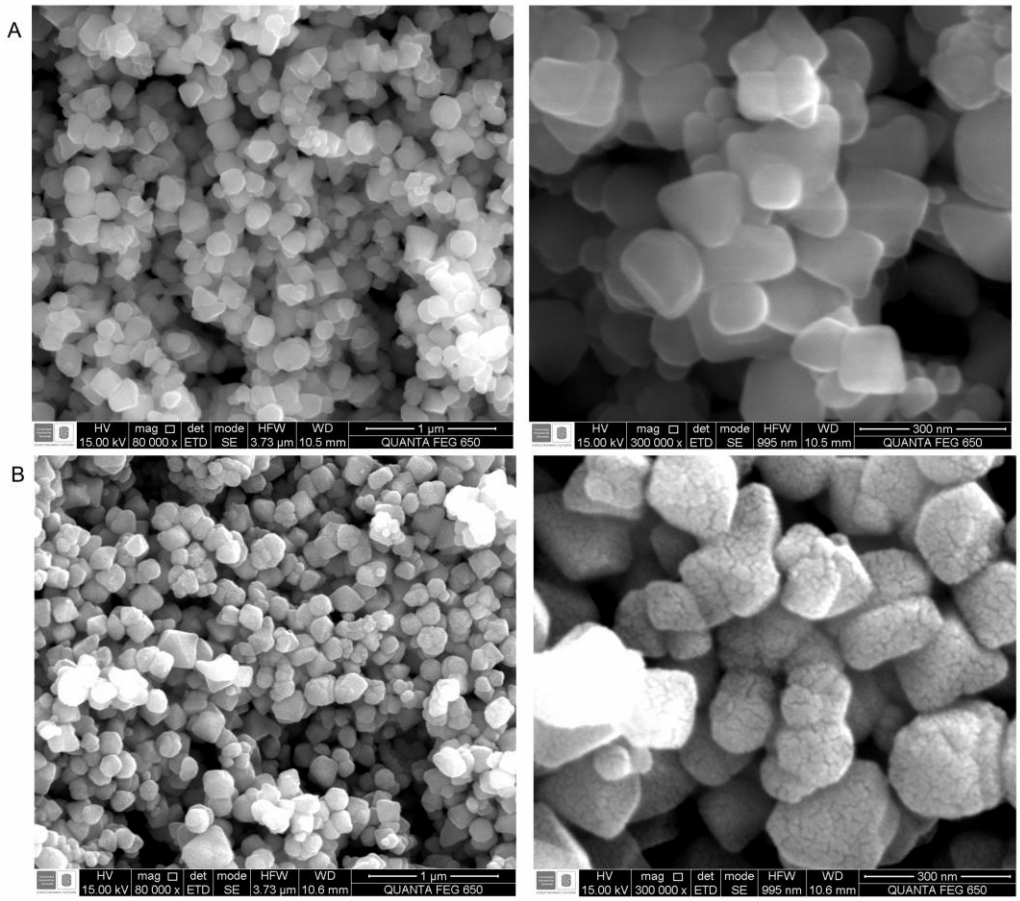

3.4.3 Magnetic evaluation

The magnetization of Fe_3O_4/A_{1S} (*i.e.*, $fN_{A1S-\omega}$) samples measured as a function of $\vec{H}^A$ at room temperature implied the analysis of the influence of the surfactant and adsorbed asphaltenes, as they could have impacted the interparticle mean distances and, thus, the magnetic dipole-dipole interactions. Likewise, considering that all the samples showed typical polydisperse log-normal distribution of mostly superparamagnetic particles (see Figure 19), we explored some

considerations to justify the analysis of the $\vec{M}$ against $\vec{H}^A$ curves with the Langevin function (270), as detailed below.

The nanoparticles were assumed to be in thermodynamic equilibrium at any field value, as they nearly showed a single magnetization branch with zero coercivity and remanence (see Figure 19B). Thus, the expression established by Chantrell *et al.* (276) for the susceptibility χ was considered appropriate (Eq. 32), see also (63). Therefore,

$$\chi = N\left(\frac{\mu_0}{3k_B T}\right)\langle\mu^2\rangle + [C \cong 0] \tag{32}$$

Where N is the total number of particles per volume, μ_0 is the vacuum susceptibility, k_B is the Boltzmann constant, T the absolute temperature, $\langle\mu^2\rangle$ is the expected square of the log-normally distributed nanoparticle magnetic moment, and C is the diamagnetic contribution of the sample holder and the organic coating materials. Note that susceptibility is defined in terms of the Curie's Law (*i.e.,* magnetization of the specimen is inversely proportional to the temperature).

In the high-magnetic field zone, the Zeeman energy is much higher than the anisotropy energy. Mathematically, $\mu_0\mu H^E \gg KV_N$; where μ is the particle magnetic moment, K is the effective uniaxial anisotropy, $V_N = \frac{\pi {D_N}^3}{6}$ is the mean volume of a magnetic core (assuming a spherical form of diameter D_N (64). Hence, the magnetization is well described by the sum of Langevin-like contributions from each particle moment, weighted by the log-normal distribution function of moments $f(\mu)$.

$$M(H^E, T) \approx N\int \mu\, L(x) f(\mu) d\mu + CH^E; \quad \mu_0\mu H^E \gg KV_N \tag{33}$$

where $L(x)$ is the Langevin model, defined as depicted in Eq. 34.

$$L(x) = \coth(x) - \frac{1}{x} \tag{34}$$

The independent variable is defined as $x = \frac{\mu_0 \mu H^E}{k_B T}$.

Since the Langevin description does not include anisotropy effects, it is necessary to estimate a critical magnetic field $H_{crit.} = \frac{KV_N}{\mu_0 \mu}$, above which, the expression deduced by Chantrell *et al.* (276) for magnetization in the high-magnetic field zone is valid (Eq. 35).

$$M(H^E, T) \cong M_s \left(1 - \frac{a}{H^E}\right) + CH^E \tag{35}$$

where $a = \frac{k_B T}{\langle \mu \rangle \mu_0}$, and the saturation magnetization is defined as $M_s = N\langle \mu \rangle$. Here, $\langle \mu \rangle$ is the mean magnetic moment.

Based on the first statement, related to the analysis of the influence of each coating fraction (polymeric surfactant and asphaltenes), we implemented a solution algorithm to obtain an approximation of the individual mass fractions (magnetic cores m_N, surfactant m_{Surf}, and adsorbed asphaltenes m_A) and their influence on the magnetic interparticle interactions. Thus, M_s values between 58 and 71 emu/g (277) were considered in the model based analysis (Figure S5), being $M_s = 58.7\ emu/g$ the value with the more accurate statistical parameters, as detailed below. Accordingly, the estimation of m_N and m_{Surf} was possible, understanding that the mass of the magnetic cores (m_N) can be deduced from $m_N = \frac{\mu_s}{M_s}$, where μ_s is the experimental magnetic moment of the sample measured at the maximum magnetic field strength. Furthermore, m_{Surf} was estimated from a simple mass balance (see Eq. 36) in the standard sample fN_{A1S-0} (*i.e.*, $m_A = 0$) and considering that the total mass (m_T) for each VSM measurement was a known quantity.

$$m_A = m_T - m_N \left(1 + \frac{m_{Surf}}{m_N}\right) \quad (36)$$

Note that the ratio $\frac{m_{Surf}}{m_N}$, initially estimated from fN_{A1S-0}, was constant in all samples as we were dealing with the same functionalized nanoparticles. Based on these balances, the estimations of m_A were in excellent agreement with the theoretical asphaltene concentration of the stock dispersions (0,1 ,1 and 10 $wt.\%$). Thus, the volumetric fractions ϕ_N, ϕ_{Surf} and ϕ_A were calculated, assuming densities of $\rho_N = 5000\, kg/m^3$ (278, 279), $\rho_{Surf} = 880\ kg/m^3$, $\rho_A = 1160\ kg/m^3$ (280); according to the reported in the literature.

In that regard, the validation of the algorithm solution was based on the following arguments: i) the estimated $\langle\mu\rangle$ should be in accordance with the experimental and theoretical values reported in the literature for Fe_3O_4 nanoparticles (281, 282). ii) The deduced diameter, $D_N = \sqrt[3]{\frac{6\langle\mu\rangle}{\pi M_s}}$ (assuming that the nanoparticles are spherical), obtained from the magnetization expression at high magnetic fields (Eq. 35), should be in accordance with the mean diameter calculated from the TEM distribution analysis. Nevertheless, it is important to mention that, both arguments must have proven the inequality $\mu_0 \mu H^E \gg KV_N$, to be valid. iii) The calculated volume fraction of the surfactant and magnetic cores (ϕ_N and ϕ_{Surf}) should be within the ranges reported by Ferrotec Corporation, which are 68.4-76.7 $vol.\%$ for the magnetic cores, and 23.3-31.6 $vol.\%$ for the surfactant (283).

On this basis, Figure 19 shows the isothermal magnetization of the $fN_{A1S-\omega}$ specimens, and the adjusted (volume) magnetization curves of the magnetic cores after the mass balance correction procedure. As discussed before, the powders behave as polydisperse systems,

practically in thermodynamic equilibrium. As illustrated in the insert of Figure 19B, the only difference observed was a slight augment of the slopes at low fields, when the asphaltene concentration was increased. These differences were quantified by fitting the experimental data of each sample with a linear function, $\vec{M} = \kappa \vec{H}^A$, where κ is the slope of $M(H^A)$ at the origin, *i.e.*, $\kappa = \lim_{H^A \to 0} \frac{\partial M}{\partial H^A}$. The estimated values of κ are depicted in Figure 20. As it was expected, there was a dependency with the asphaltene concentration, which was approximately equivalent to an exponential growth factor of 0.79. For example, at the highest concentration fN_{A1S-10} (or, equivalently, $\phi_N = 0.091$), κ reached the maximum value with an increase in the order of 2.71. Furthermore, it was demonstrated that the DMF correction (Eq. 28, continuous line in Figure 20) showed an excellent agreement ($AdjR^2 = 0.989$) with the experimentally calculated κ. The adjusted χ and N_u^E were also within the ranges reported in the literature (271, 284).

Figure 19

A. Isothermal magnetization cycles of $\boldsymbol{fN_{A1S-\omega}}$ *samples, displaying mostly superparamagnetic behavior. B. Rescaled magnetization curves of the* $\boldsymbol{fN_{A1S-\omega}}$ *magnetic cores. The insert figure represents the low-magnetic field interval* $(\pm\sim\mathbf{2\times10^4}\ \boldsymbol{A/m})$ *employed to the estimation of the apparent susceptibly* $\boldsymbol{\kappa}$.

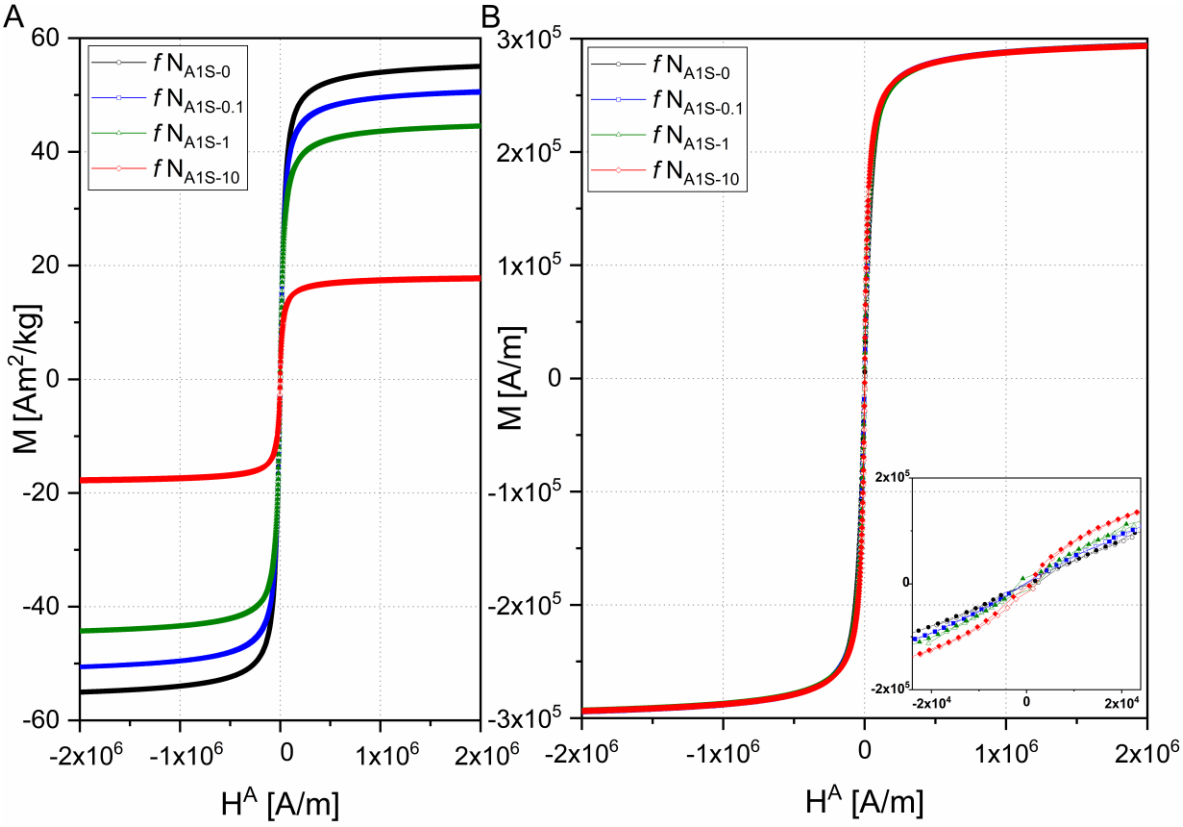

On the other hand, for the high magnetic field strengths, we assumed that the anisotropy energy did not modify substantially the Langevin-like response of the magnetic moments, thus, the fitting of the cycles was conducted using Eq. 35, as it is schematically represented in Figure 21. As a result, the fitting of the curves led to the parameters shown in Table 8. Hence, assuming $K = 2\times10^4\ J/m^3$ (267), we estimated $H_{crit.} = 5.42\times10^4\ A/m$. This estimation makes the

implemented model reasonably justified since the ranges of H^E were considerably higher than the critical value, leading to the inequality $\mu_0 \mu H^E \gg KV_N$. Furthermore, the calculated volume fractions and the nominal particle diameter laid within the values reported by the manufacturer (283). Equally important, the estimation of the total magnetic moment per formula unit $\langle \mu_{Fe} \rangle = 2.34\ \mu_B$ was obtained considering a cubic cell parameter $a = 0.839\ nm$ and 24 Fe ions per cell (267), as well as taking the calculated $V_N = \frac{\pi D^3}{6} = 4.39 \times 10^{-25} m^3$. Interestingly, $\langle \mu_{Fe} \rangle$ was in excellent agreement with the experimental values reported in the literature (281, 282, 284).

Figure 20

Calculated apparent susceptibilities $\boldsymbol{\kappa}$ *as a function of the volume fractions of the magnetic cores* $\boldsymbol{\phi_N}$ *in the low-magnetic field zone. The continuous line corresponds to the DMF analysis Eq. 28 (64, 267, 269).*

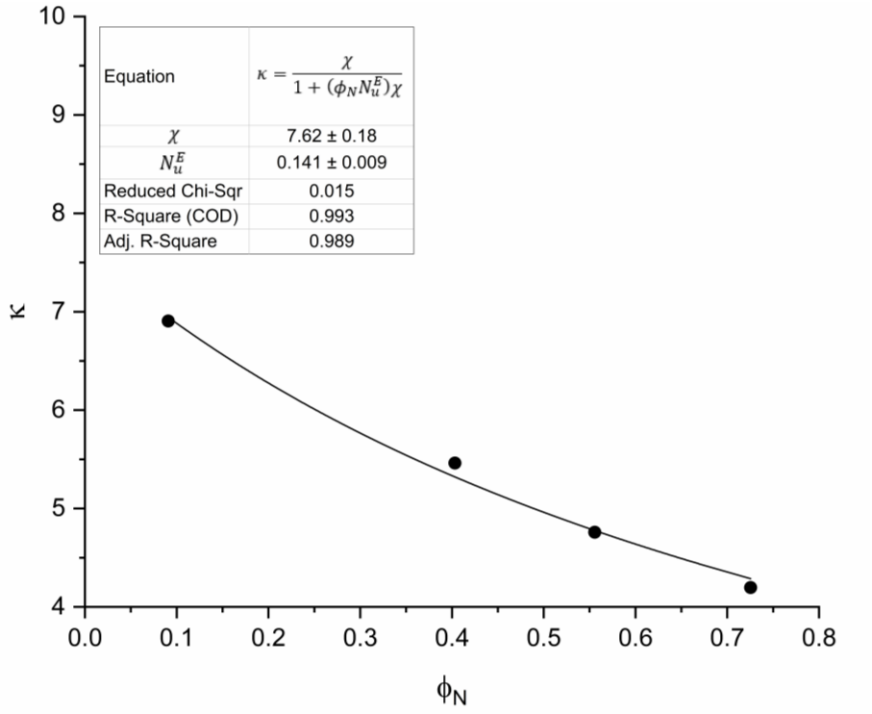

Table 8

Calculated parameters such as mean apparent nanoparticle magnetic moment $\langle \boldsymbol{\mu} \rangle$*, total magnetic moment per formula unit* $\langle \mu_{\boldsymbol{Fe}} \rangle$*, the volume fractions of the magnetic cores and the surfactant (*$\boldsymbol{\phi_N}$ *and* $\boldsymbol{\phi_{Surf}}$*), the diameter of the magnetic cores (*$\boldsymbol{D_N}$*), the critical magnetic field and magnetic flux density (*$\boldsymbol{H_{crit.}}$ *and* $\boldsymbol{B_{crit.}}$*), the nanoparticle magnetic moment standard deviation (*$\boldsymbol{SD}$*).*

$\langle \boldsymbol{\mu} \rangle [\boldsymbol{\mu_B}]^*$	$\langle \mu_{\boldsymbol{Fe}} \rangle [\boldsymbol{\mu_B}]^*$	$\boldsymbol{\phi_N}$	$\boldsymbol{\phi_{Surf}}$	$\boldsymbol{D_N}$ $[\boldsymbol{nm}]$	$\boldsymbol{H_{crit.}}$ $[\boldsymbol{A/m}]$	$\boldsymbol{B_{crit.}}$ $[\boldsymbol{T}]$	$\boldsymbol{SD}[\boldsymbol{\mu_B}]$	$\frac{\boldsymbol{SD}}{\langle \boldsymbol{\mu} \rangle}$
$\boldsymbol{1.46 \times 10^4}$	2.34	0.73	0.27	9.59	5.42×10^4	0.07	1.38×10^4	0.95

*Bohr magneton.

Figure 21

Isothermal magnetization cycles of $\boldsymbol{fN_{A1S-0}}$ *adjusted to the Eq. 32 in the high-magnetic field zone.*

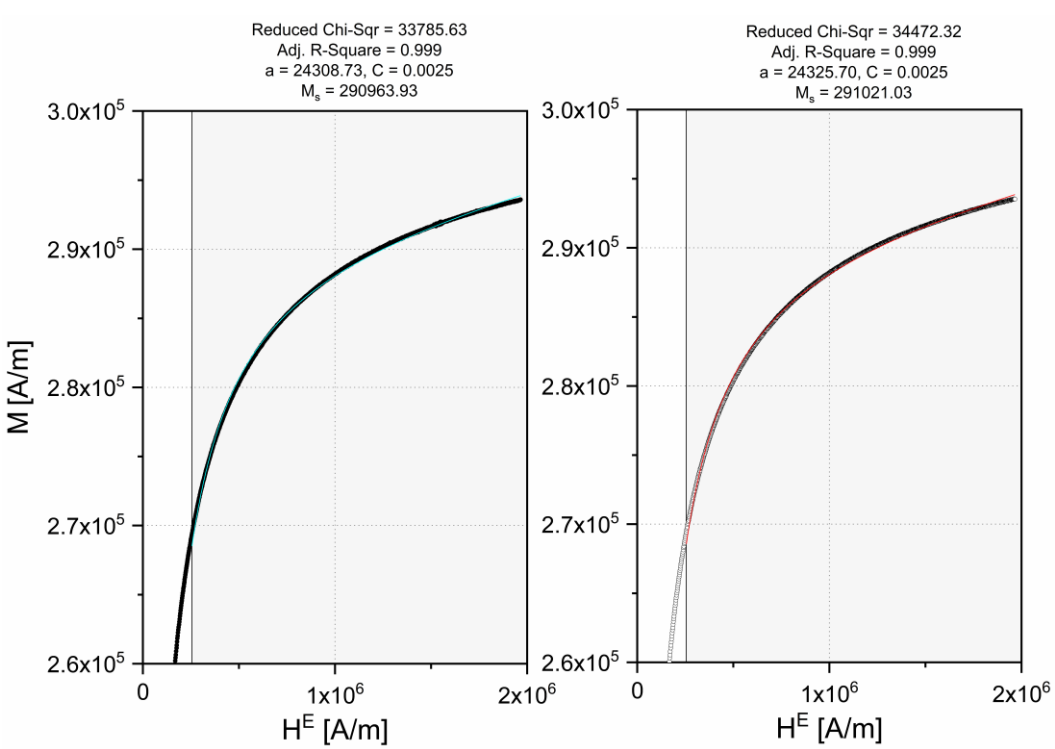

MAGNETORHEOLOGY OF HEAVY OIL-FERROFLUID MIXTURES.

For further validation, the morphology and distribution of the nanoparticles were analyzed by TEM, as shown in Figure 22. The nanoparticles exhibited, in general, homogenously spheroidal shape. The obtained number-weighted diameter histogram was fitted to a log-normal distribution function, leading to the calculation of the parameters shown in Table 9. The low standard deviation confirmed a narrow size distribution, and the estimated mean magnetic core diameter $\langle D_N \rangle$ further demonstrated the validity of the modeling section. As proved, the relation $\frac{SD}{\langle \mu \rangle}$ was also in the same order of magnitude of the one calculated using the Chantrell equations (Eq. 34 and 35).

Table 9

Calculated parameters obtained from the model adjustment of the obtained TEM number weighted diameter histogram.

$\boldsymbol{D_N}$ $[\boldsymbol{nm}]$	$\langle \boldsymbol{V_N} \rangle$ $[\boldsymbol{m^3}]$	$\langle \boldsymbol{\mu} \rangle [\boldsymbol{\mu_B}]$	$\boldsymbol{\sigma_V}$*	$\boldsymbol{SD}[\boldsymbol{\mu_B}]$	$\frac{\boldsymbol{SD}}{\langle \boldsymbol{\mu} \rangle}$
$\mathbf{9.43}$	4.39×10^{-25}	1.39×10^{4}	0.68	1.34×10^{4}	0.97

*$\boldsymbol{\sigma_V}$ is the volume standard deviation.

Figure 22

TEM images of Fe_3O_4 nanoparticles (scale bar of 20 nm). Annotations indicate the mean size distribution and standard deviation determined from a fit to the lognormal size distribution.

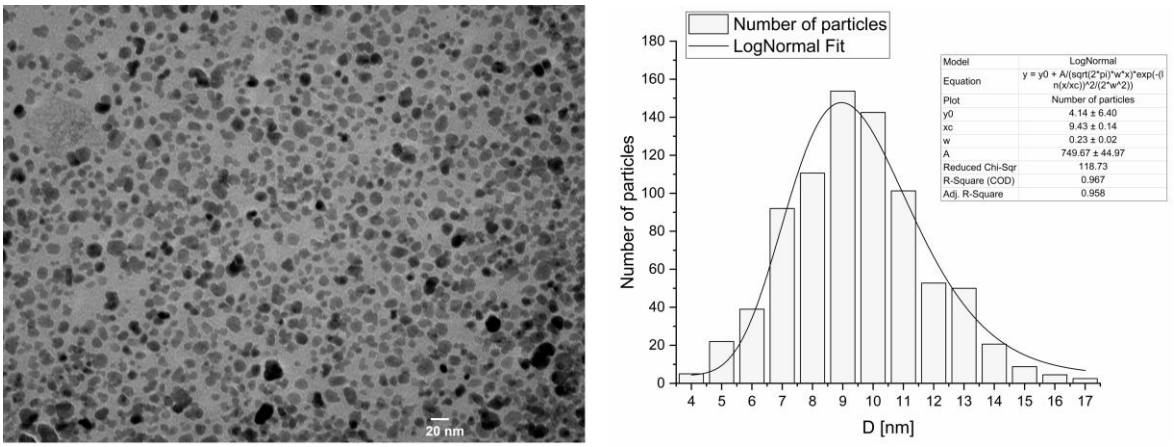

Accordingly, it was demonstrated that the strength of the magnetic dipolar interactions was noticeably diminished by the adsorbed asphaltenes, enabling us to validate the DMF correction, as it was previously suggested by Sánchez *et al.* (267) and Normile *et al.* (269) The decrease in the dipolar interactions was ascribed to the induction of steric repulsive effects, as evidenced by the increase of the apparent magnetic susceptibility (κ), which was found to be proportional to the mass concentration of asphaltenes. Furthermore, the coupling of the corrected χ and the Chantrell models under low- and high-magnetic field regimes, proved to be a convenient and efficient tool for the analysis and description of these complex interacting magnetic systems, leading to the accurate calculation of the nanoparticles magnetic properties. Equally important, the model-based analysis served as a solid piece of quantitative evidence that the asphaltenes are completely adsorbed on the surface of the nanoparticles in the form of layers. This result not only supported the well-proven surface activity of asphaltenes but was also a useful approach to demonstrate the potential of metal oxide nanoparticles as adsorbent agents with the imminent advantage of magneto-controllable features.

3.4.4 Magnetorheological characterization

On the grounds of the results previously reported in (2), concerning the induction of magnetoviscous effects (*i.e.*, increases in the viscosity (56)) on heavy crude oils/Fe_3O_4 KBFs systems, one of the main observations related to the magnitude of these sudden viscosity increases was their correlation with the rheological complexity of the heavy oils, *i.e.*, those systems with higher viscoelasticity and viscosity, produced the most negative impacts on the stimulated magnetoviscosity. Furthermore, recognizing the well-proven leading role of asphaltenes on the elasticity properties (2, 138, 144), we complemented the discussion initiated in (2), by studying

the impact of the modified magnetic interparticle interactions of nanoparticles/asphaltene complexes on the magnetorheological properties of heavy oils.

As shown in Figure 23, it was evaluated the functional dependency of the dynamic moduli (G', G'') on the asphaltene mass concentration, using the modified maltenes ($M^{m}_{1S-\omega}$) and crude oil (C^{m}_{1}), under the presence of a uniform magnetic field (region II, $B = 0.094\ T$). Interestingly, in the absence of A_{1S} (M^{m}_{1S-0}), the relative increase in both dynamic moduli overlapped (secondary axis at the right of the graph, $\delta G'/G' = \left[G'_{(B\neq 0)} - G'_{(B=0)}\right]/G'_{(B=0)}$, and $\delta G''/G''$). However, appreciable differences were observed when variable amounts of A_{1S} were added to the carrier fluids. As illustrated, the systems with the lower concentration of A_{1S} ($M^{m}_{1S-0.1}$ and M^{m}_{1S-1}) reached the maximum increase of G' (around 20%). Nevertheless, higher concentrations of A_{1S} exhibited reduced impacts. For example, in the sample C^{m}_{1}, the increase in G' was lower to the one observed for the standard sample (M^{m}_{1S-0}). Based on the above, it could be established that below certain critical concentrations, asphaltenes stimulated "enhanced" positive changes $+\delta G'/G'$, which might be interpreted as additional physical attractive forces. By way of illustration, Wang *et al* (285, 286) observed weak van der Waals attractive forces when two asphaltene-coated surfaces approach each other in heptol systems, leading to interdigitation (*i.e.,* side chains of asphaltene molecules penetrate the opposite asphaltene layer) and entanglement of both side of asphaltene coats. These phenomena have also been well-recognized in other works (286-288). In this regard, these enhanced increases are presumably the contribution of interdigitation phenomena and magnetic dipolar interactions between the magnetic cores. Although, under the low concentrations (0.1 and 1.0 $wt.\%$), A_{1S} molecules are barely able to saturate the surface, which favors interdigitation; both attractive forces could be gradually hindered if the concentration of

A_{1S} increases since the aliphatic swelling side chains are more exposed, as a result of some degree of association (285). The above can be attributed to the appearance of steric repulsions between asphaltene aggregates when the coated-nanoparticle complexes approach each other, as established on the basis of Alexander-de Gennes theory (see (286)), and proved in the previous section (see Section 3.4.3).

In consideration of the foregoing, it could be expected that the asphaltene-coated nanoparticles (fundamentally, below 1 mg/mL) are subjected to attractive forces, which stimulate the formation of *aggregates*, even in the absence of magnetic fields. Furthermore, it is well known that magnetic dipolar energy increases with the nanoparticle magnetic core volume. Consistently, it has been experimentally observed that Fe oxide magnetic cores with sizes of 10 nm or less, dispersed in colloids, have just a very mild tendency to produce spontaneous dipolar aggregates, mainly isotropic (289). The above suggests that under a moderate applied magnetic field, *i.e.,* far from the saturation field, the shape of the aggregates should not change abruptly. This statement was made considering that moderate fields are energetically deficient to break these aggregates and form new structures with lower dipolar energy (such as anisotropic chains oriented in the direction of the magnetic field). From this perspective, it seems reasonable to compare the results of the powder (Section 3.4.3) and colloidal specimens under moderate magnetic fields, as in both cases, the effective demagnetizing factors should be quantitatively equivalent. In this regard, we can infer that the reduced magnetic effect on the dynamic moduli is in line with the modeling-based procedure of the magnetometry measurements. It is important to highlight that it is still required further evidence to elucidate to which extent the demagnetizing factors of colloidal and powder arrangements are comparable.

Figure 23

*Time dependency of the dynamic moduli (**G′** and **G"**) of the magnetic modified maltenes* $\boldsymbol{M^{m}_{1S-\omega}}$ *and crude oil* $\boldsymbol{C^{m}_{1}}$ *measured at 15°C, 10 rad/s, 1 and 10% of strain for* $\boldsymbol{C^{m}_{1}}$ *and* $\boldsymbol{M^{m}_{1S-\omega}}$*; respectively. At region I: the magnetic flux density was* $\boldsymbol{B = 0}$*, region II:* $\boldsymbol{B = 0.094\ T}$*, and region III:* $\boldsymbol{B = 0}$.

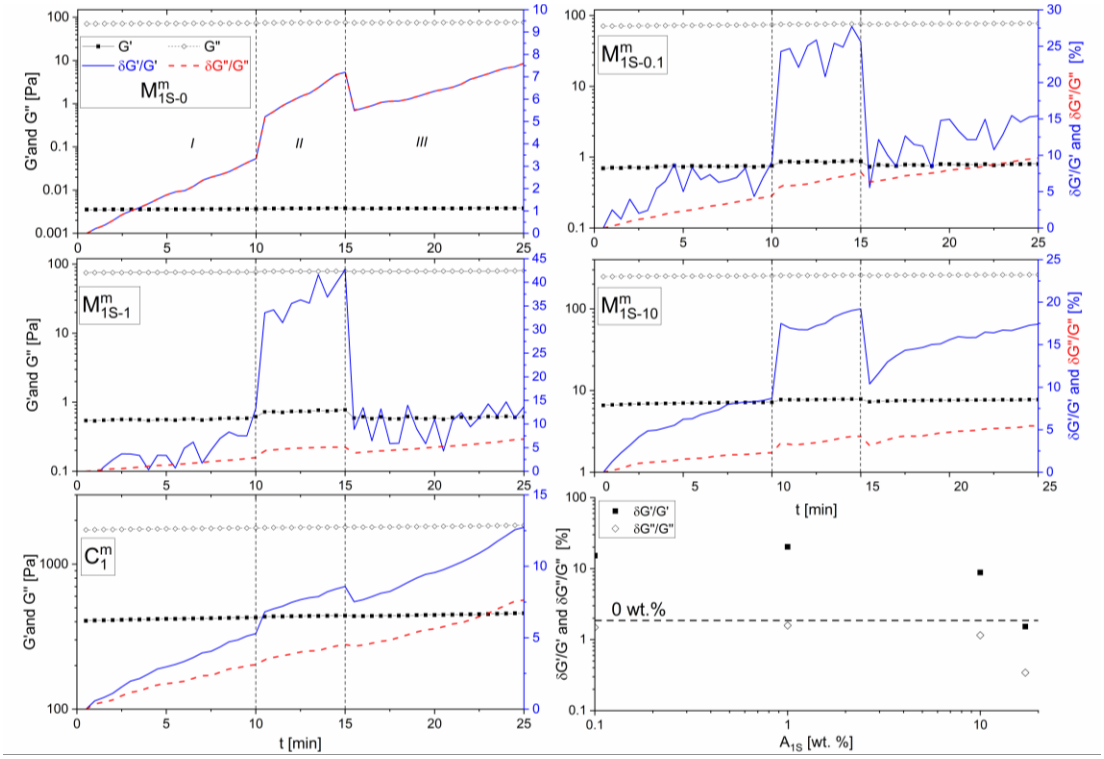

3.5 Conclusions

The surface activity of asphaltenes and their repercussion on the magnetorheological properties of heavy crude oils were analyzed. The results proved that the asphaltene adsorption follows rapid mechanisms described by the phenomenological external mass transfer (EMT) model, obeying, predominantly, mass transfer resistance in the laminar sublayer around the adsorbent nanoparticles. At the equilibrium, it was strengthened the well-recognized

approximation of monolayer asphaltene coverage of the surface, which is adequately described by the Langmuir model. Concerning the role of the heavy resins on the adsorption isotherms, this study proposed some physical interpretations based on the grounds established in the literature, from which, it was observed that the concentration of resins influences the asphaltene colloidal state and their affinity with the nanoparticles binding sites, *i.e.*, a lower concentration of heavy resins ($15\ wt.\%$) promoted increases in the affinity towards asphaltene adsorption and decreases in the adsorption capacity, while at the higher concentration ($30\ wt.\%$), this tendency was reversed. By virtue of these findings, we studied the implications of the adsorbed asphaltenes on the ordering and strength of the magnetic dipolar interactions in nanoparticles/asphaltenes powder state configurations. It was possible to describe for the first time, the existence of a functionally proportional dependency of the apparent magnetic susceptibility with the asphaltene concentration, proving that this fraction was completely adsorbed in the form of layers onto the nanoparticles surface and led to the appearance of steric repulsive effects. Furthermore, it was argued that the coupling of the corrected intrinsic magnetic susceptibility and the Chantrell models, were suitable for calculating the magnetic properties of the nanoparticles/asphaltenes specimens. On the other hand, from the magnetic modified dynamic moduli, we could infer that, in the colloidal state configuration, additional attractive interactions such as interdigitation may be present at certain asphaltenes concentrations ($< 1.0\ wt.\%$), which could lead to the natural formation of nanoparticles/asphaltenes isotropic aggregates in the absence of a magnetic field. Finally, from a thermodynamic perspective, under moderate magnetic field, the morphological features of these aggregates should not change dramatically, which could enable a direct extrapolation of the demagnetizing factors obtained with the nanoparticles/asphaltenes powders

and, thus, the application of the modeling-based procedure for powders to colloidal state configurations.

3.6 Supplementary information

Figure S1

A. Adsorption spectra of asphaltene (A_1) suspensions at different concentrations, before and after the precipitation of asphaltene/nanoparticles complexes. B. Calibration curve of asphaltenes (A_1) at a wavelength of 405 nm.

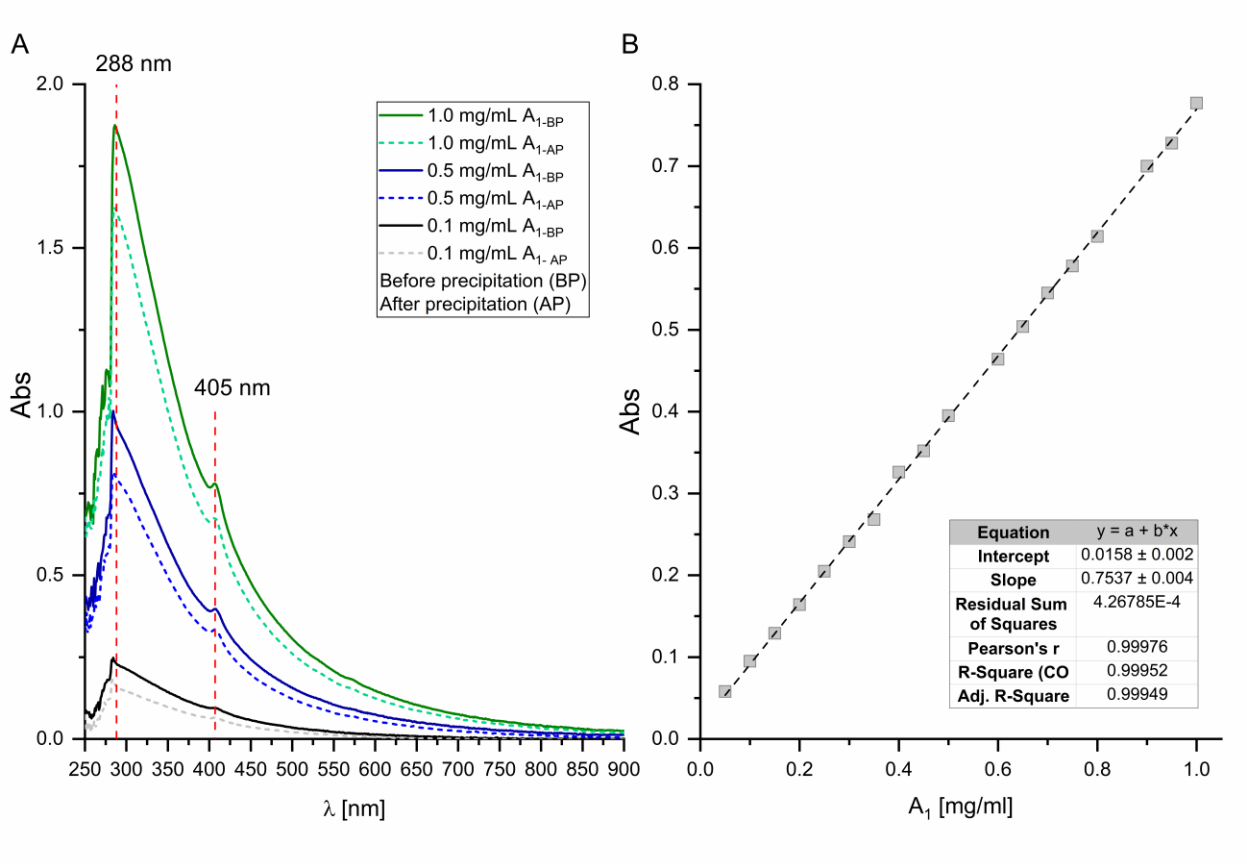

Figure S2

FTIR spectra of the asphaltenes, nanoparticles, asphaltene/nanoparticle and asphaltene/resin/nanoparticle complexes.

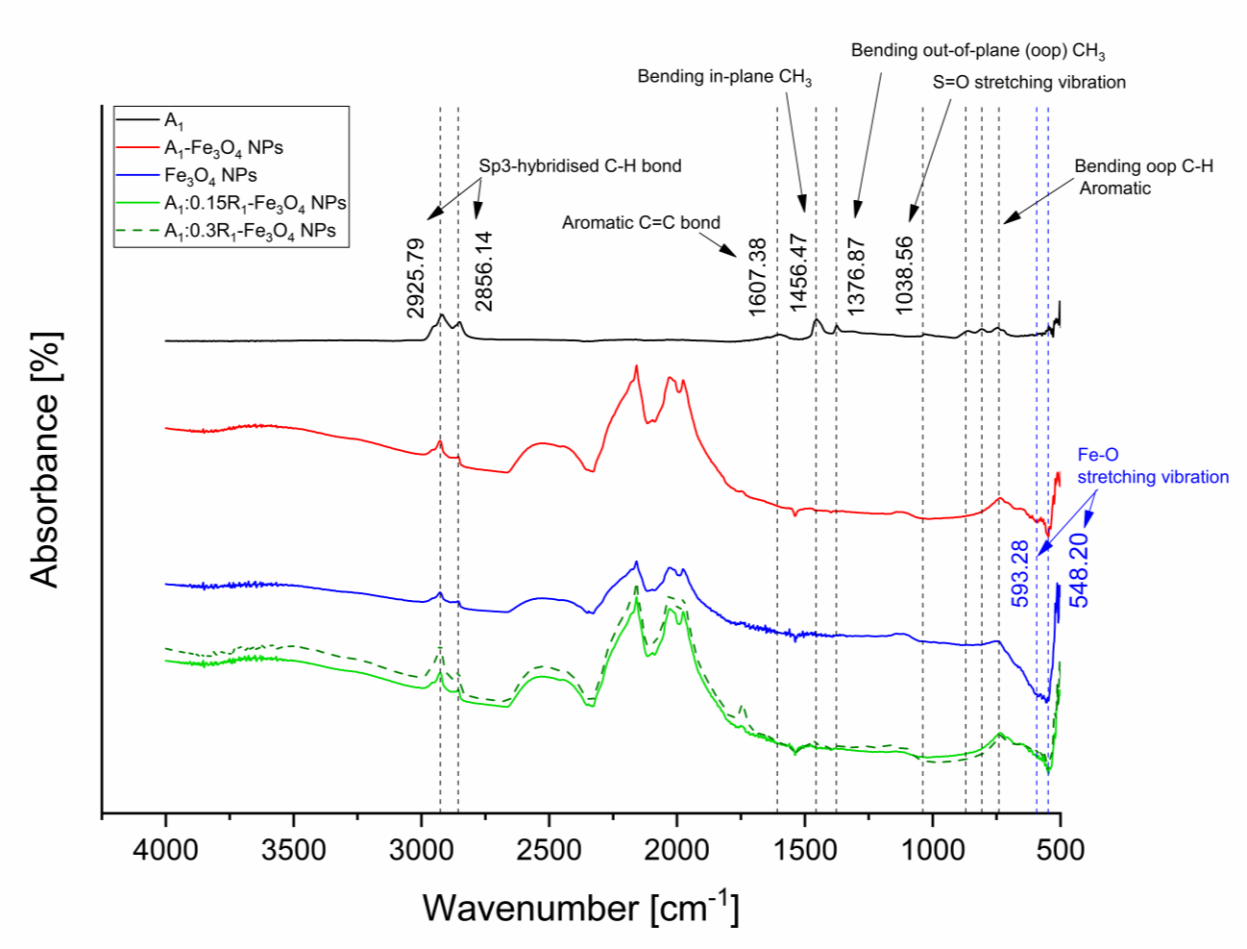

Figure S3

A. Efficiency $E = [(C_0 - C_{eq})/C_0] \cdot 100$ *and, B. Adsorption capacity* $q = [(C_0 - C_{eq})/m] \cdot V$ *as a function of* Fe_3O_4 *nanoparticles concentration.*

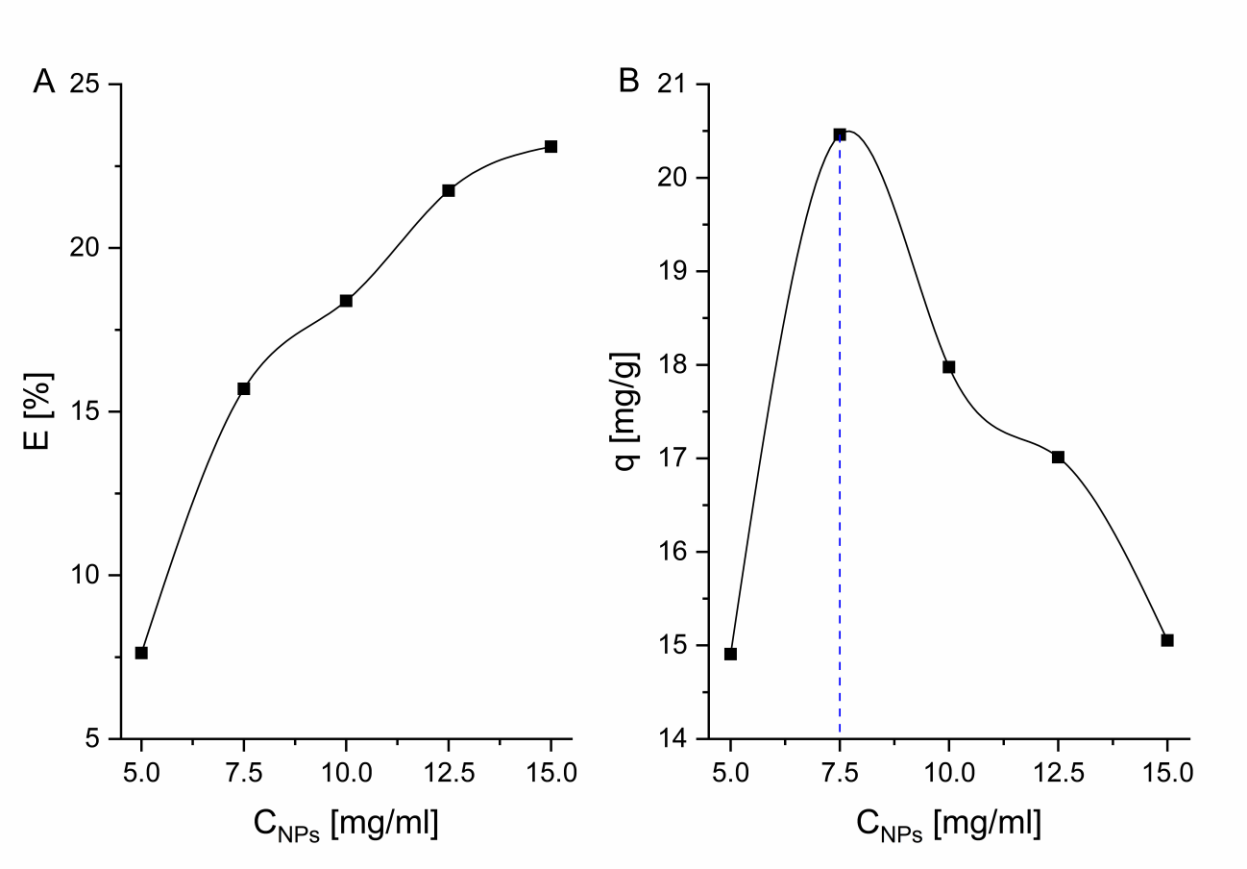

Figure S4

EDS analyses of A. Asphaltenes, B. nanoparticles, and C. asphaltene/nanoparticles complexes.

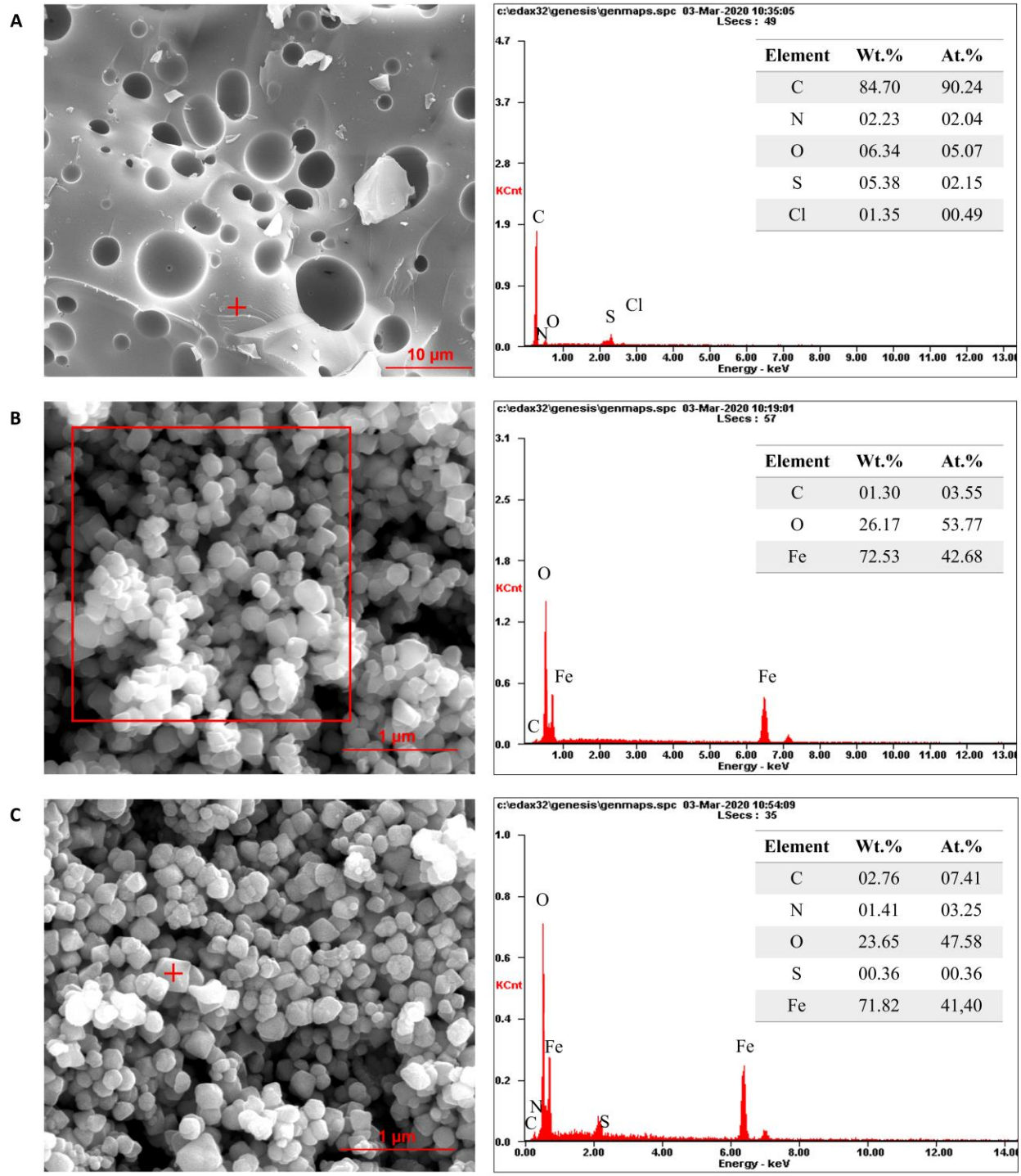

Figure S5

Calculated apparent susceptibilities κ as a function of the volume fractions of the magnetic cores ϕ_N in the low-magnetic field zone, using different M_s values. The continuous line corresponds to the DMF analysis.

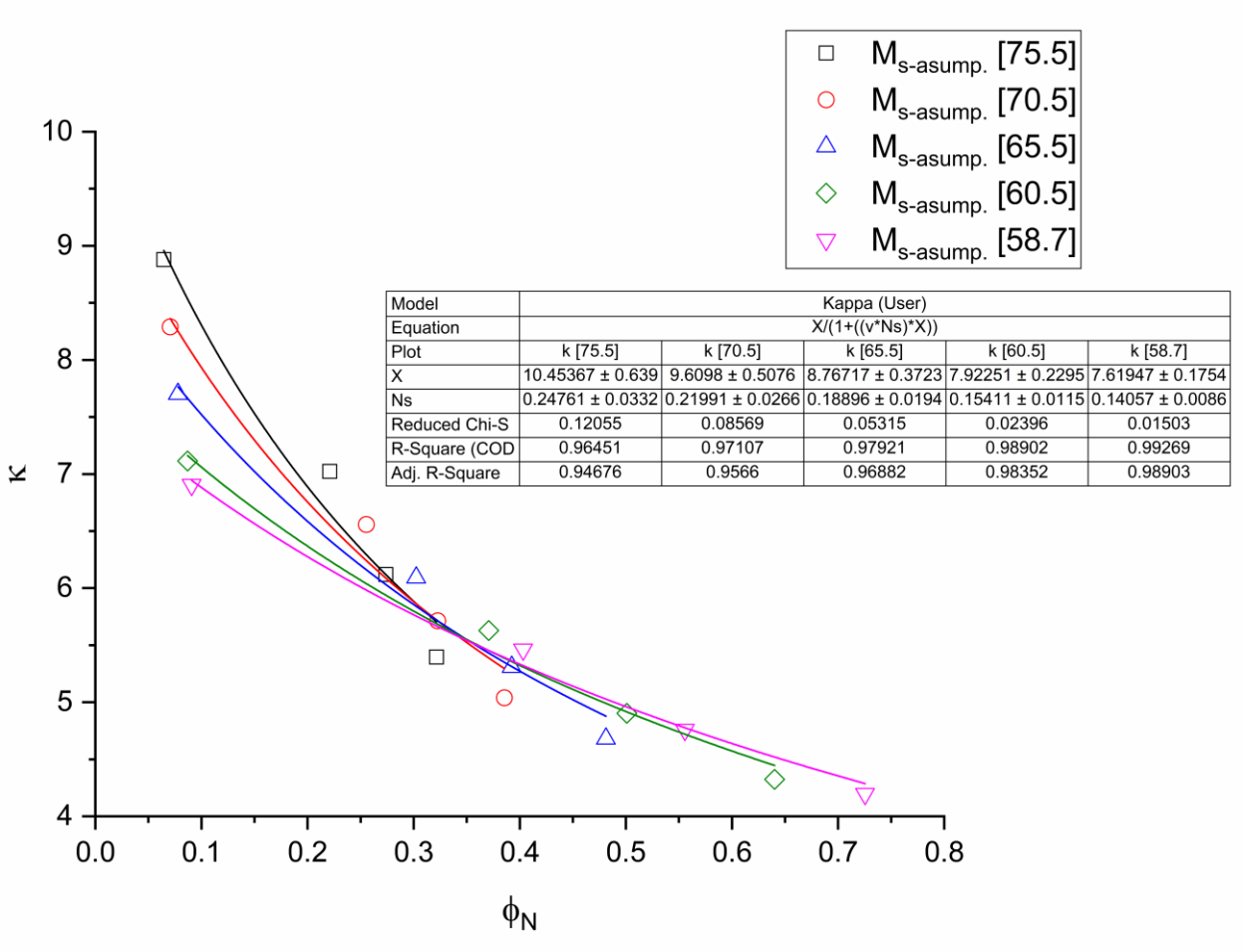

Model	Kappa (User)				
Equation	X/(1+((v*Ns)*X))				
Plot	k [75.5]	k [70.5]	k [65.5]	k [60.5]	k [58.7]
X	10.45367 ± 0.639	9.6098 ± 0.5076	8.76717 ± 0.3723	7.92251 ± 0.2295	7.61947 ± 0.1754
Ns	0.24761 ± 0.0332	0.21991 ± 0.0266	0.18896 ± 0.0194	0.15411 ± 0.0115	0.14057 ± 0.0086
Reduced Chi-S	0.12055	0.08569	0.05315	0.02396	0.01503
R-Square (COD	0.96451	0.97107	0.97921	0.98902	0.99269
Adj. R-Square	0.94676	0.9566	0.96882	0.98352	0.98903

4 Toward understanding induced microstructural changes of magnetic modified crude oils by applying non-linear rheology and magnetometry

4.1 Abstract

Adsorptive phenomena involving iron oxide-based superparamagnetic nanoparticles and asphaltenes have emerged as promising technological alternatives since outstanding structural changes inside the oil matrices are promoted (*e.g.*, inhibiting the formation of complex long-range viscoelasticity). It has also been proven the effect of adsorbed asphaltenes on the magnetic dipolar interactions of dispersed iron oxide-based nanoparticles in magnetic-modified heavy oils (*i.e.*, mixtures of kerosene-based ferrofluids and heavy oil), proving the formation of multiple asphaltene layers which stimulate a steric repulsive barrier between particles. Despite the discussed hindering phenomena, this research successfully demonstrated the applicability and effectiveness of the sequence of physical processes (SPP) framework to provide intra-cycle structure-rheological interpretations during the nonlinear viscoelastic characterization of a magnetic-modified heavy oil, upon the application of an external field. The analysis proved that disordered asphaltene aggregates are highly extended and naturally formed in the absence of the magnetic field. In contrast, in the presence of a uniform field, using a controlled rate magneto-rheometer, the formation of interacting structural aggregates of several hundred nanometers was observed, analogous to ferrofluids-magnetically controlled suspensions. These results were validated through the development of a phenomenological model that effectively captures the intricate processes involved in the formation and reorientation of aggregates based on the experimental data acquired from zero-field cooled (ZFC) and field-cooled (FC) magnetization curves. The analysis of these curves revealed a distinct blocking temperature distribution at around 274 K, which was

successfully linked to the Brownian relaxation phenomenon exhibited by nanoparticle aggregates, based on demagnetizing field concepts. In this regard, this research provided a precise extension of the description of the effect of magnetic fields on the microstructural organization of complex magnetically modified fluids using non-linear rheology and magnetometry.

4.2 Introduction

Bitumen and heavy crude oils exhibit complex rheological behavior, such as viscoelasticity and thixotropy, which encompass a combination of multiple mechanical properties due to the intricate interplay of several thermodynamically dependent molecular structures (290-292). It has been established that the elastic behavior emerges mainly from multifunctional network associations; while the viscous behavior results from the movement of more mobile constituents, mostly aromatics (292), striving to overcome inherent constraints (291). Despite the extensive and occasionally controversial literature on intramolecular interaction descriptions, models such as the classical (133, 293) and thermodynamic (294) colloidal, fractal (295), Yen (296) and Yen-Mullins (297), solubilization (lyophilic) (298, 299), and micromechanical (292), all converge on recognizing the pivotal role of asphaltene aggregates in the atypical non-Newtonian features exhibited by these fluids. Accordingly, the study of the rheological behavior, as well as its interlink with network structure arrangements is fundamental for optimizing extraction and transportation processes. Dynamic oscillatory shear tests offer multiple advantages as they yield a broad spectrum of material responses, encompassing transitions from solid to liquid states and spanning from linear to nonlinear behavior (300). Fundamentally, they consist of subjecting the material to a sinusoidal deformation and measuring the resulting mechanical response as a function of time or frequency. The oscillatory shear test can be divided into linear viscoelastic (LVE) (small amplitude

oscillatory shear, SAOS) and non-linear regimes (large amplitude oscillatory shear, LAOS); and it can be analyzed by applying an amplitude sweep of strain (γ) or stress (σ) at a fixed frequency (ω), to determine the transition point at which the dynamic moduli (first-harmonic moduli) become dependent on the strain or stress amplitude $G'(\omega, \gamma\ or\ \sigma)$ and $G''(\omega, \gamma\ or\ \sigma)$; *i.e.*, the system diverges from linearity (see Fig. 1 of Ref. (301)). In the LVE regime, the strain amplitude is sufficiently small that the oscillatory stress response is sinusoidal with amplitude-independent coefficients. In the non-linear regime, the resulting periodic stress waveform becomes distorted and deviates from a sinusoidal wave or elliptical features in Lissajous plots (300-305).

So far, most of the investigations have been limited to studying the linear viscoelastic (LVE) rheological properties of bitumen and heavy crude oils. Abivin et al. (144) characterized the zero-shear viscosity and linear viscoelasticity of a set of heavy crude oils from different origins (Asia and North, Central, and South America) over a wide range of temperatures (-50°C to 50°C), including steady-shear experiments and SAOS tests. The main observations established that the differences in their rheological properties, ranging from a purely viscous to a weak gel-like behavior, depend on their compositional features, *i.e.*, the elastic character seemed to be related to the higher concentration of asphaltenes. However, the authors did not model their linear viscoelasticity to describe the mechanical behavior of the heavy oils in terms of their compositional structure. Yusoff *et al.*, (306) on the other hand, presented an extensive literature review on the modeling of LVE rheological properties of bituminous binders. The review begins by describing the non-linear multivariable models in the 1950s, which were replaced by empirical algebraic equations (also known as phenomenological or constitutive). These equations are based on a mathematical formulation adjusted to an experimental main curve and their parameters are mostly

without physical meaning. The progression shifted towards mechanical models that incorporate the combination of elements such as springs (storage modulus-Hooke's Model), dashpots (loss modulus-Newton's Model) and parabolic elements (creep compliance). Most of these models rely on implementing the empirical Time-Temperature Superposition Principle (TTSP), and models such as the Williams-Landel-Ferry and Arrhenius equations to construct master curves that effectively describe the dynamic behavior over a wider frequency spectrum (138, 307). The main advantage of these approaches lies in their flexibility to adjust to any experimental curve of dynamic moduli (G' and G'') and complex properties (195). Table 10 summarizes some of these models with special mention of their drawbacks.

Table 10

Linear viscoelastic mechanical models used for bituminous binders and mixtures.

	Constitutive Equation	Drawbacks
Huet Model (**306**, **308**)	*It has a continuous spectrum, i.e., can be represented by an infinity of Kelvin-Voigt elements in series or Maxwell elements in parallel.* $G^* = G_\infty/(1 + o(i\omega\tau)^{-k} + (i\omega\tau)^{-h})$ where, $G^*$is the complex modulus, h and k are the parabolic creep elements such as $0 < k < h < 1$, o is a dimensionless constant, τ is the characteristic time, ω is the angular frequency.	Absence of a viscous element for simulating permanent deformation. Not suitable to model bituminous mixtures at very low frequencies and/or high temperatures $\left(\lim_{\omega\tau\to 0} G^* \approx 0\right)$.
Huet–Sayegh Model (**306**, **308**)	*It has a continuous spectrum.* $G^* = (G_\infty - G_0)/(1 + o(i\omega\tau)^{-k} + (i\omega\tau)^{-h})$ $\lim_{\omega\tau\to 0} G^* \approx G_0$ $\tau = a + bT + cT^2$	Not suitable to model binders at very low frequencies where it is equivalent to a parabolic element instead of a linear dashpot.

	where, G_0 is the elastic modulus, a, b, c are regression parameters representing the material characteristics.	Absence of a viscous element for simulating permanent deformation.
Di Benedetto and Neifar (DBN) Model (**306**, **309**, **310**)	*It is a special case of the Kelvin–Voigt (GKV) mode with elastoplastic (EPi) elements instead of elastic (Ei) elements only. In the linear viscoelastic (LVE) domain corresponds to the GKV model (.* $$G^* = \left((1/G_0) + \sum_{i=1}^{n} 1/(G_i + i\omega\eta_i(T)) \right)^{-1}$$ where, $\eta_i(T)$ is a viscosity function of the temperature.	Suitable for bituminous binders and mixtures in the LVE domain, but its calibration requires the parameters of the 2S2P1D model using an optimization in the frequency range.
2S2P1D Model (**306**, **308**, **310**, **311**)	*It has a continuous spectrum.* $$G^* = G_0 + (G_\infty - G_0)/(1 + o(i\omega\tau)^{-k} + (i\omega\tau)^{-h} + (i\omega\tau\beta)^{-1})$$ where, β is a dimensionless constant. As the TTSP is verified (311): $$\tau(T) = a_T(T)\tau_0$$ where, $\tau_0$is τ at a chosen reference temperature T_r. The shift factor at the temperature T, $a_T(T)$, can be given by the William-Landel-Ferry (WLF) equation: $\log a_T(T) = -C_1(T - T_r)/(C_2 + T - T_r)$ C_1, C_2 are constants.	Not completely suitable for polymer modified binders (PMB) at high temperatures.

While most of these models effectively capture the linear mechanical properties of bitumen and heavy crude oils, they fail to accurately describe the behavior in flow assurance, since these processes often involve significant and rapid deformations. Behzadfar and Hatzikiriakos (138) achieved an accurate representation of the rheological properties of bitumen, employing a combination of the Generalized Maxwell Model in the LVE regime and the separable

Kaye-Bernstein-Kearsley-Zepas (K-BKZ) single-integral constitutive equation (shown in Eq. 37) (195, 203, 312, 313), through stress relaxation experiments (to determine the damping function $h(\gamma)$), and start-up of and cessation of steady shear flow tests to validate the model.

$$\sigma(t) = \int_{-\infty}^{t} \left\{ 2\frac{\partial u(I_B, II_B, t-t')}{\partial I_B}\boldsymbol{B}(t,t') - 2\frac{\partial u(I_B, II_B, t-t')}{\partial II_B}\boldsymbol{B}^{-1}(t,t') \right\} dt' \tag{37}$$

where, $u(I_B, II_B, t-t')$ is a time-dependent elastic energy kernel function, $\boldsymbol{B}$ is the Finger deformation tensor, and I_B, II_B are the invariants of $\boldsymbol{B}$.

Nevertheless, in this kind of experimental tests (stress relaxation experiments) is difficult to find the exact value of the limit strain, up to which the material undergoes the transition to non-linearity (301). Thus, it is still necessary the incorporation of sophisticated rheometric techniques such as the above-discussed LAOS tests, to attain more precise observations in the transition regime, as well as a complete waveform analysis; especially in the case of materials with strong time-dependent behavior, such as bitumen and heavy crude oils (307). Considering that the material functions are not easily interchangeable in LAOS, several authors have proposed different approaches to understanding the nonlinearity of viscoelastic materials. Table 11 chronologically summarizes some of the most relevant prior approaches. It is also worth noting that research about the complete waveform during oscillatory recording is still very limited with bitumen and heavy crude oil. Padmarekha *et al.* (314) studied the linear and non-linear behavior of three samples of modified (Crum rubber-CR and Styrelf) and neat bitumen by estimating the minimum-strain (G'_M) and large-strain (G'_L) moduli (315) to quantify the geometrical symmetry of the Lissajous–Bowditch curves, the results showed that the materials presented a non-linear behavior between

30-40 °C (applying 1% and 5% strain amplitudes); moreover, a good agreement was found with the experimental data and a frame-invariant non-linear constitutive model. Recently, Shan *et al.* (307) proposed a protocol to analyze the non-linear rheological behavior of neat and styrene-butadiene-styrene SBS/CR composited modified bitumen (CMB) in LAOS stress (controlled-stress tests), using Fourier-transform (FT) rheology and strain decomposition method represented as a series of orthogonal Chebyshev polynomials (316). Matching results of the intrinsic non-linearity value ($Q_0 \equiv \lim_{\sigma_0 \to 0} (I_3/I_1(\sigma_0))/{\sigma_0}^2$, where I_i is the relative intensity of the i Fourier harmonic, and σ_0 is the shear-stress amplitude) and the third-order elastic and viscous Chebyshev coefficients, which quantitatively describe the mechanical behavior of the stress, showed that bitumen exhibits predominantly stress softening and stress thinning over a wide temperature range, but its modification produces stress stiffening at some stress and frequency levels at higher temperatures. Wu *et al.* (317) studied the non-linear rheological properties of SBS/CR CMB in LAOS stress tests as a function of CR content, although they observed stress softening under all tested conditions, which was pointed up with the inclusion of CR. Gulzar *et al.* (318, 319) employed terminally blended crumb rubber (CR-TB) modified asphalt, demonstrating predominant shear thinning and strain softening at higher temperatures, while strain stiffening was observed at nearly room-temperature.

Table 11

Quantitative approaches for analyzing stress waverform responses to LAOS

$\boldsymbol{\sigma_{xy} = \gamma_0 \sum_{n=1,odd}^{\infty} G'_n(\omega,\gamma_0)\, sin(n\omega t) + G''_n(\omega,\gamma_0)\, cos(n\omega t)}$

	where, $\boldsymbol{\gamma_0}$ is the strain amplitude, $\boldsymbol{G'_n}$ and $\boldsymbol{G''_n}$ are the amplitudes of the *nth* harmonics with frequencies $\boldsymbol{n\omega}$.	
	Physical Interpretations	
Fourier transform (FT) rheology (301, 302)	**Stress decomposition (SD) (315, 320)**	$\sigma_{xy} = \sigma'_{xy} + \sigma''_{xy} = \gamma_0 \sum_{n=1,odd}^{\infty} G'_n(\omega,\gamma_0)\, sin(n\omega t) + \gamma_0 \sum_{n=1,odd}^{\infty} G''_n(\omega,\gamma_0)\, cos(n\omega t)$
	Chebyshev description (315)	$\sigma_{xy} = \sigma'(x;\omega,\gamma_0) + \sigma''(y;\omega,\gamma_0) = \gamma_0 \sum_{n=1,odd}^{\infty} e_n(\omega,\gamma_0)T_n(x) + \gamma_0 \sum_{n=1,odd}^{\infty} v_n(\omega,\gamma_0)T_n(y)$ where, $x = \gamma/\gamma_0$ and y= $\dot{\gamma}/\gamma_0$ are the normalized strain and strain-rate. The coefficients e_n [Pa] and v_n [Pa·s] represent elastic and viscous contributions, respectively.
Power series (321)		$\sigma_{xy} = \sum_{m=1,odd}^{\infty} \gamma_0^m \sum_{n=1,odd}^{m} G'_{nm}(\omega)\, sin(n\omega t) + G''_{nm}(\omega)\, cos(n\omega t)$
Characteristic functions (301, 322)		$\sigma_{xy} = \sigma_l + \sigma_r + \sigma_t + \sigma_{st}$ where, σ_l, σ_r, σ_t, σ_{st} are sinusoidal, rectangular, triangular, and saw tooth functions, describing the linear response, strain softening, strain hardening, shear bands or wall slip; respectively.
Dynamic sequence of physical processes (SPP) (303, 305, 323)		$\sigma_{xy} = G'_t\gamma + G''_t(\dot{\gamma}/\omega) + \left(\sigma_y - G'_t\gamma_e\right) = G'_t(\gamma - \gamma_e) + G''_t(\dot{\gamma}/\omega) + \sigma_y$ The instantaneous moduli are defined as: $G'_t \equiv -B_\gamma/B_\sigma = \partial\sigma/\partial\gamma$ $G''_t \equiv -B_{\dot{\gamma}/\omega}/B_\sigma = \partial\sigma/\partial(\dot{\gamma}/\omega)$ where, $B = [B_\gamma, B_{\dot{\gamma}/\omega}, B_\sigma]$ represent the binormal vector of the Frenet-Serret apparatus. An instantaneous viscosity (η_t) and a single modulus (G_t) have been defined alternatively as (300): $G'_t \equiv -B_\gamma/B_\sigma$

$$\eta_t \equiv -B_{\dot{\gamma}}/B_{\sigma}$$

As shown, LAOS is a highly advantageous technique for evaluating the mechanical relaxation mechanisms in bitumen when undergoes substantial deformations. The tests prove particularly valuable in analyzing the structural modifications, referred to as structural yielding (324), that arise as a function of temperature, frequency, strain/stress amplitude, and modifier content. Building upon this precedent, this research was headed toward the exploration of implementing LAOS tests to evaluate the rheological impacts of integrating magnetic stimulated iron oxide nanoparticles into the crude oil matrix, specifically under conditions that closely mimic transportation and start-up flow scenarios. We stem from two key precedents. On the one hand, in previous research (3), we provided evidence that the inclusion of nanoparticles promotes asphaltene surface adsorption forming multiple layers, which led to the appearance of steric repulsions that diminished the magnetic dipolar interactions. Nevertheless, the induction of magnetoviscous effects was proved, such as those observed in ferrofluids (2). On the other hand, some experimental approaches conducted with commercial ferrofluids have demonstrated the induction of direct ferrohydrodynamic pumping; *i.e.,* sinusoidally time-varying magnetic fields traveling axially along a cylindrical pipe length can generate a locally non-uniform rotating field within the ferrofluid, which induces gradients in the nanoparticle rotation and, thus, radial shear that drives the flow (75). Among the significant findings, Mao *et al.* (75) argued that the mechanism behind body pumping involves the formation of dynamic short-chain structures, fundamentally, dimers. To support this claim, the authors effectively developed a generalized model of the magnetic susceptibility accounting for multiple nanoparticle core sizes (Eq. 38). As mentioned before, coupling between the physical rotation of the particles and the surrounding

liquid medium is required, but the non-interacting nanoparticles exhibited dominance of Néel relaxation (*i.e.*, free rotation of the magnetic moment overcoming the anisotropy barrier, while the particle remains fixed). Thus, the alignment of the experimental findings with the proposed model served to substantiate the phenomenon of particle aggregation in the ferrofluid, thereby inducing Brownian relaxation mechanisms characterized by the synchronized rotation of both magnetic moment and particle (14).

$$\chi_o(D_c) = (\mu_0 M_d^2 \phi_T / 3k_B T)\left(P_d V_{d,c} + (1 - P_d)V_c\right) \quad (38)$$

where, μ_0 is the magnetic permeability of vacuum, M_d is the domain magnetization, $\phi_T$is the volume percentage of the solid nanoparticles within the total ferrofluid volume, k_B is the Boltzmann constant, T is the ferrofluid temperature in Kelvin, V_c and $V_{d,c}$ are the magnetic core volume of each nanoparticle, and dimer, respectively. $P_d \ll 1$ represents the dimer core volume fraction (over the total nanoparticle core volume), it was assumed that it does not substantially alter the size distribution of singlets, *i.e.*, $V_{d,c}/2$ is the average core volume of each particle within a dimer.

We believe that this phenomenon may hold the potential to expand the range of applications in crude oil transportation and start-up flow, by linking analogous principles. However, the structural complexity of oils brings up multiple uncertainties, such as the above-discussed magnetic interaction diminution caused by the adsorbed asphaltenes. To abord some of these inquiries, particularly the feasibility to induce the formation and/or reorientation of magnetic chain arrangements inside complex viscoelastic systems, we have proposed a combined approach employing LAOS tests and magnetometry. From the former, we applied the sequence of physical (SPP) framework, since previous studies have demonstrated that the SPP metrics provide accurate

intra-cycle structure-rheological interpretations, including plastic deformation, elastic to viscous transition, and stress overshoot (324). According to this approach, the presence of a magnetic field induces the formation of short-range structures within the material, resulting in a sudden increase in its mechanical properties. These transformative changes can be readily detected by analyzing the information obtained from the intra-cycle transitions. From magnetometry, isothermal magnetization loops were measured over a temperature range from 50 to 320 K, and modeled using the generalized asymptotic fitting method of ferrosolid magnetization at high magnetic fields (325). Additionally, zero-field cooled (ZFC) and field-cooled (FC) magnetization curves were studied, from which a distinct blocking temperature distribution at approximately 274 K was detected and linked to the Brownian relaxation of nanoparticle aggregates. To effectively validate this assumption, a phenomenological model that describes the formation and reorientation of these aggregates was proposed. Finally, these combined findings provided compelling evidence for the formation of short-chain structures of a few hundred-nanometer sizes in viscoelastic matrices. To the best of our knowledge, this research marks the pioneering exploration of the synergy between rheology and magnetometry in understanding the formation and alignment of magnetic structures, but also paves the way for investigating the induction of magnetic structures when dealing with ferrofluids, an intricate subject that has historically posed significant technical challenges.

4.3 Materials and Methods

4.3.1 Materials

A Colombian heavy crude oil (C_1) was used as a model sample. Comprehensive details of the compositional characterization can be consulted in Contreras-Mateus *et al.* (3) In brief, the SARA fractionation analysis (254-256) determined saturates, aromatics, resins, and asphaltenes

concentrations of 24.5, 24.6, 25.21, and 25.0 wt.%, respectively. Likewise, an API gravity (257) of 11.46 was reported.

On the other hand, the ferrofluid was formulated using toluene (EMSURE® grade, Merck) as the carrier fluid, and functionalized hydrophobic magnetic iron oxide nanoparticles of the series EMG1300M from Ferrotec (USA) Corporation (9.43±0.14 nm, TEM) with iron oxide content between 60 and 80 wt.%, and saturation magnetization in the order of 58.7 emu/g (3).

4.3.2 Formulation of the magnetic modified heavy crude oil model

The sample formulation was carried out according to a previously well-established methodology (3), as follows: the nanoparticles were dispersed (at 20 wt.%), and stabilized through ultrasonication (for 15 min) in toluene, resulting in the formation of the ferrofluid. Subsequently, the ferrofluid was mixed with C_1 sample at a mass ratio of 0.2:1; respectively. Finally, the mixture (hereinafter, $C_{1\text{-}5}$) was agitated for 15 h at 350 rpm and 50 °C, followed by an additional 6 h ultrasonication.

4.3.3 Characterization of the non-linear rheological properties in LAOS experiments

LAOS tests were conducted on an MCR 302 Physica-Anton-Paar strain-controlled rheometer, equipped with the RheoCompass LAOS module, and coupled with a Magneto-Rheological Device (MRD) that induces a magnetic flux density of up to 1 Tesla (MRD170/1T). A parallel-plate (PP) geometry with diameter D=20 mm, truncation (gap) h=0.4 mm, and temperature T= 278.15 K was employed. The temperature stability was maintained with an external temperature control system (T-CS) paired with the MRD (2). Additionally, adhesive-backed, waterproof round shape sandpaper (180 grit) was attached to both the top and bottom plates to inhibit slip at the surface; immediately after, the zero-gap calibration was completed.

MAGNETORHEOLOGY OF HEAVY OIL-FERROFLUID MIXTURES.

The shear-strain amplitude oscillatory sweep tests were conducted in accordance with a standardized protocol, as follows: a thermodynamic stabilization of the sample was performed for 10 min at a constant temperature and a zero-shear rate, followed by a pre-shear consisting of subjecting the sample to a constant shear rate of 10 s^{-1} for 3 minutes; finally, a recovery stage was included, maintaining a zero-shear rate for 30 min. The same sample was submitted to three cycles of strain-sweep from 0.01 to 1000% at a constant oscillation frequency of 10 rad/s. Finally, the linear and non-linear responses were saved by RheoCompass™ Software and Option Raw Data provided by Anton Paar. A schematic representation of the protocol algorithm is shown in Figure 24.

Figure 24

Shear-strain-amplitude sweep protocol.

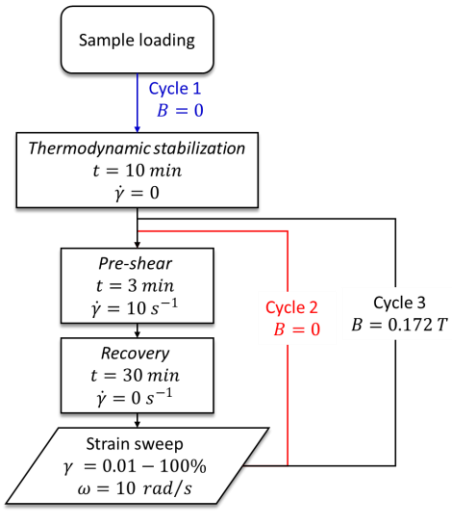

Each cycle involved the study of a fundamental aspect; therefore, the linear and non-linear behavior was initially measured in the absence of the magnetic field (B=0). In the second cycle (B=0), the analysis focused on the *steric hardening* (133) of bitumen, considering Lesueur's

insights on the time-dependent growth effect of the mechanical properties, which has been established that follows a power law and has been associated with the build-up of a stronger asphaltenes network. Finally, the effect of a perpendicular constant magnetic field (B ≠0) was evaluated.

For each test, the experimental first harmonic storage and loss dynamic moduli (G', G'') were plotted as a function of the shear-strain amplitude. Likewise, the elastic and viscous Lissajous-Bowditch 2D and 3D trajectories were plotted and analyzed by applying the sequence of physical (SPP) framework. The parameters of the SPP methodology were estimated by implementing the instant-use add-on function $FrenetSerretSystem[\langle x_1, \ldots, x_n \rangle, t]$ included in the Wolfram Language of Mathematica v. 13.2 software.

4.3.4 Physicochemical characterization

4.3.4.1 Nanoparticles

X-ray Diffraction - XRD pattern was acquired using a Bruker D8 Advance diffractometer with DaVinci geometry, in the range of 4-70° with a 2θ step of 0.020° and a sampling time of 3 s per step. Voltage and current were set at 40 kV and 40 mA, respectively. The qualitative analysis of the XRD pattern was carried out with the software Diffrac.EVA V.5.2.

^{57}Fe Mossbauer spectra at 300 K were taken in transmission geometry with a nominal 50 mCi ^{57}Co source in the Rh matrix driven by a triangular velocity wave.

4.3.5 Magnetometric characterization

A vibrating-sample magnetometer (VSM) with the physical properties measurement system (PPMS®, Quantum Design) was used to measure isothermal magnetization loops (M vs H) at different temperatures (50, 180, 250, 280, 300, and 320 K) in the H range between $-3 \cdot 10^4$

and $3 \cdot 10^4$ Oe, as well as the zero-field cooled (ZFC) and field-cooled (FC) magnetization curves over the temperature range 5-320 K with H=100 Oe.

4.3.5.1 Theoretical approaches of the isothermal magnetization curves M vs H

Although the fundamental focus of this research lies in studying the formation and reorientation of magnetic aggregates influenced by asphaltene adsorption; as a first approach, we employed the generalized asymptotic fitting method of ferrosolid magnetization at high magnetic fields proposed by Actis et al.,(325) which was derived from the partition function formalism and the Stoner-Wohlfarth model for single domain nanoparticles and, thus, magnetic dipolar interactions are neglected. We have chosen the ferrosolid model (instead of the ferrofluid one(276)) since nanoparticle anisotropy effects cannot be ignored in the case of fluids with high enough viscosity, as it happens in our case. The expressions obtained for poly-sized ferrosolids with randomly oriented magnetic nanoparticles (FSR) in terms of the applied magnetic field are shown in Eq. 39 and 40 for low (LF) and high (HF) magnetic fields, respectively.

$$\textbf{LF} \qquad M_{FSR}^{P}(H) \approx n\langle\mu\rangle(\mu_0 H/3k_B T)(\langle\mu^2\rangle/\langle\mu\rangle) = (n\langle\mu^2\rangle/3k_B T)\boldsymbol{\mu_0 H} \tag{39}$$

$$\begin{aligned} M_{FSR}^{P}(H) \approx n\langle\mu\rangle\Big[1 - \big((k_B T/\langle\mu\rangle)(\mathbf{1}/\boldsymbol{\mu_0 H})\big) - \Big((4/15)\big(K_{eff}/M_S\big)^2\big(\mathbf{1}/(\boldsymbol{\mu_0 H})^2\big)\Big) \\ \textbf{HF} \qquad + \Big(\Big((4/3)(k_B T/\langle\mu\rangle) \\ - \big((16/105)\big(K_{eff}/M_S\big)\big)\Big)\big(K_{eff}/M_S\big)^2\big(\mathbf{1}/(\boldsymbol{\mu_0 H})^3\big)\Big)\Big] \end{aligned} \tag{40}$$

where, n is the particle density, μ_0 the vacuum permeability, k_B the Boltzmann constant, H the magnetic field strength, T the temperature, $\langle\mu\rangle$ the mean magnetic moment, and $\langle\mu^2\rangle$ the mean square magnetic moment.

For the purposes of this investigation, we have employed the truncated expression up to H^{-2}, which is an accurate and common approximation reported in the literature (326, 327).

4.3.5.2 Theoretical derivation of the susceptibility (χ) and coercivity (H_c) of a distribution of monodomain nanoparticles

In this research, the log-normal distribution function of the magnetic-core diameter (D_N) polydispersity histogram of the EMG-1300M nanoparticles, as fitted by Contreras-Mateus *et al.* (3) using TEM (Table 12), was integrated into the below-derived expressions.

Table 12

Parameters of the $\boldsymbol{P(D_i)}$ log-normal distribution function (3).

$\boldsymbol{P_N(D_i) = P_0 + \left(A/\left(\sigma D_i\sqrt{2\pi}\right)\right)e^{\left(\left(-\ln(D_i/D_N)\right)^2\right)/(2\sigma^2)}}$			
$\boldsymbol{P_0}$	$\boldsymbol{A}$	$\boldsymbol{\sigma}$	$\boldsymbol{D_N}$ $[\boldsymbol{nm}]$
4.14 ± 6.40	749.67 ± 44.97	0.23 ± 0.02	9.43 ± 0.14

Defining $P_N(D_i)$ as the number distribution function, and $P_V(D_i)$ as the volume distribution function, as shown in Eq. 41 and 42.

$$P_N(D_i) = N_i/N_m \tag{41}$$

$$P_V(D_i) = (N_i V_i)/V_m \tag{42}$$

where, N_i are the number of particles with diameter D_i, $V_i = \pi D_i^3/6$ the volume of a particle with diameter D_i, $N_m = \sum_i N_i$ and $V_m = \sum_i N_i V_i$ are the total number and volume of particles, respectively.

Now, focusing on the vicinity of the magnetic coercivity field (H_{Ci}), the magnetization $\big(M_i(H)\big)$ can be approximated to a linear expression as depicted in Eq. 43.

$$M_i(H) = \chi_i H + \alpha_i \tag{43}$$

At $H = H_{Ci}$, $M_i = 0$, thus $\alpha_i = -\chi_i H_{Ci}$; where, H_{Ci}, χ_i, α_i are the magnetic coercivity, susceptibility, and remanence of particles with volume V_i; respectively.

In this region of interest, the magnetic moment of the nanoparticle's distribution can be defined as established in Eq. 44.

$$\begin{aligned}\mu(H,T) &= \sum_i N_i V_i M_i(H,T) = H\sum_i N_i V_i \chi_i(T) - \sum_i N_i V_i H_{Ci}(T)\chi_i(T) \\ &= \sum_i \big(H - H_{Ci}(T)\big) N_i V_i \chi_i(T)\end{aligned} \tag{44}$$

On the other hand, $d\mu(H,T)/dH = V_m\chi(T)$, then, $\chi(T)$ can be deduced from Eq. 44, as illustrated in Eq. 45.

$$\chi(T) = \sum_i P_V(D_i)\,\chi_i(T) \tag{45}$$

Furthermore, $H_C(T)$ corresponds to the condition $\mu(H,T) = 0$, thus,

$$0 = \sum_i \big(H_C(T) - H_{Ci}(T)\big) N_i V_i \chi_i(T) = V_m \sum_i \big(H_C(T) - H_{Ci}(T)\big) P_V(D_i)\chi_i(T)$$

$$H_C(T) = \left(\sum_i H_{Ci}(T) P_V(D_i)\chi_i(T)\right) \Big/ \left(\sum_i P_V(D_i)\chi_i(T)\right) \tag{46}$$

Eq.46 shows that the coercivity of a polydisperse nanoparticle sample can be estimated as an average of the coercivities of each size weighed with the products of the volume probabilities by the low-field susceptibilities.

MAGNETORHEOLOGY OF HEAVY OIL-FERROFLUID MIXTURES.

In the extended Stoner-Wohlfarth model at finite temperature, below the blocking temperature T_{Bi}, the non-interacting nanoparticles with diameter D_i have a coercivity field, as shown in Eq 47 (61, 328).

$$H_{Ci}(T) = H_C(0)\left[1 - \left((k_B T/KV_i)\left(\ln\left(\tau_{exp}/\tau_0\right)\right)\right)^m\right], T \le T_{Bi} \quad (47)$$

where, K is the average magnetic anisotropy constant, τ_{exp} the measurement time of the experiment, τ_0 is a constant of the order of ~10^{-9} s for ferromagnetic and ferrimagnetic materials $\left(\ln\left(\tau_{exp}/\tau_0\right) \approx 25\right)$ taken from the Quantum Design VSM, m is an exponential factor in the range of 1/2-3/4 (61, 329, 330), $T_{Bi} = (KV_i)/\left(k_B \ln\left(\tau_{exp}/\tau_0\right)\right)$ is the blocking temperature corresponding to the nanoparticles of size D_i. For $T > T_{Bi}$, it can be assumed that $H_{Ci}(T) = 0$, considering that the nanoparticles of volume V_i have already reached the equilibrium.

Likewise, at low-field condition, nanoparticles susceptibility can be approximated using Eq 48.

$$\chi_i(T) = \mu_0\left[\left(\left(M_s(T, D_i)\right)^2 V_i\right)/(3k_B T)\right] \quad (48)$$

Thus, Eq. 45 and 46 can be expressed as,

$$\chi(T) = (\mu_0/(3k_B T))\sum_i \left(M_s(T, D_i)\right)^2 V_i P_V(D_i) \quad (49)$$

$$H_C(T) = H_C(0)\left[1 - \left(\left(\sum_i \left(M_s(T, D_i)\right)^2 V_i P_V(D_i)\left((k_B T/KV_i)\left(\ln\left(\tau_{exp}/\tau_0\right)\right)\right)^m\right)\Big/\left(\sum_i \left(M_s(T, D_i)\right)^2 V_i P_V(D_i)\right)\right)\right] \quad (50)$$

We have assumed the $M_S(T, D_i)$ dependency, as shown in Eq. 51.

$$M_S(T, D_i) = M_{S-\infty}(T)(1 - e^{(-D_i/D_c(T))}) \quad (51)$$

where, $M_{S-\infty}(T) = M_{S-\infty}^{300} f(T)$; $f(T)$ is a normalized exponential ad-hoc function of the experimental saturation magnetization values $M_{S-exp}(T)$ with respect to $M_{S-exp}(300\,K)$, $M_{S-\infty}^{300}$ is the bulk saturation magnetization at 300 K, $D_c(T)$ is a size parameter that defines the curvature of the function per each temperature, and it was calculated to accomplish the condition that the mean value $\langle M_S(D_i)\rangle \approx M_{S-exp}(T)$, as established in Eq. 52.

$$\langle M_S(D_i)\rangle = \left(\sum_i M_s(T, Di) P_V(D_i)\right) \Big/ \left(\sum_i P_V(D_i)\right) \approx M_{S-exp}(T) \tag{52}$$

4.4 Results and Discussions

4.4.1 LAOS characterization

In Figure 25, the first-harmonic dynamic moduli $(\mathrm{G}', \mathrm{G}'')$ of $C_{1\text{-}5}$ sample are depicted as functions of strain amplitude (γ); as expected, the system presents the typical liquid-like behavior of colloidal suspensions at low concentration (below the glass transition volume fraction), exhibiting $\mathrm{G}'' > \mathrm{G}'$ in the γ spectrum (331, 332). Furthermore, the well-discussed steric hardening of bitumen was validated in the second cycle. This phenomenon is characterized by a heat-reversible hardening effect, attributed to the gradual formation of stronger asphaltene networks over time (133). To highlight, a rotation of the Lissajous-Bowditch curves between each cycle was also observed (Figure 26), which could be associated with the time-dependency (thixotropy) of the sample.

In the presence of the magnetic field (B ≠0), on the other hand, it can be noted a more significant increase in the moduli, particularly in G'. This observation aligns with the findings of a previous study, which already demonstrated this effect (inset of Figure 25) (3).

MAGNETORHEOLOGY OF HEAVY OIL-FERROFLUID MIXTURES.

In line with the analysis approach adopted in other investigations (300, 324), we have directed our focus towards examining the stress ($\sigma(t)$) response of the material under two different strain amplitudes ($\gamma_i = 6.31\%$ and $\gamma_j = 63.1\%$) and angular frequency of ω=10 rad/s, encompassing MAOS (medium-amplitude oscillatory shear) and LAOS regimes. From the former, Figure 26(A and B) shows nearly elliptical Lissajous curves elicited by $C_{1\text{-}5}$; this result was supported by the absence of inflection points, as described by the second derivative of the parametric function $\sigma(\gamma)$, represented in Figure 27A. The Lissajous-Bowditch curves further elucidated the influence of the magnetic field (represented by the solid black curve), as the ellipses extend more prominently along the σ-axis. By implementing the quantitative analysis of the time-dependent SPP metrics represented by the parametric plot of $\omega\eta_t$ vs G_t (Figure 28A), it is observed that the deltoid trajectories reside in the predominantly viscous zone (above the line $\omega\eta_t = G_t$) for the three cycles, and encompass values that closely approximate the first harmonic ($G' = 290.16, 331.7, 408.77$ Pa and $G'' = 497.51, 602.06, 772.02$ Pa; respectively). These observations, according to Park and Rogers (324), suggest that the sample may experience subtle intra-cycle structural-rheological transitions, which can be attributed to sequential changes involving, disruption of soft chain structures, reinforcement of soft chain structures leading to viscous dissipation, and weakening of slightly rigid structures contributing to viscous dissipation. It is also worth noting that, in the B≠0 cycle, the deltoid is displaced towards higher values along both axial axes, emphasizing the potential influence of the magnetic field on the naturally formed aggregates within the system.

Figure 25

Dynamic moduli, $\boldsymbol{G'}$ *and* $\boldsymbol{G''}$ *depicted by* $C_{1\text{-}5}$*, at frequency* $\boldsymbol{\omega = 10\ rad/s}$ *and temperature* $\boldsymbol{T = 278.15\ K}$*, applying three cycles, in the absence of the magnetic field B=0 (blue), steric hardening cycle B=0 (red), and B ≠0 (black). The inset shows time dependency of* $\boldsymbol{G'}$ *and* $\boldsymbol{G''}$ *measured at* $\boldsymbol{T = 288.15\ K}$*,* $\boldsymbol{\omega = 10\ rad/s}$*,* $\boldsymbol{\gamma = 1\%}$*, a pulse of magnetic field (B=0.094 T) was applied between 5-10 min, the axis on the right represents the relative changes* $\boldsymbol{\delta G'/G'}$ *and* $\boldsymbol{\delta G''/G''}$*; adapted from (3).*

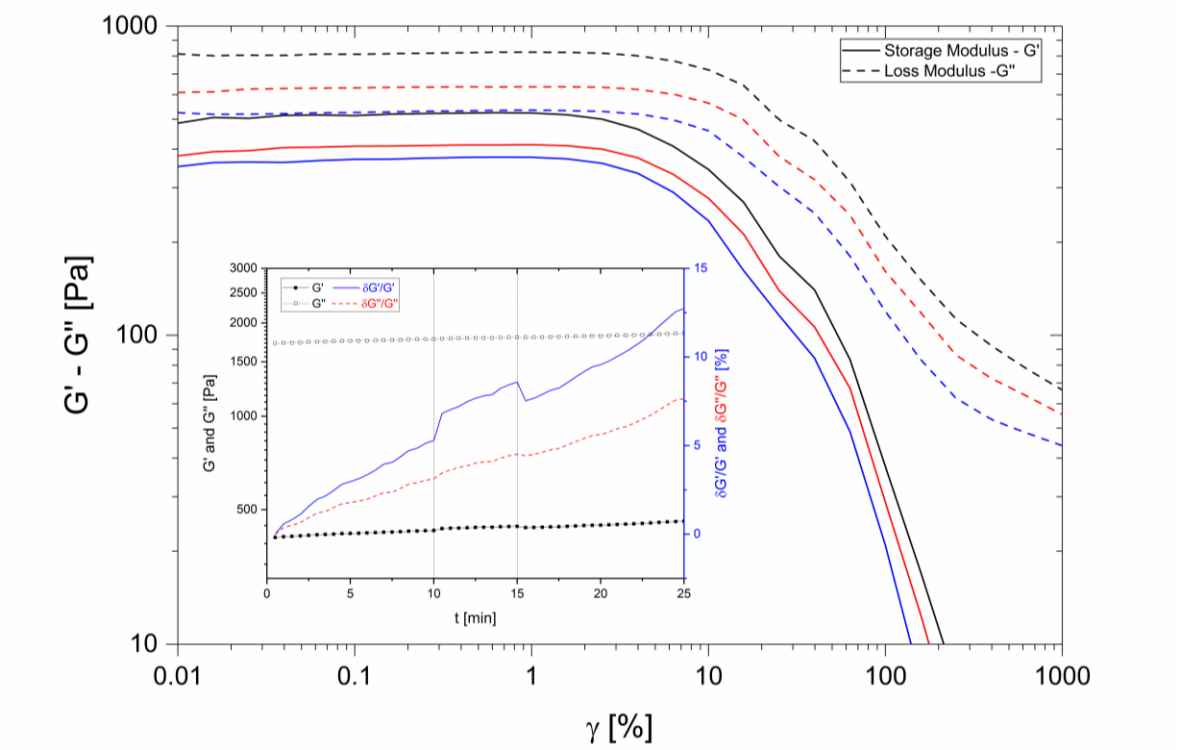

Under LAOS regime, the Lissajous-Bowditch curves exhibit nonelliptical trajectories, as illustrated in Figure 26(C and D). Similarly, in the presence of the magnetic field B≠0, a slight extension of the cycle area along σ-axis was evidenced. Nevertheless, an intriguing distinction between the cycles becomes apparent when estimating the second derivative of the parametric

function $\sigma(\gamma)$. In the absence of the magnetic field, B=0, a slight alteration in concavity was observed, indicated by the change in sign of $\partial^2\sigma/\partial\gamma^2$ (Figure 27B, blue and dashed red curves). In contrast, this inflection point was absent in the B≠0 cycle. These observations were substantiated by the SPP metrics shown in Figure 28B; only in the absence of field, the deltoid curve exhibited a transition from $\omega\eta_t < 0$ to $\omega\eta_t > 0$, while $G_t \sim 0$ (light blue and light red curves in the region close to the origin). As stated by Park and Rogers (324), this behavior is identified as viscoplastic deformation, which can be interpreted as a rheological manifestation of the broken network structure with a lack of a rigid chain structure. Conversely, in the presence of the field B≠0, the deltoid trajectory is localized on $\omega\eta_t > 0$. It was also distinguished sequential processes involving, i) recovery of the network structure, fundamentally, in the B=0 cycles, described as a transition from viscoplastic to viscoelastic behavior ($G_t: \sim 0 \rightarrow \max(G_t)$, and $\omega\eta_t: \min(\omega\eta_t) \rightarrow \omega\eta_t \gg 0$); ii) early stage yielding with stretching and rupture of a few bonds in the three cycles, understood as a transition from elastic to viscous behavior ($G_t: \max(G_t) \rightarrow \min(G_t)$, and $\omega\eta_t: \omega\eta_t \gg 0 \rightarrow \max(\omega\eta_t)$), and iii) late stage yielding accompanying catastrophic network structure failure, fundamentally, in the B=0 cycles, explained as a transition from a soft chain structure to individual particles and small flocs ($G_t: \min(G_t) \rightarrow \sim 0$, and $\omega\eta_t: \max(\omega\eta_t) \rightarrow \min(\omega\eta_t)$) (324). We further emphasize that the deltoid trajectories are elicited mainly in the viscous zone (above $\omega\eta_t = G_t$) in the three cycles, suggesting that the formed structures are predominantly soft in nature, i.e., short-chains in terms of the rigidity theory (324, 333). These statements were reinforced with the 2D parametric space representation of $\omega\eta_t$ vs G_t at 10 rad/s, displaying the amplitude sweep data (Figure 29), as suggested by Choi *et al.* (300). It is observed from Figure 29 that, the deltoids change their orientation and size when increasing the strain amplitude; likewise, the extent of the

area occupied by the deltoids serves as a direct indication of the multiple instantaneous viscoelastic states experienced by the material. In contrast to the average values of the SPP metrics (G', G''), the expansive ranges attained by the sample offer a more distinct representation of the linear and non-linear viscoelastic properties. For illustrative purposes, the region occupied by the deltoids in the absence of the magnetic field has been shaded, proving that the magnetic field contributes to the stiffness and thickening of the sample in the whole range of γ spectrum.

Finally, it is observed that the stress waveform transitioned from a weakly sharp "saw-tooth" shape to a rounded-end rectangular shape, due to the influence of the magnetic field. Hyun *et al.* (301, 334) previously presented a comprehensive analysis of the type and spatial distribution of structures formed in complex fluids, focusing on the stress waveform characteristics. By way of illustration, the authors proved that a 4 wt.% aqueous solution of Xanthan gum forming a disordered and extended weakly gel-like structure, described a saw tooth shape of stress; while a hard gel formed by a poly(ethylene oxide)–poly(propylene oxide)–poly(ethylene oxide) (PEO–PPO–PEO) 20 wt.% solution, characterized by a close-packed arrangement of micelles, displayed stress waveforms with rectangular profiles. Against this background, the results provide compelling evidence that the magnetic field influences the size and spatial orientation of the isotropic natural-formed aggregates. Accordingly, these formed field-aligned anisometric short-chain structures actively oppose the flow, leading to a sudden increase in the mechanical properties, a phenomenon that has been previously proven by in-situ small-angle scattering techniques using small-angle X-ray scattering (SAXS) and small-angle neutron radiation (SANS) (335-337). It is also noteworthy to highlight that, a few works have studied the non-linear rheological properties using magneto-rheological fluids (338-341), although in this case, the

particles are micron-sized and the structures formed can be column-like (even, branched intricate network (341)) with hundreds of orders of magnitude larger. Some of them have established that the intracycle elastic nonlinearity seems to be more affected by the magnetic field (338, 340). Furthermore, a few investigations employing magneto/electro rheological (MR/ER) suspensions, have also observed a transition of the elastic Lissajous-Bowditch curves from ellipse to rounded-end rectangular-like form, due to the effect of higher magnetic/electric fields (340-342). The physical explanation of the shape suggests a viscoplastic behavior of the suspension. As the strain gradually increases, the stress levels remain stable until the structure reaches its yield point. However, upon reversing the direction of strain, the stress is rapidly released (341, 343).

While it is reasonable to expect that the magnetic structures formed in our system should reach a size of a few hundred nanometers, and although a direct comparison to MR fluids should not be feasible; we highlight that some additional physical-attractive phenomena, such as interdigitation of the adsorbed asphaltenes, may contribute to the formation of even larger size aggregates (3). However, further investigation is required. Finally, it seems important to mention that, to the best of our knowledge, the utilization of LAOS techniques and the SPP approach with nano-magnetic suspensions (or ferrofluids) has not been reported in the existing literature.

Figure 26

A. Elastic Lissajous-Bowditch (e L-B) curve, and B. Viscous Lissajous-Bowditch (v L-B) in MAOS regime ($\boldsymbol{\gamma = 6.31\%}$). C. e L-B curve, and D. v L-B curve in LAOS regime ($\boldsymbol{\gamma = 63.1\%}$). Three cycles were applied on $C_{1\text{-}5}$, in the absence of magnetic field B=0 (blue), steric hardening cycle B=0 (red dashed), and under a magnetic field B =0.172 T (black).

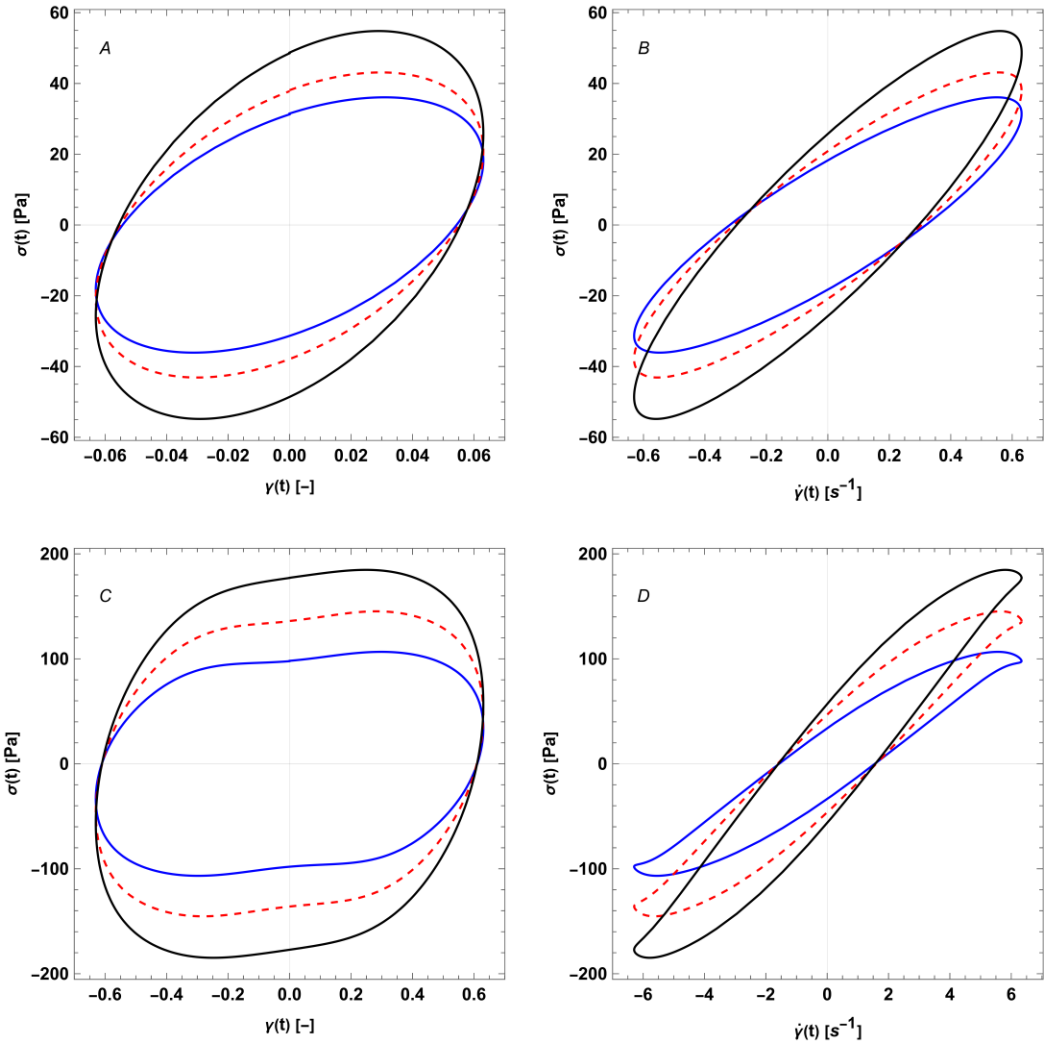

Figure 27

Parametric plot of $\frac{\partial^2 \tau}{\partial \gamma^2}$ *vs* $\boldsymbol{\gamma}$ *in A. MAOS, and B. LAOS regimes. Three cycles were applied on* $C_{1\text{-}5}$*, in the absence of magnetic field B=0 (blue), steric hardening cycle B=0 (red dashed), and B =0.172 T (black).*

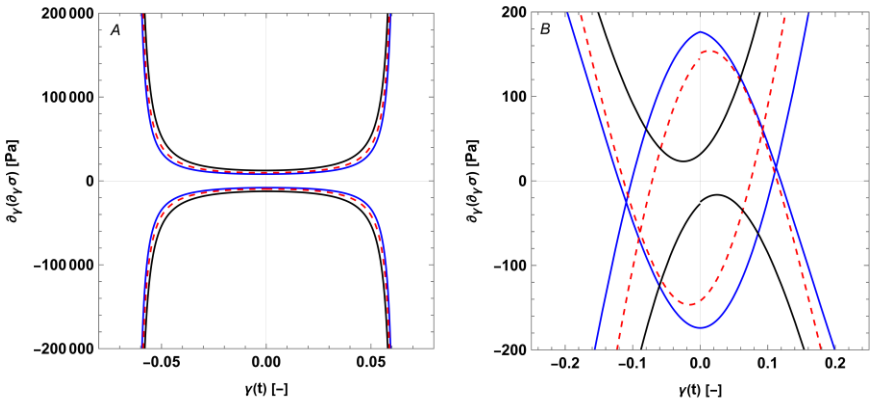

Figure 28

Two-dimensional visualization of viscoelastic SPP metrics, represented by the parametric plot of $(\boldsymbol{\omega \eta_t})$ *vs* $(\boldsymbol{G_t})$ *in A. MAOS, and B. LAOS regimes. Three cycles were applied on* $C_{1\text{-}5}$*, in the absence of magnetic field B=0 (blue), steric hardening cycle B=0 (red dashed), and B =0.172 T (black).*

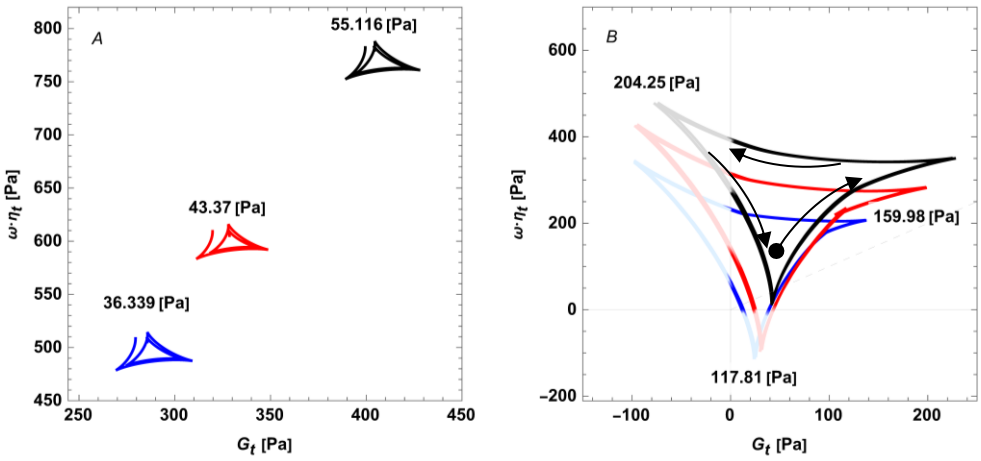

Figure 29

Enhanced strain amplitude sweep in the parametric space ($\boldsymbol{\omega\eta_t}$) vs ($\boldsymbol{G_t}$) at 10 rad/s, A. In the absence of the magnetic field B=0 (cycle 1), and B. in the presence of the magnetic field B =0.172 T. (red dots represent the first harmonic dynamic moduli)

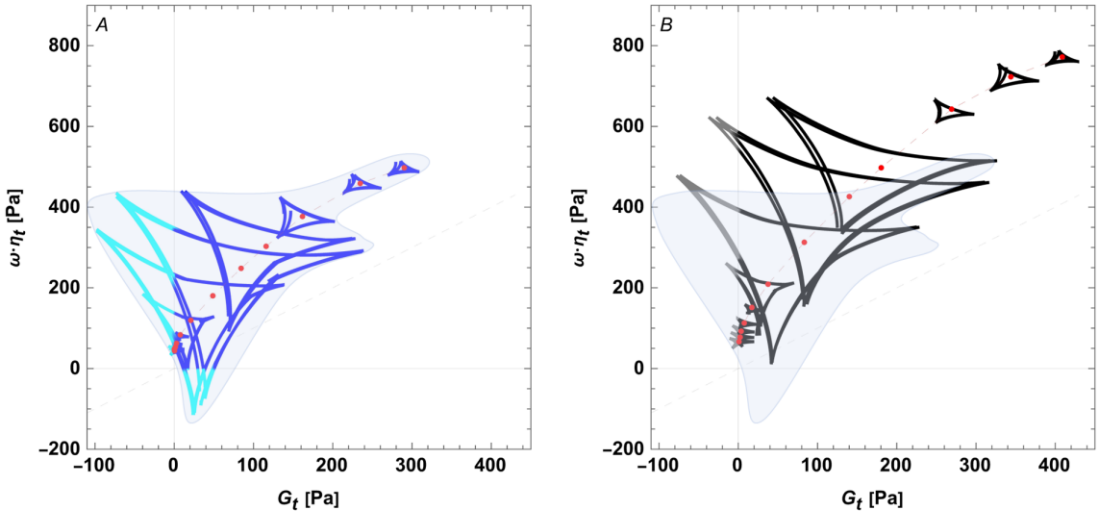

4.4.2 Physicochemical characterization

Figure 30

Nanoparticles XRD patterns.

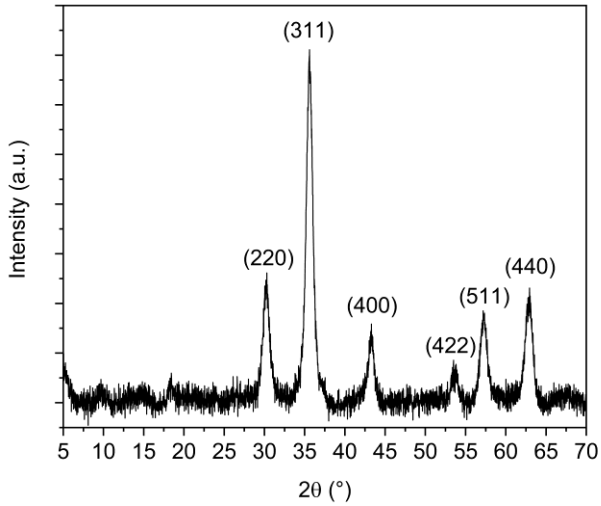

The analysis of the XRD pattern confirmed the presence of magnetite with cubic cell (space group Fd-3m) as the only phase in the nanoparticles, corresponding to the PDF 01-071-6337. As it is noted in Figure 30, the pattern is composed of broad peaks, which is consistent with nanometric samples. Furthermore, the crystallite size was estimated by using the Scherrer equation (Eq. 53) (344).

$$L = \frac{K\lambda}{\beta * \cos\theta} \tag{53}$$

where, L is the crystallite size, K is a shape factor, taken in this work as 0.9, λ is the X-ray wavelength in nm (i.e., 0.15406 nm), β is the line broadening at half the maximum intensity (Full Width Half Maximum-FWHM) at the corresponding diffraction angle θ. Estimations of the crystallite size were made using the signals located at 2θ = 30.2, 35.6, 75.2, and 62.9°, and the obtained values are exhibited in Table 13.

Correspondingly, the average crystallite size was found to be 8.6 ± 0.4 nm. This result agrees with the particle size estimated by Contreras Mateus *et al*. (3) from TEM and suggests that each nanoparticle is composed of a single magnetite crystal.

Table 13

Parameters for crystallite size calculations using the Scherrer equation.

Peak indices	**hkl**	**2θ position**		**FWHM**	**Crystallite size**
		°	**Radians**	**Radians**	**nm**
220		30.23±0.0120	(5.276±0.0021) $\cdot 10^{-1}$	0.0179±0.0005	8.002±0.2220
311		35.61±0.0039	(6.214±0.0007) $\cdot 10^{-1}$	0.0177±0.0002	8.245±0.0758
511		57.25±0.0165	(9.992±0.0029) $\cdot 10^{-1}$	0.0175±0.0007	9.044±0.3526
440		62.86±0.0134	(10.97±0.0023) $\cdot 10^{-1}$	0.0182±0.0006	8.933±0.2724
			Average		8.6 ± 0.44

Figure 31

Mössbauer effect spectrum. The inset represents an approximate correlation between sub-spectra and nanoparticle sizes. To obtain this correlation, Néel relaxation times were calculated at 300 K using values of τ_0, K_{eff}, and V presented in this work. Relaxation times have been tentatively assigned to the sub-spectra within the frame of H.H Wickman results.(345)

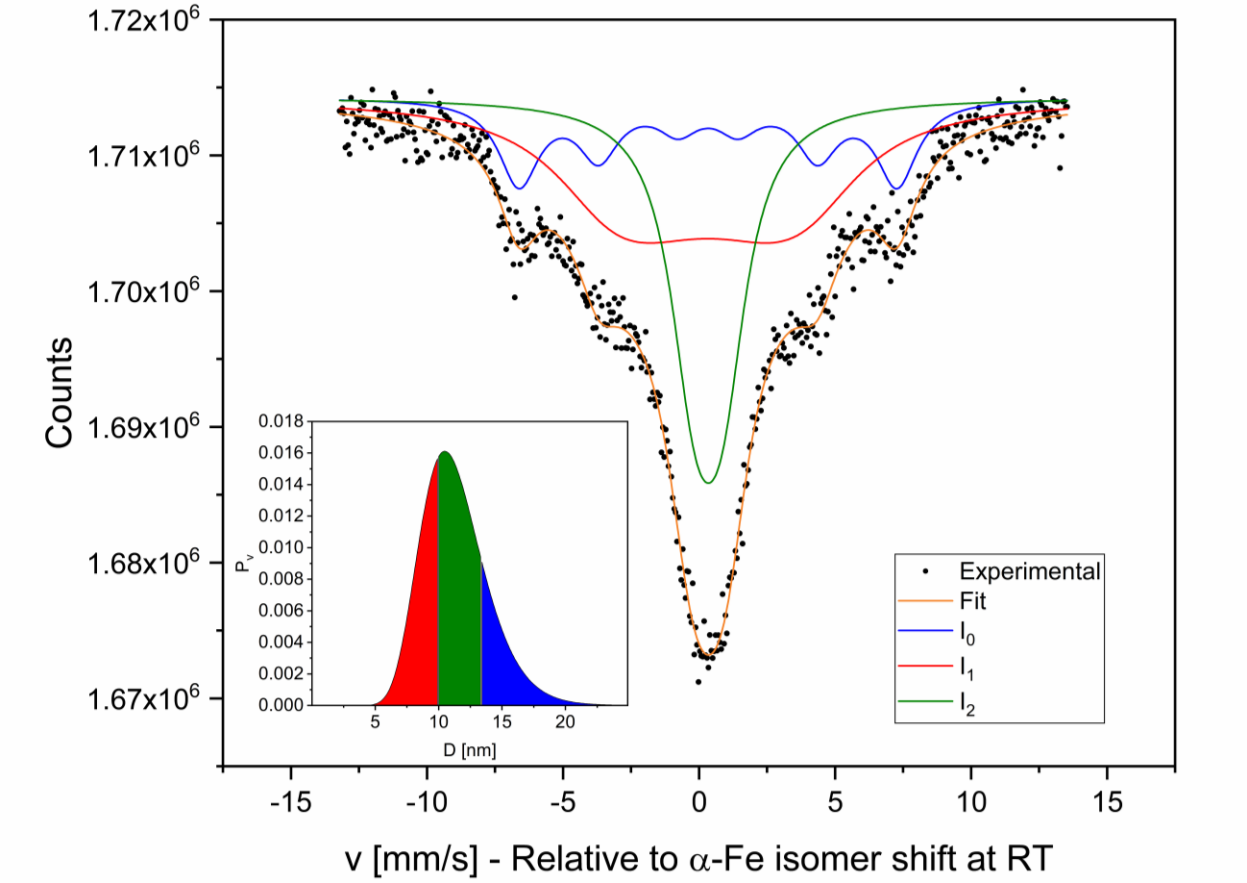

The nanoparticles powder was mildly grounded to facilitate absorber preparation. Then, 39 mg of the ground powder was uniformly distributed in a sample holder of 2 cm inner diameter, producing an absorber of mass thickness $t' = 0.012$ g/cm^2. The number of Mössbauer isotope nuclei per mass unit was estimated from magnetite density and crystal structure data, as 1.75×10^{20} g^{-1}, and the effective thickness was calculated as $t = 3.9$.

The Mössbauer spectrum spans from about -10 mm/s to 10 mm/s and presents evidence for strong magnetic relaxation. The effect of atomic moment relaxation is a fast fluctuation of the hyperfine field at the probe sites and gives rise to the rather smooth spread of the resonant absorption. Consequently, the maximum absorption relative to the spectrum background is about 0.023. Hence, saturation effects can be disregarded, even when effective thickness does not match the condition $t << 1$.

The three sub-spectra drawn in different colors are an attempt to interpret the result in terms of the nanoparticle size distribution. The blue sub-spectrum accounts for 20.3 % of the spectral area and presents the sextet structure of a rather well-defined magnetic hyperfine interaction, with a mean magnetic hyperfine field value B_{hf} = 43.2(2) T, and isomer shift $\delta = 0.33(3)$ mm/s. The orange one shows a much stronger relaxation effect. Individual sextet lines are so much broadened that they cannot be distinguished from each other, although the left and right parts of the sextet still can be guessed. It corresponds to mean hyperfine parameters B_{hf} = 23(2) T and $\delta = 0.32(1)$ mm/s. The green one presents the strongest relaxation. The model used corresponds to a magnetic interaction with B_{hf} = 4.2(3) T and $\delta = 0.34(1)$ mm/s. Following H.H. Wickman (345), these sub-spectra correspond to Néel relaxation times between 10^{-9} and 10^{-8} s. Hyperfine fields are gradually reduced with respect to the values of 45.8 – 49.9 found at RT in magnetite/maghemite (as relaxation time decreases) due to the increasing averaging of opposite values.

The mean isomer shift of the whole spectrum obtained averaging the isomer shift of the three contributions with their spectral areas is $\delta_m = 0.33(1)\ mm/s$, indicating that almost all Fe ions are in a +3-charge state. Fock *et al.* (346) have provided an expression to determine the degree

of magnetite-like character of a magnetic spinel Fe oxide, from its δ_m value. In our case, this criterion indicates that the nanoparticles are 96% maghemite-like.

Based on the observed differences between X-Ray and Mössbauer analyses, the literature recognizes the complexity and ambiguity in distinguishing magnetite (F_3O_4) and maghemite (γ-Fe_2O_3) using X-ray crystallography (346, 347). Even in its fully oxidized state, maghemite can exhibit a range of structures, with the most common being the cubic *Fd-3m* space group, which is also shared by magnetite. In this structure, vacancies are randomly distributed. Additionally, maghemite may adopt the cubic $P4_132$ space group, where vacancies are partially ordered, or the tetragonal $P4_32_12$ space group, with fully ordered vacancies. The close resemblance between the *Fd-3m* and $P4_132$ structures poses challenges in accurately differentiating the phases based solely on crystallographic characteristics (346, 348). Kim *et al.* (347) proposed a quantitative complementary method for assessing the presence of a magnetite-maghemite mixture. Their approach involves peaks deconvolution, focusing particularly on the (440) and (511) high-angle peaks, which enables the identification of characteristic doublets indicative of the presence of both phases in the mixture. Applying the method, the presence of a single peak at 57.25 ± 0.016° was observed in (511), closely aligning with the value defined by the authors as the maghemite peak (57.3°). Accordingly, the absence of the characteristic (210) and (211) peaks of the maghemite in Figure 30 is not a sufficient criterion for phase identification. The above validates the deconvolution method, and, essentially, Mössbauer spectroscopy as one of the most reliable quantitative data.

4.4.3 Magnetometric characterization

4.4.3.1 Isothermal magnetization curves

The asymptotic LF (Eq. 39) and HF (Eq. 40) expressions of the FSR model were fitted to the anhysteretic magnetization curves of $C_{1\text{-}5}$ sample at different temperatures. These anhysteretic curves were constructed applying the procedure proposed by Allia *et al.* (349), to facilitate the analysis. For the temperature range between 180 – 320 K, the measured magnetization and anhysteretic curves are virtually identical. However, at 50 K, the magnetization loop exhibited a small coercivity of 1600 A/m, which justified the analysis of the anhysteretic curve by the equilibrium models as the FSR.

We also defined the ranges of magnetic field for these expressions, verifying that the ratio of $\left((4/15)\left(K_{eff}/M_S\right)^2(1/(\mu_0 H)^2)\right)/\left((k_B T/\langle\mu\rangle)(1/\mu_0 H)\right)$ should lie in values that provide relevant information on the parameters accompanying H^{-2} term (*i.e.*, K_{eff}). As shown in Eq. 54 (325).

$$\mu_0 H \gg (4/15)\left(K_{eff}/M_S\right)^2(\langle\mu\rangle/k_B T) = \mu_0 H_1 \tag{54}$$

The H_1 estimated values remain between 98-147 $kA\cdot m^{-1}$ at the studied temperatures. On the other hand, this expression is a good approximation of the actual magnetization curve at high enough fields, thus, as a compromise, the HF expression was fitted at $H \geq |390|$ $kA\cdot m^{-1}$.

By way of illustration, Figure 32 and Figure 33 depict the LF and HF fitted curves at 300 K, as well as the adjusted parameters, which correspond to the average of both magnetization branches.

Figure 32

Experimental values and low-field (LF) fitting of the FSR model.

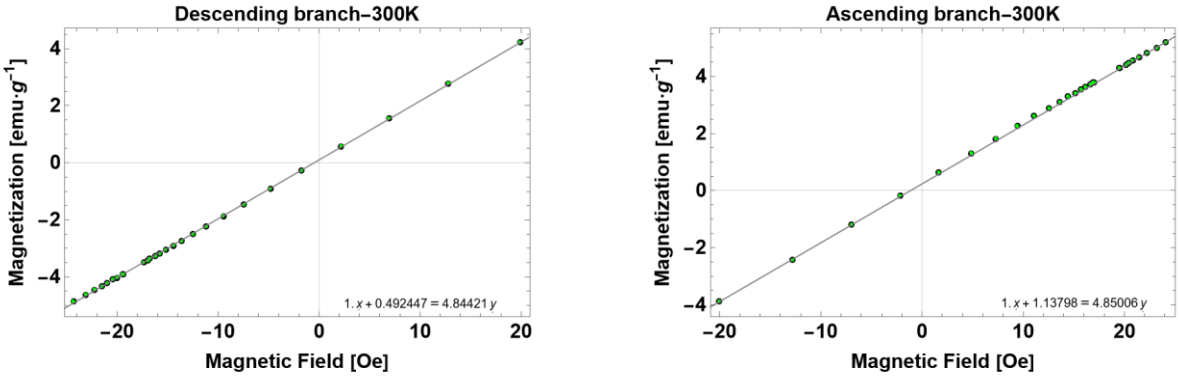

Figure 33

Experimental values and high-field (HF) fitting of the FSR model (up to H^{-2}). The blue and red curves of the right are the zoom of the fitted HF interval.

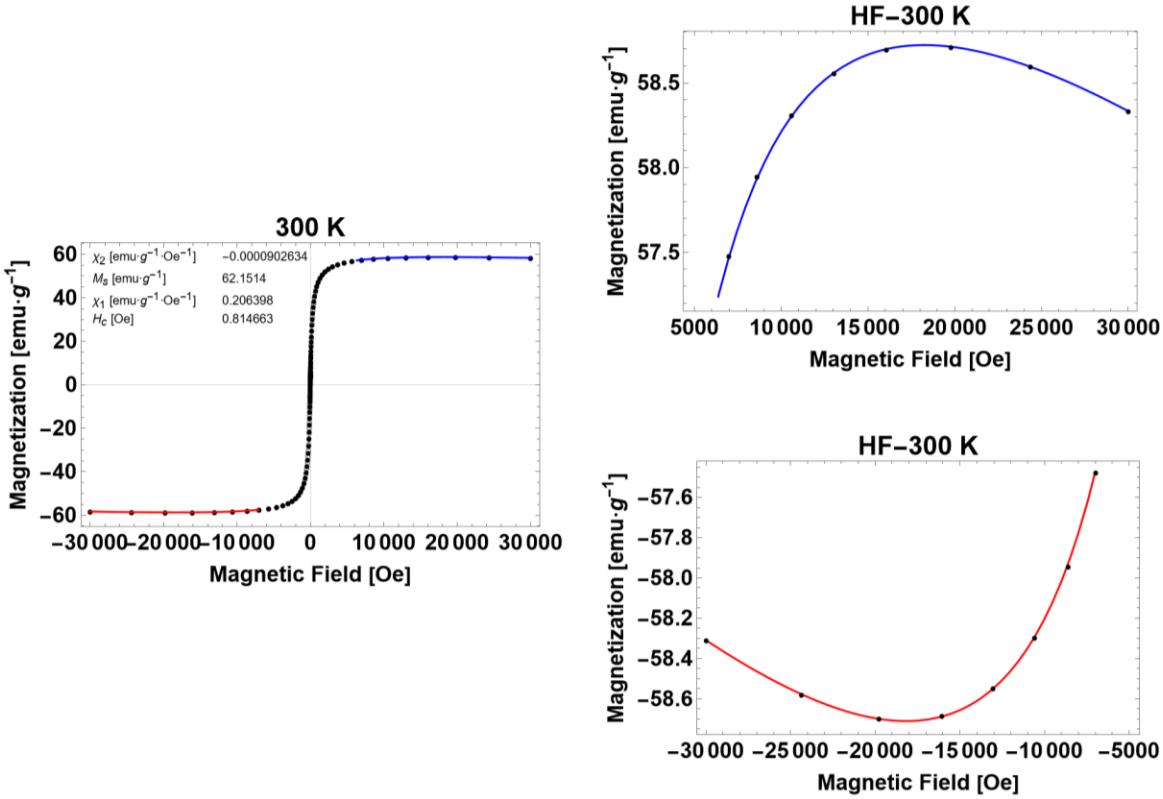

MAGNETORHEOLOGY OF HEAVY OIL-FERROFLUID MIXTURES.

Figure 34 summarizes the complete set of the estimated parameters as a function of the temperature; whose range of values, fundamentally for $M_s, \kappa, H_C, \langle\mu\rangle$ (Figure 34 B,C,D,F), aligns closely with those reported in the existing literature (279, 350, 351). We have implemented the notation of κ for the apparent (measured) susceptibility. A second sample at a lower nanoparticle concentration (C_{11}, 0.8 wt.%) was included for comparative purposes (filled plot markers), as expected, the mean nanoparticle magnetic moment was higher with C_{11}, $\langle\mu_{corr}\rangle$, which is compelling evidence of the formation of aggregates under the influence of the magnetic field as the nanoparticles concentration increases; as previously established by Kechrakos and Trohidou (352) and theoretically proved by other authors (349, 353). According to the conclusions drawn by Allia *et al.*, (349) the magnetization curve for an assembly of interacting moments can still be represented by a distribution of equilibrium functions (*i.e.*, Langevin functions when anisotropy can be disregarded), with the proviso that the estimated susceptibility, and particle magnetic moment and size are lower than the actual values. Indeed, the model for magnetic dipolar interactions (ISP) formulated by Allia et al. is founded on the assumption of an apparent moment (μ_a) and particle density (n_a) in the fitted M(H) function, as depicted in Eq. 55 and 56, which justifies the functional dependence of n (Figure 34E) on temperature. For example, for monodisperse nanoparticles,

$$M = n\mu L(\alpha_a) \tag{55}$$

$$\mu_a = \left(1/\left(1 + (T^*/T)\right)\right)\mu;\ n_a = (1 + (T^*/T))n \tag{56}$$

$L(\alpha) = \coth\alpha - (1/\alpha)$ is the Langevin function, where $\alpha = \mu_0\mu H/k_B T$ for a superparamagnetic assembly of identical and non-interacting moments of magnitude μ. In the ISP formulation, on the other hand, the argument of the Langevin function is modified by an apparent

temperature, defined as $T_a = T + T^*$, where T* is related to the dipolar energy ε_D. Thus, $\alpha_a = \mu_0\, \mu H / k_B (T + T^*)$. Allia's model was later improved by the MFISP one, which introduces the concept of an effective demagnetizing tensor to explain the effects of the interparticle dipolar interactions (267).

Figure 34

Set of estimated parameters of the FSR model (Eq. 39 and 40) for $C_{1\text{-}1}$ and $C_{1\text{-}5}$ (empty plot markers) samples.(325) A. The ratio of the effective anisotropic constant and the saturation magnetization ($\boldsymbol{K_{eff}/M_S}$), B. the saturation magnetization of the magnetic-core phase ($\boldsymbol{M_S}$), C. Ferromagnetic susceptibility of the magnetic-core phase ($\boldsymbol{\kappa}$), D. The coercivity field ($\boldsymbol{H_C}$), E. The number of particles per volume unit in the sample. ($\boldsymbol{n}$), and F. The corrected magnetic moment was calculated by approximating the particle density by its value at 320 K, at which the effect of interactions is the lowest, i.e., $\langle \boldsymbol{\mu_{corr}(T)} \rangle = \langle \boldsymbol{\mu sample(T)} \rangle / \boldsymbol{n(320)}$.

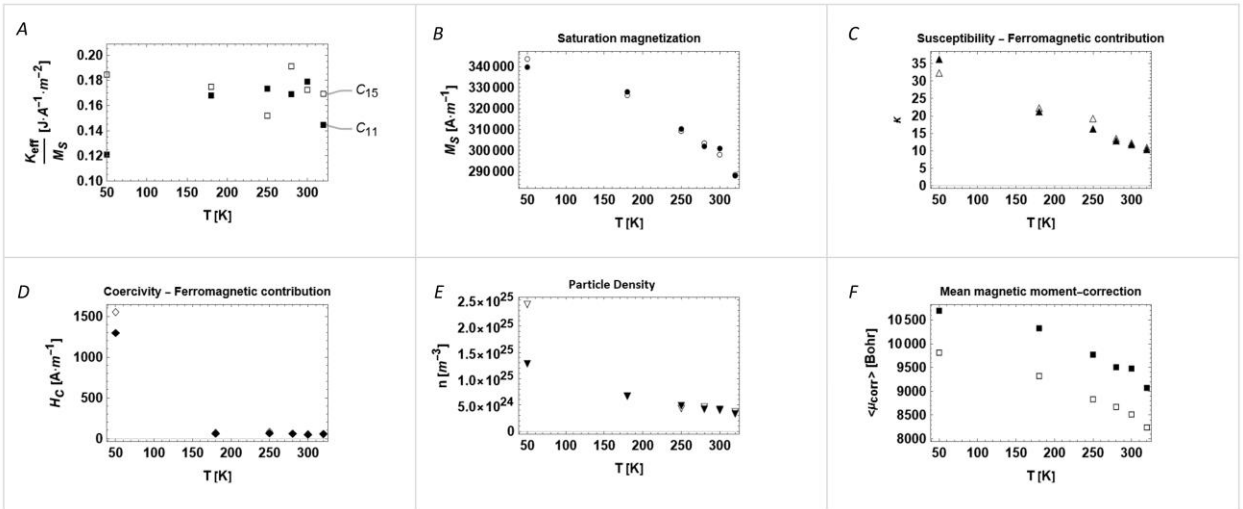

4.4.3.2 Susceptibility (κ) and coercivity (H_c)

Now, the estimated parameters of the FSR model were fitted to the deduced theoretical expressions of the susceptibility ($\chi(T)$) and coercivity ($H_C(T)$), as outline in Eq. 49 and 50, respectively. Likewise, the values of M_s at each temperature for the Ferrotec particles, estimated in agreement with the value of $M_S = 58.7\ \text{emu} \cdot \text{g}^{-1}$ at 300 K found by Contreras-Mateus *et al.* (3), were fitted to an exponential ad-hoc function (Figure 35), assuming $M_{S-\infty} = 400\ \text{kA} \cdot \text{m}^{-1}$ at 300 K (354, 355), as established in Eq. 51. This approach led to the inclusion of a continuous expression of $M_s(D_i, T)$ appropriate for the analysis of $\chi(T)$ and $H_C(T)$. As shown in Figure 36, the models suitably describe the functional dependence of κ and H_C on temperature. We highlight that, the κ value estimated at 50 K was excluded of the model, considering that the sample is not in equilibrium. Nunes *et al.* (356) obtained an equivalent expression of χ and H_C in terms of the distribution of blocking temperatures $(f(T_B))$, although they considered the coexistence of both the blocked and superparamagnetic nanoparticles, which implied a modification in the $H_C(T)$ equation that reflected the linear superposition of both contributions (see Fig 1 of Ref. (356)); however, after some mathematical contrivances in Eq. 50, the equivalence with Nunes expression can be easily demonstrated.

Figure 35

A. Evolution of $\boldsymbol{M_{S-\infty}}(\boldsymbol{T})$. *B. Fitted function of* $\boldsymbol{D_C}(\boldsymbol{T})$. *The plot markers are the estimated values based on Eq. 52. C. Normalized saturation magnetization* $\boldsymbol{f}(\boldsymbol{T})$ *for* $C_{1\text{-}5}$ *sample. The plot markers are the estimated values from Eq. 40 (Up to* H^{-2}*).*

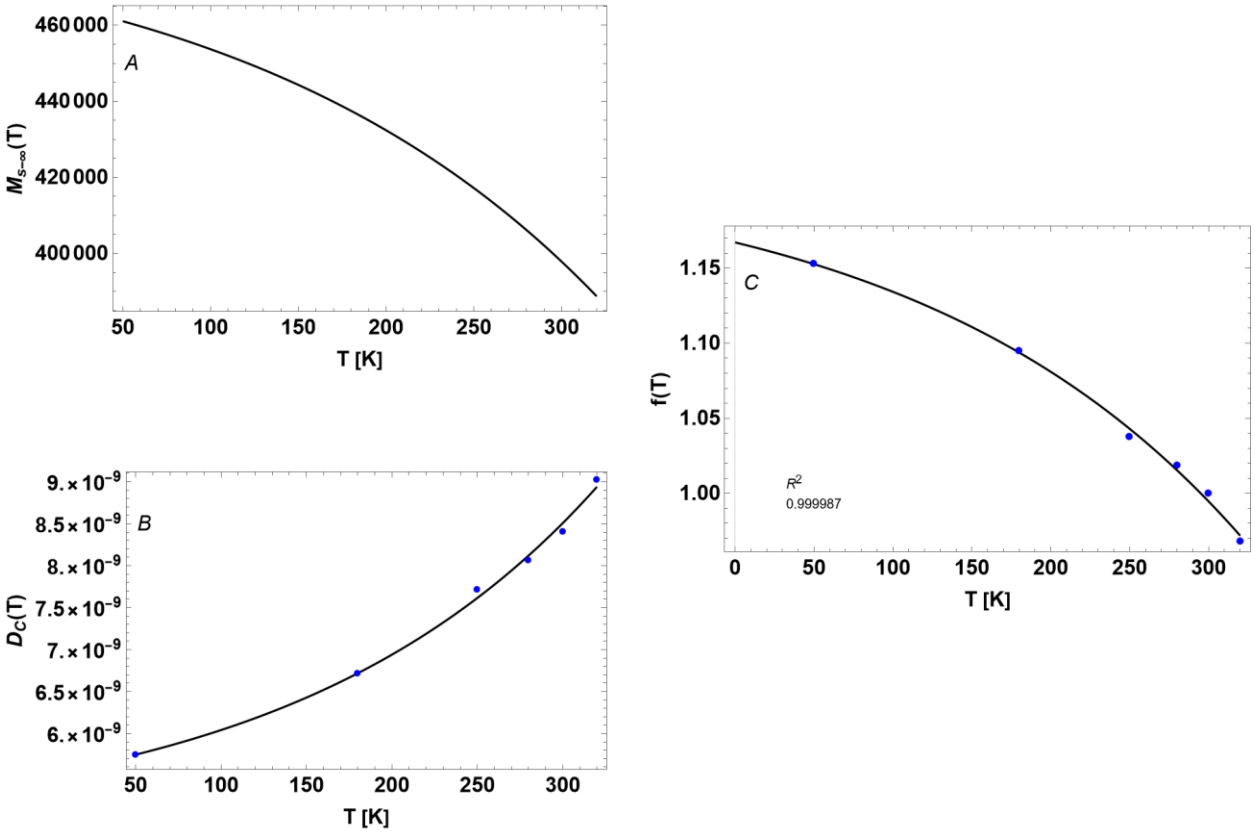

Figure 36

*A. Magnetic susceptibility (**κ**) for $C_{1\text{-}5}$ sample, obtained from Eq. 39. The line corresponds to the deduced theoretical expression (Eq. 49). B. Magnetic coercivity ($\boldsymbol{H_c}$) for $C_{1\text{-}5}$ sample, obtained from Eq.39. The line corresponds to the deduced theoretical expression (Eq. 50).*

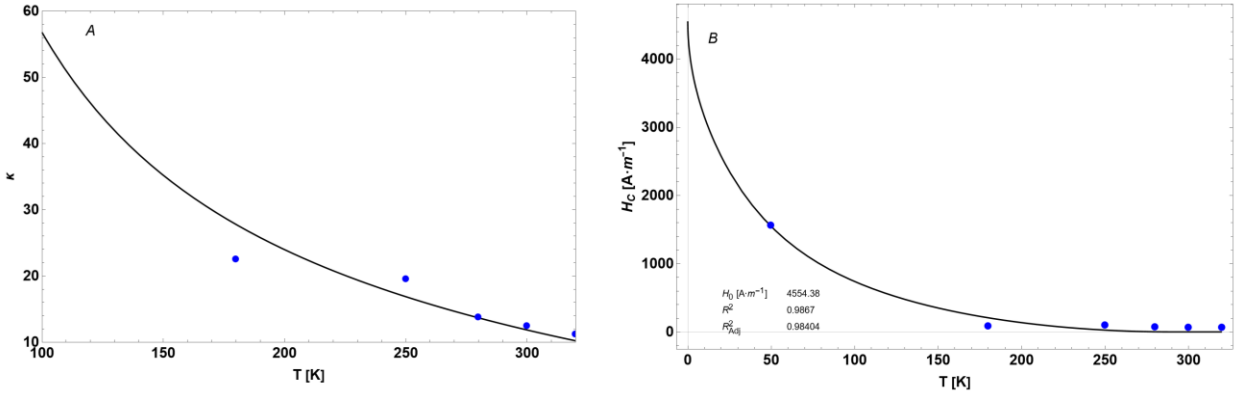

4.4.3.3 Zero-field cooled (ZFC) and field-cooled (FC) magnetization curves

The ZFC-FC routine was performed in accordance with the classical protocol, but it incorporated an initial procedure to correct potential remanent field errors, a common occurrence in Quantum Design instruments (357). This correction involved setting a nominal negative magnetic field that effectively nullified the magnetic moment in the sample at room temperature (RT). From this state, the sample was cooled to the lowest temperature (5K), then heated up to 320 K under the application of a constant magnetic field (100 Oe), to finally cooled it again in the presence of the field. ZFC and FC moments were measured while warming the sample up. On the other hand, as we are dealing with a poly-size sample, reasonably well described by a log-normal distribution, we have implemented the approach proposed by Micha *et al.* (358, 359), consisting of calculating the temperature derivative of the difference between ZFC and FC curves ($\partial(\mu_{ZFC} - \mu_{FC})/\partial T$), to estimate the blocking temperature distribution (T_B). The T_B is defined as

the transition region to thermodynamic equilibrium, when the thermal energy is related to the anisotropy barrier by $K_{eff}V \sim ln(\tau_{exp}/\tau_0)k_BT$, being τ_{exp} the experimental time window, and τ_0 the inverse of the attempt frequency for the particle's moment to overcome the anisotropy barrier.

Figure 37 depicts the ZFC-FC magnetization derivative, $\partial(\mathrm{M_{ZFC}} - \mathrm{M_{FC}})/\partial \mathrm{T}$, alongside the corresponding ZFC-FC experimental curve as an inset. As discussed, the curves are characteristic of nanoparticles and reveal a broad blocking region in the T spectrum, attributed to the polydispersity of the sample. Likewise, an unusual phenomenon characterized by the presence of a second local maximum (~274 K) was observed before reaching the irreversibility temperature (T_{irr} ~300 K). A detailed discussion is presented below.

The blocking temperature distribution corresponding to the first peak (T_{B1}) has been appropriately fitted with a log-normal distribution function, yielding a mean value, $\langle T_{B1} \rangle = 40.12\ K$, and a standard deviation, $\sigma_{B1} = 50.07\ K$. Furthermore, we made a comparison between the particles volumes distribution obtained by TEM data and $\partial(M_{ZFC} - M_{FC})/\partial T$ curve, by employing the relations applied in Ref. (359, 360), as follows.

$$T_B = (KV)/\left(k_B \ln\left(\tau_{exp}/\tau_0\right)\right) \tag{57}$$

where, $\ln\left(\tau_{exp}/\tau_0\right) \approx 25$.(358, 359)

By implementing an optimization methodology towards non-linear least squares adjustment of TEM and $\partial(M_{ZFC} - M_{FC})/\partial T$ data, we determined the effective value of $K = 15044.7\ J \cdot m^{-3}$, which is reasonably close to that reported for magnetite nanoparticles at temperatures around 40 K (267, 361), validating the implemented Micha adjustment approach (refer to Figure S6, supplementary information).

This T_{B1} distribution can be attributed to the Néel relaxation mechanism, particularly when considering the fusion temperature of toluene (178.15 K) and the glass transition temperature of C_1 (215.88 K) estimated by DSC, which imply that the sample at this temperature range predominantly exhibits solid-like behavior. Equally important to mention is that the nanoparticles present a significantly lower Néel relaxation time ($\tau_{\text{Néel}}$) compared to the Brownian relaxation time (τ_B, Figure S7) within the studied temperature domain, where τ_B was estimated using an extrapolation of the sample viscosity values obtained experimentally at higher temperatures. As a result, the condition that $\tau_{\text{Néel}}$ is approximately equal to the time window of the experiment is satisfied, *i.e.*, $\tau_{Néel} \sim \tau_{exp} \sim 100\ s$. The above argument is consistent with the Mössbauer spectrum measured at RT, which proved the presence of magnetic hyperfine interactions strongly affected by magnetic relaxation phenomena. This conclusion is supported by the calculated $\tau_{Néel}(300K) \sim 10^{-8} s$, approximately matching the time window of Mössbauer spectrometry using the 14.4 keV transition of ^{57}Fe.

On the other hand, we attributed the second T_{B2} distribution to the Brownian relaxation mechanism on the nanoparticle aggregates, considering that at this temperature the viscosity (η) of the modified crude oil decreases sufficiently so that the Brown relaxation time of the aggregates, $\tau_B^A = (3\eta V_h^A)/(k_B T)$, is comparable to the time window of the experiment (τ_{exp}), where V_h^A is the hydrodynamic volume of the aggregates. On the other hand, it has been established that the more suitable orientation of the nanoparticle easy axes or aggregates (lower demagnetizing factor) with the magnetic field leads to a further increase in magnetization for the same applied field strength. Based on that, during cooling and in the absence of the magnetic field, it is expected that the aggregates will remain fixed with random orientations, leading to an average aggregate

demagnetizing factor, associated with the aggregates shape (s), of $\langle N_{ZFC}^{sA} \rangle = 1/3$. Upon heating and in the presence of the magnetic field, after reaching the condition $\tau_B^A = \tau_{exp}$ for each volumetric aggregate, they will align with the field and their average demagnetizing factor will have a lower value, $\langle N_{ZFC}^{sA} \rangle < 1/3$. This will decrease the demagnetizing field (H^D), which results in a higher effective field (H^E), leading to an increase in the magnetic moment of the sample (which will asymptotically approach μ_{FC}).‡‡‡

‡‡‡ We designated the shape demagnetizing factor (N^{sA}) to the one determined solely by the specimen shape, in this case, by the average aggregate shape. This is the demagnetizing factor that must be used to estimate the internal demagnetizing field $H_D = N^{sA} \cdot M_A$, where M_A is the magnetization of the aggregate calculated as its magnetic moment divided by its volume. The effective demagnetizing factor (N_{Eff}) is the factor that must be used when H_D is calculated as $H_D = N_{Eff} \cdot M$, where M is the magnetization of the magnetic part of the aggregate, *i.e.*, the one given by the quotient of the aggregate moment and the volume of the particles contained in the aggregate. The values given so far correspond to N^{sA}.

Figure 37

Log-normal fit of $\boldsymbol{\partial(M_{ZFC} - M_{FC})/\partial T}$ *at 40.12 K (continuous black line), and Lorentz fit of the second peak of* $\boldsymbol{\partial(M_{ZFC} - M_{FC})/\partial T}$ *at 273.96 K (continuous magenta line). Inset corresponds to the ZFC and FC experimental curves.*

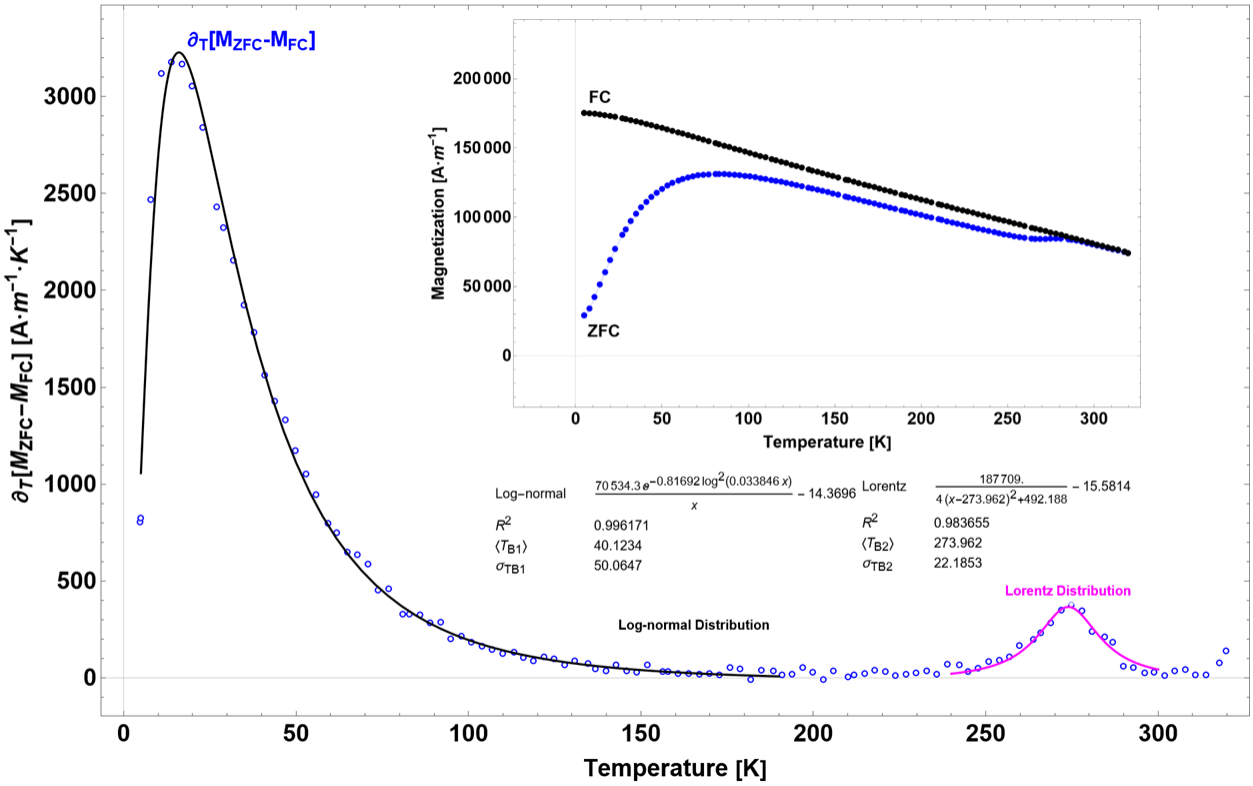

To validate the above assumptions, we first focused on determining whether the sole activation of the Brownian mechanism in non-aggregated nanoparticles is a decisive factor in inducing a change in the susceptibility. Carrey *et al.* (63) estimated the reduced magnetization curves (M/Ms) of anisotropic systems at thermal equilibrium with the easy axes randomly oriented in space for various values of a dimensionless parameter associated with the anisotropy energy ($\sigma = KV/k_BT$) as a function of another dimensionless parameter associated with the Zeeman energy ($\xi = \mu_0 M_s VH/k_BT$), see Fig. 2B of Ref. (63). Assuming for our sample,

$2 \times 10^4 \leq K \leq 3 \times 10^4\ J \cdot m^{-3}$, $D = 10\ nm$, $T = 250\ K$, $M_S = 311145\ A \cdot m^{-1}$, $H = 100\ Oe$; therefore, $3.03 \leq \sigma \leq 4.55$ and $\xi = 0.47$, and evaluating in the M/Ms curves of Carrey et al, it is concluded that the susceptibility of the blocked nanoparticles remains nearly indistinguishable from that predicted by the Langevin model. As a result, the conclusion drawn from this observation is that the activation of the Brownian mechanism in non-aggregated nanoparticles does not significantly influence their susceptibility. Consequently, this effect cannot be ascribed to the unblocking phenomenon observed at T_{B2}. Furthermore, as proved in DSC experiments, the sample does not experience any phase change in the studied temperature range (Figure S8). The above, in turn, supports the hypothesis that the Brownian unblocking observed is attributed to nanoparticle aggregates.

The following is a detailed description and modeling of the T_{B2} unblocking phenomenon of aggregates. In the first place, the appropriate expressions for the susceptibility of ZFC and FC are established, as shown in Eq. 58 and 59.

$$\kappa_{ZFC}(T) = (1 - f)\kappa^{NP}(T) + [(f^R)\kappa_O^A(T) + (f - f^R)\,\kappa_R^A(T)] \tag{58}$$

$$\kappa_{FC}(T) = (1 - f)\kappa^{NP}(T) + (f)\kappa_O^A(T) \tag{59}$$

Additionally, $\kappa_{ZFC}(T)$ can also be expressed as,

$$\kappa_{ZFC}(T) = (1 - f)\kappa^{NP}(T) + (f)\kappa^A(T) \tag{60}$$

Where, $\kappa^A(T)$ are the values of the aggregate susceptibility while it is getting oriented, *i.e.*, while it transitions from its random value $\kappa_R^A(T)$ to its oriented one $\kappa_O^A(T)$; N is the total number

of nanoparticles in the sample, κ^{NP} is the susceptibility of non-aggregated nanoparticles, f is the fraction of nanoparticles in aggregates, $f^R = \left(P_{accum}(T)\right)/N$ is the fraction of nanoparticles that have already reoriented, thus, P_{accum} is the accumulated number of nanoparticles in aggregates that have already reoriented at temperature T during the ZFC measurement.

If a general shape is assumed for the aggregates, for instance, assuming a prolate spheroidal model with the same relations between the spheroid's main axis a, b, the values $\kappa_O^A(T)$ and $\kappa_R^A(T)$ are independent from the size of the aggregate.

When $P_{accum} = 0$, then,

$$\kappa_{ZFC}(T) = (1 - f)\kappa^{NP}(T) + f\kappa_R^A(T) \tag{61}$$

When $P_{accum} = fN$, then,

$$\kappa_{ZFC}(T) = (1 - f)\kappa^{NP}(T) + f\kappa_O^A(T) = \kappa_{FC}^A(T) \tag{62}$$

It is worth now introducing the value $\kappa_{ZFC}^*(T)$, which is the extrapolation of κ_{ZFC} before the unblocking, towards higher temperatures,

$$\kappa_{ZFC}^*(T) = (1 - f)\kappa^{NP}(T) + f\kappa_R^A(T) \tag{63}$$

Figure 38A depict the ZFC-FC measured magnetic moments (μ_{ZFC}, μ_{FC}), as well as the linear (μ_{FC}, $\mu_{ZFC}^*(T)$) and non-linear ($\mu_{ZFC}(T)$) ad-hoc functions used to fit these data (continuous lines) to subsequently estimate the susceptibility curves (Figure 38B), $\kappa_{ZFC}(T)$, $\kappa_{ZFC}^*(T)$, $\kappa_{FC}(T)$. An assumption was made, regarding the moment of the non-interacting nanoparticles ($\mu^{NP}(T)$), which is expected to be higher than the aggregate state, as established by Allia *et al*. (349).

Figure 38

The ZFC-FC magnetic moment curves; the red dashed line is an assumption of the behavior of the magnetic moment of non-interacting magnetic nanoparticles, which is expected to be higher than the aggregated state. B. The ZFC-FC susceptibilities were estimated at H= 100 Oe.

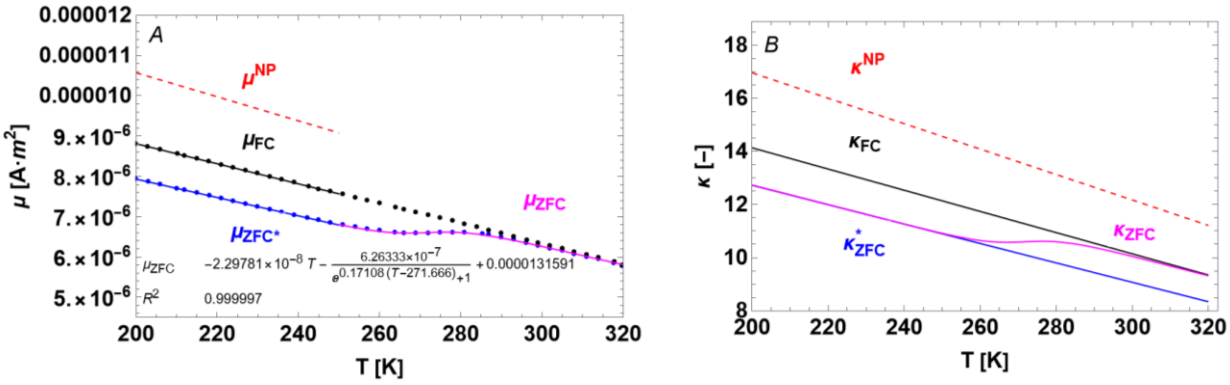

The change of the magnetic moment by unit of increasing temperature, that the sample experiences during the progressive unblocking of the aggregates can be described as,

$$d\Delta\mu(T)/dT = HV_B^A P(V_B^A)[\kappa_{FC}(T) - \kappa^*_{ZFC}(T)](dV_B^A/dT) \quad (64)$$

$$d\Delta\mu(T)/dT = HV_B^A P'(V_B^A)[\kappa_{FC}(T) - \kappa^*_{ZFC}(T)] \quad (65)$$

Where $P(V_B^A)dV_B^A$ is the number of unblocked aggregates with volumes between V_B^A and $V_B^A + dV_B^A$, and, as established in Eq. 66, $P'(T)dT$ is defined as the number of unblocked aggregates in the temperature interval dT.

$$P'(T)dT = P(V_B^A(T))(dV_B^A/dT)dT \quad (66)$$

The aggregate blocking volume is defined by means of the Brown expression,

$$V_B^A(T) = k_B T\tau_{exp}/(3\eta(T)) \quad (67)$$

Using the experimental data for η(T) (Figure S9), $\partial(\mu_{ZFC} - \mu_{FC})/\partial T$, $H = 100\ Oe$, $\tau_{exp} = 100\ s$, and $(\kappa_{FC}(T) - \kappa^*_{ZFC}(T)))$, it is expected to recover $P'(T)$, as shown in Eq. 68.

$$P'(T) = [3\eta(T)(d\Delta\mu(T)/dT)]/\left[Hk_BT\tau_{exp}\left(\kappa_{FC}(T) - \kappa^*_{ZFC}(T)\right)\right] \quad (68)$$

Figure 39B illustrates the numerical values of P′(T) estimated from the measured η(T) and $\partial(\mu_{ZFC} - \mu_{FC})/\partial T$ curves. As shown in Figure 39A (see also Figure 37), the $\partial(\mu_{ZFC} - \mu_{FC})/\partial T$ data has been appropriately fitted with an ad hoc function (i.e. a Lorentz distribution function), yielding a mean value, $\langle T_{B2}\rangle = 274$ K, and a standard deviation, $\sigma_{B2} = 22.19$ K.

Figure 39

A. The $\boldsymbol{\partial(\mu_{ZFC} - \mu_{FC})/\partial T}$ *curve fitted to a Lorentz distribution function. B. The number of unblocked aggregates per temperature unit* $\boldsymbol{P'(T)}$ *estimated with Eq. 66, the blue dashed line corresponds to the approximation using the experimental data.*

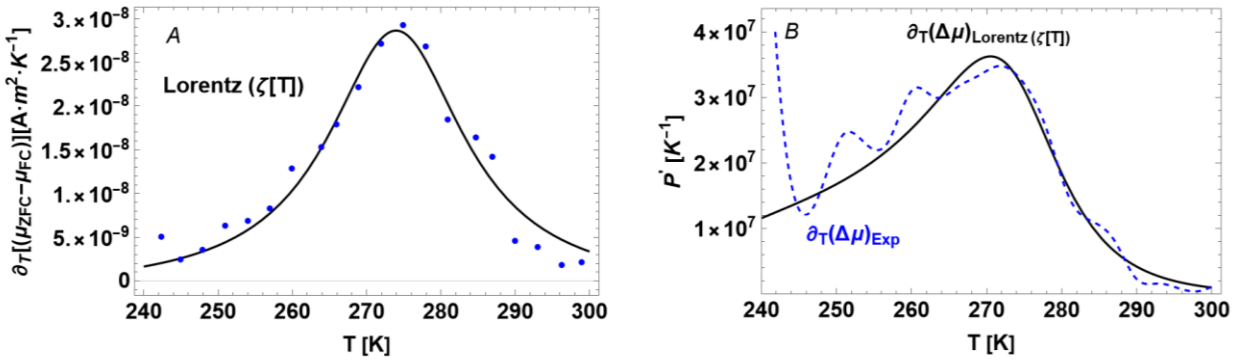

Furthermore, when considering the magnetic diameter estimated by TEM,(3) $D_N = 9.43 \cdot 10^{-9}\ m$, as well as the magnetic core volume, $V_N = \pi D_N^3/6$, and incorporating the contribution of the surfactant and asphaltenes, which can be approximated (3), $\delta = \sqrt[3]{6V_N/(0.54\,(\pi D_N^3/6))} - 1$; the volume of a particle can be estimated as,

$$V_p = \left(\pi\left(D_N(1+\delta)\right)^3\right)/6 \approx 8.13 \cdot 10^{-25}\ m^3 \quad (69)$$

Based on Eq. 67 and 69, the total number of particles in an aggregate unblocked at temperature T is expressed as,

$$N_{NP}^{A}(T) = V_{B}^{A}(T)/V_{p} \tag{70}$$

In the same way, the number of particles in the total of aggregates which unblock at temperature T is stated as,

$$P'_{NP}(T) = P'(T)P_{accum}(T) \tag{71}$$

Accordingly, Figure 40 illustrates the calculated $N_{NP}^{A}(T)$, $P'_{NP}(T)$, as well as the accumulated number of nanoparticles in the total unblocking aggregates as a function of T, $P_{accum}(T)$. As shown, the accumulated sum is approximately $1.02 \cdot 10^{14}$. Now, from the isothermal magnetization loops, we calculated $2.96 \cdot 10^{14}$, as the total number of nanoparticles in the sample (Figure 34E). Thus $f \approx 0.34$, i.e., 34% is the fraction of nanoparticles in aggregates.

Figure 40

A. The total number of particles per unit volume of an aggregate as a function of ***T****. B. The number of particles in the aggregates unblocked at temperature* ***T****. C. the accumulated number of nanoparticles in the total unblocking aggregates as a function of* ***T****.*

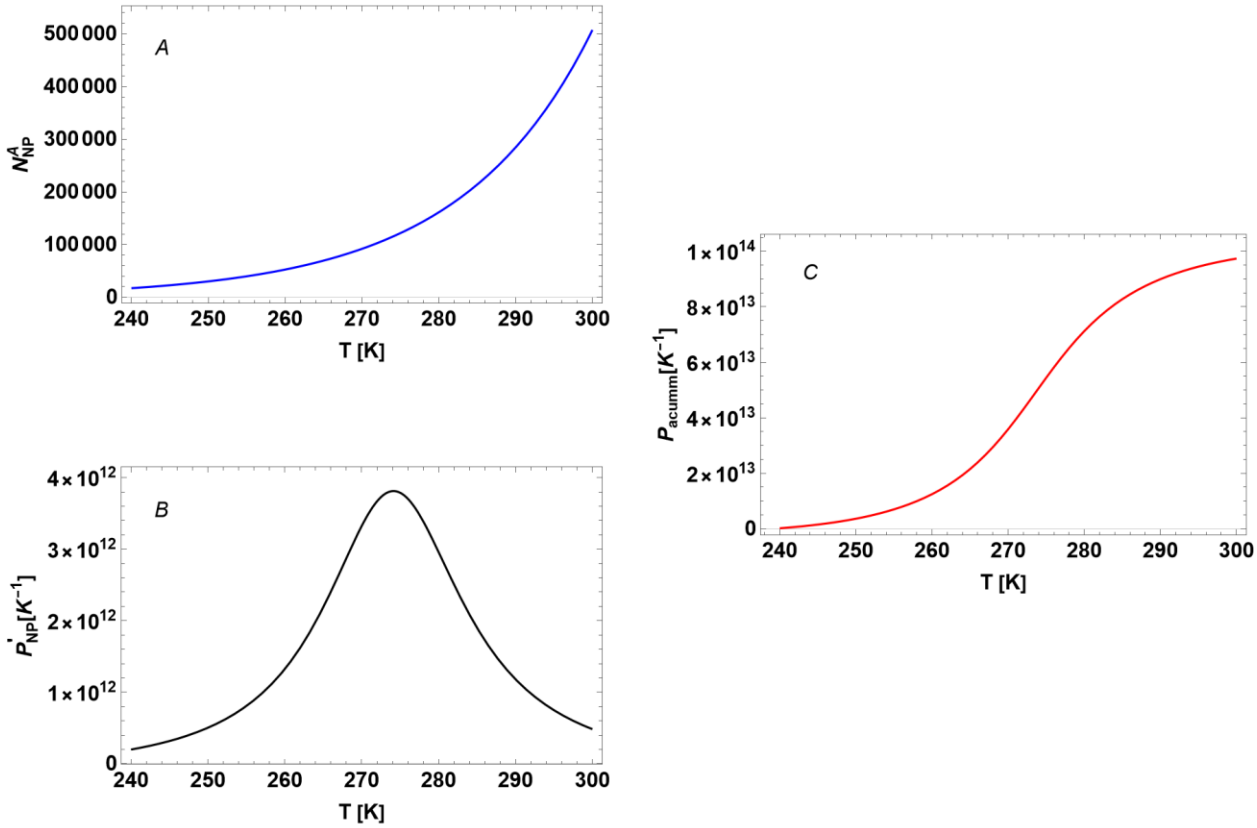

Following this, it is attempted to analyze the result obtained for $P'(T)$ considering the following relation, obtained from Eq. 62 and 63.

$$\kappa_{FC}(T) - \kappa^*_{ZFC}(T) = f[\kappa^A_O(T) - \kappa^A_R(T)] \tag{72}$$

The objective is to attain conclusions regarding $\kappa^A_R(T)$, $\kappa^A_O(T)$, and f. From this, we will have a glimpse on the aggregates shape and/or their degree of reorientation.

Additional considerations should be made:

The maximum value of κ_O^A takes place for very anisotropic aggregates, with an aspect relation $a/b \to \infty$, in which case, $\kappa_O^A \to \chi$, the nanoparticle intrinsic susceptibility, which is defined as, $\chi = \mu_0 \langle {\mu_p}^2 \rangle / \left(3 \langle V_p \rangle k_B T\right)$.

If the nanoparticle aggregates are compact, when they are randomly oriented (*i.e.,* at the beginning of the ZFC curve), they will exhibit a mean demagnetizing factor in the order of 1/3. In general, it is assumed the effective demagnetizing factor as $N^E = \phi^{NP,A} \cdot N^A$, where $\phi^{NP,A}$ and N^A are the volumetric concentration of nanoparticles in the aggregate and the demagnetizing factor of the aggregates, respectively.

Even if the aggregates are compact, the presence of the polymeric and asphaltene layers onto the nanoparticle surfaces contributes ~23.3-31.6% of the volume of an aggregate, which implies that the mean volume fraction of the nanoparticles in the aggregate should be $\phi^{NP,A} = \left(D_N/D_p\right)^3 \sim 0.54$; where D_p is the total diameter of the particle, considering the surfactant and the asphaltenes; a value of 11.6 nm was assumed. Hence, the effective demagnetizing factor of the randomly oriented aggregates should be, $N_R^{E,A} = (1/3)\phi^{NP,A} \sim 0.18$, as long as, $0 \leq N_O^{E,A} \leq N_R^{E,A}$. Now, if the aggregates are isotropic, $N_O^{E,A} = N_R^{E,A}$. If the aspect relation $a/b \to \infty$ ($\kappa_O^A \to \chi \sim \kappa^{NP}$), then, $N_O^{E,A} \to 0$.

From the expression,

$$\kappa = \chi/(1 + N^E \chi) \tag{73}$$

It can be deduced,

$$N_O^{E,A} = N_R^{E,A} - (1/\kappa_R^A - 1/\kappa_O^A) = 0.18 - [\kappa_{FC}(T) - {\kappa^*}_{ZFC}(T)]/f \tag{74}$$

In Eq. 39, the total variation experienced by the susceptibilities of the aggregates is used. Therefore, it is possible to have an idea on how the effective demagnetizing factor of the aggregates $N^{E,A}$ changes as the aggregates get oriented, by using the susceptibility $\kappa^A(T)$ expressed in Eq. 25.

$$N^{E,A} = N_R^{E,A} - (1/\kappa_R^A - 1/\kappa^A) \tag{75}$$

In this case,

$$\kappa^A(T) = \kappa_{ZFC}(T)/f - \kappa^{NP}(T)(1-f)/f \tag{76}$$

With the complete set of equations, and taking the approximations of $\kappa_{ZFC}(T)$, $\kappa^*_{ZFC}(T)$, $\kappa_{FC}(T)$, $\kappa^{NP}(T)$ (Figure 38B), κ^A, κ_R^A and κ_O^A can be estimated as depicted in Figure 41.

Figure 41

Magnetic susceptibility of nanoparticles in the aggregates while getting oriented ($\boldsymbol{\kappa^A}$), in reoriented (unblocked, $\boldsymbol{\kappa_O^A}$), and randomly oriented (blocked, $\boldsymbol{\kappa_R^A}$) aggregates.

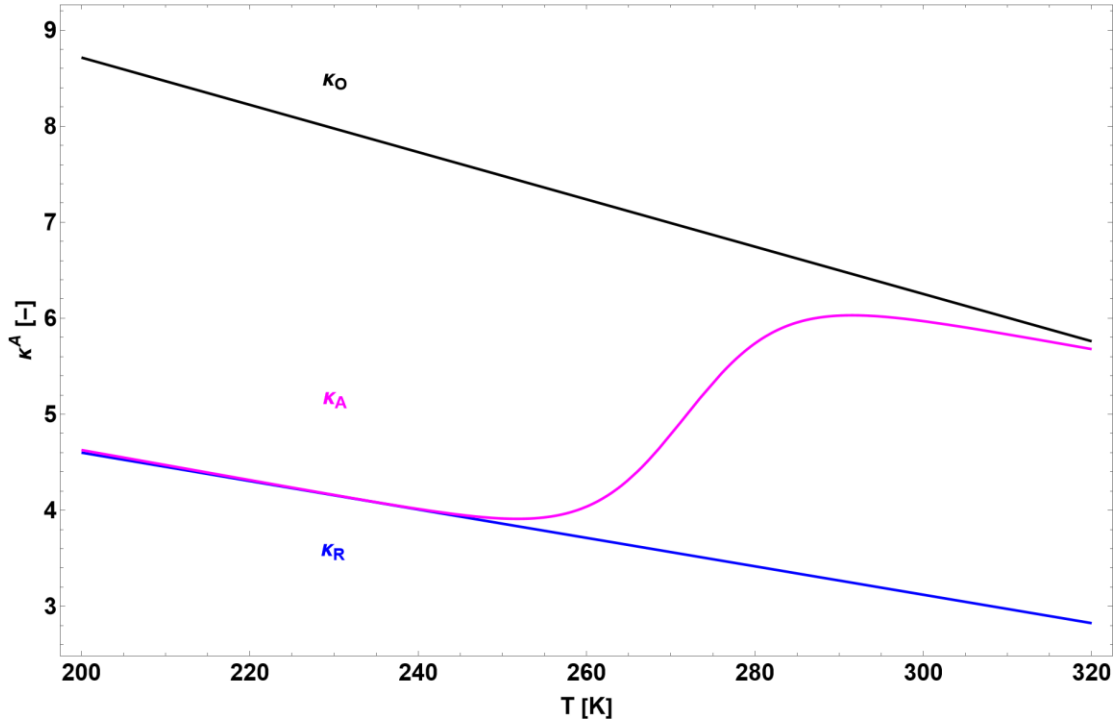

Finally, Figure 42 illustrates the evolution of the effective demagnetizing factor of the aggregates $N^{E,A}$, as they get oriented (Eq. 40). The depicted results support the assumptions made in the development of the model, demonstrating that the effective demagnetizing factor effectively evolves towards values lower than 1/3; i.e.,$\langle N_{ZFC}^{sA} \rangle < 1/3$.

Figure 42

Evolution of the effective demagnetizing factor of the aggregates $\boldsymbol{N^{E,A}}$ *(Eq. 40), The dashed blue line did not consider the polymeric and asphaltene layers.*

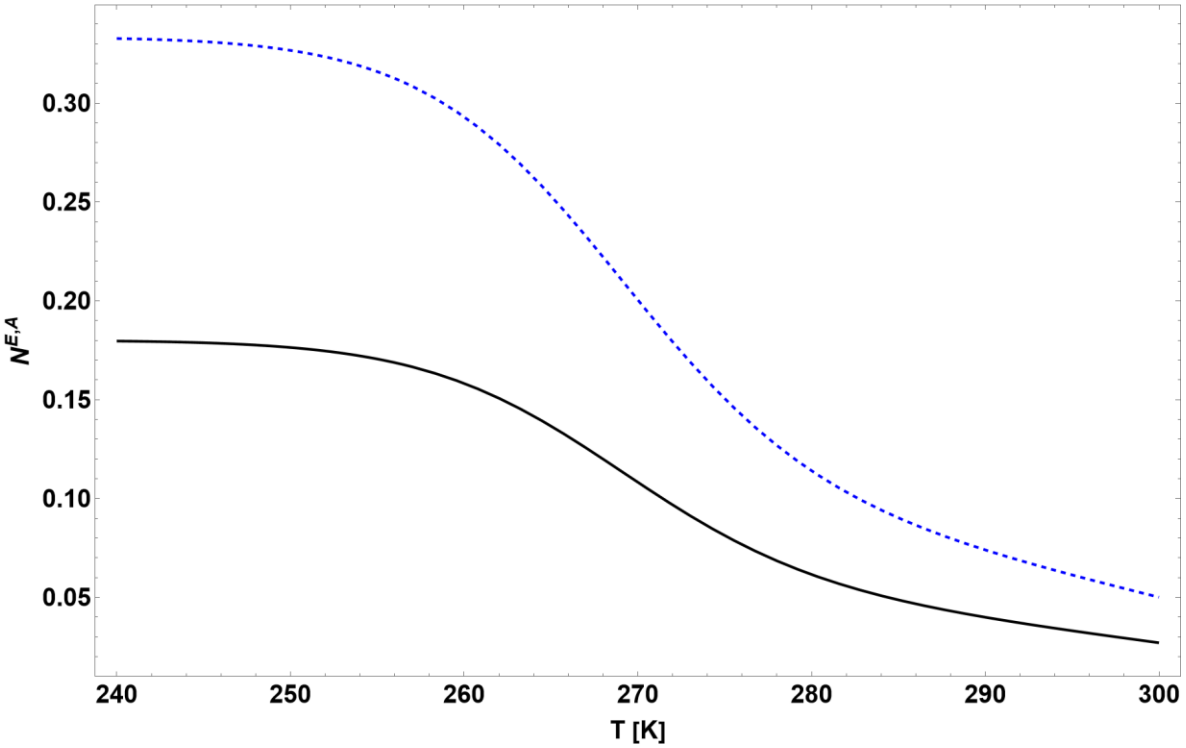

Based on the functional dependence of $N^{E,A}$, the mean value of the eccentricity (ξ) can be estimated from the theoretical expression of the demagnetizing factor of a prolate spheroid (61), as follows,

$$\langle N^{E,A} \rangle \approx N_z = \frac{1}{p^2 - 1}\left[\left(\frac{1}{2\xi}\ln\left(\frac{1+\xi}{1-\xi}\right)\right) - 1\right] \quad (77)$$

where, $\langle N^{E,A} \rangle \approx \frac{\left(\int_{240}^{300} N^{E,A}(T)dT\right)}{(300-240)}$ is an approximate expression of the mean value of $N^{E,A}$, $p = \frac{a}{b}$, $b = c < a$, and $\xi = \sqrt{\frac{p^2-1}{p}}$.

According to Eq. 77, the eccentricity $\xi \approx 0.94$. Now, estimating the volume of the aggregates, $V^A \approx 0.8 V_B^A(T)$[§§§], it is possible to obtain the evolution of the major and minor axes of the aggregates (a, b), as illustrated in Figure 43. Based on the above, the model proved the formation of aggregates with a mean size in the order of ~530 nm.

Figure 43

A. Evolution of the volume of the aggregates. B. Major and minor axes (a,b).

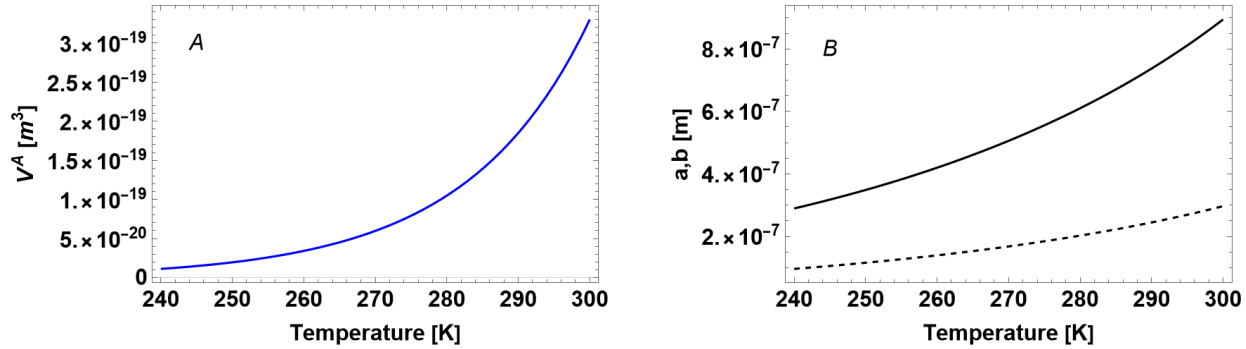

[§§§] Assuming a filling factor of 0.8.

4.5 Conclusions

The nonlinear magnetorheological properties and induced intra-cycle structural transitions of a mixture of heavy crude oil and ferrofluid ($C_{1\text{-}5}$) have been studied and modeled using the sequence of physical (SPP) framework. The results demonstrated a sudden and considerable increase in the mechanical properties upon magnetic field application, accompanied by changes in the intra-cycle processes, particularly at high strain amplitudes (LAOS), such as the absence of viscoplastic deformation attributed to a rheological manifestation of a broken network structure with a lack of rigid chain structure. Additionally, the stress waveform experienced a distinctive transition from a weakly sharp "saw-tooth" shape to a rounded-end rectangular shape, which has been associated with the formation of magnetic structures in magnetorheological fluids. We applied complementary magnetometry techniques, such as isothermal magnetization curves, which were successfully modeled using the generalized asymptotic fitting method of ferrosolid magnetization at high magnetic fields. Likewise, the ZFC-FC magnetization protocols were studied and revealed a distinctive blocking temperature distribution at nearly 274 K, within the temperature range studied in LAOS experiments. This distribution was associated with the Brownian relaxation of nanoparticle aggregates of several hundred nanometers reoriented in the direction of the magnetic field as a function of temperature. To support our findings, we proposed a phenomenological model based on the estimation of effective demagnetizing factors of the formed and reoriented aggregates, using parameters derived from the isothermal magnetization curves and well-supported information from existing literature, thereby ensuring rigor in the results.

MAGNETORHEOLOGY OF HEAVY OIL-FERROFLUID MIXTURES.

The combination of LAOS and magnetometry led to effectively demonstrate that aggregates of magnetic nanoparticles occur spontaneously in heavy crude oils modified by the addition of a ferrofluid, and these aggregates are anisotropic and align preferentially parallel to an applied magnetic field. Indeed, the above also comprises a technically complex phenomenon to study in ferrofluids. Finally, it is important to note that our proposed model solely describes the reorientation of aggregates, and further research is required to understand their arrangements and potential structure growth due to dipolar magnetic interactions, as a function of the magnetic field.

4.6 Supplementary information

Figure S6

Fitted log-normal distribution as a function of the size $\partial(M_{ZFC} - M_{FC})/\partial D)$ from ZFC-FC magnetization curves (Red), and log-normal distribution function obtained from TEM (Blue).

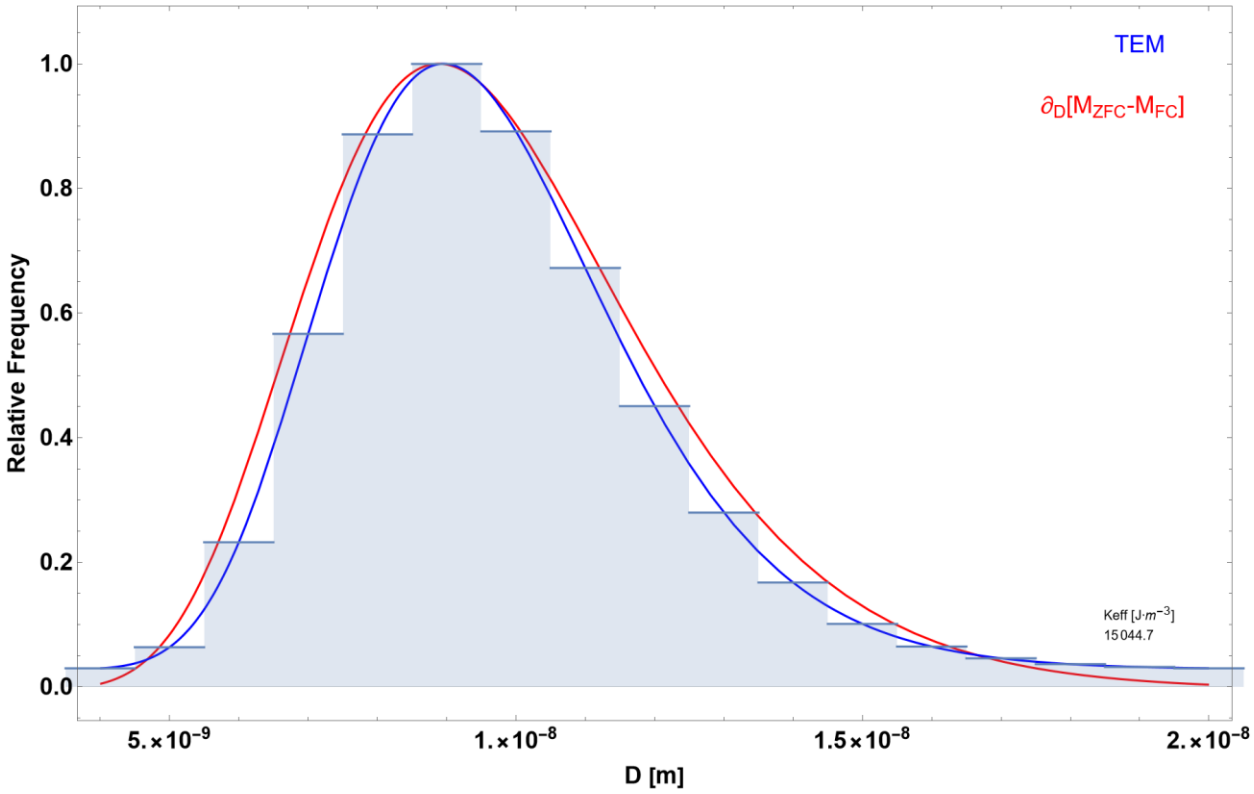

Figure S7

Brownian and Néel relaxation times as a function of the temperature. Assuming a nominal diameter of the magnetic core equal to 10 nm, a hydrodynamic diameter of 20 nm, effective anisotropy constant $K=2\cdot10^{4}\ J\cdot m^{-3}$, $\tau_0=10^{-9}$.

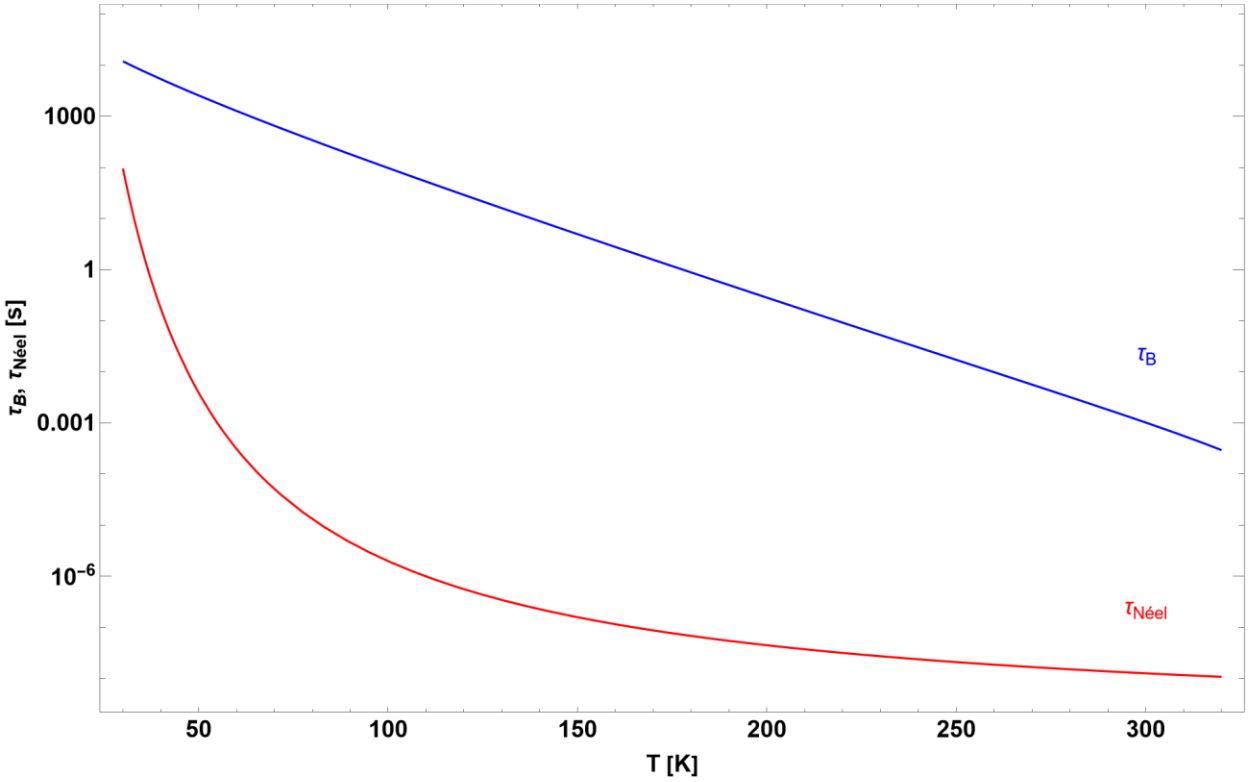

4.6.1.1 Magnetic modified heavy crude oil (C_{1-5})

Differential Scanning Calorimetry-DSC, the differential thermogram was acquired using a DSC Discovery, TA Instruments, Inc. (USA). The samples were subjected to heating loops in the range of -40 °C to 40 °C, at a heating rate of 3 °C /min, and under nitrogen purge gas of 50 ml/min.

Figure S8

DSC curves for C_{1-5}, under dynamic nitrogen atmosphere (50 ml min^{-1}), at a heating rate of 3 °C min^{-1}.

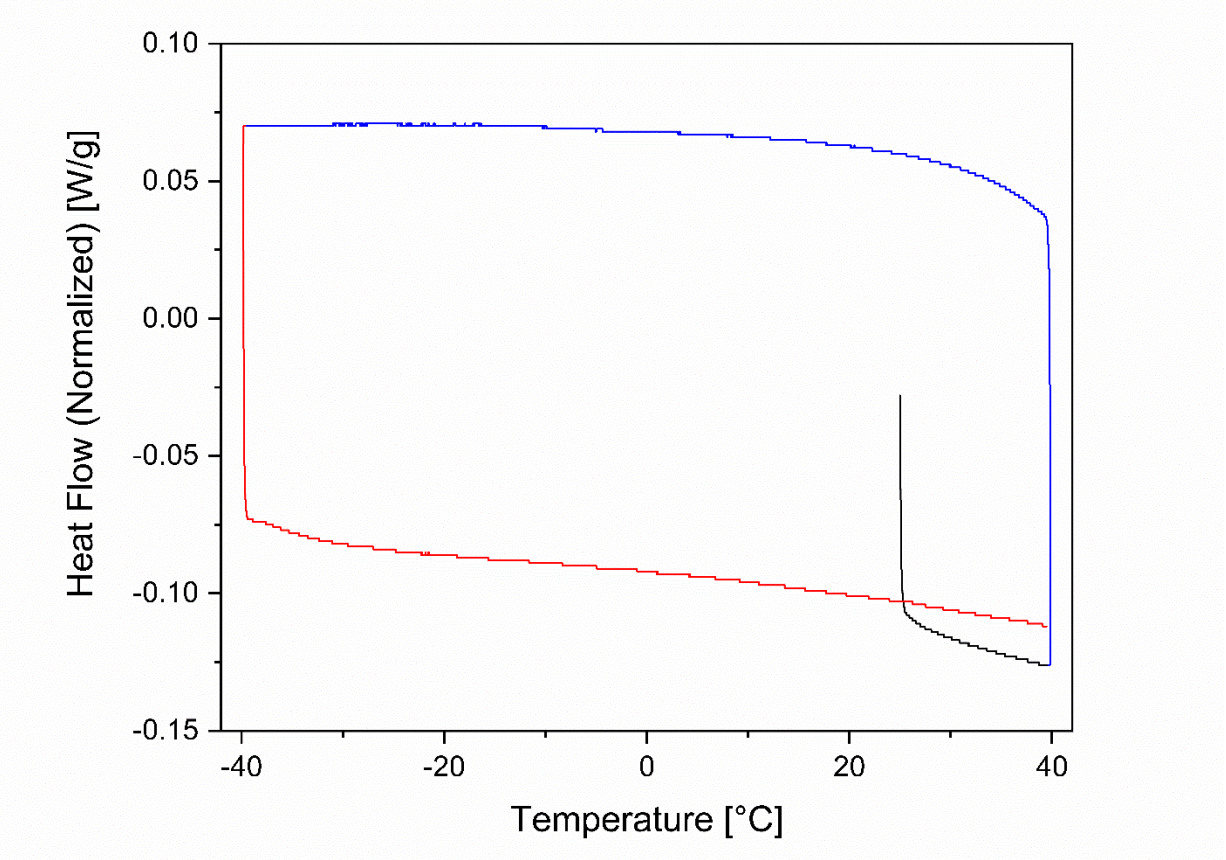

Figure S9

Fitted viscosity function of $C_{1\text{-}5}$. The blue points are the experimental values measured as a function of the temperature.

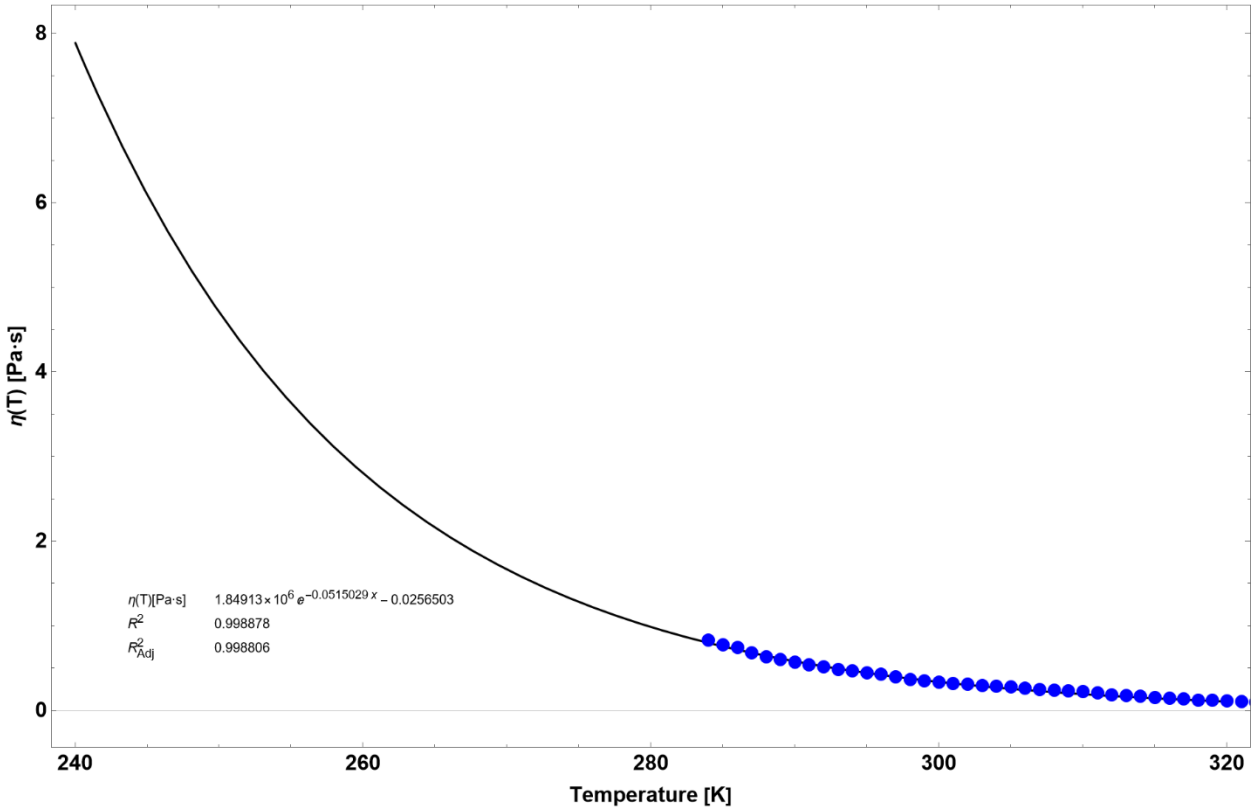

MAGNETORHEOLOGY OF HEAVY OIL-FERROFLUID MIXTURES.

General remarks and ongoing research

It seems important to begin by emphasizing that this Doctoral thesis has effectively undertaken the ambitious foundational objectives it initially aimed to address. Despite the numerous challenges, uncertainties, and complexities presented by heavy crude oils and ferrofluids, a comprehensive investigation into the effects of external magnetic fields on these mixtures has been successfully accomplished. The envisioned hierarchical framework was designed to study the magnetically triggered rheological and structural phenomena, encompassing scales from macroscopic to microscopic. Mindful of the vast array of potential outcomes within these systems, our endeavors have led to a comprehensive understanding of a fraction of the numerous probabilities within this intricate universe. Therefore, we succinctly outline the key insights demonstrated within the scope of this thesis:

- The appearance of magnetoviscous effects is a plausible occurrence in rheologically complex matrices.
- The establishment of a model elucidating the functional correlation between the apparent magnetic susceptibility and asphaltene concentration has revealed that these fractions are adsorbed onto nanoparticle surfaces forming layers, consequently stimulating steric repulsion phenomena. On this basis, magnetometry represents a reliable technique to evaluate asphaltene adsorption on magnetic nanoparticles.
- In the colloidal state configuration, additional attractive interactions such as interdigitation may be present at certain asphaltenes concentrations (< 1.0 wt.%), which could lead to the natural formation of nanoparticles/asphaltene isotropic aggregates in the absence of a magnetic field.

MAGNETORHEOLOGY OF HEAVY OIL-FERROFLUID MIXTURES.

- The synergy of rheological large amplitude oscillatory (LAOS) tests and magnetometry represents a remarkable alternative approach to demonstrate the formation and alignment of magnetic structural arrangements under the action of an external magnetic field.
- The adsorbed asphaltenes promote the spontaneous formation of aggregates, whose orientation could be manipulated by external magnetic fields to induce favorable flow properties of heavy crude oils.

Building upon this foundation, the ongoing research should pivot towards application-oriented approaches. This could entail experimental data to support pipeline flow scenarios, thereby paving the way to assess the feasibility of integrating magnetic-based technologies within the context of the petroleum industry. As an ultimate phase, this thesis was geared towards the design of a flowline system aimed at studying the effect of alternative magnetic field configurations (longitudinal linear increasing and oscillating) with the potential of enhancing the flow properties of mixtures of heavy crude oils and ferrofluids, as observed in magnetorheological fluids by the induction of Kelvin-body forces and “negative viscosity” effects. A concise description of the equipment and a selection of preliminary results are presented:

A flow line system was designed to investigate the alterations in the volumetric flow of a ferrofluid and a ferrofluid emulsion when subjected to non-uniform magnetic fields linearly increasing in the axial direction. As model matrices, a ferrofluid composed of magnetic oxide nanoparticles dispersed in kerosene at a concentration of 0.87 vol.% was employed, as well as an emulsion formulated by combining the ferrofluid with a solution of hexadecylpyridinium chloride monohydrate in a 1:1 volumetric ratio, with the latter present at a concentration of 2.5 w/v% in

deionized water. The experimental setup operates on the basis of a constant-pressure piston driving system, coupled with a programmable logic controller (PLC) that monitors and modifies the output flow rate of a positive displacement pump that injects ethanol to one of the isolated chambers of the piston, due to the input signal produced by a pressure transducer located in this chamber. Likewise, a solenoid winding array, comprising six coils of varying diameters connected in series, was mounted around a section of the flow pipeline; generating static or oscillating linear increasing magnetic fields in the axial direction (Figure 44). The effect of the magnetic field strength and frequency, as well as the operating pressure, were evaluated, showing that, under some specific conditions, significant fluid accelerations (up to ~30%) were reached due to the action of the magnetic field. The highest acceleration with the ferrofluid was observed under an oscillating field, applying an alternating current (AC) of 0.117 A and a frequency of 400 Hz, and AC of 0.061 A and 800 Hz of frequency for the ferrofluid emulsion (Figure 45). The observed phenomena were attributed to the induction of “negative” viscosity effects and Kelvin-type magnetic body forces, due to the influence of an increasing oscillating magnetic field. Additionally, the experiment revealed that the ferrofluid exhibited a deceleration tendency towards the end, possibly because of the formation of nanoparticle aggregates that obstructed the flow path.

Finally, it is highlighted that this flowline design has successfully shown to be a suitable setting for future research in this field.

Figure 44

Schematic representation of the coupled magnetic device.

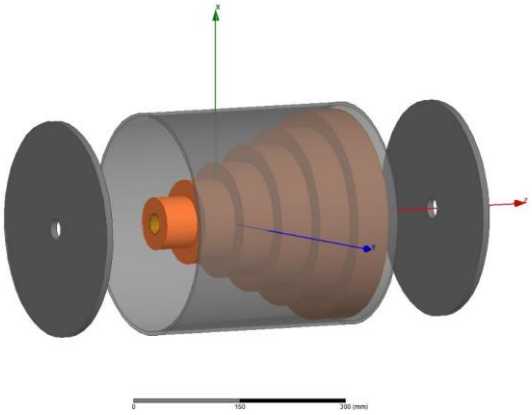

Figure 45

Selective results of the flow of a ferrofluid and a ferrofluid emulsion in a laboratory-scale flowline system, under the effect of alternating linearly increasing magnetic fields.

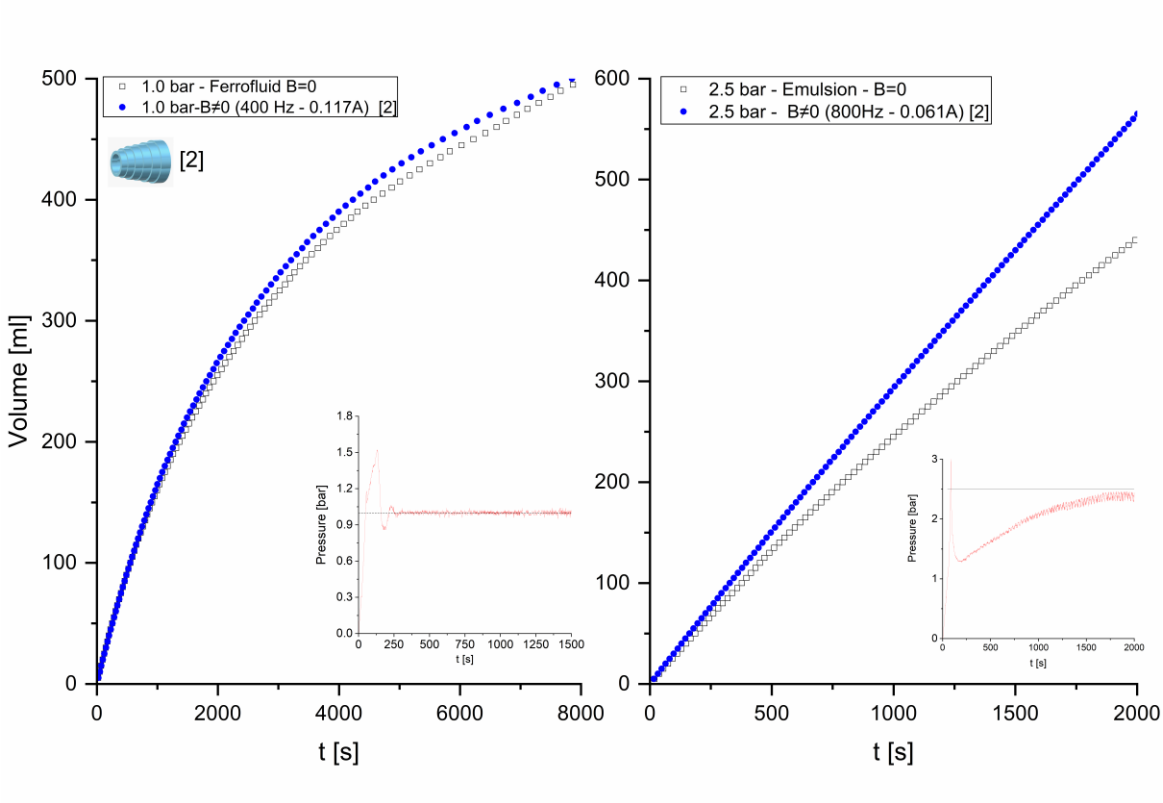

References

1. Contreras-Mateus M, Hethnawi A, Mheibesh Y, Montoya T, Hashlamoun K, Bakir M, et al. Applications of Nanoparticles in Energy and the Environment: Enhanced Oil Upgrading and Recovery and Cleaning up Energy Effluents. Energy Transition: Climate Action and Circularity. ACS Symposium Series. 1412: American Chemical Society; 2022. p. 169-267.

2. Contreras–Mateus MD, López–López MT, Ariza-León E, Chaves–Guerrero A. Rheological implications of the inclusion of ferrofluids and the presence of uniform magnetic field on heavy and extra-heavy crude oils. Fuel. 2021;285:119184.

3. Contreras–Mateus MD, Sánchez FH, Cañas-Martínez DM, Nassar NN, Chaves–Guerrero A. Effect of asphaltene adsorption on the magnetic and magnetorheological properties of heavy crude oils and Fe3O4 nanoparticles systems. Fuel. 2022;318:123684.

4. IEA (2021). World Energy Outlook 2021 IEA, Paris2021 [Available from: https://www.iea.org/reports/world-energy-outlook-2021.

5. Taborda EA, Franco CA, Ruiz MA, Alvarado V, Cortés FB. Experimental and Theoretical Study of Viscosity Reduction in Heavy Crude Oils by Addition of Nanoparticles. Energy & Fuels. 2017;31(2):1329-38.

6. Taborda EA, Alvarado V, Franco CA, Cortés FB. Rheological demonstration of alteration in the heavy crude oil fluid structure upon addition of nanoparticles. Fuel. 2017;189:322-33.

7. Aristizábal-Fontal JE, Cortés FB, Franco CA. Viscosity reduction of extra heavy crude oil by magnetite nanoparticle-based ferrofluids. Adsorption Science & Technology. 2017:026361741770430-.

8. Torres-Díaz I, Rinaldi C. Recent progress in ferrofluids research: novel applications of magnetically controllable and tunable fluids. Soft Matter. 2014;10(43):8584-602.

9. Kole M, Khandekar S. Engineering applications of ferrofluids: A review. Journal of Magnetism and Magnetic Materials. 2021;537:168222.

10. Imran M, Affandi AM, Alam MM, Khan A, Khan AI. Advanced biomedical applications of iron oxide nanostructures based ferrofluids. Nanotechnology. 2021;32(42):422001.

11. Boroun S, Larachi F. Role of magnetic nanoparticles in mixing, transport phenomena and reaction engineering—challenges and opportunities. Current Opinion in Chemical Engineering. 2016;13:91-9.

12. Bera A, Babadagli T. Status of electromagnetic heating for enhanced heavy oil/bitumen recovery and future prospects: A review. Applied Energy. 2015;151:206-26.

13. Deatsch AE, Evans BA. Heating efficiency in magnetic nanoparticle hyperthermia. Journal of Magnetism and Magnetic Materials. 2014;354:163-72.

14. Rosensweig RE. Ferrohydrodynamics: Courier Corporation; 2013.

15. Fannin PC. Magnetic Spectroscopy as an Aide in Understanding Magnetic Fluids. In: Odenbach S, editor. Ferrofluids: Magnetically Controllable Fluids and Their Applications. Berlin, Heidelberg: Springer Berlin Heidelberg; 2002. p. 19-32.

16. Greff J, Babadagli T. Use of nano-metal particles as catalyst under electromagnetic heating for in-situ heavy oil recovery. Journal of Petroleum Science and Engineering. 2013;112:258-65.

17. Ali H, Soleimani H, Yahya N, Khodapanah L, Sabet M, Demiral BMR, et al. Enhanced oil recovery by using electromagnetic-assisted nanofluids: A review. Journal of Molecular Liquids. 2020;309:113095.

18. Soleimani H, Yahya N, Latiff NRA, Zaid HM, Demira BMR, Amighian J. Novel Enhanced Oil Recovery Method Using Co2+xFe2+1-xFe3+2O4 as Magnetic Nanoparticles Activated by Electromagnetic Waves. Journal of Nano Research. 2014;26:111-6.

19. Hassan YM, Guan BH, Zaid HM, Hamza MF, Adil M, Adam AA, et al. Application of Magnetic and Dielectric Nanofluids for Electromagnetic-Assistance Enhanced Oil Recovery: A Review. Crystals. 2021;11(2).

20. Zaid HM, Wan Azahar WA, Soleimani H, Ahmad Latiff NR, Shafie A, Lee KC, et al. Effect of Nickel: Zinc Ratio in Nickel-Zinc-Ferrite Nanoparticles as Surfactant on Recovery Efficiency in Enhanced Oil Recovery. Journal of Nano Research. 2014;29:115-20.

21. Soleimani H, Latiff NRA, Yahya N, Sabet M, Khodapanah L, Kozlowski G, et al. Synthesis and Characterization of Yttrium Iron Garnet (YIG) Nanoparticles Activated by Electromagnetic Wave in Enhanced Oil Recovery. Journal of Nano Research. 2016;38:40-6.

22. Soleimani H, Ahmad Latiff NR, Yahya N, Zaid HM, Sabet M, Guan BH, et al. Effect of Annealing Temperature on the Crystallization of Hematite-Alumina (Fe2O3-Al2O3) Nanocomposite and its Influence in EOR Application. Journal of Nano Research. 2014;29:105-13.

23. Adil M, Lee K, Mohd Zaid H, Ahmad Latiff NR, Alnarabiji MS. Experimental study on electromagnetic-assisted ZnO nanofluid flooding for enhanced oil recovery (EOR). PLOS ONE. 2018;13(2):e0193518.

24. Adil M, Mohd Zaid H, Kean Chuan L. Electromagnetically-induced change in interfacial tension and contact angle of oil droplet using dielectric nanofluids. Fuel. 2020;259:116274.

25. Zhou K, Zhou X, Liu J, Huang Z. Application of magnetic nanoparticles in petroleum industry: A review. Journal of Petroleum Science and Engineering. 2020;188:106943.

26. Vipulanandan C, Mohammed A, Samuel RG. Smart Bentonite Drilling Muds Modified with Iron Oxide Nanoparticles and Characterized Based on the Electrical Resistivity and Rheological Properties with Varying Magnetic Field Strengths and Temperatures. Offshore Technology Conference2017. p. D041S5R05.

27. Vipulanandan C, Maddi AR, Ganpatye AS. Smart Spacer Fluid Modified with Iron Oxide Nanoparticles for In-Situ Property Enhancement was developed for Cleaning Oil Based Drilling Fluids and Characterized Using the Vipulanandan Rheological Model. Offshore Technology Conference2018. p. D041S56R05.

28. Wang H, Lin K-Y, Jing B, Krylova G, Sigmon GE, McGinn P, et al. Removal of oil droplets from contaminated water using magnetic carbon nanotubes. Water Research. 2013;47(12):4198-205.

29. Tskhadaya ND, Bykov IY, Chuprov IF, Lanina TD, Smirnov YG, Lutoev AA. Substantiating parameters of the neodymium magnetic separator construction for afterpurification of emulsified reservoir water (Russian). Neftyanoe khozyaystvo - Oil Industry. 2017;2017(08):112-5.

30. Ko S, Prigiobbe V, Huh C, Bryant S, Bennetzen MV, Mogensen K. Accelerated Oil Droplet Separation from Produced Water Using Magnetic Nanoparticles. SPE Annual Technical Conference and Exhibition2014. p. SPE-170828-MS.

31. Ko S, Kim ES, Park S, Daigle H, Milner TE, Huh C, et al. Oil Droplet Removal from Produced Water Using Nanoparticles and Their Magnetic Separation. SPE Annual Technical Conference and Exhibition2016. p. D031S57R03.

32. Peng J, Liu Q, Xu Z, Masliyah J. Novel Magnetic Demulsifier for Water Removal from Diluted Bitumen Emulsion. Energy & Fuels. 2012;26(5):2705-10.

33. Wang Q, Prigiobbe V, Huh C, Bryant SL, Mogensen K, Bennetzen MV. Removal of Divalent Cations from Brine Using Selective Adsorption onto Magnetic Nanoparticles. International Petroleum Technology Conference2014. p. IPTC-17901-MS.

34. Prigiobbe V, Ko S, Wang Q, Huh C, Bryant SL, Bennetzen MV. Magnetic Nanoparticles for Efficient Removal of Oilfield “Contaminants”: Modeling of Magnetic Separation and Validation. SPE International Symposium on Oilfield Chemistry2015. p. D021S09R07.

35. Sengupta S. An Innovative Approach to Image Fracture Dimensions by Injecting Ferrofluids. Abu Dhabi International Petroleum Conference and Exhibition2012. p. SPE-162365-MS.

36. Aderibigbe A, Cheng K, Heidari Z, Killough J, Fuss T, Stephens WT. Detection of Propping Agents in Fractures Using Magnetic Susceptibility Measurements Enhanced by Magnetic Nanoparticles. SPE Annual Technical Conference and Exhibition2014. p. SPE-170818-MS.

37. An C, Yan B, Alfi M, Mi L, Killough JE, Heidari Z. Estimating spatial distribution of natural fractures by changing NMR T2 relaxation with magnetic nanoparticles. Journal of Petroleum Science and Engineering. 2017;157:273-87.

38. Rahmani AR, Athey AE, Chen J, Wilt MJ. Sensitivity of dipole magnetic tomography to magnetic nanoparticle injectates. Journal of Applied Geophysics. 2014;103:199-214.

39. Huh C, Nizamidin N, Pope GA, Milner TE, Bingqing W. Hydrophobic paramagnetic nanoparticles as intelligent crude oil tracers. Google Patents; 2015.

40. Kalra M, Meribout DMM, Saied I. Modeling and Simulation Study for Black Powder Detection in Gas-Oil Pipelines Using Magnetic Particle Imaging and its Hardware Realization. Abu Dhabi International Petroleum Exhibition & Conference2016. p. D012S103R004.

41. Chang S, Yun W, Eichmann SL, Poitzsch ME, Wang W. Magnetic SERS Composite Nanoparticles for Microfluidic Oil Reservoir Tracer Detection and Nanoprobe Applications. ACS Applied Nano Materials. 2019;2(2):997-1004.

42. Shekhawat DS, Aggarwal A, Agarwal S, Imtiaz MD. Magnetic Recovery-Injecting Newly Designed Magnetic Fracturing Fluid with Applied Magnetic Field for EOR. SPE Asia Pacific Hydraulic Fracturing Conference2016. p. D012S0R4.

43. Kothari N, Raina B, Chandak K, Iyer V, Mahajan H. Application of Ferrofluid for Enhanced Surfactant Flooding in EOR. SPE EUROPEC/EAGE Annual Conference and Exhibition2010. p. SPE-131272-MS.

44. Yahya N, Kashif M, Shafie A, Soleimani H, Zaid HM, Latiff NRA. Improved Oil Recovery by High Magnetic Flux Density Subjected to Iron Oxide Nanofluids. Journal of Nano Research. 2014;26:89-99.

45. Soares FS-M, Prodanovic M, Huh C. Excitable Nanoparticles for Trapped Oil Mobilization. SPE Improved Oil Recovery Symposium2014. p. SPE-169122-MS.

46. Esmaeilnezhad E, Van SL, Chon BH, Choi HJ, Schaffie M, Gholizadeh M, et al. An experimental study on enhanced oil recovery utilizing nanoparticle ferrofluid through the application of a magnetic field. Journal of Industrial and Engineering Chemistry. 2018;58:319-27.

47. Bera A, Babadagli T. Effect of native and injected nano-particles on the efficiency of heavy oil recovery by radio frequency electromagnetic heating. Journal of Petroleum Science and Engineering. 2017;153:244-56.

48. Haindade Z, Bihani AD, Javeri S, Jere C. Enhancing Flow Assurance Using Co-Ni Nanoparticles For Dewaxing Of Production Tubing. SPE International Oilfield Nanotechnology Conference and Exhibition2012. p. SPE-157119-MS.

49. Davidson A, Huh C, Bryant SL. Focused Magnetic Heating Utilizing Superparamagnetic Nanoparticles for Improved Oil Production Applications. SPE International Oilfield Nanotechnology Conference and Exhibition2012. p. SPE-157046-MS.

50. Mehta P, Huh C, Bryant SL. Evaluation of superparamagnetic nanoparticle-based heating for flow assurance in subsea flowlines. International Petroleum Technology Conference2014. p. IPTC-18090-MS.

51. Panthi K, Mohanty KK, Huh C. Precision Control of Gel Formation Using Superparamagnetic Nanoparticle-Based Heating. SPE Annual Technical Conference and Exhibition2015. p. D021S6R02.

52. Esmaeilnezhad E, Van SL, Choi HJ, Chon BH, Schaffie M, Gholizadeh M, et al. Conformance control in oil reservoir based on magnetorheological behavior of nanoparticle suspension. Journal of Environmental Management. 2019;231:1127-34.

53. Bera A, Kumar S. 17 - Applications of magnetic nanoparticles in thermal enhanced oil recovery. In: Hussain CM, Patankar KK, editors. Fundamentals and Industrial Applications of Magnetic Nanoparticles: Woodhead Publishing; 2022. p. 527-53.

54. Yakasai F, Jaafar MZ, Bandyopadhyay S, Agi A, Sidek MA. Application of iron oxide nanoparticles in oil recovery – A critical review of the properties, formulation, recent advances and prospects. Journal of Petroleum Science and Engineering. 2022;208:109438.

55. Wang N, Zhao Y, Prodanović M, Balhoff MT, Huh C. 12012 fundamental mechanisms behind nanotechnology applications in oil and gas: Emerging nano-EOR processes. Frontiers in Nanotechnology. 2022;4.

56. Odenbach S, Thurm S. Magnetoviscous Effects in Ferrofluids. In: Odenbach S, editor. Ferrofluids: Magnetically Controllable Fluids and Their Applications. Berlin, Heidelberg: Springer Berlin Heidelberg; 2002. p. 185-201.

57. Yamaguchi H. Magnetic Fluid and Flow. In: Yamaguchi H, editor. Engineering Fluid Mechanics. Dordrecht: Springer Netherlands; 2008. p. 497-542.

58. Charles SW. The Preparation of Magnetic Fluids. In: Odenbach S, editor. Ferrofluids: Magnetically Controllable Fluids and Their Applications. Berlin, Heidelberg: Springer Berlin Heidelberg; 2002. p. 3-18.

59. Shliomis MI. Effective viscosity of magnetic suspensions. Soviet Physics—JETP 1972;34 (6):1291-4.

60. Galal MM. Stability Properties of Ferromagnetic Fluids in the Presence of an Oblique Field and Mass and Heat Transfer. Physica Scripta. 2002;65(6):490.

61. Cullity BD, Graham CD. Introduction to magnetic materials: John Wiley & Sons; 2011.

62. Rosensweig RE. Basic Equations for Magnetic Fluids with Internal Rotations. In: Odenbach S, editor. Ferrofluids: Magnetically Controllable Fluids and Their Applications. Berlin, Heidelberg: Springer Berlin Heidelberg; 2002. p. 61-84.

63. Carrey J, Mehdaoui B, Respaud M. Simple models for dynamic hysteresis loop calculations of magnetic single-domain nanoparticles: Application to magnetic hyperthermia optimization. Journal of Applied Physics. 2011;109(8):083921.

64. Actis DG, Muñoz Medina GA, Velásquez AA, Pereda C, Sanchez LM, Alvarez VA, et al. Dipolar interactions among magnetic dipoles of iron oxide particles dispersed in mili-size hydrogel beads. Journal of Magnetism and Magnetic Materials. 2020;513:166993.

65. Larachi F, Desvigne D. Ferrofluid magnetoviscous control of wall flow channeling in porous media. China Particuology. 2007;5(1):50-60.

66. Larachi F, Desvigne D. Ferrofluid induced-field effects in inhomogeneous porous media under linear-gradient dc magnetic fields. Chemical Engineering and Processing: Process Intensification. 2007;46(8):729-35.

67. Larachi Fç, Desvigne D. Magnetoviscous control of wall channeling in packed beds using magnetic nanoparticles—Volume-average ferrohydrodynamic model and numerical simulations. Chemical Engineering Science. 2006;61(5):1627-57.

68. Shliomis MI, Morozov KI. Negative viscosity of ferrofluid under alternating magnetic field. Physics of Fluids. 1994;6(8):2855-61.

69. Shliomis MI, Lyubimova TP, Lyubimov DV. FERROHYDRODYNAMICS: AN ESSAY ON THE PROGRESS OF IDEAS. Chemical Engineering Communications. 1988;67(1):275-90.

70. Bacri JC, Perzynski R, Shliomis MI, Burde GI. ``Negative-Viscosity" Effect in a Magnetic Fluid. Physical Review Letters. 1995;75(11):2128-31.

71. Rosensweig RE. “Negative Viscosity” in a Magnetic Fluid. Science. 1996;271(5249):614-.

72. Chaves A, Gutman F, Rinaldi C. Torque and Bulk Flow of Ferrofluid in an Annular Gap Subjected to a Rotating Magnetic Field. Journal of Fluids Engineering. 2006;129(4):412-22.

73. Chaves A, Rinaldi C, Elborai S, He X, Zahn M. Bulk Flow in Ferrofluids in a Uniform Rotating Magnetic Field. Physical Review Letters. 2006;96(19):194501.

74. Chaves A, Torres-Diaz I, Rinaldi C. Flow of ferrofluid in an annular gap in a rotating magnetic field. Physics of Fluids. 2010;22(9):092002.

75. Mao L, Elborai S, He X, Zahn M, Koser H. Direct observation of closed-loop ferrohydrodynamic pumping under traveling magnetic fields. Physical Review B. 2011;84(10):104431.

76. Zahn M, Greer DR. Ferrohydrodynamic pumping in spatially uniform sinusoidally time-varying magnetic fields. Journal of Magnetism and Magnetic Materials. 1995;149(1):165-73.

77. Zahn M, Pioch LL. Ferrofluid flows in AC and traveling wave magnetic fields with effective positive, zero or negative dynamic viscosity. Journal of Magnetism and Magnetic Materials. 1999;201(1):144-8.

78. Sawada T, Tanahashi T, Ando T. Two-dimensional flow of magnetic fluid between two parallel plates. Journal of Magnetism and Magnetic Materials. 1987;65(2):327-9.

79. Kamiyama S, Okubo M, Fujisawa F. Recent developments of technology in magnetic fluid experiments. Experimental Thermal and Fluid Science. 1992;5(5):641-51.

80. Borglin SE, Moridis GJ, Oldenburg CM. Experimental Studies of the Flow of Ferrofluid in Porous Media. Transport in Porous Media. 2000;41(1):61-80.

81. Zakinyan A, Mkrtchyan L, Grunenko V, Dikansky Y. Ferrofluid Capillary Rise in Porous Medium Under the Action of Nonuniform Magnetic Field. Journal of Fluids Engineering. 2016;139(1).

82. Zahn M, Rosensweig R. Stability of magnetic fluid penetration through a porous medium with uniform magnetic field oblique to the interface. IEEE Transactions on Magnetics. 1980;16(2):275-82.

83. Zahn M, Rosensweig RE. Magnetic field gradient effects on magnetic fluid stabilization. Journal of Magnetism and Magnetic Materials. 1987;65(2):293-300.

84. Miranda JA. Rotating Hele-Shaw cells with ferrofluids. Physical Review E. 2000;62(2):2985-8.

85. Jackson DP, Miranda JA. Controlling fingering instabilities in rotating ferrofluids. Physical Review E. 2003;67(1):017301.

86. Verma AP, Rajput AK. Instabilities in displacement processes through porous media with magnetic fluid. Journal of Magnetism and Magnetic Materials. 1987;65(2):330-4.

87. Shah RC, Verma AP. Fingero-imbibition phenomenon through porous media with magnetic fluid. Indian journal of engineering & materials sciences. 1998;5(6):411-5.

88. Parikh AK, Mehta MN, Pradhan VH, editors. Mathematical modeling and analysis of Fingero-Imbibition phenomenon in vertical downward cylindrical homogeneous porous matrix. 2013 Nirma University International Conference on Engineering (NUiCONE); 2013 28-30 Nov. 2013.

89. Flament C, Pacitto G, Bacri JC, Drikis I, Cebers A. Viscous fingering in a magnetic fluid. I. Radial Hele-Shaw flow. Physics of Fluids. 1998;10(10):2464-72.

90. Pacitto G, Flament C, Bacri JC. Viscous fingering in a magnetic fluid. II. Linear Hele–Shaw flow. Physics of Fluids. 2001;13(11):3196-203.

91. Miranda JA, Widom M. Parallel flow in Hele-Shaw cells with ferrofluids. Physical Review E. 2000;61(2):2114-7.

92. Rosensweig RE, Zahn M, Shumovich R. Labyrinthine instability in magnetic and dielectric fluids. Journal of Magnetism and Magnetic Materials. 1983;39(1):127-32.

93. Moatimid GM. Nonlinear Kelvin-Helmholtz instability of two miscible ferrofluids in porous media. Zeitschrift für angewandte Mathematik und Physik ZAMP. 2005;57(1):133-59.

94. Lorenz C, Zahn M. Hele-Shaw Ferrohydrodynamics for Rotating and dc Axial Magnetic Fields. Physics of Fluids. 2003;15(9):S4-S.

95. Rhodes S, Perez J, Elborai S, Lee S-H, Zahn M. Ferrofluid spiral formations and continuous-to-discrete phase transitions under simultaneously applied DC axial and AC in-plane rotating magnetic fields. Journal of Magnetism and Magnetic Materials. 2005;289:353-5.

96. Elborai S, Kim DK, He X, Lee SH, Rhodes S, Zahn M. Self-forming, quasi-two-dimensional, magnetic-fluid patterns with applied in-plane-rotating and dc-axial magnetic fields. Journal of Applied Physics. 2005;97(10):10Q303.

97. Jackson DP, Miranda JA. Confined ferrofluid droplet in crossed magnetic fields. The European Physical Journal E. 2007;23(4):389-96.

98. Kaloni PN, Mahajan A. Stability of magnetic fluid motions in a saturated porous medium. Zeitschrift für angewandte Mathematik und Physik. 2011;62(3):529-38.

99. Bashtovoi V, Kuzhir P, Reks A. Capillary ascension of magnetic fluids. Journal of Magnetism and Magnetic Materials. 2002;252:265-7.

100. Reza Rahmani A, Prodanović M, Bryant SL, Huh C. Quasi-static analysis of a ferrofluid blob in a capillary tube. Journal of Applied Physics. 2012;111(7):074901.

101. Gohil VP, Meher R. Effect of Viscous Fluid on the Counter-Current Imbibition Phenomenon in Two-Phase Fluid Flow Through Heterogeneous Porous Media with Magnetic Field. Iranian Journal of Science and Technology, Transactions A: Science. 2019;43(4):1799-810.

102. Huang T, Yao J, Huang Z, Yin X, Xie H, Zhang J. Numerical simulation on ferrofluid flow in fractured porous media based on discrete-fracture model. Open Physics. 2017;15(1):370-8.

103. Huang T, Liao X, Huang Z, Wang R. Numerical Simulation of Ferrofluid Flow in Heterogeneous and Fractured Porous Media Based on Finite Element Method. Frontiers in Earth Science. 2021;9.

104. Moridis GJ, Borglin SE, Oldenburg CM, Becker A. Theoretical and experimental investigations of ferrofluids for guiding and detecting liquids in the subsurface. FY 1997 annual report. United States; 1998 1998-03-01.

105. El-Amin MF, Brahimi T. Numerical Modeling of Magnetic Nanoparticles Transport in a Two-Phase Flow in Porous Media. SPE Reservoir Characterisation and Simulation Conference and Exhibition2017. p. D011S02R02.

106. Prodanovic M, Ryoo S, Rahmani AR, Kuranov R, Kotsmar C, Milner TE, et al. Effects of Magnetic Field on the Motion of Multiphase Fluids Containing Paramagnetic Particles in Porous Media. SPE Improved Oil Recovery Symposium2010. p. SPE-129850-MS.

107. El-Amin MF, Saad AM, Salama A, Sun S. Modeling and Analysis of Magnetic Nanoparticles Injection in Water-Oil Two-Phase Flow in Porous Media under Magnetic Field Effect. Geofluids. 2017;2017:3602593.

108. Divandari H, Hemmati-Sarapardeh A, Schaffie M, Ranjbar M. Integrating synthesized citric acid-coated magnetite nanoparticles with magnetic fields for enhanced oil recovery: Experimental study and mechanistic understanding. Journal of Petroleum Science and Engineering. 2019;174:425-36.

109. Wang N, Liu Y, Cha L, Prodanovic M, Balhoff M. Microfluidic and Numerical Investigation of Trapped Oil Mobilization with Hydrophilic Magnetic Nanoparticles. SPE Annual Technical Conference and Exhibition2020. p. D031S29R08.

110. Wang N, Liu Y, Cha L, Balhoff MT, Prodanovic M. Experimental Investigation of Trapped Oil Mobilization with Ferrofluid. SPE Journal. 2022;27(01):753-70.

111. Amrouche F, Gomari SR, Islam M, Xu D. A novel hybrid technique to enhance oil production from oil-wet carbonate reservoirs by combining a magnetic field with alumina and iron oxide nanoparticles. Journal of Cleaner Production. 2021;281:124891.

112. Amrouche F, Blunt MJ, Iglauer S, Short M, Crosbie T, Cordero E, et al. Using magnesium oxide nanoparticles in a magnetic field to enhance oil production from oil-wet carbonate reservoirs. Materials Today Chemistry. 2023;27:101342.

113. Bear J. Dynamics of fluids in porous media: Courier Corporation; 2013.

114. Patel HS, Meher R. Simulation of Imbibition Phenomena in Fluid Flow through Fractured Heterogeneous Porous Media with Different Porous Materials. Journal of Applied Fluid Mechanics. 2017;10(5):1451-60.

115. Scheidegger AE. The physics of flow through porous media. University of Toronto. Toronto Press, 353p; 1974.

116. Oldenburg CM, Borglin SE, Moridis GJ. Numerical Simulation of Ferrofluid Flow for Subsurface Environmental Engineering Applications. Transport in Porous Media. 2000;38(3):319-44.

117. Pooladi-Darvish M, Firoozabadi A. Cocurrent and Countercurrent Imbibition in a Water-Wet Matrix Block. SPE Journal. 2000;5(01):3-11.

118. Ju B, Fan T. Experimental study and mathematical model of nanoparticle transport in porous media. Powder Technology. 2009;192(2):195-202.

119. Ryoo S, Rahmani AR, Yoon KY, Prodanovic M, Kotsmar C, Milner TE, et al. Theoretical and Experimental Investigation of the Motion of Multiphase Fluids Containing Paramagnetic Nanoparticles in Porous Media. SPE Annual Technical Conference and Exhibition2010. p. SPE-134879-MS.

120. Rinaldi C, Chaves A, Elborai S, He X, Zahn M. Magnetic fluid rheology and flows. Current Opinion in Colloid & Interface Science. 2005;10(3):141-57.

121. Joseph A, Mathew S. Ferrofluids: Synthetic Strategies, Stabilization, Physicochemical Features, Characterization, and Applications. ChemPlusChem. 2014;79(10):1382-420.

122. Zeuner A, Richter R, Rehberg I. Experiments on negative and positive magnetoviscosity in an alternating magnetic field. Physical Review E. 1998;58(5):6287-93.

123. Felderhof BU. Flow of a ferrofluid down a tube in an oscillating magnetic field. Physical Review E. 2001;64(2):021508.

124. Felderhof BU, Kroh HJ. Hydrodynamics of magnetic and dielectric fluids in interaction with the electromagnetic field. The Journal of Chemical Physics. 1999;110(15):7403-11.

125. Schumacher KR, Sellien I, Knoke GS, Cader T, Finlayson BA. Experiment and simulation of laminar and turbulent ferrofluid pipe flow in an oscillating magnetic field. Physical Review E. 2003;67(2):026308.

126. Krekhov AP, Shliomis MI, Kamiyama S. Ferrofluid pipe flow in an oscillating magnetic field. Physics of Fluids. 2005;17(3):033105.

127. Gazeau F, Baravian C, Bacri JC, Perzynski R, Shliomis MI. Energy conversion in ferrofluids: Magnetic nanoparticles as motors or generators. Physical Review E. 1997;56(1):614-8.

128. Zeuner A, Richter R, Rehberg I. On the consistency of the standard model for magnetoviscosity in an alternating magnetic field. Journal of Magnetism and Magnetic Materials. 1999;201(1):191-4.

129. Papadopoulos PK, Vafeas P, Hatzikonstantinou PM. Ferrofluid pipe flow under the influence of the magnetic field of a cylindrical coil. Physics of Fluids. 2012;24(12):122002.

130. Henjes K. Maxwell's equations and vorticity: A note on the viscosity of magnetic fluids. Journal of Magnetism and Magnetic Materials. 1995;146(3):L236-L40.

131. Krauß R, Liu M, Reimann B, Richter R, Rehberg I. Pumping fluid by magnetic surface stress. New Journal of Physics. 2006;8(1):18.

132. Huc AY. Heavy crude oils - From Geology to Upgrading - An Overview. France: Editions Technip; 2010.

133. Lesueur D. The colloidal structure of bitumen: Consequences on the rheology and on the mechanisms of bitumen modification. Advances in Colloid and Interface Science. 2009;145(1–2):42-82.

134. Merola MC, Carotenuto C, Gargiulo V, Stanzione F, Ciajolo A, Minale M. Chemical–physical analysis of rheologically different samples of a heavy crude oil. Fuel Processing Technology. 2016;148:236-47.

135. Hasan SW, Ghannam MT, Esmail N. Heavy crude oil viscosity reduction and rheology for pipeline transportation. Fuel. 2010;89(5):1095-100.

136. Martínez-Palou R, Mosqueira MDL, Zapata-Rendón B, Mar-Juárez E, Bernal-Huicochea C, de la Cruz Clavel-López J, et al. Transportation of heavy and extra-heavy crude oil by pipeline: A review. Journal of Petroleum Science and Engineering. 2011;75(3-4):274-82.

137. Sjöblom J, Aske N, Auflem IH, Brandal Ø, Havre TE, Sæther Ø, et al. Our current understanding of water-in-crude oil emulsions.: Recent characterization techniques and high pressure performance. Advances in Colloid and Interface Science. 2003;100:399-473.

138. Behzadfar E, Hatzikiriakos SG. Viscoelastic properties and constitutive modelling of bitumen. Fuel. 2013;108:391-9.

139. Mouazen M, Poulesquen A, Vergnes B. Correlation between thermal and rheological studies to characterize the behavior of bitumen. Rheologica Acta. 2011;50(2):169-78.

140. Behzadfar E, Hatzikiriakos SG. Rheology of bitumen: Effects of temperature, pressure, CO2 concentration and shear rate. Fuel. 2014;116:578-87.

141. Behzadfar E, Karamikamkar S, Hatzikiriakos SG. Rheology and diffusivity of bitumen with liquid and supercritical CO2. Fuel. 2019;244:431-8.

142. Shayan NN, Mirzayi B. Adsorption and Removal of Asphaltene Using Synthesized Maghemite and Hematite Nanoparticles. Energy & Fuels. 2015;29(3):1397-406.

143. Giraldo-Dávila D, Chacón-Patiño ML, McKenna AM, Blanco-Tirado C, Combariza MY. Correlations between Molecular Composition and Adsorption, Aggregation, and Emulsifying Behaviors of PetroPhase 2017 Asphaltenes and Their Thin-Layer Chromatography Fractions. Energy & Fuels. 2018;32(3):2769-80.

144. Abivin P, Taylor SD, Freed D. Thermal Behavior and Viscoelasticity of Heavy Oils. Energy & Fuels. 2012;26(6):3448-61.

145. Mortazavi-Manesh S, Shaw JM. Thixotropic Rheological Behavior of Maya Crude Oil. Energy & Fuels. 2014;28(2):972-9.

146. Nassar NN. Asphaltene Adsorption onto Alumina Nanoparticles: Kinetics and Thermodynamic Studies. Energy & Fuels. 2010;24(8):4116-22.

147. Muñoz JAD, Ancheyta J, Castañeda LC. Required Viscosity Values To Ensure Proper Transportation of Crude Oil by Pipeline. Energy & Fuels. 2016;30(11):8850-4.

148. Hart A. A review of technologies for transporting heavy crude oil and bitumen via pipelines. Journal of Petroleum Exploration and Production Technology. 2014;4(3):327-36.

149. Tao R, Gu GQ. Suppressing turbulence and enhancing liquid suspension flow in pipelines with electrorheology. Physical Review E. 2015;91(1):012304.

150. Rocha N, González C, Marques LCdC, Vaitsman DS. A preliminary study on the magnetic treatment of fluids. Petroleum science and technology. 2000;18(1-2):33-50.

151. Tao R, Xu X. Reducing the viscosity of crude oil by pulsed electric or magnetic field. Energy & fuels. 2006;20(5):2046-51.

152. Loskutova YV, Yudina NV, Pisareva SI. Effect of magnetic field on the paramagnetic, antioxidant, and viscosity characteristics of some crude oils. Petroleum Chemistry. 2008;48(1):51-5.

153. Evdokimov IN, Kornishin KA. Apparent Disaggregation of Colloids in a Magnetically Treated Crude Oil. Energy & Fuels. 2009;23(8):4016-20.

154. Jiang C, Zhao K, Zhao LJ, Jin WJ, Yang YP, Chen SH. Probing Disaggregation of Crude Oil in a Magnetic Field with Terahertz Time-Domain Spectroscopy. Energy & Fuels. 2014;28(1):483-7.

155. Khalaf MH, Mansoori GA, Yong CW. Magnetic treatment of petroleum and its relation with asphaltene aggregation onset (an atomistic investigation). Journal of Petroleum Science and Engineering. 2019;176:926-33.

156. Gonçalves JL, Bombard AJF, Soares DAW, Carvalho RDM, Nascimento A, Silva MR, et al. Study of the factors responsible for the rheology change of a Brazilian crude oil under magnetic fields. Energy & Fuels. 2011;25(8):3537-43.

157. Tao R, Du E, Tang H, Xu X. Neutron scattering studies of crude oil viscosity reduction with electric field. Fuel. 2014;134:493-8.

158. Tao R. Application of Electrorheology to Improve Crude Oil Flowing Properties Through Pipeline. InTech; 2016.

159. Gonçalves JL, Bombard AJF, Soares DAW, Alcantara GB. Reduction of paraffin precipitation and viscosity of Brazilian crude oil exposed to magnetic fields. Energy & Fuels. 2010;24(5):3144-9.

160. Ivakhnenko OP, Potter DK. Magnetic susceptibility of petroleum reservoir fluids. Physics and Chemistry of the Earth, Parts A/B/C. 2004;29(13):899-907.

161. Nassar NN, Hassan A, Pereira-Almao P. Metal Oxide Nanoparticles for Asphaltene Adsorption and Oxidation. Energy & Fuels. 2011;25(3):1017-23.

162. Franco CA, Nassar NN, Ruiz MA, Pereira-Almao P, Cortés FB. Nanoparticles for Inhibition of Asphaltenes Damage: Adsorption Study and Displacement Test on Porous Media. Energy & Fuels. 2013;27(6):2899-907.

163. Taborda EA, Franco CA, Lopera SH, Alvarado V, Cortés FB. Effect of nanoparticles/nanofluids on the rheology of heavy crude oil and its mobility on porous media at reservoir conditions. Fuel. 2016;184:222-32.

164. Aristizábal-Fontal JE, Cortés FB, Franco CA. Viscosity reduction of extra heavy crude oil by magnetite nanoparticle-based ferrofluids. Adsorption Science & Technology. 2017;36(1-2):23-45.

165. Ezeonyeka NL, Hemmati-Sarapardeh A, Husein MM. Asphaltenes Adsorption onto Metal Oxide Nanoparticles: A Critical Evaluation of Measurement Techniques. Energy & Fuels. 2018;32(2):2213-23.

166. Fritschy G, Papirer E. Interactions between a bitumen, its components and model fillers. Fuel. 1978;57(11):701-4.

167. Nassar NN, Hassan A, Carbognani L, Lopez-Linares F, Pereira-Almao P. Iron oxide nanoparticles for rapid adsorption and enhanced catalytic oxidation of thermally cracked asphaltenes. Fuel. 2012;95:257-62.

168. González MF, Stull CS, López-Linares F, Pereira-Almao P. Comparing Asphaltene Adsorption with Model Heavy Molecules over Macroporous Solid Surfaces. Energy & Fuels. 2007;21(1):234-41.

169. Drummond C, Israelachvili J. Fundamental studies of crude oil–surface water interactions and its relationship to reservoir wettability. Journal of Petroleum Science and Engineering. 2004;45(1):61-81.

170. Franco CA, Lozano MM, Acevedo S, Nassar NN, Cortés FB. Effects of Resin I on Asphaltene Adsorption onto Nanoparticles: A Novel Method for Obtaining Asphaltenes/Resin Isotherms. Energy & Fuels. 2016;30(1):264-72.

171. Khalil M, Jan BM, Tong CW, Berawi MA. Advanced nanomaterials in oil and gas industry: Design, application and challenges. Applied Energy. 2017;191:287-310.

172. McTague JP. Magnetoviscosity of Magnetic Colloids. The Journal of Chemical Physics. 1969;51(1):133-6.

173. Hall WF, Busenberg SN. Viscosity of magnetic suspensions. The Journal of Chemical Physics. 1969;51:137-44.

174. Shliomis MI, Morozov KI. Negative viscosity of ferrofluid under alternating magnetic field. Physics of Fluids 1994;6(8):2855-61.

175. Bacri JC, Perzynski R, Shliomis MI, Burde GI. "Negative-Viscosity" Effect in a Magnetic Fluid. Physical Review Letters. 1995;75(11):2128-31.

176. Moskowitz R, Rosensweig RE. Nonmechanical torque-driven flow of a ferromagnetic fluid by an electromagnetic field. Applied Physics Letters. 1967;11(10):301-3.

177. Chaves A, Zahn M, Rinaldi C. Spin-up flow of ferrofluids: Asymptotic theory and experimental measurements. Physics of Fluids. 2008;20(5):053102.

178. Chaves A, Torres-Diaz I, Rinaldi C. Flow of ferrofluid in an annular gap in a rotating magnetic field. Physics of Fluids 2010;22(9):92002.

179. Mao L, Koser H. Ferrohydrodynamic pumping in spatially traveling sinusoidally time-varying magnetic fields. Journal of Magnetism and Magnetic Materials. 2005;289:199-202.

180. Ali N, Zhang B, Zhang H, Zaman W, Li X, Li W, et al. Interfacially active and magnetically responsive composite nanoparticles with raspberry like structure; synthesis and its applications for heavy crude oil/water separation. Colloids and Surfaces A: Physicochemical and Engineering Aspects. 2015;472:38-49.

181. Ali N, Zhang B, Zhang H, Li W, Zaman W, Tian L, et al. Novel Janus magnetic micro particle synthesis and its applications as a demulsifier for breaking heavy crude oil and water emulsion. Fuel. 2015;141:258-67.

182. Liang J, Du N, Song S, Hou W. Magnetic demulsification of diluted crude oil-in-water nanoemulsions using oleic acid-coated magnetite nanoparticles. Colloids and Surfaces A: Physicochemical and Engineering Aspects. 2015;466:197-202.

183. Xiong Y, Huang X, Liu J, Lu L, Peng K. Preparation of magnetically responsive bacterial demulsifier with special surface properties for efficient demulsification of water/oil emulsion. Renewable Energy. 2017.

184. Farrokhi F, Jafari Nasr MR, Rahimpour MR, Arjmand M, Vaziri SA. Application of a novel magnetic nanoparticle as demulsifier for dewatering in crude oil emulsion. Separation Science and Technology. 2018;53(3):551-8.

185. Pavía-Sanders A, Zhang S, Flores JA, Sanders JE, Raymond JE, Wooley KL. Robust Magnetic/Polymer Hybrid Nanoparticles Designed for Crude Oil Entrapment and Recovery in Aqueous Environments. ACS Nano. 2013;7(9):7552-61.

186. Santagata E, Baglieri O, Tsantilis L, Vercelli A. Development of test protocols for the analysis of magneto-rheological properties of field-responsive bituminous binders. American Journal of Applied Sciences. 2014;11(3):505-19.

187. Shekhawat DS, Aggarwal A, Agarwal S, Imtiaz MD. Magnetic Recovery-Injecting Newly Designed Magnetic Fracturing Fluid with Applied Magnetic Field for EOR. Beijing, China: Society of Petroleum Engineers; 2016.

188. ASTM D6560-12. Standard Test Method for Determination of Asphaltenes (Heptane Insolubles) in Crude Petroleum and Petroleum Products West Conshohocken, PA2012 [Available from: www.astm.org.

189. ASTM D70-18a. Standard Test Method for Density of Semi-Solid Asphalt Binder (Pycnometer Method) West Conshohocken, PA: ASTM International; 2018 [Available from: www.astm.org.

190. López-López MT, Durán JDG, Delgado AV, González-Caballero F. Stability and magnetic characterization of oleate-covered magnetite ferrofluids in different nonpolar carriers. Journal of Colloid and Interface Science. 2005;291(1):144-51.

191. López-López MT, de Vicente J, Bossis G, González-Caballero F, Durán J. Preparation of stable magnetorheological fluids based on extremely bimodal iron–magnetite suspensions. Journal of Materials Research. 2005;20(4):874-81.

192. Chin BD, Park JH, Kwon MH, Park OO. Rheological properties and dispersion stability of magnetorheological (MR) suspensions. Rheologica Acta. 2001;40(3):211-9.

193. Tan L, Liu B, Glebe U, Böker A. Magnetic Field-Induced Assembly of Superparamagnetic Cobalt Nanoparticles on Substrates and at Liquid–Air Interface. Langmuir. 2018;34(46):13993-4002.

194. Hoepfner MP, Fogler HS. Multiscale Scattering Investigations of Asphaltene Cluster Breakup, Nanoaggregate Dissociation, and Molecular Ordering. Langmuir. 2013;29(49):15423-32.

195. Morrison FA. Understanding rheology: Oxford University Press, USA; 2001.

196. Chailleux E, Ramond G, Such C, De La Roche C. A mathematical-based master-curve construction method applied to complex modulus of bituminous materials. Road Materials and Pavement Design. 2006;7(sup1):75-92.

197. Ferry JD. Viscoelastic properties of polymers: John Wiley & Sons; 1980.

198. Soto-Castruita E, Ramírez-González PV, Martínez-Cortés U, Quiñones-Cisneros SE. Effect of the Temperature on the Non-Newtonian Behavior of Heavy Oils. Energy & Fuels. 2015;29(5):2883-9.

199. Vargas XA, Afanasjeva N, Álvarez M, Marchal PH, Choplin L. Asphalt rheology evolution through thermo-oxidation (aging) in a rheo-reactor. Fuel. 2008;87(13):3018-23.

200. Meyer V, Pilliez J, Habas J-P, Montel F, Creux P. Rheological Evidence of the Diffusionnal Aggregation of Asphaltenes in Extra-Heavy Crude Oils. Energy & Fuels. 2008;22(5):3154-9.

201. Mouazen M, Poulesquen A, Vergnes B. Influence of Thermomechanical History on Chemical and Rheological Behavior of Bitumen. Energy & Fuels. 2011;25(10):4614-21.

202. Winter HH. Analysis of dynamic mechanical data: inversion into a relaxation time spectrum and consistency check. Journal of Non-Newtonian Fluid Mechanics. 1997;68(2):225-39.

203. Macosko CW. Rheology: principles, measurements, and applications: Wiley-vch; 1994.

204. Baumgaertel M, Winter HH. Determination of discrete relaxation and retardation time spectra from dynamic mechanical data. Rheologica Acta. 1989;28(6):511-9.

205. Ghannam MT, Hasan SW, Abu-Jdayil B, Esmail N. Rheological properties of heavy & light crude oil mixtures for improving flowability. Journal of Petroleum Science and Engineering. 2012;81:122-8.

206. Nassar NN, Betancur S, Acevedo S, Franco CA, Cortés FB. Development of a Population Balance Model to Describe the Influence of Shear and Nanoparticles on the Aggregation and Fragmentation of Asphaltene Aggregates. Industrial & Engineering Chemistry Research. 2015;54(33):8201-11.

207. Mezger TG. The rheology handbook: for users of rotational and oscillatory rheometers: Vincentz Network GmbH & Co KG; 2006.

208. Dimitriou CJ, McKinley GH. A comprehensive constitutive law for waxy crude oil: a thixotropic yield stress fluid. Soft Matter. 2014;10(35):6619-44.

209. Mukherjee A, Sharma D, Chauhan SS, Singh H. Time-Dependent and Shear-Dependent Transient Viscosity of an Alumina Suspension. 2015;36(7):951-69.

210. Petekidis G, Moussaïd A, Pusey PN. Rearrangements in hard-sphere glasses under oscillatory shear strain. Physical Review E. 2002;66(5):051402.

211. Merhi D, Lemaire E, Bossis G, Moukalled F. Particle migration in a concentrated suspension flowing between rotating parallel plates: Investigation of diffusion flux coefficients. 2005;49(6):1429-48.

212. Krishnan GP, Beimfohr S, Leighton DT. Shear-induced radial segregation in bidisperse suspensions. Journal of Fluid Mechanics. 1996;321(-1):371-93.

213. Masson JF, Polomark GM, Collins P. Time-Dependent Microstructure of Bitumen and Its Fractions by Modulated Differential Scanning Calorimetry. Energy & Fuels. 2002;16(2):470-6.

214. Soto-Aquino D, Rinaldi C. Magnetoviscosity in dilute ferrofluids from rotational Brownian dynamics simulations. Physical Review E. 2010;82(4):046310.

215. Pop LM, Odenbach S. Capillary viscosimetry on ferrofluids. Journal of Physics: Condensed Matter. 2008;20(20):204139.

216. Pop LM, Odenbach S. Investigation of the microscopic reason for the magnetoviscous effect in ferrofluids studied by small angle neutron scattering. Journal of Physics: Condensed Matter. 2006;18(38):S2785-S802.

217. Odenbach S. MAGNETOVISCOUS AND VISCOELASTIC EFFECTS IN FERROFLUIDS. International Journal of Modern Physics B. 2000;14(16):1615-31.

218. Ghasemi E, Mirhabibi A, Edrissi M. Synthesis and rheological properties of an iron oxide ferrofluid. Journal of Magnetism and Magnetic Materials. 2008;320(21):2635-9.

219. Masoud Hosseini S, Fazlali A, Ghasemi E, Ahmadi Moghaddam H, Salehi M. Rheological properties of a γ-Fe2O3 paraffin-based ferrofluid. Journal of Magnetism and Magnetic Materials. 2010;322(23):3792-6.

220. Jiang C, Leung CW, Pong PWT. Magnetic-Field-Assisted Assembly of Anisotropic Superstructures by Iron Oxide Nanoparticles and Their Enhanced Magnetism. Nanoscale Research Letters. 2016;11(1):189.

221. Mousavi NSS, Khapli SD, Kumar S. Direct observations of field-induced assemblies in magnetite ferrofluids. Journal of Applied Physics. 2015;117(10):103907.

222. IEA (2022). World Energy Outlook 2022 IEA, Paris2022 [Available from: https://www.iea.org/reports/world-energy-outlook-2022.

223. Anisimov MA, Ganeeva YM, Gorodetskii EE, Deshabo VA, Kosov VI, Kuryakov VN, et al. Effects of Resins on Aggregation and Stability of Asphaltenes. Energy & Fuels. 2014;28(10):6200-9.

224. Pereira JC, López I, Salas R, Silva F, Fernández C, Urbina C, et al. Resins: The Molecules Responsible for the Stability/Instability Phenomena of Asphaltenes. Energy & Fuels. 2007;21(3):1317-21.

225. Adams JJ. Asphaltene Adsorption, a Literature Review. Energy & Fuels. 2014;28(5):2831-56.

226. Sadegh Mazloom M, Hemmati-Sarapardeh A, Husein MM, Shokrollahzadeh Behbahani H, Zendehboudi S. Application of nanoparticles for asphaltenes adsorption and oxidation: A critical review of challenges and recent progress. Fuel. 2020;279:117763.

227. Hosseinpour N, Khodadadi AA, Bahramian A, Mortazavi Y. Asphaltene Adsorption onto Acidic/Basic Metal Oxide Nanoparticles toward in Situ Upgrading of Reservoir Oils by Nanotechnology. Langmuir. 2013;29(46):14135-46.

228. Balestrin LBdS, Cardoso MB, Loh W. Using Atomic Force Microscopy To Detect Asphaltene Colloidal Particles in Crude Oils. Energy & Fuels. 2017;31(4):3738-46.

229. Mirzayi B, Shayan NN. Adsorption kinetics and catalytic oxidation of asphaltene on synthesized maghemite nanoparticles. Journal of Petroleum Science and Engineering. 2014;121:134-41.

230. Liu H, Liu Z, Guo A, Chen K, Sun S, Wang Z. Peptizing Effect of the Native Heavy Resin Fraction on Asphaltenes. Energy & Fuels. 2018;32(3):3380-90.

231. Derakhshani-Molayousefi M, McCullagh M. Deterring Effect of Resins on the Aggregation of Asphaltenes in n-Heptane. Energy & Fuels. 2020;34(12):16081-8.

232. Soorghali F, Zolghadr A, Ayatollahi S. Effects of Native and Non-Native Resins on Asphaltene Deposition and the Change of Surface Topography at Different Pressures: An Experimental Investigation. Energy & Fuels. 2015;29(9):5487-94.

233. León O, Contreras E, Rogel E, Dambakli G, Acevedo S, Carbognani L, et al. Adsorption of Native Resins on Asphaltene Particles: A Correlation between Adsorption and Activity. Langmuir. 2002;18(13):5106-12.

234. Ramirez-Corredores MM. Chapter 2 - Asphaltenes. In: Ramirez-Corredores MM, editor. The Science and Technology of Unconventional Oils. Amsterdam: Academic Press; 2017. p. 41-222.

235. Koots JA, Speight JG. Relation of petroleum resins to asphaltenes. Fuel. 1975;54(3):179-84.

236. Marques LCC, Pereira JO, Bueno AD, Marques VS, Lucas EF, Mansur CRE, et al. A study of asphaltene-resin interactions. Journal of the Brazilian Chemical Society. 2012;23(10):1880-8.

237. Rogel E. Molecular Thermodynamic Approach to the Formation of Mixed Asphaltene−Resin Aggregates. Energy & Fuels. 2008;22(6):3922-9.

238. Sedghi M, Goual L. Role of Resins on Asphaltene Stability. Energy & Fuels. 2010;24(4):2275-80.

239. Acevedo S, Guzman K, Ocanto O. Determination of the Number Average Molecular Mass of Asphaltenes (Mn) Using Their Soluble A2 Fraction and the Vapor Pressure Osmometry (VPO) Technique. Energy & Fuels. 2010;24(3):1809-12.

240. Chang C-L, Fogler HS. Stabilization of Asphaltenes in Aliphatic Solvents Using Alkylbenzene-Derived Amphiphiles. 1. Effect of the Chemical Structure of Amphiphiles on Asphaltene Stabilization. Langmuir. 1994;10(6):1749-57.

241. Zhong X, Chen J, An R, Li K, Chen M. A state-of-the-art review of nanoparticle applications with a focus on heavy oil viscosity reduction. Journal of Molecular Liquids. 2021;344:117845.

242. Mironov N, Milordov D, Tazeeva E, Tazeev D, Abilova G, Yakubova S, et al. Impact of Asphaltenes on the Adsorption Behavior of Petroleum Vanadyl Porphyrins: Kinetic and Thermodynamic Aspects. Energy & Fuels. 2021;35(18):14527-41.

243. Farooq U, Patil A, Panjwani B, Simonsen G. Review on Application of Nanotechnology for Asphaltene Adsorption, Crude Oil Demulsification, and Produced Water Treatment. Energy & Fuels. 2021;35(23):19191-210.

244. Igder M, Hosseinpour N, Biyouki AA, Bahramian A. Control of Asphaltene Aggregation in Reservoir Model Oils along the Production Streamline by Fe3O4 and NiO Nanoparticles. Energy & Fuels. 2018;32(6):6689-97.

245. Varamesh A, Hosseinpour N. Prediction of Asphaltene Precipitation in Reservoir Model Oils in the Presence of Fe3O4 and NiO Nanoparticles by Cubic Plus Association Equation of State. Industrial & Engineering Chemistry Research. 2019;58(10):4293-302.

246. Nassar NN, Hassan A, Pereira-Almao P. Comparative oxidation of adsorbed asphaltenes onto transition metal oxide nanoparticles. Colloids and Surfaces A: Physicochemical and Engineering Aspects. 2011;384(1):145-9.

247. Abu Tarboush BJ, Husein MM. Oxidation of asphaltenes adsorbed onto NiO nanoparticles. Applied Catalysis A: General. 2012;445-446:166-71.

248. Rezvani H, Kazemzadeh Y, Sharifi M, Riazi M, Shojaei S. A new insight into Fe3O4-based nanocomposites for adsorption of asphaltene at the oil/water interface: An experimental interfacial study. Journal of Petroleum Science and Engineering. 2019;177:786-97.

249. Abbas H, Manasrah AD, Saad AA, Sebakhy KO, Bouhadda Y. Adsorption of Algerian Asphaltenes onto Synthesized Maghemite Iron Oxide Nanoparticles. Petroleum Chemistry. 2021;61(1):67-75.

250. Kazemzadeh Y, Eshraghi SE, Kazemi K, Sourani S, Mehrabi M, Ahmadi Y. Behavior of Asphaltene Adsorption onto the Metal Oxide Nanoparticle Surface and Its Effect on Heavy Oil Recovery. Industrial & Engineering Chemistry Research. 2015;54(1):233-9.

251. Rudrake A, Karan K, Horton JH. A combined QCM and XPS investigation of asphaltene adsorption on metal surfaces. Journal of Colloid and Interface Science. 2009;332(1):22-31.

252. Alboudwarej H, Pole D, Svrcek WY, Yarranton HW. Adsorption of Asphaltenes on Metals. Industrial & Engineering Chemistry Research. 2005;44(15):5585-92.

253. Balabin RM, Syunyaev RZ, Schmid T, Stadler J, Lomakina EI, Zenobi R. Asphaltene Adsorption onto an Iron Surface: Combined Near-Infrared (NIR), Raman, and AFM Study of the Kinetics, Thermodynamics, and Layer Structure. Energy & Fuels. 2011;25(1):189-96.

254. ASTM D6560-17. Standard Test Method for Determination of Asphaltenes (Heptane Insolubles) in Crude Petroleum and Petroleum Products. ASTM International, West Conshohocken, PA, 2017, www.astm.org.

255. ASTM D1319-20a. Standard Test Method for Hydrocarbon Types in Liquid Petroleum Products by Fluorescent Indicator Adsorption. ASTM International, West Conshohocken, PA, 2020, www.astm.org.

256. ASTM D2549 - 02(2017). Standard Test Method for Separation of Representative Aromatics and Nonaromatics Fractions of High-Boiling Oils by Elution Chromatography. ASTM International, West Conshohocken, PA, 2017, www.astm.org.

257. ASTM D70 / D70M-21. Standard Test Method for Specific Gravity and Density of Semi-Solid Asphalt Binder (Pycnometer Method). ASTM International, West Conshohocken, PA, 2021, www.astm.org.

258. Worsfold PJ. SPECTROPHOTOMETRY | Overview. In: Worsfold P, Townshend A, Poole C, editors. Encyclopedia of Analytical Science (Second Edition). Oxford: Elsevier; 2005. p. 318-21.

259. Evdokimov IN, Losev AP. On the Nature of UV/Vis Absorption Spectra of Asphaltenes. Petroleum Science and Technology. 2007;25(1-2):55-66.

260. Alboudwarej H, Jakher RK, Svrcek WY, Yarranton HW. Spectrophotometric Measurement of Asphaltene Concentration. Petroleum Science and Technology. 2004;22(5-6):647-64.

261. Hung AM, Fini EH. Absorption spectroscopy to determine the extent and mechanisms of aging in bitumen and asphaltenes. Fuel. 2019;242:408-15.

262. Guo X, Wang J. A general kinetic model for adsorption: Theoretical analysis and modeling. Journal of Molecular Liquids. 2019;288:111100.

263. Wang J, Guo X. Adsorption kinetic models: Physical meanings, applications, and solving methods. Journal of Hazardous Materials. 2020;390:122156.

264. Nassar NN, Ringsred A. Rapid Adsorption of Methylene Blue from Aqueous Solutions by Goethite Nanoadsorbents. Environmental Engineering Science. 2011;29(8):790-7.

265. Ruthven DM. Principles of adsorption and adsorption processes: John Wiley & Sons; 1984.

266. Hines AL, Maddox RN. Mass transfer: fundamentals and applications: Prentice-Hall Englewood Cliffs, NJ; 1985.

267. Sánchez FH, Mendoza Zélis P, Arciniegas ML, Pasquevich GA, Fernández van Raap MB. Dipolar interaction and demagnetizing effects in magnetic nanoparticle dispersions: Introducing the mean-field interacting superparamagnet model. Physical Review B. 2017;95(13):134421.

268. Mercado DF, Cipollone M, González MC, Sánchez FH. Yerba Mate applications: Magnetic response of powders and colloids of iron oxide nanoparticles coated with Ilex paraguariensis derivatives. Journal of Magnetism and Magnetic Materials. 2018;462:13-21.

269. Normile PS, Andersson MS, Mathieu R, Lee SS, Singh G, De Toro JA. Demagnetization effects in dense nanoparticle assemblies. Applied Physics Letters. 2016;109(15):152404.

270. Coey JMD. Magnetism and Magnetic Materials. Cambridge: Cambridge University Press; 2010.

271. Moreno R, Poyser S, Meilak D, Meo A, Jenkins S, Lazarov VK, et al. The role of faceting and elongation on the magnetic anisotropy of magnetite Fe3O4 nanocrystals. Scientific Reports. 2020;10(1):2722.

272. Plazinski W, Rudzinski W, Plazinska A. Theoretical models of sorption kinetics including a surface reaction mechanism: A review. Advances in Colloid and Interface Science. 2009;152(1):2-13.

273. Tsiamis A, Taylor SE. Adsorption Behavior of Asphaltenes and Resins on Kaolinite. Energy & Fuels. 2017;31(10):10576-87.

274. Giraldo J, Nassar NN, Benjumea P, Pereira-Almao P, Cortés FB. Modeling and Prediction of Asphaltene Adsorption Isotherms Using Polanyi's Modified Theory. Energy & Fuels. 2013;27(6):2908-14.

275. Ekholm P, Blomberg E, Claesson P, Auflem IH, Sjöblom J, Kornfeldt A. A Quartz Crystal Microbalance Study of the Adsorption of Asphaltenes and Resins onto a Hydrophilic Surface. Journal of Colloid and Interface Science. 2002;247(2):342-50.

276. Chantrell R, Popplewell J, Charles S. Measurements of particle size distribution parameters in ferrofluids. IEEE Transactions on Magnetics. 1978;14(5):975-7.

277. Liong S, Moore RL. DC and AC Measurements of Magnetite Nanoparticulates and Implications for Nonlinear Response. MRS Proceedings. 2008;1138:1138-FF03-30.

278. Chen DX, Sanchez A, Taboada E, Roig A, Sun N, Gu HC. Size determination of superparamagnetic nanoparticles from magnetization curve. Journal of Applied Physics. 2009;105(8):083924.

279. Ozkaya T, Toprak MS, Baykal A, Kavas H, Köseoğlu Y, Aktaş B. Synthesis of Fe3O4 nanoparticles at 100°C and its magnetic characterization. Journal of Alloys and Compounds. 2009;472(1):18-23.

280. Elkahky S, Lagat C, Sarmadivaleh M, Barifcani A. A comparative study of density estimation of asphaltene structures using group contribution methods and molecular dynamic simulations for an Australian oil field. Journal of Petroleum Exploration and Production Technology. 2019;9(4):2699-708.

281. Cai YP, Chesnel K, Trevino M, Westover A, Harrison RG, Hancock JM, et al. Orbital and spin moments of 5 to 11 nm Fe3O4 nanoparticles measured via x-ray magnetic circular dichroism. Journal of Applied Physics. 2014;115(17):17B537.

282. Pérez N, Bartolomé F, García LM, Bartolomé J, Morales MP, Serna CJ, et al. Nanostructural origin of the spin and orbital contribution to the magnetic moment in Fe3−xO4 magnetite nanoparticles. Applied Physics Letters. 2009;94(9):093108.

283. Ferrotec Corporation. Safety Data Sheet. EMG 1300M Polymer Coated Dry Magnetic Nanoparticles. 2019 [Available from: https://ferrofluid.ferrotec.com/wp-content/uploads/sites/3/emg1300sds.pdf.

284. Rajan A, Sharma M, Sahu NK. Assessing magnetic and inductive thermal properties of various surfactants functionalised Fe3O4 nanoparticles for hyperthermia. Scientific Reports. 2020;10(1):15045.

285. Wang S, Liu J, Zhang L, Masliyah J, Xu Z. Interaction Forces between Asphaltene Surfaces in Organic Solvents. Langmuir. 2010;26(1):183-90.

286. Natarajan A, Xie J, Wang S, Liu Q, Masliyah J, Zeng H, et al. Understanding Molecular Interactions of Asphaltenes in Organic Solvents Using a Surface Force Apparatus. The Journal of Physical Chemistry C. 2011;115(32):16043-51.

287. Abu Tarboush BJ, Husein MM. Adsorption of asphaltenes from heavy oil onto in situ prepared NiO nanoparticles. Journal of Colloid and Interface Science. 2012;378(1):64-9.

288. Wang J, van der Tuuk Opedal N, Lu Q, Xu Z, Zeng H, Sjöblom J. Probing Molecular Interactions of an Asphaltene Model Compound in Organic Solvents Using a Surface Forces Apparatus (SFA). Energy & Fuels. 2012;26(5):2591-9.

289. Klokkenburg M, Erné BH, Wiedenmann A, Petukhov AV, Philipse AP. Dipolar structures in magnetite ferrofluids studied with small-angle neutron scattering with and without applied magnetic field. Physical Review E. 2007;75(5):051408.

290. Bazyleva AB, Hasan MDA, Fulem M, Becerra M, Shaw JM. Bitumen and Heavy Oil Rheological Properties: Reconciliation with Viscosity Measurements. Journal of Chemical & Engineering Data. 2010;55(3):1389-97.

291. Wang Y, Wang W, Wang L. Understanding the relationships between rheology and chemistry of asphalt binders: A review. Construction and Building Materials. 2022;329:127161.

292. Eberhardsteiner L, Füssl J, Hofko B, Handle F, Hospodka M, Blab R, et al. Influence of asphaltene content on mechanical bitumen behavior: experimental investigation and micromechanical modeling. Materials and Structures. 2015;48(10):3099-112.

293. Pfeiffer JP, Saal RNJ. Asphaltic Bitumen as Colloid System. The Journal of Physical Chemistry. 1940;44(2):139-49.

294. Leontaritis KJ, Mansoori GA. Asphaltene Flocculation During Oil Production and Processing: A Thermodynamic Collodial Model. SPE International Symposium on Oilfield Chemistry1987. p. SPE-16258-MS.

295. Park SJ, Ali Mansoori G. Aggregation and Deposition of Heavy Organics in Petroleum Crudes. Energy Sources. 1988;10(2):109-25.

296. Dickie JP, Yen TF. Macrostructures of the asphaltic fractions by various instrumental methods. Analytical Chemistry. 1967;39(14):1847-52.

297. Mullins OC. The Modified Yen Model. Energy & Fuels. 2010;24(4):2179-207.

298. Redelius P. Asphaltenes in Bitumen, What They Are and What They Are Not. Road Materials and Pavement Design. 2009;10(sup1):25-43.

299. Cosultchi A, Bosch P, Lara V. Small-angle X-ray scattering study of oil- and deposit-asphaltene solutions. Colloid and Polymer Science. 2003;281(4):325-30.

300. Choi J, Nettesheim F, Rogers SA. The unification of disparate rheological measures in oscillatory shearing. Physics of Fluids. 2019;31(7):073107.

301. Hyun K, Wilhelm M, Klein CO, Cho KS, Nam JG, Ahn KH, et al. A review of nonlinear oscillatory shear tests: Analysis and application of large amplitude oscillatory shear (LAOS). Progress in Polymer Science. 2011;36(12):1697-753.

302. Wilhelm M. Fourier-Transform Rheology. Macromolecular Materials and Engineering. 2002;287(2):83-105.

303. Kamkar M, Salehiyan R, Goudoulas TB, Abbasi M, Saengow C, Erfanian E, et al. Large amplitude oscillatory shear flow: Microstructural assessment of polymeric systems. Progress in Polymer Science. 2022;132:101580.

304. Rogers SA, Lettinga MP. A sequence of physical processes determined and quantified in large-amplitude oscillatory shear (LAOS): Application to theoretical nonlinear models. Journal of Rheology. 2011;56(1):1-25.

305. Rogers SA. In search of physical meaning: defining transient parameters for nonlinear viscoelasticity. Rheologica Acta. 2017;56(5):501-25.

306. Yusoff NIM, Shaw MT, Airey GD. Modelling the linear viscoelastic rheological properties of bituminous binders. Construction and Building Materials. 2011;25(5):2171-89.

307. Shan L, He H, Wagner NJ, Li Z. Nonlinear rheological behavior of bitumen under LAOS stress. Journal of Rheology. 2018;62(4):975-89.

308. Olard F, Di Benedetto H. General “2S2P1D” Model and Relation Between the Linear Viscoelastic Behaviours of Bituminous Binders and Mixes. Road Materials and Pavement Design. 2003;4(2):185-224.

309. Di Benedetto H, Mondher N, Sauzéat C, Olard F. Three-dimensional Thermo-viscoplastic Behaviour of Bituminous Materials: The DBN Model. Road Materials and Pavement Design. 2007;8(2):285-315.

310. Gayte P, Di Benedetto H, Sauzéat C, Nguyen QT. Influence of transient effects for analysis of complex modulus tests on bituminous mixtures. Road Materials and Pavement Design. 2016;17(2):271-89.

311. Nguyen HM, Pouget S, Di Benedetto H, Sauzéat C. Time-temperature superposition principle for bituminous mixtures. European Journal of Environmental and Civil Engineering. 2009;13(9):1095-107.

312. Bird RB, Armstrong RC, Hassager O. Dynamics of polymeric liquids. Volume 1: fluid mechanics. A Wiley-Interscience Publication, John Wiley & Sons. 1987.

313. Giacomin AJ, Jeyaseelan RS, Samurkas T, Dealy JM. Validity of separable BKZ model for large amplitude oscillatory shear. Journal of Rheology 1993;37(5):811-26.

314. Padmarekha A, Chockalingam K, Saravanan U, Deshpande AP, Krishnan JM. Large amplitude oscillatory shear of unmodified and modified bitumen. Road Materials and Pavement Design. 2013;14(sup1):12-24.

315. Ewoldt RH, Hosoi AE, McKinley GH. New measures for characterizing nonlinear viscoelasticity in large amplitude oscillatory shear. Journal of Rheology. 2008;52(6):1427-58.

316. Dimitriou CJ, Ewoldt RH, McKinley GH. Describing and prescribing the constitutive response of yield stress fluids using large amplitude oscillatory shear stress (LAOStress). Journal of Rheology. 2013;57(1):27-70.

317. Wu Y, Huang P, Yu Y, Shi C, Chen H, Wang H, et al. Nonlinear rheological performance characterization of styrene-butadiene-styrene and crumb rubber composite modified bitumen using large amplitude oscillatory shear tests. Journal of Cleaner Production. 2023;385:135712.

318. Gulzar S, Castorena C, Underwood S. An investigation into the nonlinear rheological behavior of modified asphalt binders using large amplitude oscillatory shear rheology. International Journal of Pavement Engineering. 2023;24(1):2211211.

319. Gulzar S, Underwood BS. Nonlinear Viscoelastic Response of Crumb Rubber Modified Asphalt Binder Under Large Strains. Transportation Research Record. 2020;2674(3):139-49.

320. Cho KS, Hyun K, Ahn KH, Lee SJ. A geometrical interpretation of large amplitude oscillatory shear response. Journal of Rheology. 2005;49(3):747-58.

321. Giacomin AJ, Bird RB, Johnson LM, Mix AW. Large-amplitude oscillatory shear flow from the corotational Maxwell model. Journal of Non-Newtonian Fluid Mechanics. 2011;166(19):1081-99.

322. Klein CO, Spiess HW, Calin A, Balan C, Wilhelm M. Separation of the Nonlinear Oscillatory Response into a Superposition of Linear, Strain Hardening, Strain Softening, and Wall Slip Response. Macromolecules. 2007;40(12):4250-9.

323. Lee C-W, Rogers SA. A sequence of physical processes quantified in LAOS by continuous local measures. Korea-Australia Rheology Journal. 2017;29(4):269-79.

324. Park JD, Rogers SA. Rheological manifestation of microstructural change of colloidal gel under oscillatory shear flow. Physics of Fluids. 2020;32(6):063102.

325. Actis DG, Bruvera IJ, Pasquevich GA, Mendoza Zélis P. Fixed magnetic nanoparticles: Obtaining anisotropy energy density from high field magnetization. Journal of Magnetism and Magnetic Materials. 2022;563:169962.

326. Abu-Aljarayesh I, Al-Bayrakdar A, Mahmood SH. The effect of heating on the magnetic properties of Fe3O4 fine particles. Journal of Magnetism and Magnetic Materials. 1993;123(3):267-72.

327. Nguyen LH, Oanh VTK, Nam PH, Doan DH, Truong NX, Ca NX, et al. Increase of magnetic hyperthermia efficiency due to optimal size of particles: theoretical and experimental results. Journal of Nanoparticle Research. 2020;22(9):258.

328. García-Otero J, García-Bastida AJ, Rivas J. Influence of temperature on the coercive field of non-interacting fine magnetic particles. Journal of Magnetism and Magnetic Materials. 1998;189(3):377-83.

329. Duan H-y, Wang J, Li L, Aguilar V, Zhao G-m. Magnetic properties of barium ferrite nanoparticles: Quantitative test of the Stoner–Wohlfarth theory for uniaxial single-domain magnetic particles. Physics Letters A. 2013;377(38):2659-62.

330. Enpuku K, Elrefai AL, Yoshida T, Kahmann T, Zhong J, Viereck T, et al. Estimation of the effective magnetic anisotropy constant of multi-core based magnetic nanoparticles from the temperature dependence of the coercive field. Journal of Applied Physics. 2020;127(13):133903.

331. Poulos AS, Renou F, Jacob AR, Koumakis N, Petekidis G. Large amplitude oscillatory shear (LAOS) in model colloidal suspensions and glasses: frequency dependence. Rheologica Acta. 2015;54(8):715-24.

332. Poulos AS, Stellbrink J, Petekidis G. Flow of concentrated solutions of starlike micelles under large-amplitude oscillatory shear. Rheologica Acta. 2013;52(8):785-800.

333. Papadopoulos L, Porter MA, Daniels KE, Bassett DS. Network analysis of particles and grains. Journal of Complex Networks. 2018;6(4):485-565.

334. Hyun K, Nam JG, Wilhelm M, Ahn KH, Lee SJ. Nonlinear response of complex fluids under LAOS (large amplitude oscillatory shear) flow. Korea-Australia Rheology Journal. 2003;15(2):97-105.

335. Zákutná D, Graef K, Dresen D, Porcar L, Honecker D, Disch S. In situ magnetorheological SANS setup at Institut Laue-Langevin. Colloid and Polymer Science. 2021;299(2):281-8.

336. Pop LM, Odenbach S. Investigation of the microscopic reason for the magnetoviscous effect in ferrofluids studied by small angle neutron scattering. Journal of Physics: Condensed Matter. 2006;18(38):S2785.

337. Pop LM, Odenbach S, Wiedenmann A, Matoussevitch N, Bönnemann H. Microstructure and rheology of ferrofluids. Journal of Magnetism and Magnetic Materials. 2005;289:303-6.

338. Mao R, Wang X, Cai S, Zhang G, Wang J. Quantitative investigation on the nonlinear viscoelasticity of magnetorheological gel under large amplitude oscillatory shear. Colloids and Surfaces A: Physicochemical and Engineering Aspects. 2022;655:130293.

339. Li WH, Du H, Chen G, Yeo SH, Guo N. Nonlinear viscoelastic properties of MR fluids under large-amplitude-oscillatory-shear. Rheologica Acta. 2003;42(3):280-6.

340. Wang H, Chang T, Li Y, Li S, Zhang G, Wang J, et al. Characterization of nonlinear viscoelasticity of magnetorheological grease under large oscillatory shear by using Fourier transform-Chebyshev analysis. Journal of Intelligent Material Systems and Structures. 2020;32(6):614-31.

341. Kuzhir P, Gómez-Ramírez A, López-López MT, Bossis G, Zubarev AY. Non-linear viscoelastic response of magnetic fiber suspensions in oscillatory shear. Journal of Non-Newtonian Fluid Mechanics. 2011;166(7):373-85.

342. Gamota DR, Wineman AS, Filisko FE. Fourier transform analysis: Nonlinear dynamic response of an electrorheological material. Journal of Rheology. 1993;37(5):919-33.

343. Parthasarathy M, Klingenberg DJ. Large amplitude oscillatory shear of ER suspensions. Journal of Non-Newtonian Fluid Mechanics. 1999;81(1):83-104.

344. Monshi A, Foroughi MR, Monshi MR. Modified Scherrer Equation to Estimate More Accurately Nano-Crystallite Size Using XRD. World Journal of Nano Science and Engineering. 2012;02(03):154-60.

345. Wickman HH, editor Mössbauer Paramagnetic Hyperfine Structure. Mössbauer Effect Methodology; 1966 1966//; Boston, MA: Springer US.

346. Fock J, Bogart LK, González-Alonso D, Espeso JI, Hansen MF, Varón M, et al. On the 'centre of gravity' method for measuring the composition of magnetite/maghemite mixtures, or the stoichiometry of magnetite-maghemite solid solutions, via 57Fe Mössbauer spectroscopy. Journal of Physics D: Applied Physics. 2017;50(26):265005.

347. Kim W, Suh C-Y, Cho S-W, Roh K-M, Kwon H, Song K, et al. A new method for the identification and quantification of magnetite–maghemite mixture using conventional X-ray diffraction technique. Talanta. 2012;94:348-52.

348. Jørgensen J-E, Mosegaard L, Thomsen LE, Jensen TR, Hanson JC. Formation of γ-Fe2O3 nanoparticles and vacancy ordering: An in situ X-ray powder diffraction study. Journal of Solid State Chemistry. 2007;180(1):180-5.

349. Allia P, Coisson M, Tiberto P, Vinai F, Knobel M, Novak MA, et al. Granular Cu-Co alloys as interacting superparamagnets. Physical Review B. 2001;64(14):144420.

350. Roca AG, Marco JF, Morales MdP, Serna CJ. Effect of Nature and Particle Size on Properties of Uniform Magnetite and Maghemite Nanoparticles. The Journal of Physical Chemistry C. 2007;111(50):18577-84.

351. Santoyo Salazar J, Perez L, de Abril O, Truong Phuoc L, Ihiawakrim D, Vazquez M, et al. Magnetic Iron Oxide Nanoparticles in 10−40 nm Range: Composition in Terms of Magnetite/Maghemite Ratio and Effect on the Magnetic Properties. Chemistry of Materials. 2011;23(6):1379-86.

352. Kechrakos D, Trohidou KN. Interplay of dipolar interactions and grain-size distribution in the giant magnetoresistance of granular metals. Physical Review B. 2000;62(6):3941-51.

353. Moscoso-Londoño O, Tancredi P, Muraca D, Mendoza Zélis P, Coral D, Fernández van Raap MB, et al. Different approaches to analyze the dipolar interaction effects on diluted and concentrated granular superparamagnetic systems. Journal of Magnetism and Magnetic Materials. 2017;428:105-18.

354. Safronov AP, Beketov IV, Komogortsev SV, Kurlyandskaya GV, Medvedev AI, Leiman DV, et al. Spherical magnetic nanoparticles fabricated by laser target evaporation. AIP Advances. 2013;3(5):052135.

355. Dunlop DJ, Özdemir Ö. 5.08 - Magnetizations in Rocks and Minerals. In: Schubert G, editor. Treatise on Geophysics. Amsterdam: Elsevier; 2007. p. 277-336.

356. Nunes WC, Folly WSD, Sinnecker JP, Novak MA. Temperature dependence of the coercive field in single-domain particle systems. Physical Review B. 2004;70(1):014419.

357. Quantum Design. Correcting for the Absolute Field Error using the Pd Standard 2020 [Available from: https://qd-uki.co.uk/service-support/applications-team/.

358. Micha JS, Dieny B, Régnard JR, Jacquot JF, Sort J. Estimation of the Co nanoparticles size by magnetic measurements in Co/SiO2 discontinuous multilayers. Journal of Magnetism and Magnetic Materials. 2004;272-276:E967-E8.

359. Bruvera IJ, Mendoza Zélis P, Pilar Calatayud M, Goya GF, Sánchez FH. Determination of the blocking temperature of magnetic nanoparticles: The good, the bad, and the ugly. Journal of Applied Physics. 2015;118(18):184304.

360. D'Orazio F, Lucari F, Melchiorri M, de Julián Fernández C, Mattei G, Mazzoldi P, et al. Blocking temperature distribution in implanted Co–Ni nanoparticles obtained by magneto-optical measurements. Journal of Magnetism and Magnetic Materials. 2003;262(1):111-5.

361. Kahmann T, Rösch EL, Enpuku K, Yoshida T, Ludwig F. Determination of the effective anisotropy constant of magnetic nanoparticles – Comparison between two approaches. Journal of Magnetism and Magnetic Materials. 2021;519:167402.